INFORMATION TO USERS

This manuscript has been reproduced from the microfilm master. UMI films the text directly from the original or copy submitted. Thus, some thesis and dissertation copies are in typewriter face, while others may be from any type of computer printer.

The quality of this reproduction is dependent upon the quality of the copy submitted. Broken or indistinct print, colored or poor quality illustrations and photographs, print bleedthrough, substandard margins, and improper alignment can adversely affect reproduction.

In the unlikely event that the author did not send UMI a complete manuscript and there are missing pages, these will be noted. Also, if unauthorized copyright material had to be removed, a note will indicate the deletion.

Oversize materials (e.g., maps, drawings, charts) are reproduced by sectioning the original, beginning at the upper left-hand corner and continuing from left to right in equal sections with small overlaps.

ProQuest Information and Learning
300 North Zeeb Road, Ann Arbor, MI 48106-1346 USA
800-521-0600

THE EFFECTS OF AIR COOLING ON THE FILM BLOWING PROCESS

By

VASILEIOS SIDIROPOULOS, M. Eng.

A Thesis

Submitted to the School of Graduate Studies

in Partial Fulfillment of the Requirements

for the

Doctor of Philosophy Degree

McMaster University

THE EFFECTS OF AIR COOLING ON THE FILM BLOWING PROCESS

Doctor of Philosophy (2000) McMaster University

Chemical Engineering Hamilton, Ontario

TITLE: **The Effects of Air-Cooling on the Film Blowing Process**

AUTHOR: **Vasileios Sidiropoulos**

M. Eng.

SUPERVISOR: **Dr. J. Vlachopoulos**

NUMBER OF PAGES: **xviii, 260**

ABSTRACT

The present work is concerned with the numerical simulation of air-cooling in the film blowing process. In many film blowing production lines, film cooling is the limiting stage in achieving higher productivity. At the same time, the cooling air stream affects the stability and the shaping of the molten bubble, as well as the morphology of the final film product. The cooling process ultimately affects both production rate and final film properties.

The aerodynamics of the external cooling air and the effect of air-ring design and operational setup on the cooling efficiency were examined, using turbulent airflow simulations based on the k-ε theory. Both single and dual air rings designs were studied. The results suggest that the air-ring airflow is dominated by the Venturi and Coanda effects and that the airflow patterns are very sensitive to minor air-ring design modifications. The variation of heat transfer coefficients along the bubble surface has been examined in detail.

Additional numerical simulations were performed to evaluate the performance of a typical *internal bubble cooling* (IBC) configuration. Some of the limitations of typical IBC implementations were identified and attempts were made to improve the designs using the numerical simulation as an optimization tool. The results suggest that numerical

simulations can be used to gain valuable insight on the IBC operation. Numerical simulation can be helpful in reducing the number of trial and error steps during the design and implementation of IBC systems.

The development of sizeable temperature gradients inside the melt (in the film thickness direction) was investigated using numerical simulation. Typically, large air-cooling rates at the film surface combined with the low thermal conductivity of polymers lead to significant temperature differences between the internal and external film surfaces. The result indicate that the temperature differences in the film thickness direction may be very large and, therefore, important from a design and modeling perspective.

A new methodology to calculate the film stresses is proposed, in which the temperature variations in the thickness direction and their effects on melt rheology during the blowing are taken into account. The results indicate that the film reaches the crystallization temperature having stress differences in the thickness direction. At high production rates the stress differences became more pronounced. Since the film stresses are directly related with the crystallization kinetics, it is conjectured that the final film morphology and properties are affected by the predicted stress differences in the thickness direction.

ACKNOWLEDGMENTS

In completing the present work, I would like to express my appreciation to the people and organizations that helped me during my work:

- My supervisor, Dr. John Vlachopoulos of the Chemical Engineering Department, for his professional and personal guidance and support
- The members of my Ph.D. committee Dr. Andy Hrymak and Dr. Ioannis Tsanis for their help and insight
- The Chemical Engineering Department, the School of Graduate Studies, MRCO, NSERC and the Ontario Government, for the funding of the present work.
- Ms. Elizabeth Takacs, for her help, dedication to excellence and personal work
- Dr. H. H. Winter of University of Massachusetts, Amherst, for kindly providing the IRIS® software free of charge
- The Rheology & Materials Processing Centre of the Royal Melbourne Institute of Technology (RMIT) for conducting valuable rheological characterization of polymeric materials

- Robert Krycki and Peter Giddings of Future Designs Inc. for providing designs of their commercially available air-rings to be used in the simulations
- All of my current and former fellow co-workers in CAPPA-D, but most importantly Celine Bellehumeur, Sharif Farhad, Milica Rodic who were involved at various levels with the current work
- Last but not least, my wife Marianna for her kindness, support and personal work

TABLE OF CONTENTS

LIST OF TABLES AND FIGURES

CHAPTER 1.

AN OVERVIEW OF THE FILM BLOWING PROCESS

1.1. INTRODUCTION

Blown film extrusion is the most important process for the production of thin plastic film. Materials used range from low density polyethylene (LDPE), linear low density polyethylene (LLDPE), high density polyethylene (HDPE) to metallocene polyethylene (mPE), although several other polymers are sometimes used including ethylene copolymers, propylene copolymers, polyvinyl chloride (PVC), nylon and polypropylene homopolymer (Winkler [1997] and Knittel [1996]).

In this process the polymer is melted in an extruder and the hot melt is pumped through a die to form a thin-walled tube which is simultaneously axially drawn and radially expanded. In most installations the extruder(s) are horizontal and the blown film bubble is formed vertically upward as shown in figure 1. The bubble diameter at the freeze line is usually 1.2 to 4 times larger than the die diameter (blow up ratio, BUR). The hot melt is cooled by annular streams of high-speed air from air rings externally and sometimes internally. Extruder sizes range from 50 to 200 mm in diameter with L/D ratios from 20 to 34:1. The molten polymer is pumped through die lip gaps usually ranging from

0.76 to 3 mm and is subsequently drawn down to film thickness ranging from 0.01 to 0.5 mm. Die air ring systems usually range in diameter from 150 to 900 mm, although there are also installations as small as 50mm and as large as 2500 mm in diameter. Production rates with internal bubble cooling range from 0.1 to 0.35 kg/hr per mm of layflat tubing. Coextrusion of, usually, 3 to 7 layers (sometimes up to 11) is used for production of film for food packaging. The ever increasing demand for high production rates and high quality films has led to significant developments in materials and equipment which continue to widen the range of applications and markets for blown film.

1.2. Technological Developments

The widespread use of LLDPE in blown film extrusions, which started in the late 1970's, gave a big boost to the industry with LLDPE's excellent drawability and end use properties. However, LLDPE has poor melt strength and is prone to instability. Blends of LDPE/LLDPE at 70/30 ratio are frequently used to combine the best of both polymers (LDPE, melt strength and LLDPE, drawability). Melt strength represents the maximum tension that can be applied to the melt without rupture. Drawability is the ability of the melt to be drawn down to thin gages. The low elongational viscosity and weak strain hardening allows LLDPE to be downgaged from more than 2 mm to less than 0.02 mm.

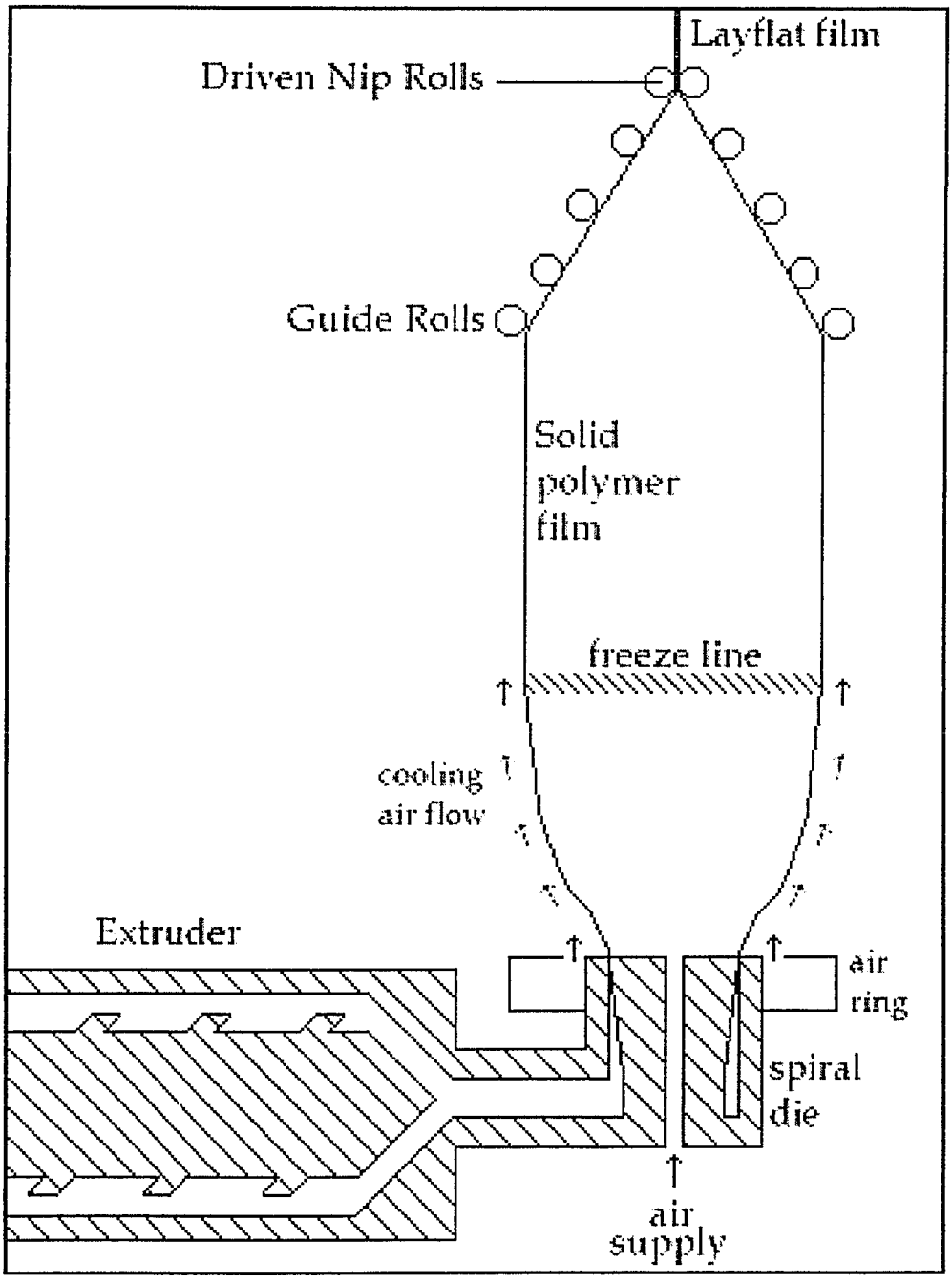

Figure 1: Schematic of the film blowing process (not to scale)

More recently the development of metallocene catalysts has led to a completely new generation of polyolefin grades with excellent end use properties. mPEs have narrower molecular weight distributions and are exhibiting less shear thinning than Ziegler-Natta polymers. Metallocene polymers have much lower melting and crystallization points. They are generally more difficult to process by film blowing installations than conventional polymers. Some grades that include long chain branching have also been developed, which are more shear thinning and partially improve processability. Still, a lot of fine-tuning of the equipment is required for successful blown film extrusion.

Side-fed dies are seldom used at present. *Spider* dies, which are so named from the *"spider"* legs that connect the mandrel to the body, are used for some applications that require tight tolerances. However, due to the axial forces on the mandrel support, sizes are limited. Also, *spider* dies produce film with undesirable weldlines behind the supports. In most blown film extrusion lines *spiral* mandrel dies are used (see figure 2). A variation of the spiral die is the type of die with the spiral on a flat surface [Perdikoulias et al, 1999]. Several such dies can be stacked for coextrusion applications. The objective of the die design is to distribute the polymer melt evenly around the annular die lips, so that thickness variations are minimized.

Bubble cooling is accomplished in most cases externally by tangentially impinging annular air jets. Relatively recent technological

developments involve dual-orifice air ring designs [Knittel & DeJonghe, 1992], which can increase the cooling capacity and stabilize low melt strength bubbles (like LLDPE).

Internal bubble cooling (IBC) is finding continuously increasing applications. Throughput rates can increase by 20% to 80% by retrofitting an existing installation with IBC, with large bubbles benefiting more than small bubbles [Knittel, 1996]. These developments in bubble cooling are extremely important because in most blown film extrusions the cooling capacity is the limiting factor [Knittel & DeJonghe, 1992].

Due to poor distribution in the die and uneven cooling after the melt exits the die lips there is always some gage variation. Systems have been developed to reduce this variation through flow modulation of the melt and/or the cooling air, but it is virtually impossible to eliminate it. Gage randomization (that is distribution of thick and thin bands) can be accomplished by employing various techniques involving rotation or oscillation of the nip collapser and bubble. Actually, some gage variation may be caused by creasing in the collapsing process, because the length elements around the bubble from the points where the bubble first touches the collapser to the nip line are not all the same (see figure 3).

The technological developments thus far have resulted in considerable growth in the film blowing industry and as the horizons expand new challenges are faced which require further development and innovation.

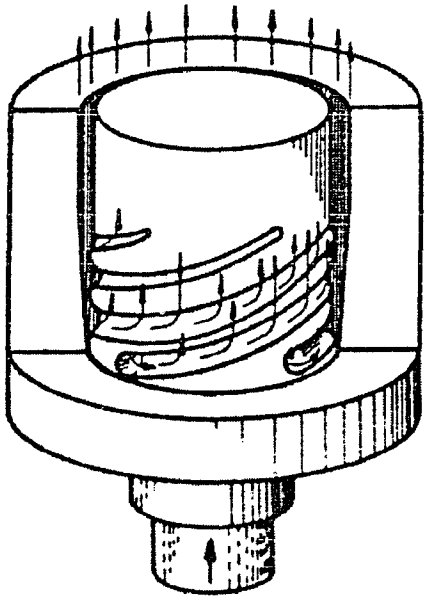

Figure 2: Operating principle of a *spiral* mandrel die

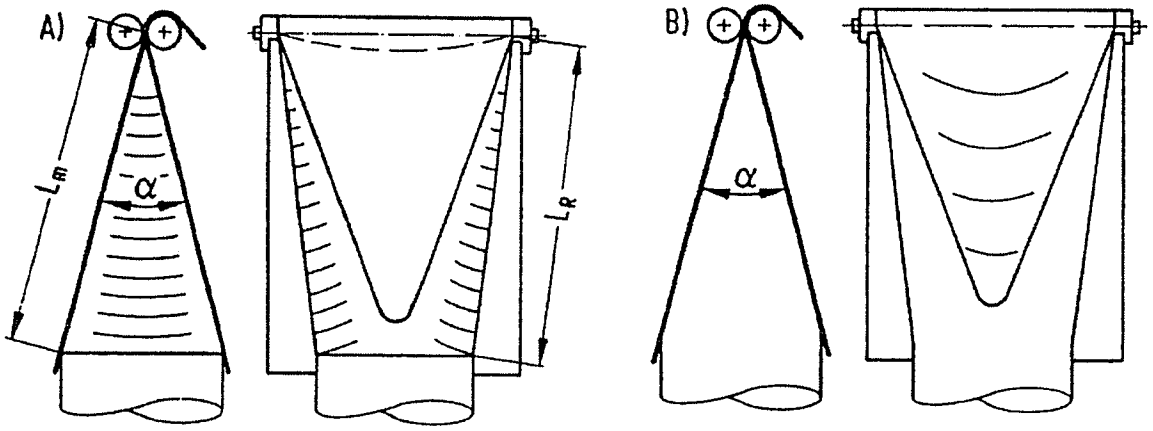

Figure 3: Creasing in the collapser resulting from:
a) length differences, b) friction

1.3. The Dynamics of Tubular Film Forming

As the molten polymer emerges from the annular die lips, the thin tube is undergoing unequal biaxial stretching. The deformation effectively ceases at the freeze line, because the stresses are not large enough to deform the solid film. On the basis of considerations for the usual production speeds and the thinness of the highly viscous melt, it is reasonable to neglect inertia forces, surface tension, air drag and gravity. Perhaps the neglect of gravity is the weakest assumption when high production rates are involved.

Figure 4 shows a sketch of an axisymmetric thin tubular film (of thickness h) with an embedded intrinsic coordinate system having unit vectors in the direction of flow **m** (*meridional*), in the *tangential* **t** and *normal* **n** directions.

Mathematical modeling of the process started with the work of Pearson & Petrie [1970a, 1970b, and 1970c]. Their approach is based on the thin membrane approximation in which the bubble is regarded as a thin shell in tension. The tension is produced by the axial traction and the pressure difference and is the driving force for the deformation of the film membrane. The thin membrane approach is almost universally followed in blown film modeling and is described in a number of publications including Tanner [1985], Han & Park [1975b], Kanai & White [1984, 1985], Cao & Campbell [1990] and many others reviewed by Sidiropoulos [1995].

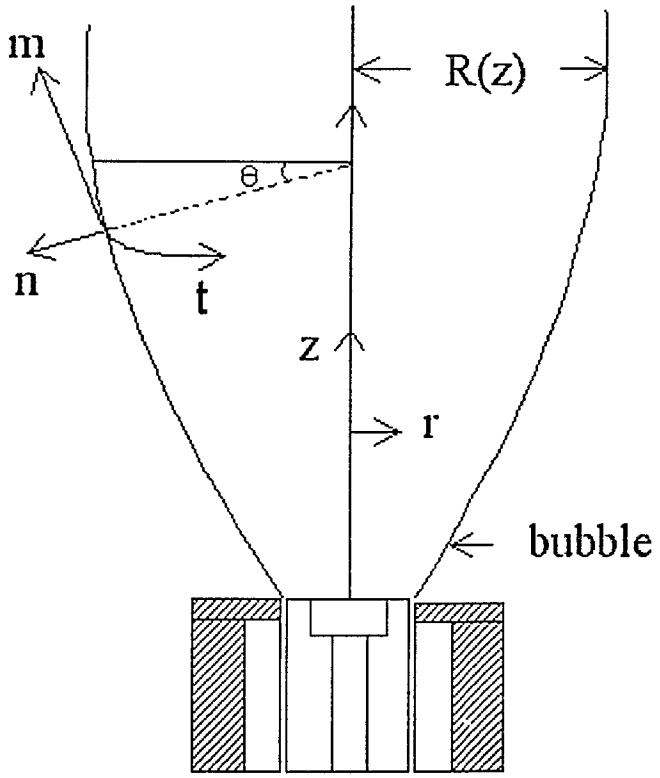

Figure 4: Blown film bubble and intrinsic coordinate system (n, m, t)

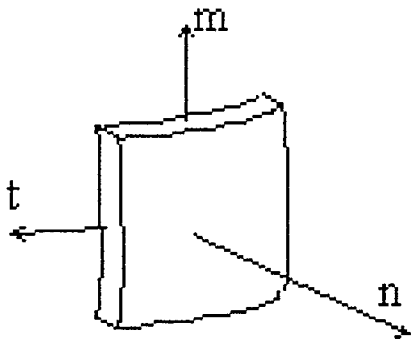

Figure 5: Element of film

Different modeling approaches (like the "quasi-cylindrical" model introduced by Liu et al, 1995) have also been suggested but so far have not been universally accepted.

In the thin membrane approximation mass conservation gives

$$Q = 2\pi R h V_m = \text{constant} \tag{1-1}$$

and upon taking the derivative with respect to **m** (the distance along the film)

$$\frac{dV_m}{dm} = -\frac{V_m}{h}\frac{dh}{dm} - \frac{V_m}{R}\frac{dR}{dm} \tag{1-2}$$

A small element of the film can be seen in figure 5. For such an element, there should be equilibrium of forces in all directions.

The equilibrium of forces in the normal direction for the thin membrane assumption is [Agassant et al, 1991]

$$\frac{\Delta P}{h} = \frac{\sigma_m}{\rho_m} + \frac{\sigma_t}{\rho_t} \tag{1-3}$$

where ρ_m, ρ_t are the curvatures in two directions m and t and ΔP is the inflation pressure.

$$\rho_m = -\left(1 + \left(\frac{dR}{dz}\right)^2\right)^{3/2}\left(\frac{d^2R}{dz^2}\right)^{-1} = -\frac{1}{\cos^3\theta}\left(\frac{d^2R}{dz^2}\right)^{-1} \tag{1-4}$$

$$\rho_t = R\left(1 + \left(\frac{dR}{dz}\right)^2\right)^{1/2} = \frac{R}{\cos\theta} \tag{1-5}$$

The force balance on any plane z gives,

$$-\pi R^2 \Delta P + 2\pi Rh\sigma_m \cos\theta = F_T = \text{constant} \qquad (1\text{-}6)$$

where F_T is the total force exerted on the thin membrane. If F_T and ΔP are known, the stress σ_m can be determined from equation 1-6 and stress σ_t from equation 1-3, i.e. from static equilibrium equations, irrespective of any constitutive equation.

1.3.1. The Newtonian Isothermal Model

By applying the Newtonian constitutive equation for the stresses to the thin membrane formulation, we finally obtain

$$\sigma_m = -\frac{\eta Q \cos\theta}{\pi Rh}\left(\frac{1}{R}\frac{dR}{dz} + \frac{2}{h}\frac{dh}{dz}\right) \qquad (1\text{-}7)$$

$$\sigma_t = \frac{\eta Q \cos\theta}{\pi Rh}\left(\frac{1}{R}\frac{dR}{dz} - \frac{1}{h}\frac{dh}{dz}\right) \qquad (1\text{-}8)$$

By substituting (1-7) and (1-8) into (1-3) and (1-6), a system of two non-linear ordinary differential equations is obtained [Tanner, 1985].

By introducing the dimensionless parameters $r=R/R_0$ and $w=h/h_0$, equation 1-6 reduces to:

$$\frac{w'}{w} = -\frac{r'}{2r} - \frac{Br^2 + F_c}{4}\left(1 + r'^2\right) \qquad (1\text{-}9)$$

where

$$F_c = \frac{F_T R_o}{\eta Q} \qquad \text{and,} \qquad B = \frac{\pi R_o^3 \Delta P}{\eta Q}$$

By substituting (1-9) into (1-3) a differential equation containing only the dimensionless radius r as the unknown is obtained

$$2r^2\left(Br^2 + F_c\right)r'' = 6r' + r\left(F_c - 3Br^2\right)\left(1 + r'^2\right) \qquad (1\text{-}10)$$

Integration of equation (1-10) provides a prediction of the bubble shape. At the die, the dimensionless radius and thickness have unit value (boundary conditions).

1.3.2. Non-Isothermal Considerations

The rate at which the tubular film is being cooled (mainly by the radial air jet(s) issuing from the air ring) has a great influence on the process because it determines the distance above the die where solidification is complete (freeze line height, FLH). Radiative heating may be responsible for as much as 20% of the heat transfer and must be taken into account. A heat balance using lumped formulation for the film [Han & Park, 1975b], gives

$$\rho C_p Q \cos\alpha \frac{dT}{dz} = -2\pi R\left(h_t\left(T - T_a\right) + \kappa\varepsilon\left(T^4 - T_a^4\right)\right) \qquad (1\text{-}11)$$

with $T=T_0$ at the die lips (boundary condition).

In equation 1-11, special consideration must be given to the local heat transfer coefficient h_t and the viscosity dependence on temperature.

Bubble shape and other kinematic variables can be reasonably well predicted [Sidiropoulos, 1995] by using h_t as a function of distance from the die lips and employing a modification of the Arrhenius expression for temperature dependence of viscosity.

1.3.3. Viscoelastic Considerations

The classical upper convected Maxwell model,

$$\boldsymbol{\tau} + \lambda \overset{\nabla}{\boldsymbol{\tau}} = 2\eta\dot{\gamma} \qquad (1\text{-}12)$$

has been used by Wagner [1976], Gupta [1980], Luo & Tanner [1985], Cain & Denn [1988] and others. The approach is generally similar to that used for the Newtonian simulations with additional complications introduced by viscoelasticity. These make the integration highly unstable, even at relatively low Weissenberg numbers. For the low Weissenberg number range examined by various investigators [Tanner, 1985 and André et al, 1998] the effect of viscoelasticity is to decrease the ultimate bubble radius.

There have also been several publications using different constitutive equations [Cao & Campbell (1990), Ashok & Campbell (1992), Cain & Denn (1988), Tas (1994) and others], including advanced integral models [Alaie & Papanastasiou, 1993]. All the constitutive equations are introduced in the same stress balance equation as explained in the beginning of this section. Authors have also noted the existence of multiple solutions [Cain & Denn (1988), André et al (1998)].

1.4. Process Stability

In film blowing flow instabilities limit the production rate and the quality of the film produced. The phenomena of sharkskin and melt fracture are known to commence when a critical wall shear stress is exceeded at the die lips. The critical value from laboratory experiments with capillaries is usually reported as 0.14 MPa, while in industrial installations much higher values are attained with the use of various additives, such as fluorocarbon polymers for LLDPE. In other processes involving polymer melt stretching such as melt spinning and film casting the phenomenon of draw resonance might be present under certain conditions. Draw resonance is a periodic fluctuation of diameter (in melt spinning) or thickness (in film casting). There have not been any relevant studies on draw resonance phenomena in film blowing.

Experimental studies on bubble stability have been reported by Han & Park [1975b] and Kanai & White [1984]. Kanai & White's results indicate that LDPE is more stable than LLDPE and HDPE. This is explained by the strong strain-hardening behavior of LDPE in extension. In industrial practice, it is well known that low melt strength materials (like LLDPE) are prone to instabilities. Dual air rings are used to control stability. It appears that stability modeling relevant to blown film production should involve the coupling of aerodynamics of air cooling and the rheology of biaxial stretching of the polymer melt. No such studies have ever been reported in the open literature thus far. However,

various types of devices and control systems have been developed for maintenance of process stability and film quality over the entire production cycle of industrial blown film lines.

1.5. NOMENCLATURE FOR CHAPTER 1

ρ : density
$\dot{\gamma}$: rate of deformation tensor
ε : emissivity
θ : slope of bubble profile
κ : Stefan-Boltzmann constant
λ : relaxation time
η : viscosity
$\boldsymbol{\tau}$: extra stress tensor
B : dimensionless pressure
C_p : heat capacity
F_c : dimensionless draw force
F_T : total force on the shell
h : film thickness
h_t : heat transfer coefficient
Q : volumetric flow rate
R : bubble radius
r : dimensionless radius
T : temperature
T_∞ : ambient air temperature
V : film velocity
w : dimensionless thickness
z : axial distance from the die
ΔP : inflation pressure
σ : total stress

Subscript o denotes values at the die lips (z=0)
Subscript L denotes values at the frost line (z=L=FLH)
Prime (') denotes derivative in the axial direction (i.e. $\varphi' = d\varphi/dz$)

CHAPTER 2.

EXTERNAL BUBBLE COOLING

The film blowing process has been the subject of many papers from the early seventies to the present day. Despite the plethora of theoretical and experimental papers, the cooling of the film bubble has not received the appropriate attention. The mechanisms of bubble cooling are not entirely understood and therefore there is little information on the influence cooling has on bubble formation, stability and film properties.

2.1. INTRODUCTION

The air cooling system is an integral part of any blown film line. It greatly affects not only the heat transfer from the molten polymer film but also the stability and the shaping of the bubble. The importance of the heat transfer in the modeling of film blowing has been examined by some researchers [Ast (1976), Butler et al (1994), Campbell et al (1992), Cao et al (1989), and Petrie (1975)]. Film cooling ultimately affects both production rate and final film properties. Most modern air ring designs are quite complex, based on an abundance of design techniques and patents. Although air-rings offer a certain flexibility in adjusting some of the air flow settings, the adjustment itself is a rather empirical process perfected by experience. Figure 6 shows the geometry of a typical air ring.

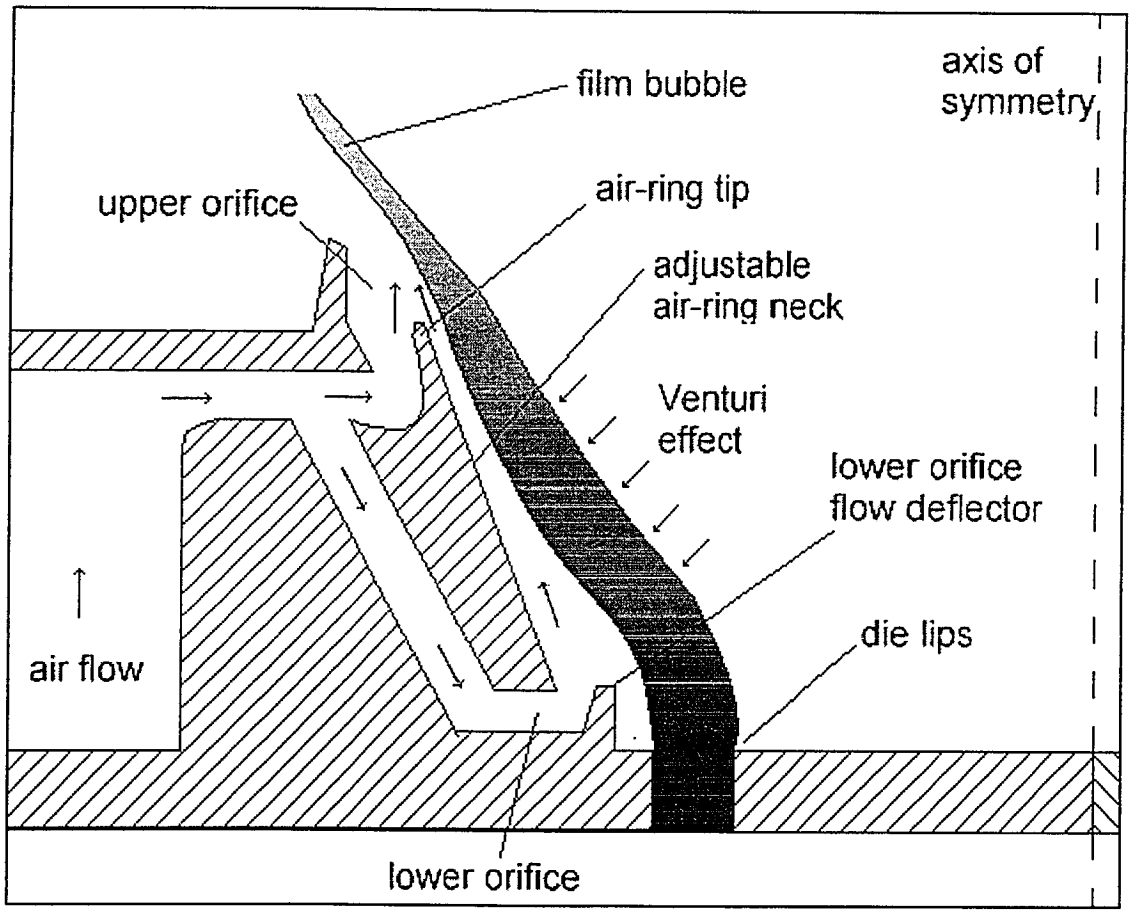

Figure 6: Geometrical details of a typical dual orifice air-ring (not to scale)

2.2. LITERATURE REVIEW

Isothermal models for film blowing (based on the balance of forces with the thin membrane approximation) started with the work of Petrie & Pearson [1970a,b,c]. Later, Petrie [1975] introduced a non-isothermal rheological model. Ast [1976] was the first one to attempt a solution of the energy equation. Wagner [1976] and Cao & Campbell [1990] introduced non-linear, non-isothermal, viscoelastic models. They realized the importance of the film temperature as a modeling parameter.

Some research has also been done on the experimental aspects of film cooling. Kanai & White [1985] studied the effect of cooling rate on crystallization. Cao et al [1989] measured the temperature gradients in the normal direction, while Nagarajan & Campbell [1995] measured transient heat transfer coefficient profiles on a *rigid bubble model.*

In most of the previous studies heat transfer has been examined semi-empirically without focusing on the actual transport mechanisms. A full analysis for the convective heat transfer (as imposed by the cooling air stream) has not been performed. Similarly, forces imposed by the cooling air and their effects on the formation of the blown film bubble have been largely neglected. Campbell et al [1992] addressed the problem by introducing a full aerodynamic analysis on the cooling air (momentum and heat transfer) by using the method of superposition of stream functions as well as macro-balances of mass and energy. Their approach had only limited success.

In the late 90's, Wolf et al [1997] and Feron et al [1997] used the finite element method to solve the equations for jets impinging on a blown film bubble using a single orifice topology. Sidiropoulos et al [1999] used numerical simulation to compare the cooling profiles of single and dual orifice air-rings. Also, Hauck & Michaeli [1998] carried out an experimental investigation of film cooling and proposed an analytical model for the calculation of the heat transfer coefficients. More recently, Akaike et al [1999] simulated a single orifice air ring and attempted to estimate how the cooling air affects the bubble formation.

2.3. The Venturi and Coanda Effects

Two important aerodynamic phenomena are associated with the cooling airflow, namely the ***Venturi*** and ***Coanda*** effects. The well known **Venturi effect** is caused when a fluid flows through a constricted area: its speed increases and the pressure drops (figure 7). In film blowing, the bubble is pulled by the partial vacuum towards the walls of the air ring.

The less known **Coanda effect** [Bourque & Newman, 1960] occurs when a free jet emerges close to a surface: the jet tends to bend, "attach" itself and flow along the surface. The surface may be flat or curved and located inclined or offset to the jet (figure 8). The Coanda effect is more pronounced near curved surfaces, and blown film bubble surfaces with the cooling air impinging on them at an angle, offer the possibility of appearance of the Coanda effect [Wright, 1981].

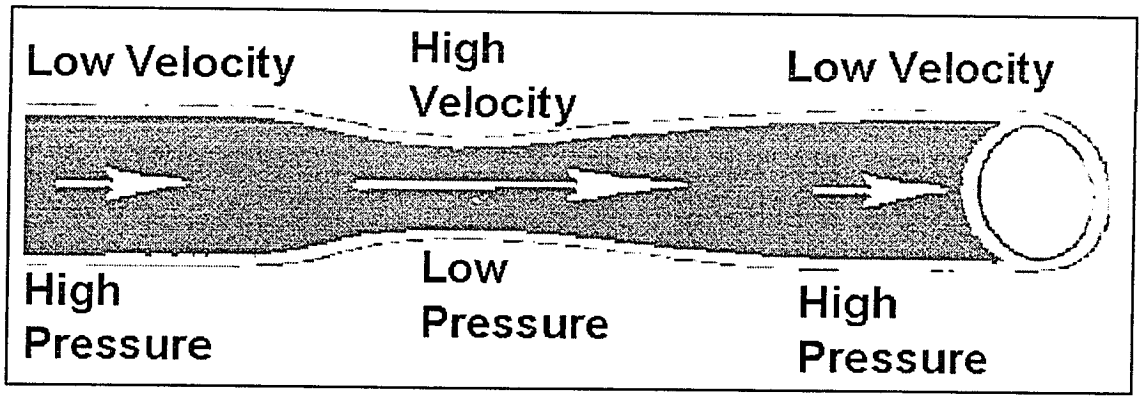

Figure 7: *Venturi effect*: when a fluid flows through a constricted area its speed increases and the pressure drops

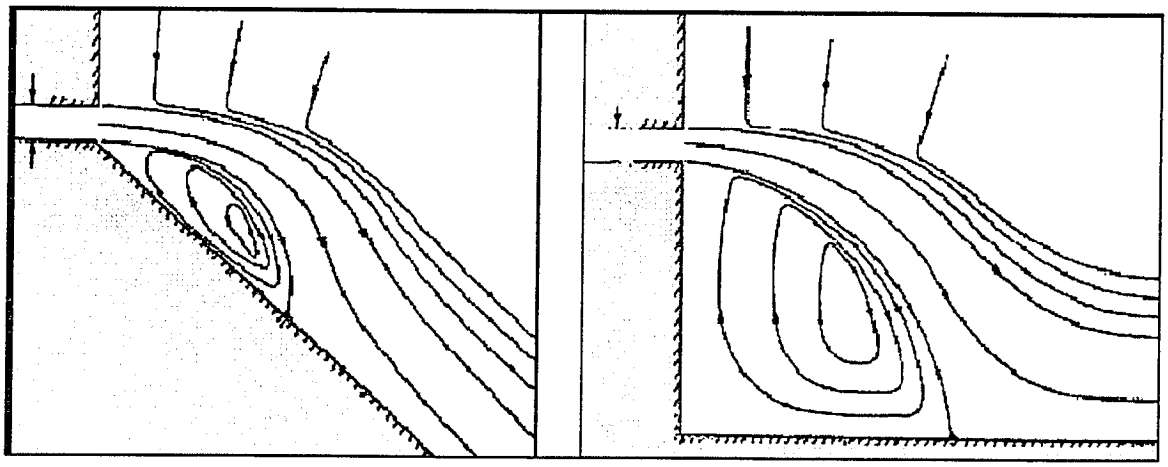

Figure 8: *Coanda effect*: a free jet emerging from a nozzle will tend to "attach" itself and flow along an inclined or offset nearby surface (flat or curved)

2.4. THEORY

The momentum transfer in the cooling air stream is determined by solving the Navier-Stokes equations given by

$$\frac{\partial(\rho u_i)}{\partial t}+\frac{\partial(\rho u_i u_j)}{\partial x_j}=\frac{\partial}{\partial x_j}\left[\mu\left(\frac{\partial u_i}{\partial x_j}+\frac{\partial u_j}{\partial x_i}\right)-\left(\frac{2}{3}\mu\frac{\partial u_k}{\partial x_k}\right)\right]-\frac{\partial p}{\partial x_i}+\rho g_i \qquad (2\text{-}1)$$

For a turbulent flow Reynolds decompositioncan be applied, where the instantaneous velocity is decomposed into the sum of a mean flow and velocity fluctuations ($u_i=U_i+u_i$□) and subsequently averaging equation 2-1 we get the transport equation:

$$\frac{\partial(\rho U_i)}{\partial t}+\frac{\partial(\rho U_i U_j)}{\partial x_j}=\frac{\partial}{\partial x_j}\left[\mu\left(\frac{\partial U_i}{\partial x_j}+\frac{\partial U_j}{\partial x_i}\right)-\left(\frac{2}{3}\mu\frac{\partial U_k}{\partial x_k}\right)\right]-\frac{\partial p}{\partial x_i}+\rho g_i+\frac{\partial}{\partial x_j}\left(-\rho\overline{u_i' u_j'}\right) \qquad (2\text{-}2)$$

Equation 2-2 has the same form as equation 2-1 but employs time averaged (instead of instantaneous) velocities or properties. Most of the fluctuating velocities vanish since the average of a fluctuating property is zero by definition. The effect of turbulence is included in the last term of equation 2-2 through the Reynolds stresses ($-\rho\overline{u_i' u_j'}$), which involve *products* of the velocity fluctuations and do not vanish with averaging.

A turbulent model expressing Reynolds stresses in terms of mean flow quantities has to be used to *close* the equations. In the current work the Renormalization Group (RNG) k-ε model was employed to achieve closure. The family of k-ε models is very frequently used in literature to

simulate fluid flows. The equations of motion constitute a modified system of Navier-Stokes equations in which there is a modified (effective) viscosity, modified force, and modified non-linear coupling [Fluent, 1996]. The RNG k-ε model is derived using a rigorous statistical technique (renormalization group theory) that employs a scale elimination procedure to avoid computational problems associated with small-scale eddies. The resulting model has a modified ε equation, accounts for low-Reynolds flow regions in the computational domain and calculates the turbulent Prandtl numbers through an analytical formula. Additionally, the scale elimination provides an effective method of calculation for relatively coarse grids at high Reynolds numbers, since excessive grid refinement may result in extremely large computational times and/or convergence difficulties.

The contribution of Reynolds stresses to the momentum balance is introduced through the concept of the *effective viscosity* (Boussinesq approximation). The effective viscosity is the sum of the molecular and the *turbulent* (or *eddy*) viscosity. It is defined in a manner *similar* to the molecular viscosity as a *turbulent exchange coefficient for momentum* [Tennekes & Lumley, 1997]. The approximation makes possible the calculation of turbulent stresses as the product of the turbulent viscosity and the local mean shear rate. Note that while the molecular viscosity is a property of the fluid with values known irrespective of flow conditions,

the turbulent viscosity is a property of the turbulent flow and is strongly dependent on the turbulent transport mechanism in the flow.

The effective viscosity in the RNG *k-ε* model is given by

$$\mu_{eff} = \mu + \mu_{tur} = \mu\left[1 + k\sqrt{\frac{\rho C_\mu}{\mu\varepsilon}}\right]^2 \qquad (2\text{-}3)$$

This relationship is applicable in both the high and low Reynolds region, making the model an excellent tool to predict a wide variety of flows. For high Re flows, $\mu_{tur} >> \mu$ and equation 2-3 may be simplified to yield

$$\mu_{eff} \approx \mu_{tur} = \rho C_\mu \frac{k^2}{\varepsilon} \qquad (2\text{-}4)$$

The simplified equation (2-4) is identical to the effective viscosity equation of the standard *k-ε* model. For the RNG *k-ε* model, the value of the constant is C_μ=0.0845 (derived analytically using RNG theory). This value is remarkably close to the 0.09 value of the standard *k-ε* model (empirically determined to fit an assortment of experimental data).

Using the concept of the *effective* viscosity the mean momentum equation for a two-dimensional flow becomes

$$\frac{\partial(\rho U_i)}{\partial t} + \frac{\partial(\rho U_i U_j)}{\partial x_j} = \frac{\partial}{\partial x_j}\left[\mu_{eff}\left(\frac{\partial U_i}{\partial x_j} + \frac{\partial U_j}{\partial x_i}\right)\right] - \frac{\partial p}{\partial x_i} \qquad (2\text{-}5)$$

The transport equations for turbulent kinetic energy and dissipation rate are derived based on similarity analysis (on the assumption that their *effective* diffusion is *similar* to the diffusion of the momentum equation)

$$\frac{\partial(\rho k)}{\partial t}+\frac{\partial(\rho u_i k)}{\partial x_i}=\frac{\partial}{\partial x_i}\left[\alpha\mu_{eff}\frac{\partial k}{\partial x_i}\right]-2\mu_{tur}S_{ij}S_{ij}-\rho\varepsilon \qquad (2\text{-}6)$$

where $S_{ij}=\frac{1}{2}\left(\frac{\partial U_i}{\partial x_j}+\frac{\partial U_j}{\partial x_i}\right)$ is the mean rate-of-strain tensor and

$$\frac{\partial(\rho\varepsilon)}{\partial t}+\frac{\partial(\rho U_i\varepsilon)}{\partial x_i}=\frac{\partial}{\partial x_i}\left[\alpha\mu_{eff}\frac{\partial\varepsilon}{\partial x_i}\right]-2C_{1\varepsilon}\frac{\varepsilon}{k}\mu_{tur}S_{ij}S_{ij}-C_{2\varepsilon}\rho\frac{\varepsilon^2}{k}-R \qquad (2\text{-}7)$$

where R is given by

$$R=\frac{C_\mu\rho\eta^3\left(1-\frac{\eta}{\eta_0}\right)\varepsilon^2}{\left(1+0.012\eta^3\right)k} \qquad (2\text{-}8)$$

with $\eta=Sk/\varepsilon$, $\eta_0=4.38$

The constants of equation 2-7 can be analytically derived as $C_{1\varepsilon}=1.42$, $C_{2\varepsilon}=1.68$ using the RNG theory. For the calculation of the inverse turbulent Prandtl number (α) in equations 2-6 and 2-7, the RNG theory provides the following formula

$$\left(\frac{\alpha-1.3929}{\alpha_o-1.3929}\right)^{0.6321}\left(\frac{\alpha+2.3929}{\alpha_o+2.3929}\right)^{0.3679}=\frac{\mu}{\mu+\mu_{tur}} \qquad (2\text{-}9)$$

where $\alpha_o=1$. For high Reynolds flows the right hand side of equation 2-9 is very small, and the inverse Prandtl number becomes $\alpha\approx1.3929$

A *similar* to momentum transport equation can also be applied for the turbulent transport of energy, which in simplified form can be written as,

$$C_p\left(\frac{\partial(\rho T)}{\partial t}+\frac{\partial(\rho U_i T)}{\partial x_i}\right)=\frac{\partial}{\partial x_i}\left[\alpha_h\mu_{eff}C_p\frac{\partial T}{\partial x_i}+U_j\mu_{eff}\left(\frac{\partial U_i}{\partial x_j}+\frac{\partial U_j}{\partial x_i}\right)\right] \quad (2\text{-}10)$$

where α_h is the inverse turbulent Prandtl number for heat transfer (calculated using equation 2-9 and $\alpha_o=k/\mu C_p$).

In the viscosity affected near-wall region, the computational grid was resolved all the way to the viscous sublayer. In the calculation, the domain is automatically subdivided into a fully turbulent region and a viscosity-affected region. In order to mark the two regions, the wall-distance based turbulent Reynolds number is defined,

$$Re_y=\frac{y\rho\sqrt{k}}{\mu} \quad (2\text{-}11)$$

For $Re_y>200$ (fully turbulent region) the RNG k-ε model (as described above) was employed. For the near wall region ($Re_y<200$) the *one-equation* model proposed by Wolfstein [1969] was employed. In the Wolfstein (near-wall) model equations 2-3 and 2-7 are simplified to

$$\mu_{eff}=\rho C_\mu\sqrt{k}\ell_\mu \quad (2\text{-}12)$$

and,

$$\varepsilon = \frac{k^{3/2}}{\ell_\varepsilon} \tag{2-13}$$

We define the length scales in equation 2-13 as [Chen & Patel, 1988]

$$\ell_\mu = yc_\ell \left[1 - exp\left(-\frac{Re_y}{A_\mu} \right) \right] \tag{2-14}$$

and,

$$\ell_\varepsilon = yc_\ell \left[1 - exp\left(-\frac{Re_y}{A_\varepsilon} \right) \right] \tag{2-15}$$

where,

$$c_\ell = \kappa C_\mu^{-3/4} \tag{2-16}$$

The constants in equations 2-14 and 2-15 are taken from Chen & Patel [1988]: A_μ=70, A_ε=2c_ℓ and κ is the Von Karman constant (0.42). Increased nodal density was used in the near-wall region to adequately capture the wall effect.

The heat transfer to the walls is calculated by using equation 2-10. The temperature derivative is calculated from the derivatives of the log-law formulation (based on the *similarity* between momentum and heat transfer [Launder & Spalding, 1974]).

2.5. Single Vs. Dual Orifice Air Rings

2.5.1. Simulation Methodology

A comparative study of the characteristics and performance of single and dual orifice air-rings has been performed. Typical designs found in the literature [Knittel & DeJonghe, 1992] were used to construct the computational grids. Both designs use direct impingement to achieve their cooling effect. Figure 9 shows an ordinary single orifice air-ring with neck, while figure 10 depicts a dual orifice air ring. The applied bubble shape is the same for both simulations and is obtained from typical LLDPE film blowing experiment [Butler et al, 1994] with blow up ratio (BUR) equal to 3. The spiral die radius is 10 cm (4") and the frost line height is 60 cm. The simulated air-rings have a height of 12 cm (equal to the height of the experimental air-ring). The airflow simulation was implemented using a finite volume computational method (FLUENT®).

In the simulation, the cooling air enters the computational domain with predetermined velocity (design parameter) and temperature (35°C). The initial turbulent intensity is set to 10%. The density of the air is assumed to be a function of both pressure and temperature. The ambient temperature is set to 27°C. The film wall is considered solid with a temperature that is gradually dropping in the axial direction. The implemented temperature profile is also based on the published experimental data [Butler et al, 1994].

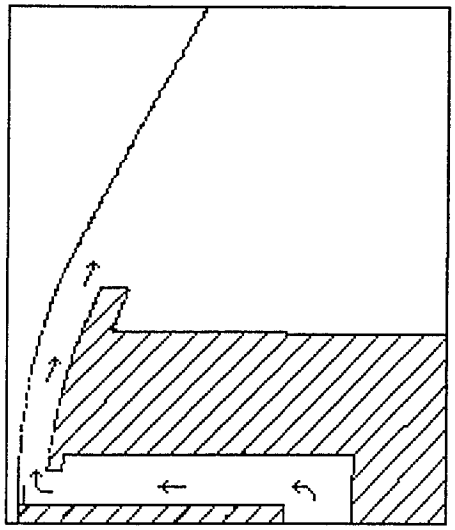

Figure 9: Single orifice air-ring with neck

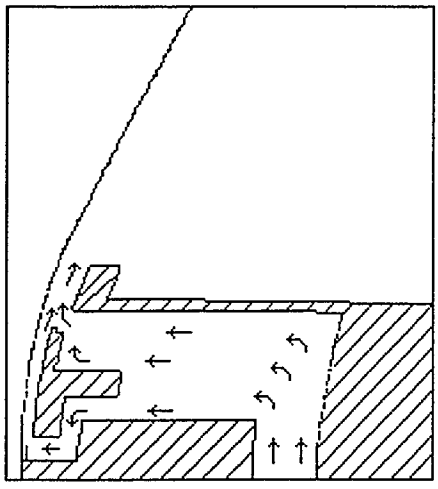

Figure 10: Simple dual orifice air ring

2.5.2. Results and Discussion

Numerical simulations were obtained for a relatively moderate air-flow rate (50 liters-of-air/s) which produces air velocities close to 10m/s at the tip (higher lip) of the air ring. The calculated streamlines for both the single and the dual orifice air-rings are shown in figure 11. In both cases the flow pattern is quite consistent after the cooling air leaves the air ring. Flow streamlines remain closely bound to the film wall and follow its curvature (Coanda effect). As the jet travels further from the air ring, entrainment of ambient air is making the wall jet wider and forces it to slow down. By the time the cooling air reaches the frost line its velocity has decreased by approximately an order of magnitude in comparison to the maximum velocity (located close to the tip of the air-ring). For both the studied cases the maximum air velocity was approximately 10 m/s, while the velocity in the vicinity of the frost line was less than 2 m/s.

The pressure induced on the film surface by the cooling-air flow was calculated. Figure 12 shows the gauge pressure profile along the film wall for the single and dual orifice air-rings. There is significant difference between the two pressure profiles.

The simulation for the single orifice air-ring shows an initial over-pressure which is created as the air flow changes direction to align with the film surface. Immediately after, the flow is forced to pass through the narrow gap between the air ring and the film. The ensuing flow acceleration generates a Venturi effect, creating a sudden under-pressure

inside the narrow gap. The gauge pressure stays negative for the total length of the gap, linearly approaching zero as the flow moves closer to the tip of the air-ring. The under-pressure reaches a maximum of about 25 Pa inside the air ring. This is nearly 30% of a typical LLDPE inflation pressure and seriously influences the bubble formation.

The calculated pressure for the dual orifice air ring reveals that a similar under-pressure is not observed. Most of the cooling air is ejected through the higher orifice and impinges directly on the film bubble. Since the angle of impingement is rather high, a percentage of the upper orifice flow tends to flow backwards in the gap (towards the lower lip). This is causing a congestion with the small amount of air that is emerging from the lower orifice and creates a significant over-pressure (instead of under-pressure) inside the gap between the air-ring neck and the film. The value of over-pressure (35 Pa) is quite significant in comparison to typical inflation pressures and may influence the bubble formation. At the exit of the air ring the relative pressure suddenly drops to zero.

The calculated pressure profiles are in agreement with visual observations found in the literature about the effect the air ring type has on bubble shape [figure 13, Knittel & DeJonghe, 1992]. In a single orifice configuration, the part of the film wall that is located close to the Venturi affected area tends to move towards the air ring (due to the calculated under-pressure), while in a dual orifice air-ring the bubble tends to move away from the air ring (this time due to the over-pressure).

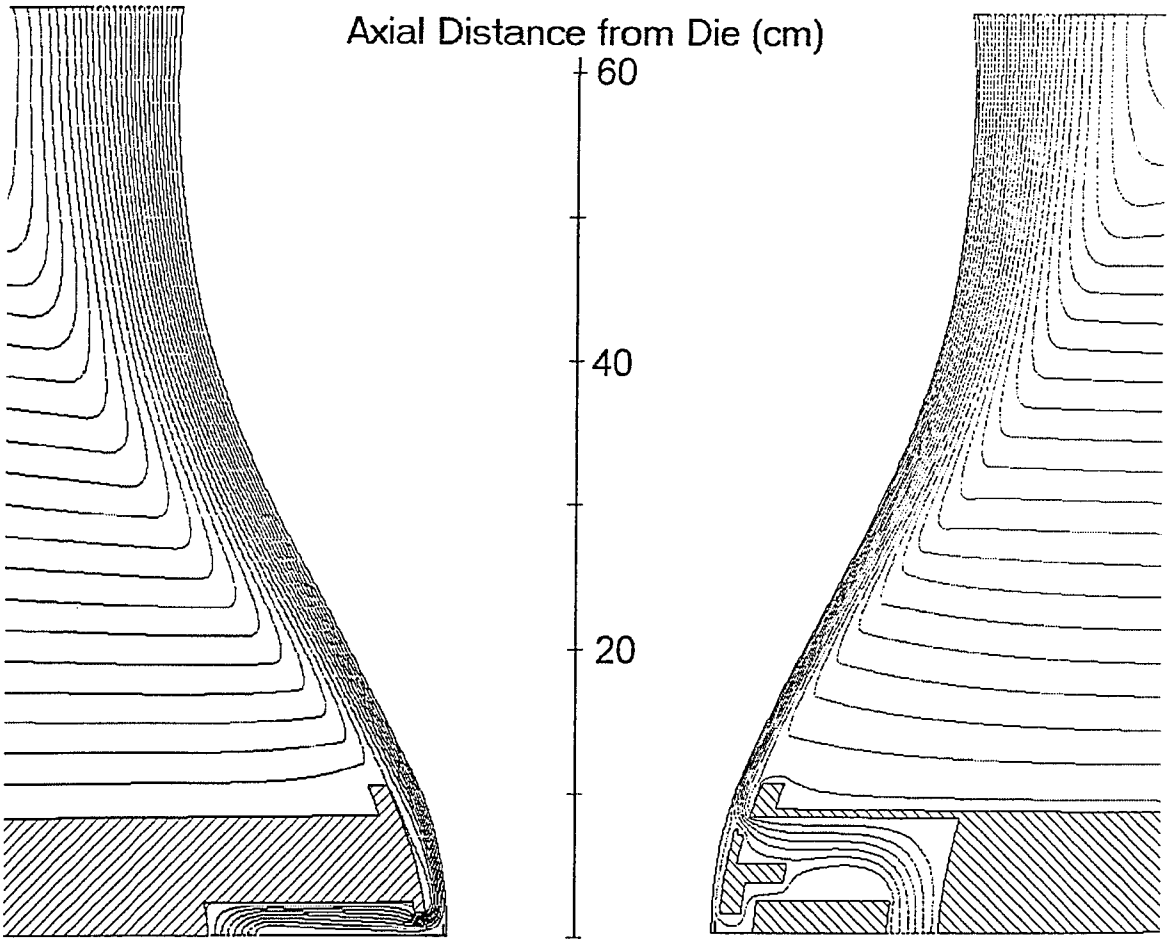

Figure 11: Calculated cooling air streamlines:

Left side: Single orifice air-ring,

Right side: Direct impingement dual orifice air-ring

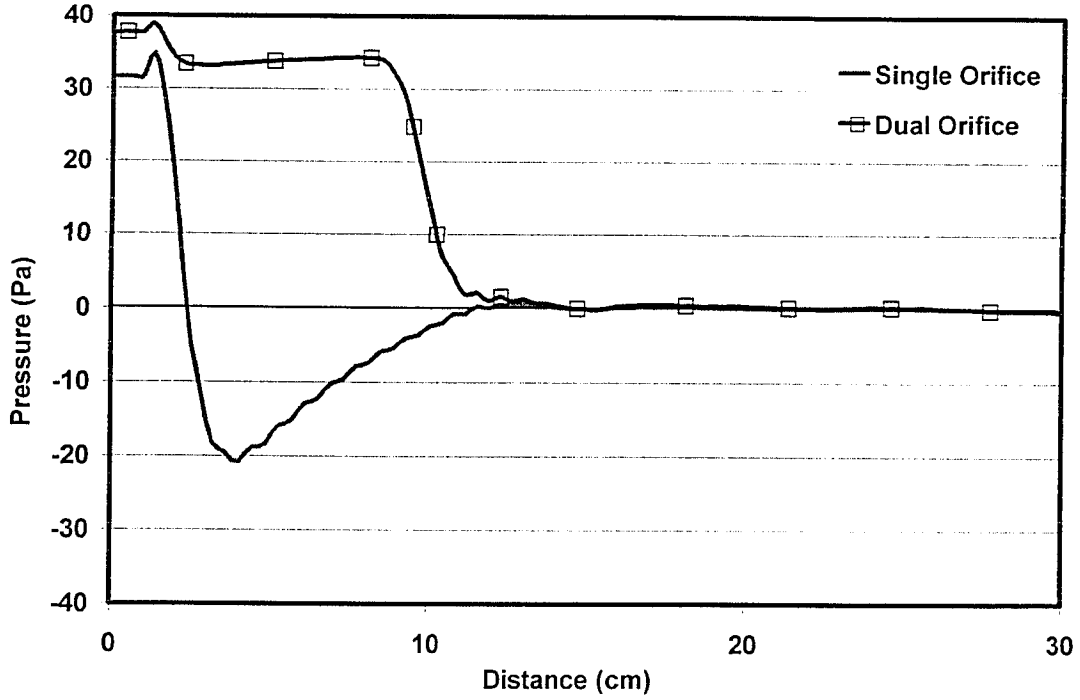

Figure 12: Gauge static pressure on the bubble surface

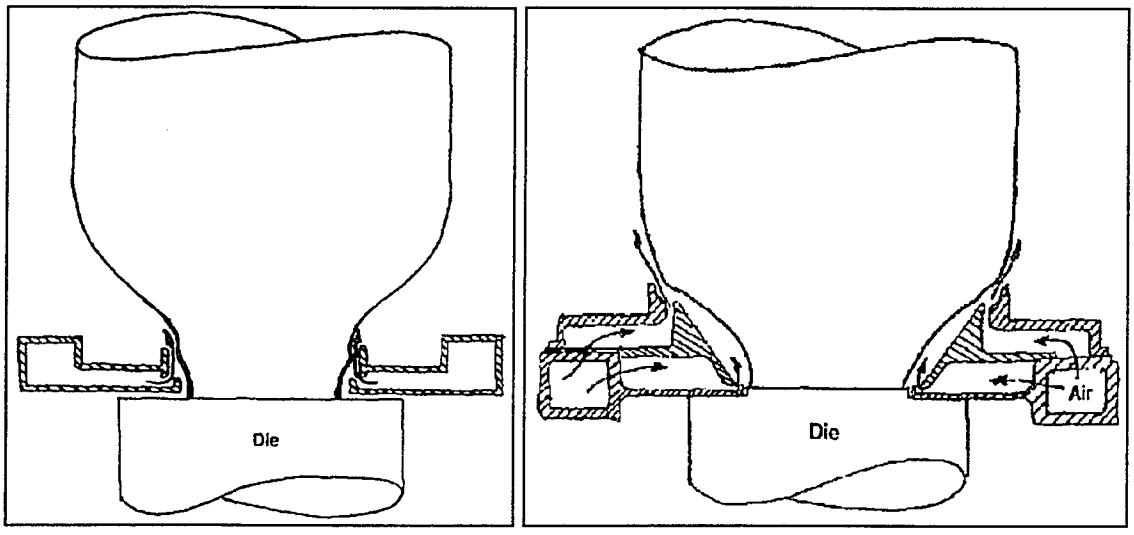

Figure 13: Drawings based on empirical observations are showing the effect of air-ring type to the bubble shape [Knittel & DeJonghe, 1992]

The calculated heat transfer coefficients on the film surface are presented on figure 14 as functions of the axial distance. The difference in the axial cooling profiles is noticeable. In the single orifice air-ring most of the heat transfer takes place very early (almost immediately after the hot film emerges from the die lips) and gradually decreases at higher axial distances. The maximum heat transfer coefficient coincides with the point where the flow changes direction to align with the bubble surface.

The heat transfer coefficient profile is different in the case of the simulated dual orifice system. This is expected as most of the flow chooses the path of least resistance and emerges through the higher orifice, leaving only a fraction of the total flow to pass through the lower orifice (figure 11). At the height of the lower lip of the air ring there is an early peak that is caused by the lower orifice flow and is similar in nature to the peak calculated in the single orifice simulation. However, due to the reduced flow volume, the peak is smaller and much narrower than the peak observed in the single orifice case. As was expected the higher orifice air-flow causes a second heat transfer coefficient peak that is broader than the first one and develops at the location of impingement (~10cm axial distance). After the second peak the heat transfer coefficient starts to decrease but it is noteworthy that a third cooling peak develops away from the air ring (at the area between 20 and 30 cm). A close examination of the flow streamlines (figure 11) fails to provide any justification for the calculated third peak.

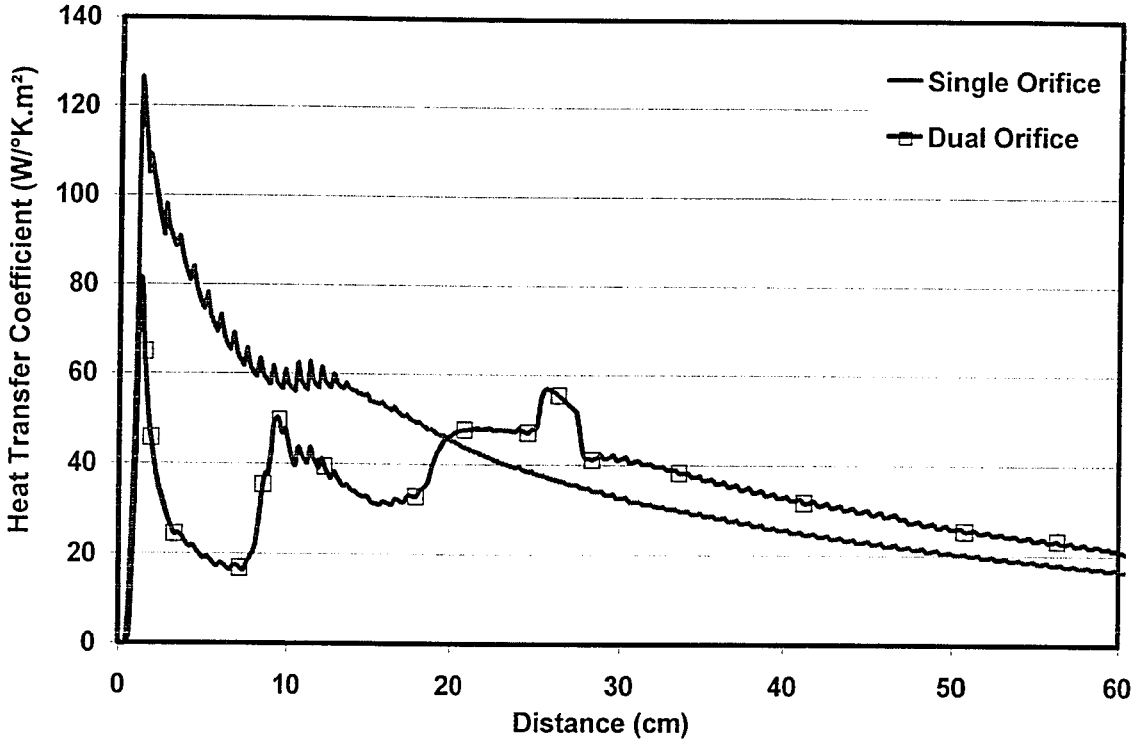

Figure 14: Heat transfer coefficient on the bubble surface vs. axial distance from the die

Figure 15 presents the calculated profiles for the kinetic energy of turbulence (k) in the computational domain. Profiles of the turbulent kinetic energy are good indicators of the areas where large scale eddies develop. The graph is informative because large scale eddies enhance the energy transport mechanism in turbulent flows. Figure 15 explains the profiles of the heat transfer coefficient (figure 14). In the single orifice case, the maximum heat transfer coefficient value coincides with the area where there is increased turbulence (air-ring neck) and decreases further from the air-ring. In the dual orifice case, the unexpected third peak in the value of the heat transfer coefficient can also be explained using figure 15. It is apparent that the maximum turbulence develops after the cooling air stream leaves the air-ring. The third cooling peak coincides with the area where the turbulence is most dominant.

Overall the results suggest a significant difference between the two air ring configurations. The studied single orifice air ring is forcing the film bubble to cool down early and most of the film deformation occurs at low film temperatures. On the other hand, the use of the dual orifice air ring spreads the convective heat transfer over a larger area. By the time the film reaches the second and third cooling peaks, significant bubble deformation has already occurred. The differences between warm and cold stretching of the film (which the two different types of air-ring instigate) are likely to influence the final film properties.

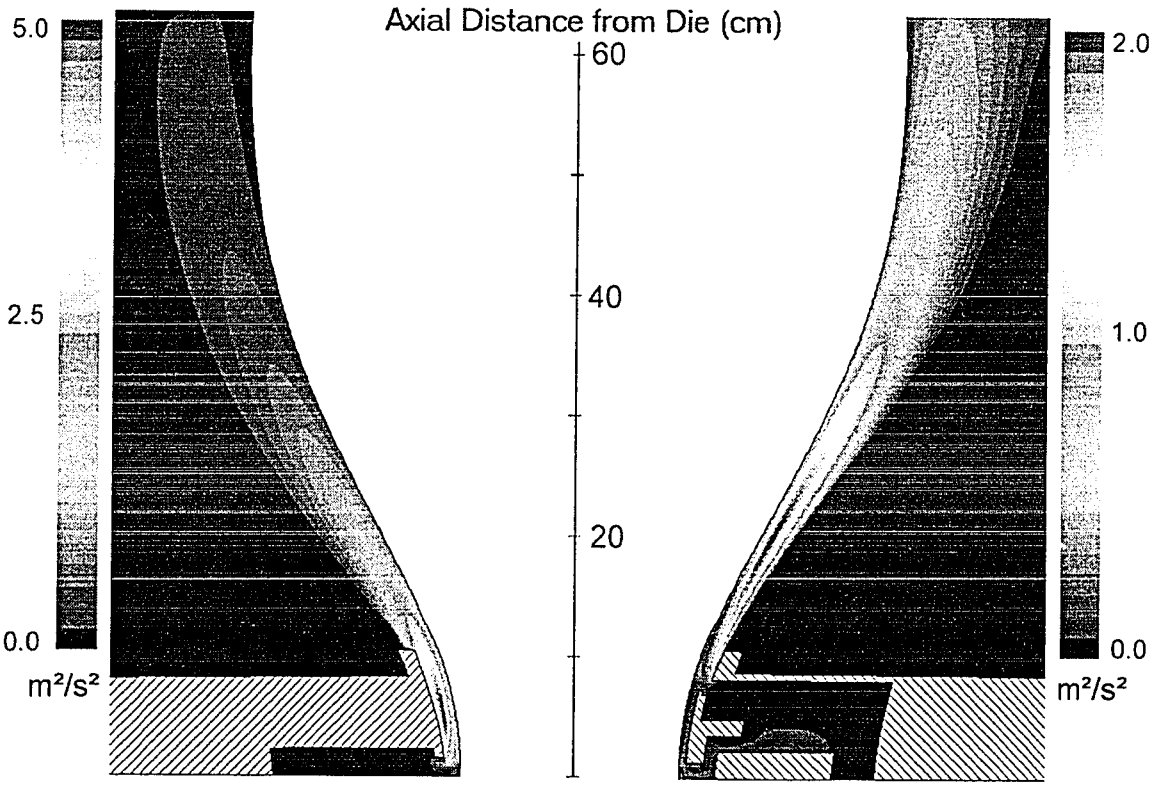

Figure 15: Kinetic energy of turbulence profiles for the single (left side) and dual (right side) orifice configurations (flow-rate 50 liters-of-air/s)

2.5.3. Dual Orifice Air-Ring Modification

Blown film lines equipped with direct impingement dual orifice air-rings can be operated only at limited production rates. Figures 12 and 13 depict the significant over-pressure that occurs in the neck of the air-ring and its effects on bubble formation. The over-pressure is tolerable at low throughputs, but as both polymer and air flow-rates increase the over pressure becomes a major cause of instability. As blown film lines became more productive in the early 80's, a modified version of the dual orifice ring was developed [Wright, 1981], in which the upper orifice flow was emerging tangentially (parallel) to the film surface.

A new set of simulations was used to quantify the differences between the traditional and the modified dual orifice air ring. The simulation methodology described in section 2.5.1 was repeated for the modified geometry of a parallel flow upper orifice (also known as "aerodynamic" air-ring -- Wright, 1981). Figure 16 shows the difference in principle behind the impinging and the parallel flow dual orifice design.

Figure 17 shows the calculated pressure profiles in the bubble surface. It is clear that the over-pressure does not occur in the case of the modified air-ring. The pressure profile shows the initial realignment peak followed by a Venturi affected, mild under-pressure zone. The calculated pressure profile of the modified dual orifice air-ring is more similar to the profile obtained for the single orifice air ring (figure 12).

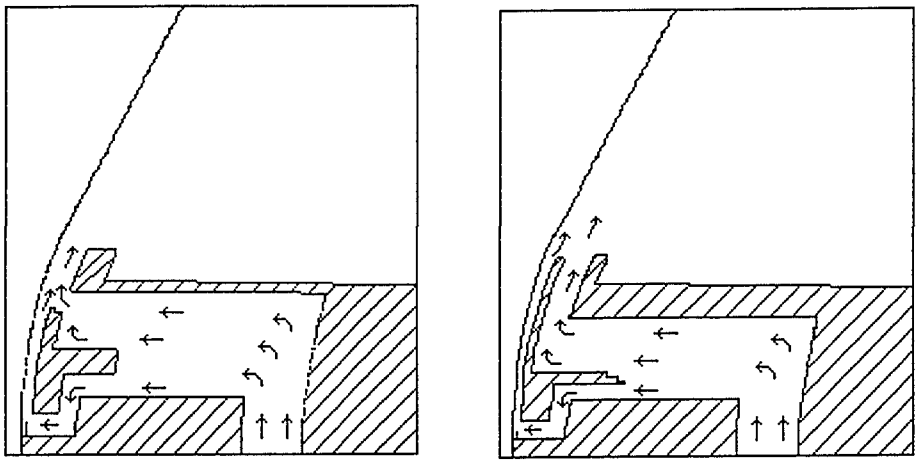

Figure 16: Impinging and parallel flow dual orifice air ring (left and right side respectively)

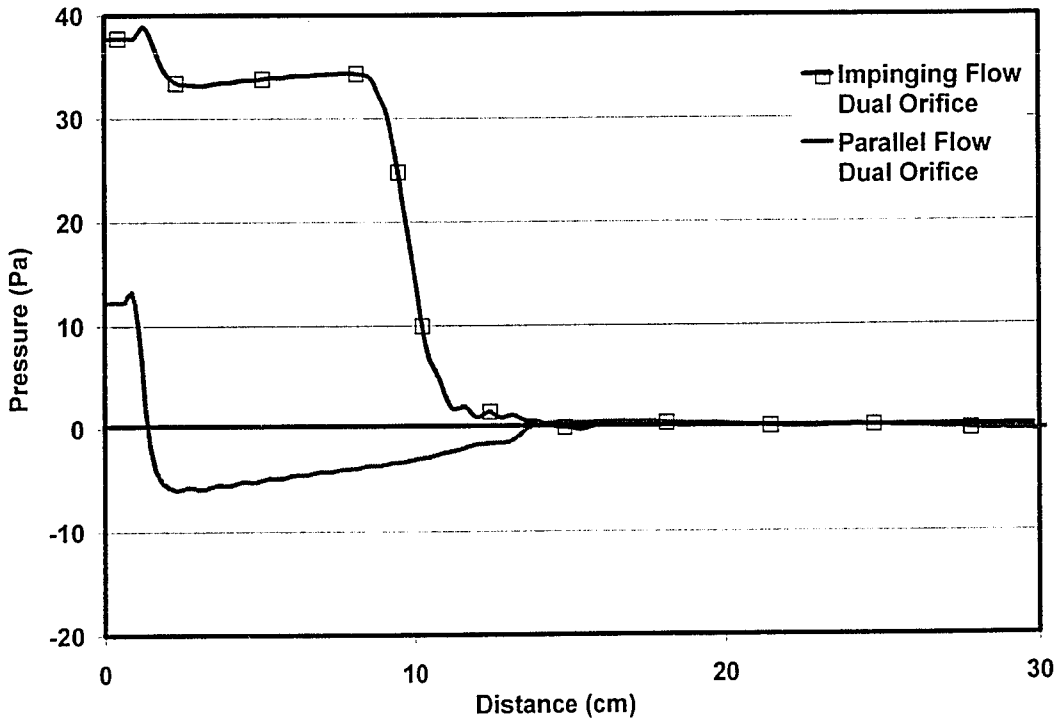

Figure 17: Gauge static pressure on the bubble surface

Figure 18 presents the calculated streamlines for the two simulations. The flow patterns look very similar as the air jet moves further away from the air-ring. The figure is zoomed in the air-ring area to accurately show the small flow differences. The differences in the flow pattern of the parallel flow air-ring (apart from the obvious absence of direct impingement) are concentrated in the increased lower orifice flow. The increase was rather expected due to the absence of the over-pressure caused by the upper flow direct impingement. One effect of the over-pressure was to reduce the lower orifice flow, because it had to pass through adverse local pressure gradients. In the absence of such obstacles (parallel flow upper orifice) a larger part of the total flow is directed through the lower orifice.

Figure 19 compares the heat transfer coefficient profile that is produced by the modified air-ring to the profile that was obtained for the direct impingement case (already presented in figure 14). As a direct result of the increased lower orifice flow, the initial cooling peak has increased in value and drops with a slower rate as the flow travels through the gap. As a result of the absence of impingement, the cooling peak at the 10 cm height is virtually non-existing. After the air exits the upper orifice the cooling capacity of the air stream increases in a manner similar to the direct impingement case. A peak in the heat transfer coefficient value can be observed close to the area where the third peak occurs in figure 14 (direct impingement dual orifice simulation).

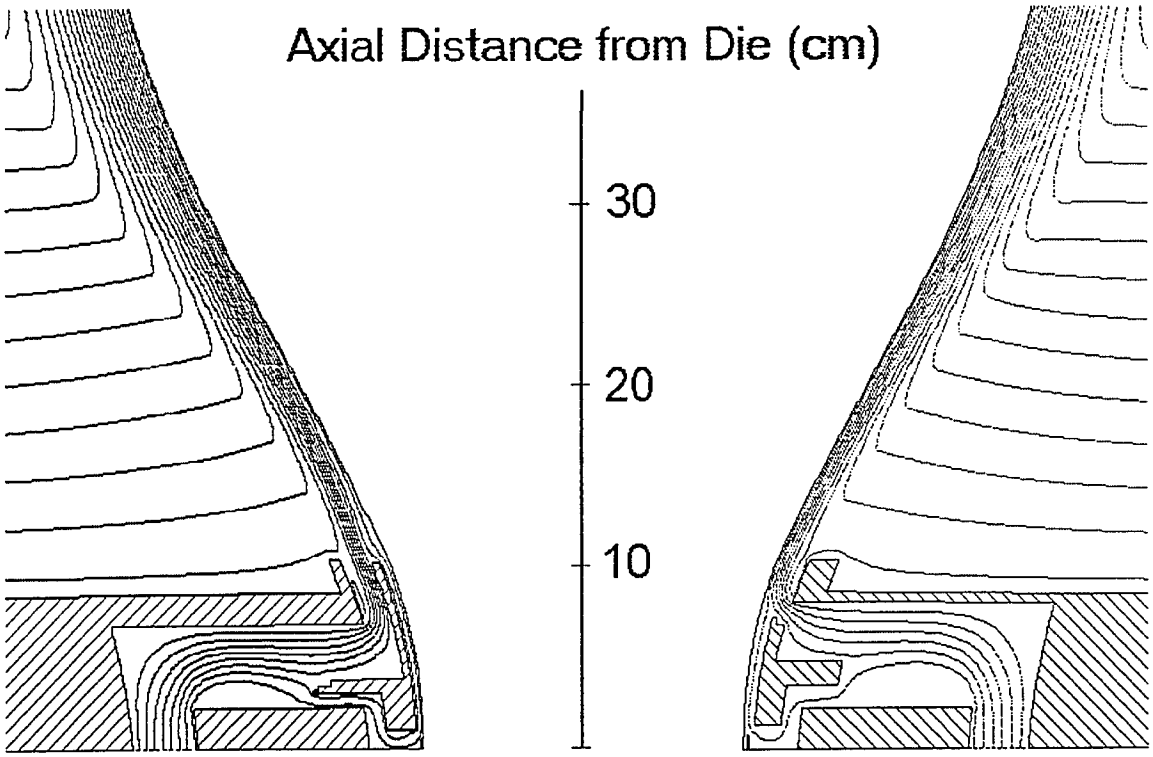

Figure 18: Cooling air streamlines (50 lt/s) for dual orifice air-rings: Left side: Parallel flow air-ring, Right side: Impingement air-ring (detail)

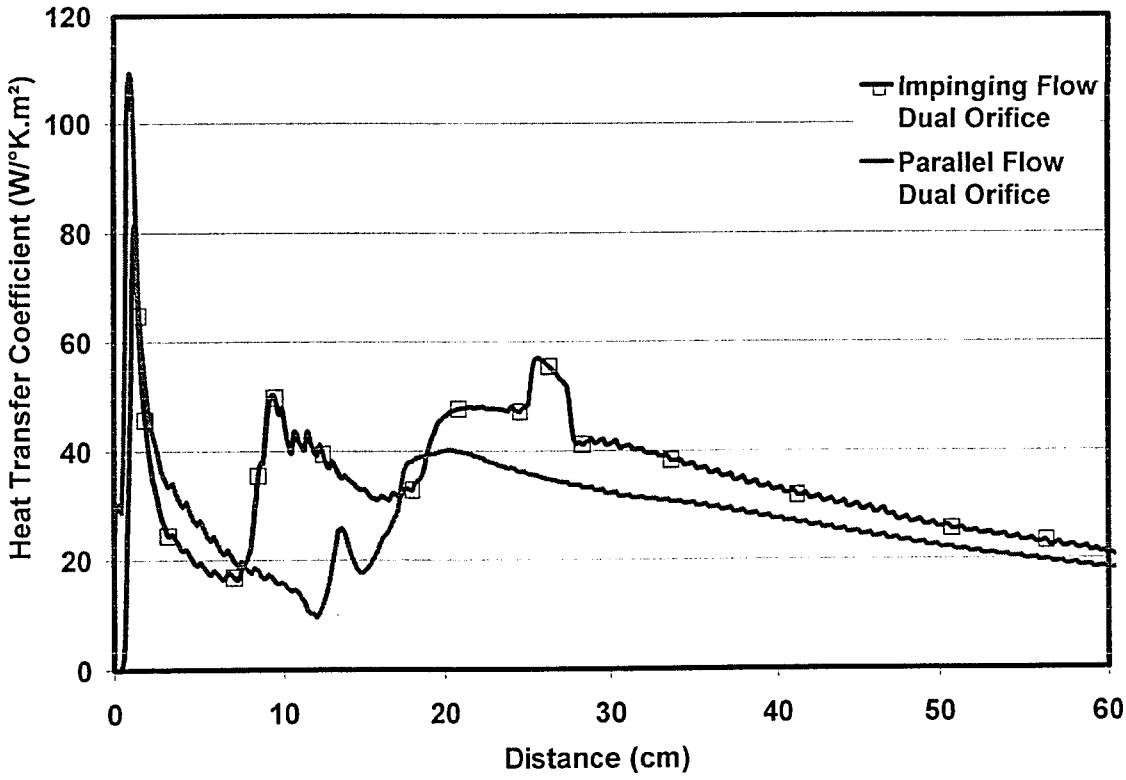

Figure 19: Heat transfer coefficient profiles for the direct impingement and parallel flow (modified) dual orifice air-rings

Figure 19 indicates that for both designs induce a heat transfer mechanism that develops after the cooling stream leaves the air-ring and is focused in the area around 20 to 30 cm from the die lips. Figure 20 shows the calculated profiles of the kinetic energy of turbulence. It indicates that turbulence that starts inside the upper orifice is enhanced by the joining of the two air streams (the flows from the upper and lower orifice) and reaches its maximum further from the tip of the air-ring.

The late development of turbulence that is shown in figure 20 can be explained by the development of large scale eddies after the airflow exits the upper orifice. Large scale eddies (which cannot develop inside the air-ring ducts due to geometrical limitations) are one of the basic contributors to the energy transport mechanisms of turbulent flows. However, such a development of large scale eddies does not occur in the case of the single orifice air-ring (see figure 15). The fact indicates that the actual mechanism of the late development of turbulence is aided by the joining of the upper and lower orifice flows at the tip of the air-ring (just before the re-combined flow exits the air-ring duct).

Figure 19 indicates that for a given air flow-rate the overall cooling capability of the modified design is clearly reduced in comparison to the direct impingement design. In practice however, parallel flow designs have phased-out the competition because they offer increased bubble stability, which in effect permits the increase of cooling air flow-rates up to 300%.

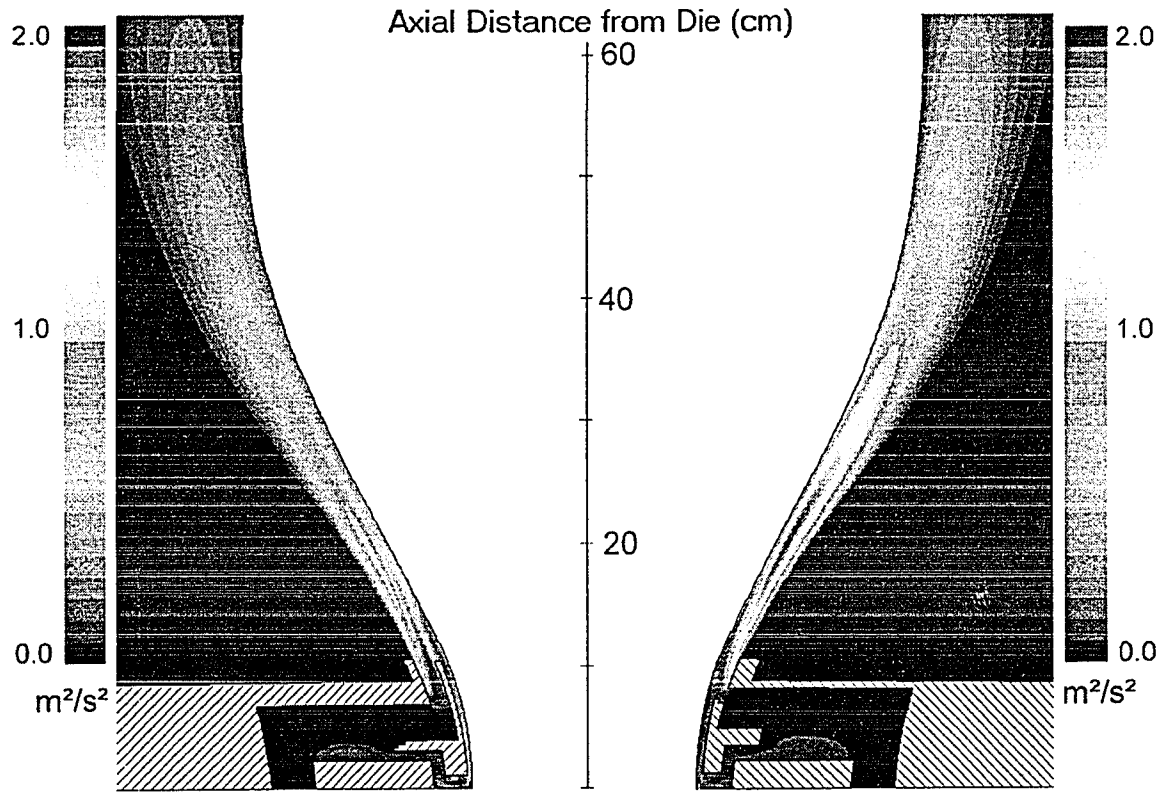

Figure 20: Kinetic energy of turbulence profiles for the parallel flow (left) and direct impingement (right) dual orifice configurations (50 liters-of-air/s)

2.6. Dual Orifice Air Ring Operation

In film blowing production, it is not uncommon for a specific air-ring design to be employed in the cooling of different blown film bubbles and under varying conditions. For example, different production lines may call for largely different cooling capacities (mainly dependent on the type of polymer and the throughput rate). Additionally, it is common in industrial practice for an existing (previously purchased) air-ring to be fitted in a different line and employed under operating conditions far removed from its previous assignment. At the same time bubble stability is more likely than not to impose strict operational limitations. More simulations were performed in order to evaluate the response of a given air-ring design to the varying operating conditions and parameters.

2.6.1. Simulation Methodology

A commercially available, adjustable dual orifice air-ring (Future Design Inc.) was simulated using a finite volume computational method (FLUENT). The air ring is designed for small bubbles with initial diameter of 2 inches. A couple of grid topologies have been examined, corresponding to an LLDPE bubble with *blow-up ratio* (BUR) of 3, as well as an HDPE *high-stalk* (a.k.a. *long-neck*) bubble shape with BUR of 4. Both bubbles have a *frost-line height* (FLH) of ~32 cm (for more details see Appendix A).

For each grid topology three operating air flow rates have been simulated, corresponding to low, medium and high cooling rates (volumetric flows 5, 12 and 25 liters-of-air/s for a 2" air-ring).

The cooling air enters the computational domain with predetermined velocity (design parameter) and temperature of 35°C. The initial turbulence intensity is set to 10%, a value typical for flows in ducts. The density of the air is assumed to be a function of both pressure and temperature. The inflow and the walls of the air ring are set to have a temperature of 35°C, slightly higher than ambient (27°C) to capture the viscous warming in the air blower. The temperature of the film wall is gradually dropping in the axial direction. The implemented temperature profile is similar to experimental profiles from literature data (see Appendix A). The shape and location of the film wall has been considered to be unaffected by the studied flow conditions.

2.6.2. Results and Discussion

Figure 21 shows the streamlines around a typical LLDPE type bubble shape. Two different flow rates are presented in the same figure (left and right side) for easy comparison. Using 25 streamlines the left side depicts the flow pattern when a medium cooling airflow rate (12 lt/s) is used, while the right side corresponds to a low flow rate (5 lt/s).

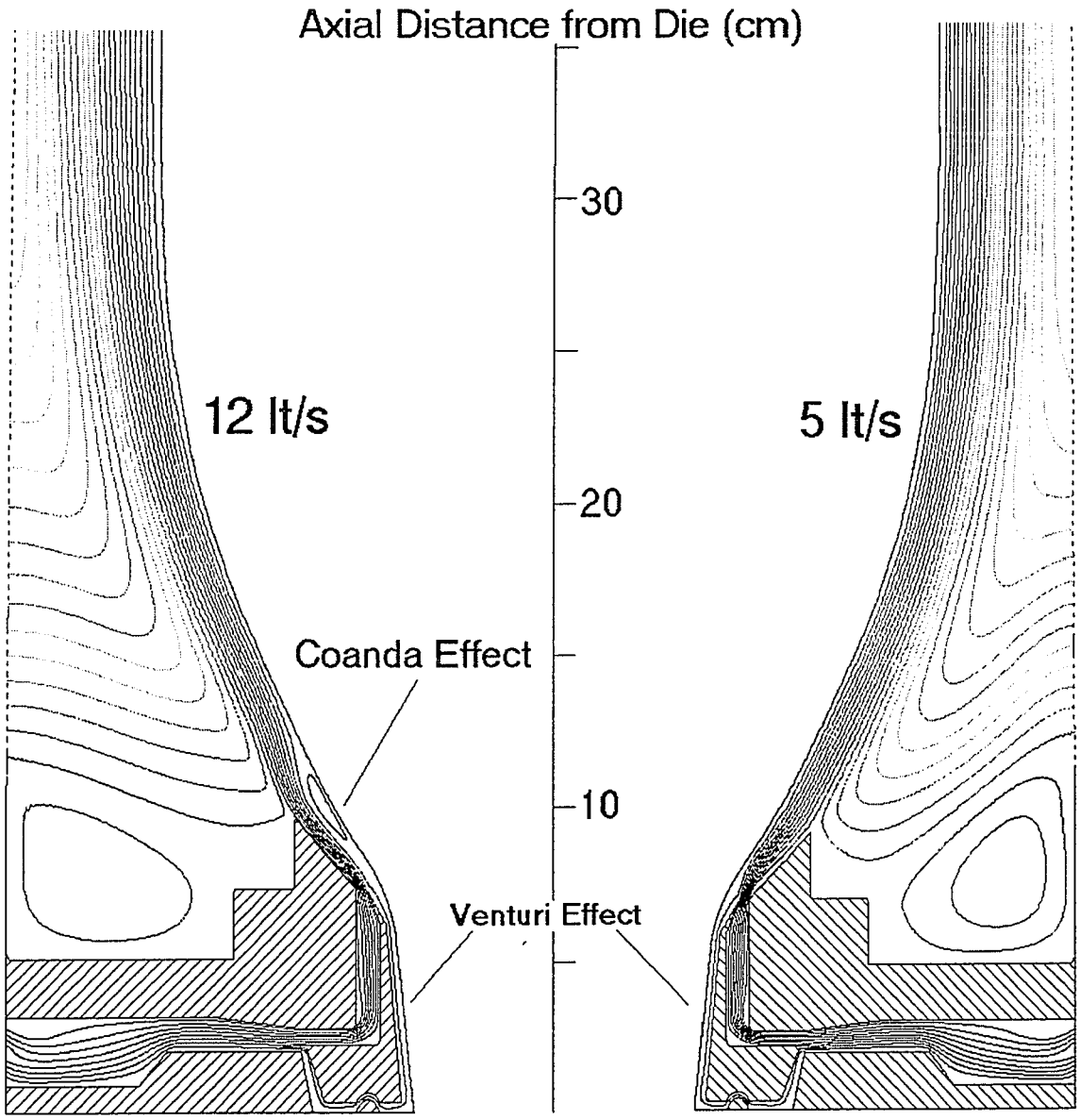

Figure 21: Cooling air streamlines around an LLDPE blown film bubble. left side: air-flow 12 lt/s, right side: air-flow 5 lt/s, 25 streamlines shown

Despite the apparent overall similarity of the two flow patterns, there are significant differences in the area where the jet from the upper orifice emerges. This is the area from where most of the cooling air is injected towards the film surface. At the exit of the upper orifice, figure 21 shows significant differences between the two simulated flow patterns. At the medium flow rate one may notice the development of a Coanda induced vortex, which is not apparent in the lower flow rate. After passing through the upper lip, the Coanda effect forces the air jet to suddenly turn and attach to the stabilization cone of the air-ring. At the end of the stabilization cone the jet experienced a second Coanda effect and is redirected, this time towards the curved bubble surface. A flow separation is also associated with the effect. Simulations at higher flow rates (25 lt/s or higher) consistently predict Coanda effects of the same nature (stabilization cone attachment and then bubble impingement).

The generation of Coanda effects at medium (or higher) flow rates may explain what operators of blown film lines often encounter in production lines: frequently, when they attempt to increase cooling by marginally increasing the air flow, they may destabilize the bubble [Moriarity, 1999]. And very often, small increases in flow rate generate instability problems that are disproportionally severe.

Figure 22 shows the streamlines for the medium and high air flow-rates (using 30 streamlines)[1]. The flow patterns appear to be very similar for the two flows. Despite the overall resemblance of the streamline development, higher flow rates create different local conditions on the bubble surface.

Figure 23 shows the heat transfer coefficient profile on the bubble surface for high, medium and low flow rates. In all the simulations, an initial cooling peak is observed at the base of the air ring where the low orifice cooling air is impinging on the polymer film. The cooling efficiency drops as the air is moving away from the impingement area. The magnitude of each peak is directly related to the airflow rate.

A second peak occurs after the rest of the air is injected through the upper orifice. In the lower flow rate simulation the second peak occurs exactly at the injection height and is similar to the first one: the heat transfer coefficient raises sharply and then slowly decreases in value as the flow moves further from the injection zone. Halfway to the frost line the cooling intensity levels-off and becomes almost constant.

---

[1] For the medium flow rate (12 lt/s) results may appear different in figures 21 and 22 due to the different number of streamlines used (25 streamlines for figure 21 and 30 streamlines for figure 22), but they are not.

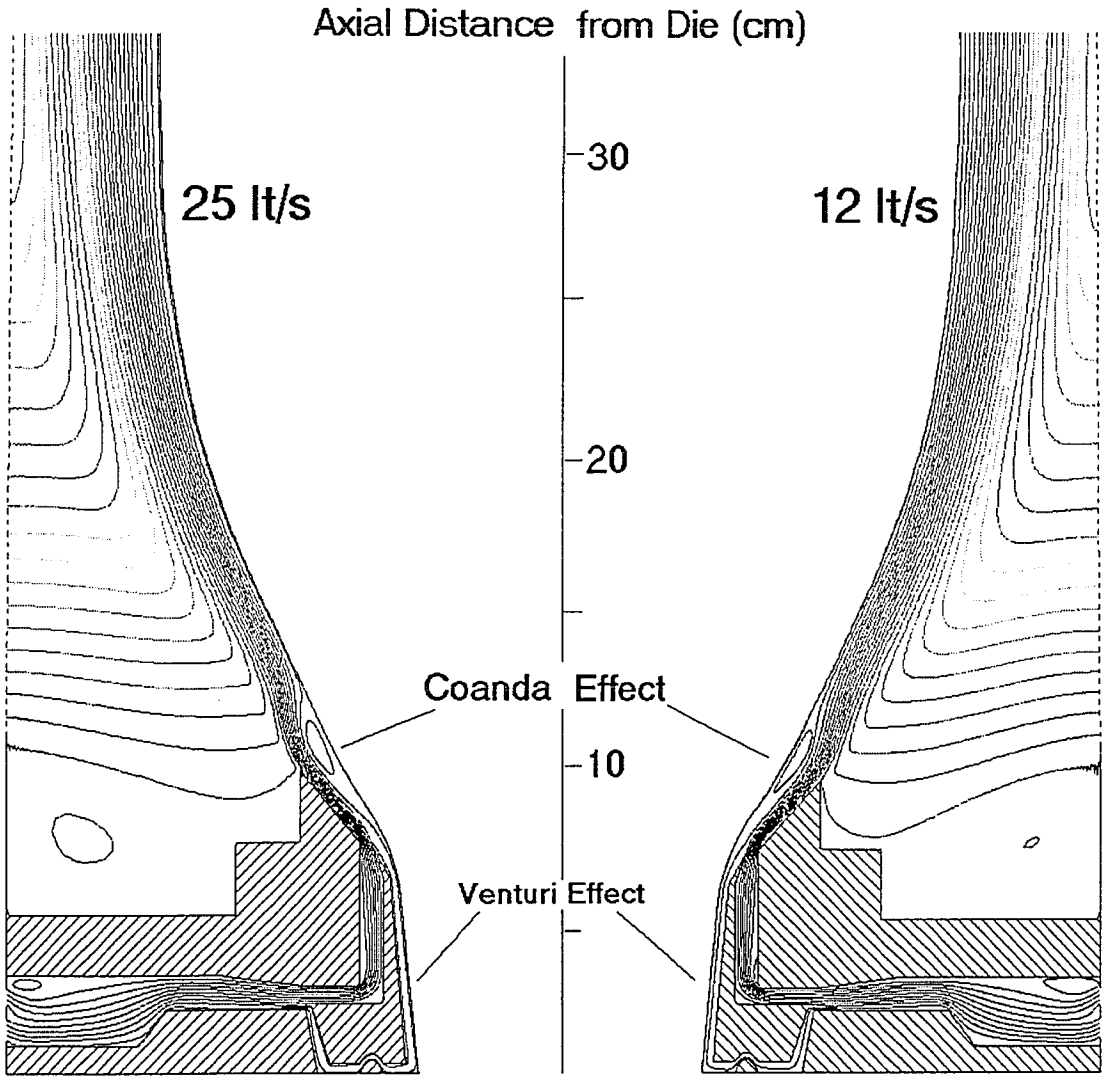

Figure 22: Cooling air streamlines around an LLDPE film bubble.
left side: air-flow 25 lt/s, right side: air-flow 12 lt/s,
30 streamlines shown

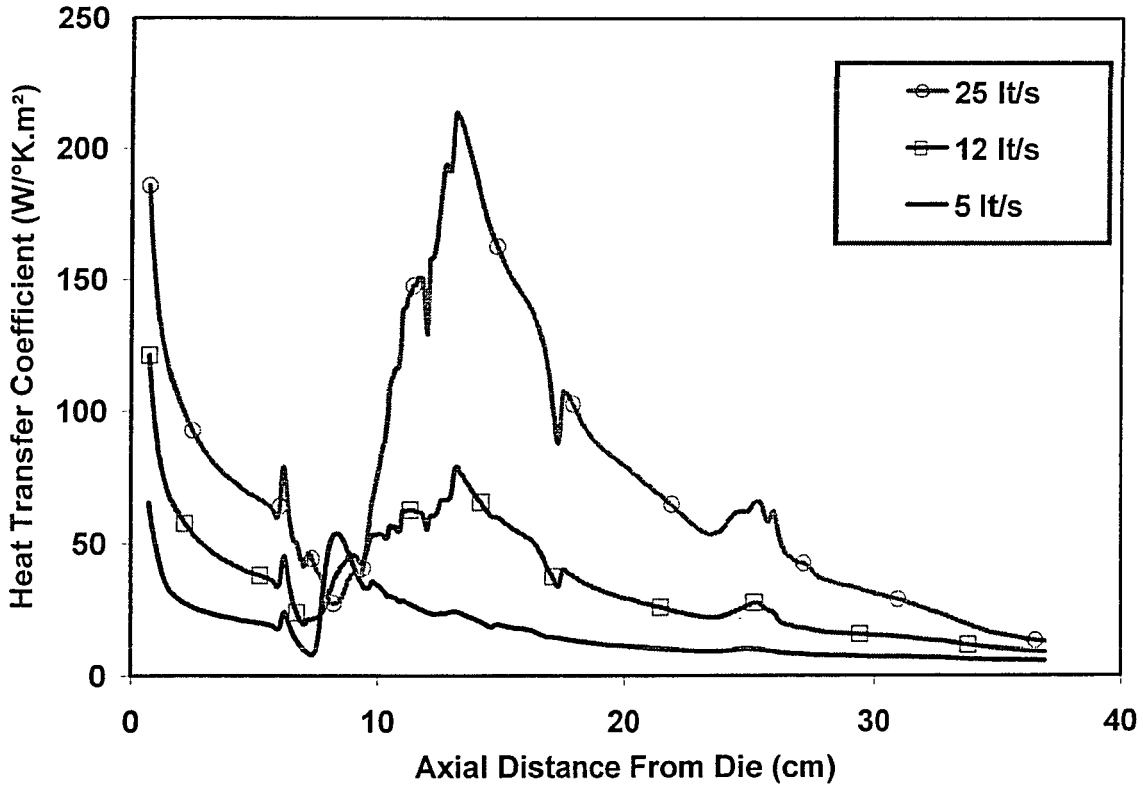

Figure 23: Heat transfer coefficient profiles on the film surface at different air flow rates (LLDPE bubble shape)

The additional simulations (where the Coanda induced vortex was present) predicted a much wider second peak, covering all of the area where Coanda effects occur. It is noteworthy that the maximum cooling intensity occurs at the area close to the tip of the stabilization cone, where the Coanda effect forces the jet to turn from and impinge on the bubble. The heat transfer coefficient value drops as the air moves higher, but the width of the second peak is extensive, causing adequate cooling even at locations close to the frost line.

The simulation suggests that the presence of the Coanda effect (and the associated flow separation) near the stabilization cone greatly influences the heat transfer capability of the cooling air stream. However, the Coanda effect may also introduce stability problems. The appearance of the Coanda effect is not gradual as the flow rate increases. At the onset of a critical flow rate the Coanda effect appears suddenly, which may initiate bubble instability.

Figure 24 presents the gauge pressure profile on the external surface of the bubble for the three characteristic volumetric air flow-rates (high, medium and low). The under-pressure caused by the Venturi effect is apparent in the air-ring neck zone (first 12 cm) and becomes increasingly significant as the flow-rate increases.

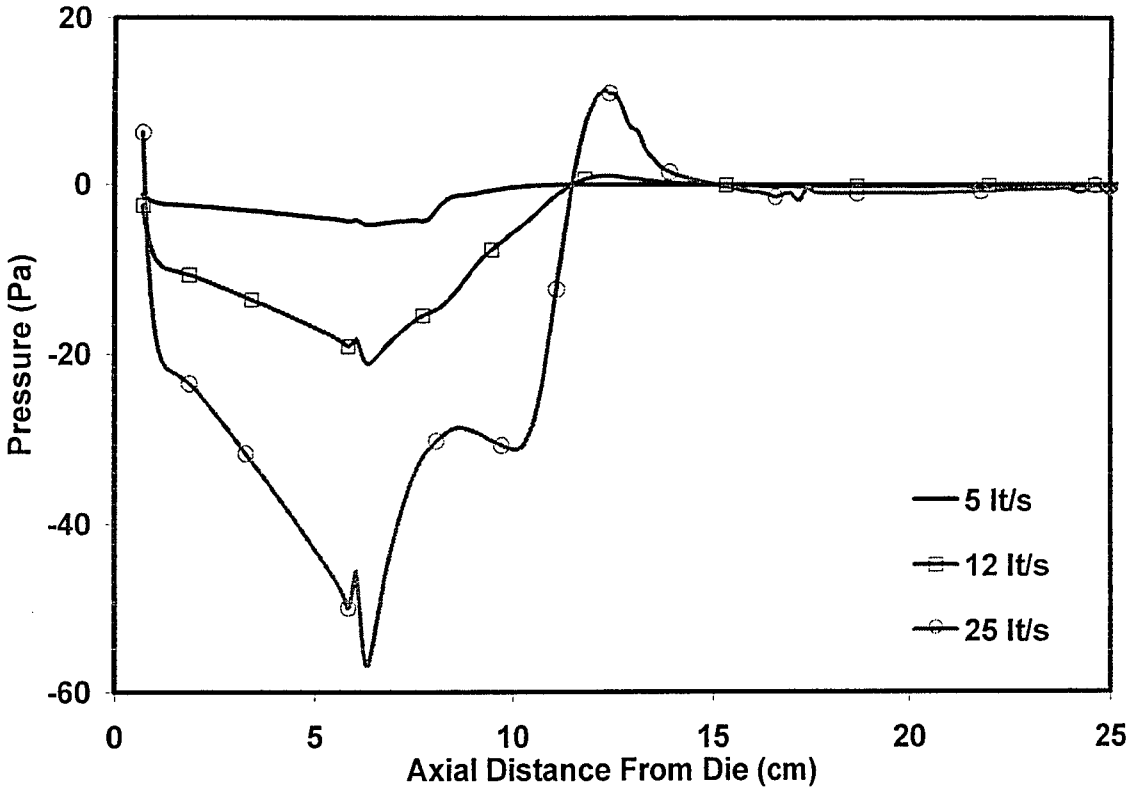

Figure 24: Gauge pressure profile on the film surface at different air flow rates (LLDPE bubble shape)

The gauge pressure stays negative as the air travels inside the gap between the air-ring and the bubble. As soon as the airflow clears the air ring, the relative pressure drops to zero. At the low flow rate, the Venturi associated pressure drop is very small. This is not surprising since decreased flow rates are only used for very delicate, low production, specialty blown films. As shown in figure 24 however, at higher flow rates the Venturi effect may become much larger. In combination with the slight over-pressure in the Coanda vortex region, large and suddenly developed pressure transients may lead to bubble instabilities at increased airflow rates.

If the possibility of adverse interactions between the Venturi and Coanda effects is carefully avoided, the Venturi effect probably helps to stabilize the bubble. Compared to typical values of the bubble inflation pressure (25~250 Pa for LLDPE films), the Venturi related under-pressure is anything but negligible. The bubble is forced to take the shape of the air-ring neck at the critical initial phases of cooling (when the bubble is still very weak), thus guaranteeing that the radial deformation of the bubble is well controlled. Modern air-rings have carefully designed neck shapes in order to avoid deformation excesses in the first moments of blowing. Additionally at high flow-rates, the Venturi

effect (axisymmetric in nature) is helping to reduce sudden lateral movements of the bubble, mainly caused by random cooling air turbulence. Thus, both the shaping and the stability of the bubble may be largely influenced by the air-ring induced Venturi effects.

A similar set of runs was performed on a grid topology simulating a high-stalk (low melt index HDPE type) bubble shape. The air-ring design and the operational flow-rates were not modified. Figure 25 compares the calculated streamlines between medium and low air flow rates, while figure 26 depicts the medium and high air flow rates. It is apparent that the behavior of the air-jet is drastically changing as flow rate increases.

Figure 25 shows the higher orifice air-jet to bend and impinge on the curved film surface although it was initially directed to flow along the stabilization cone. The calculated streamline patterns are rather similar for the two cases with only minor differences. The left side of figure 26 corresponds to a high flow rate simulation and shows quite a different jet behavior. The air jet initially attaches to the external air ring surface (much like in the LLDPE simulations) and then abruptly turns towards the film surface, creating a large vortex. The Coanda effect is easily identifiable as the main cause of all the air jet bending as well as the attachment to nearby film and/or air-ring surfaces.

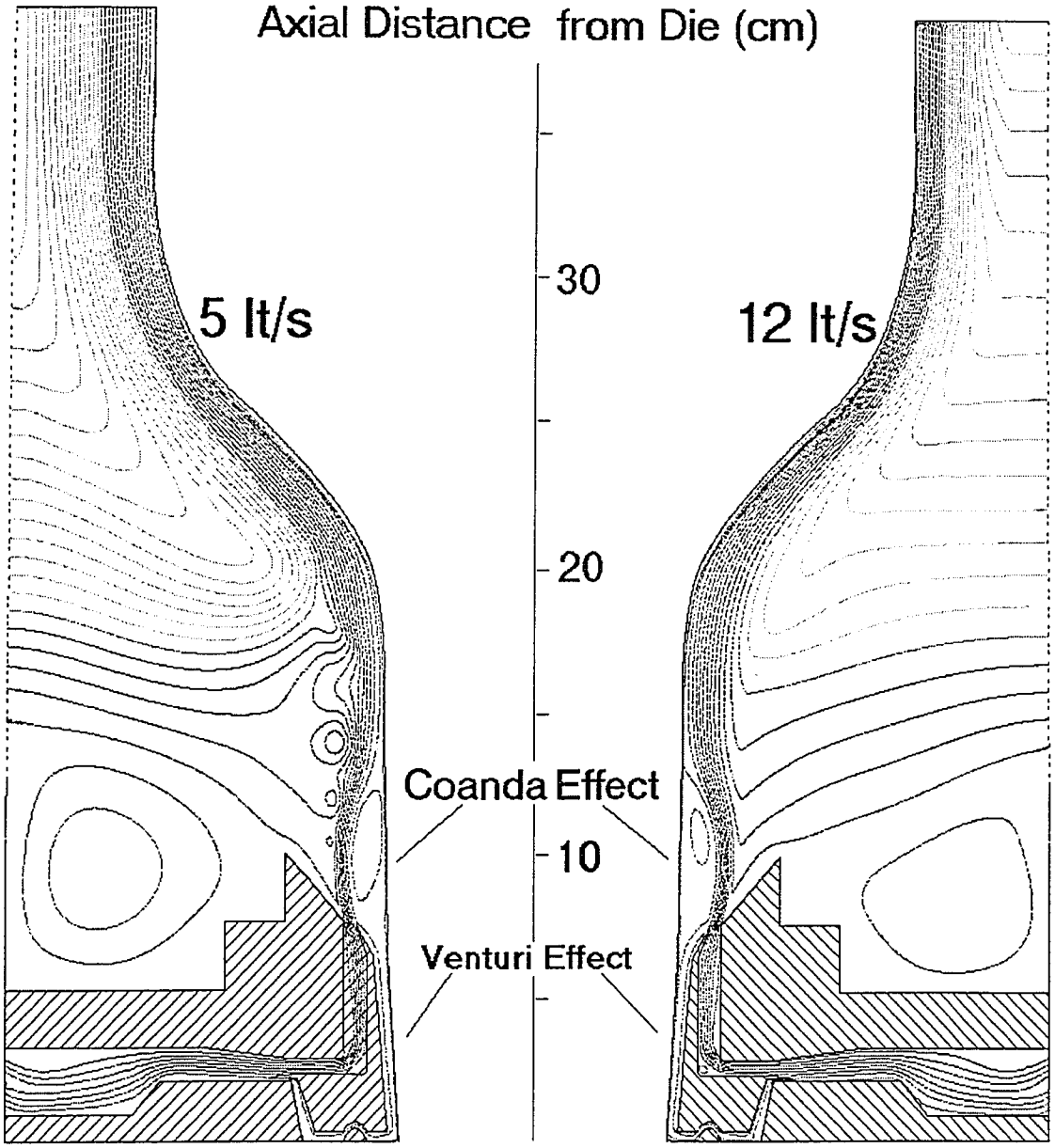

Figure 25: Cooling air streamlines around a long neck (HDPE) bubble.
left side: air flow 5 lt/s, right side: air flow 12 lt/s

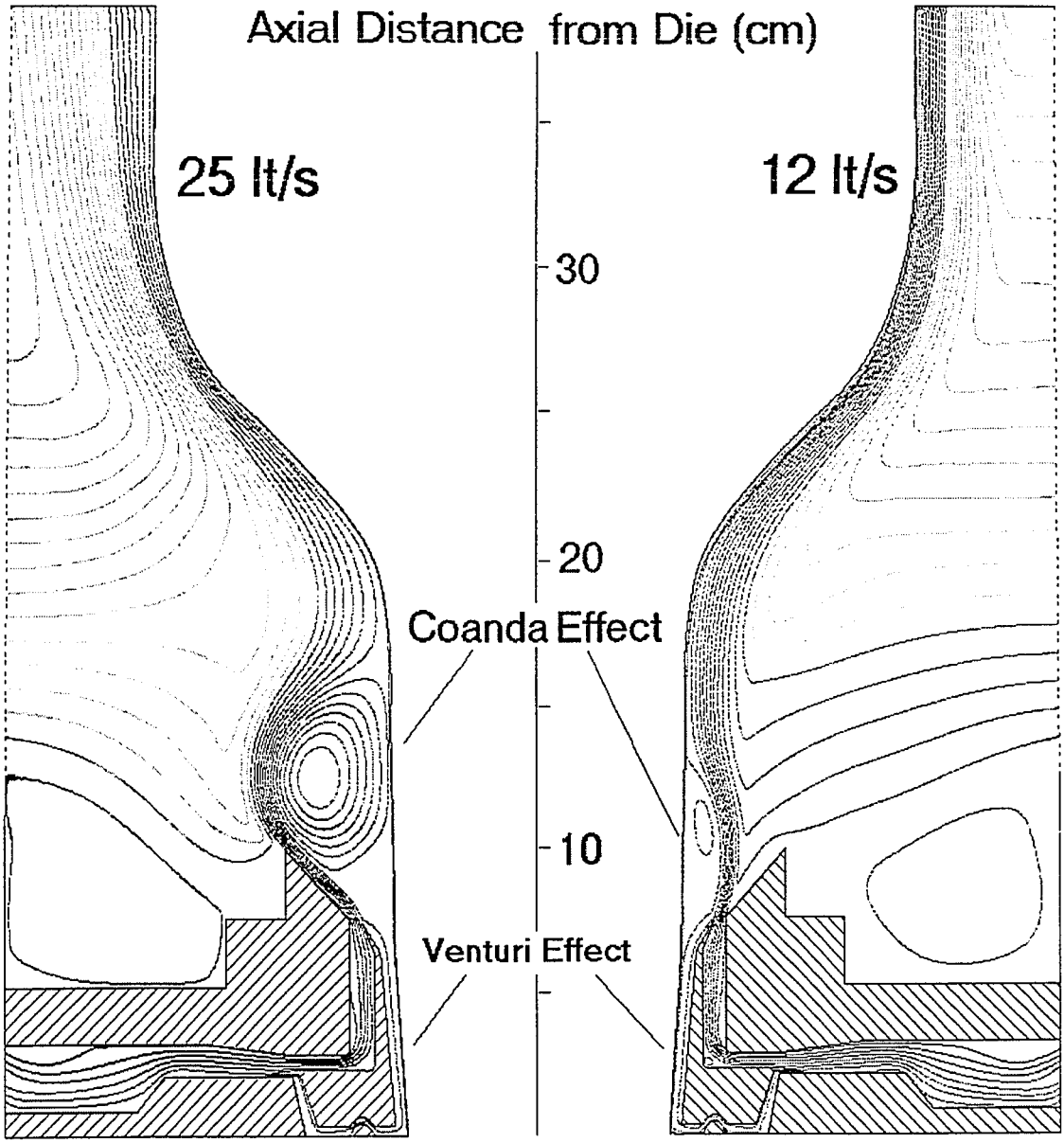

Figure 26: Cooling air streamlines around a long neck (HDPE) bubble.
left side: air flow 12 lt/s right side: air flow 25 lt/s

Away from the air ring, a significant amount of ambient air is entrained and the jet slows down significantly. In agreement with previously presented simulations (see section 2.5.2), air velocity higher up on the bubble (near the frost line) is usually one order of magnitude smaller than the velocity at the tip of the air-ring. Still, even away from the air-ring the air jet remains attached to the film surface and closely follows its curvature (a direct result of the Coanda effect).

The Venturi effect is also present in this set-up. Figure 27 presents the pressure profiles on the external surface of the bubble. Inside the air-ring neck, as the air travels through the gap, the Venturi induced pressure drop is a strong function of the air flow rate. At the location where the air-jet is forced by the Coanda effect to turn and impinge on the bubble surface, we notice a sudden rise in the external pressure. The rise is proportional to the flow rate of the air jet and ranges from insignificant (low flow rate) to relatively high (~25 Pa for the high flow rate). Figure 27 indicates that large external pressure variations may occur on the film surface as the film travels from the die lips to the frost line region. The sudden variations occur when the flow passes from Venturi effect dominated areas to areas where the Coanda effect is causing direct impingement on the bubble surface. Such large pressure variations may be responsible for serious bubble instabilities.

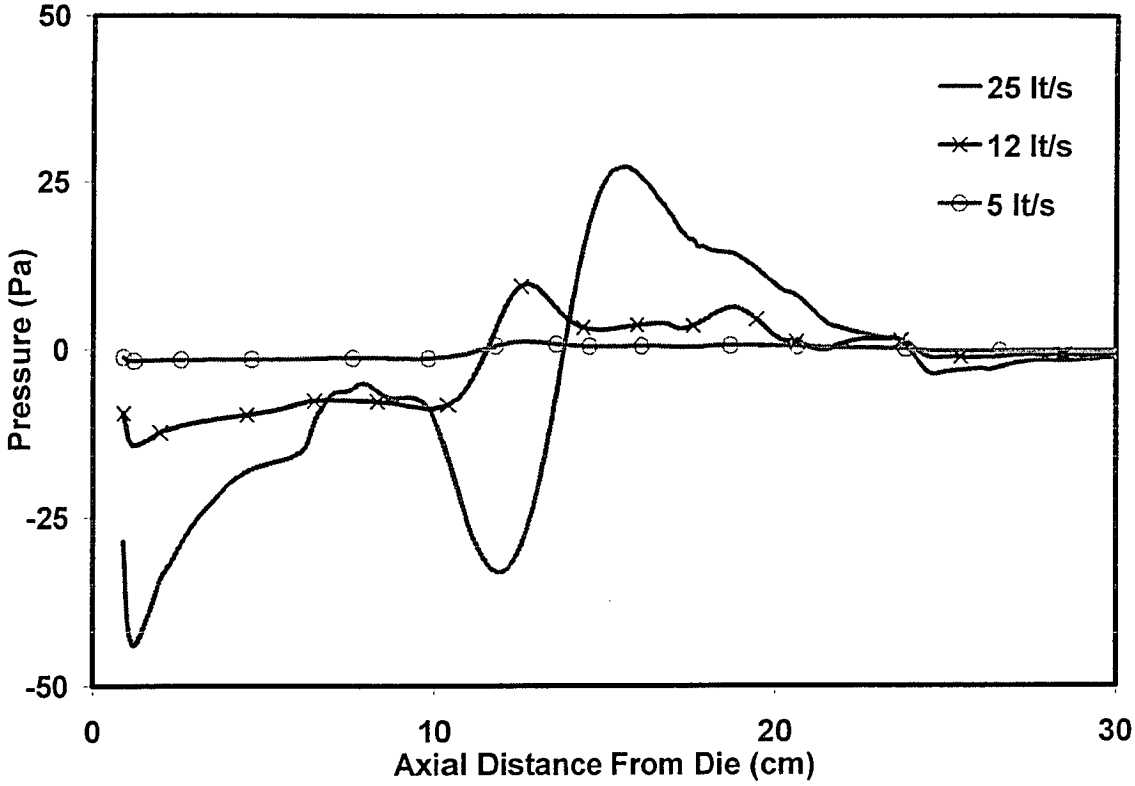

Figure 27: Gauge pressure profile on the film surface at different air flow rates (HDPE bubble shape)

Figure 28 shows the calculated heat transfer coefficient on the bubble surface for the three flow-rates shown in figures 25 and 26. There is an initial cooling peak in the area of the lower orifice. The magnitude of the peak is proportional to the corresponding airflow rates. For all flow rates a second peak develops at the point where the combined flow impinges on the film surface. The second peak is more indicative of the complex dynamics that develop as the flow-rate increases. The different pattern of the high flow-rate (streamlines shown in fig. 26) produces a cooling profile, which is spread-out over a larger area on the film bubble, resembling more a plateau than a peak. The calculated heat transfer coefficient maximum is even marginally smaller than the one predicted for the medium flow-rate. The extended width of the plateau is attributed to the large, Coanda generated, vortex that appears at the high flow-rate.

Figure 29 shows the calculated profiles of the kinetic energy of turbulence and helps to further explain the predicted cooling profiles in figure 28. The second peak in the medium flow-rate coincides with the maximum turbulence level (~6 m^2/s^2) and reduces as the air moves higher. On the other hand, the high flow-rate simulation predicts a large area of mild turbulence (with turbulent kinetic energy varying from 3 to 5 m^2/s^2) at the location where the heat transfer coefficient plateau exists. The presented results illustrate the complexity of the bubble cooling mechanisms and partially explain why increases in cooling capacity often cannot be met by simply increasing the flow-rate of an existing air-ring.

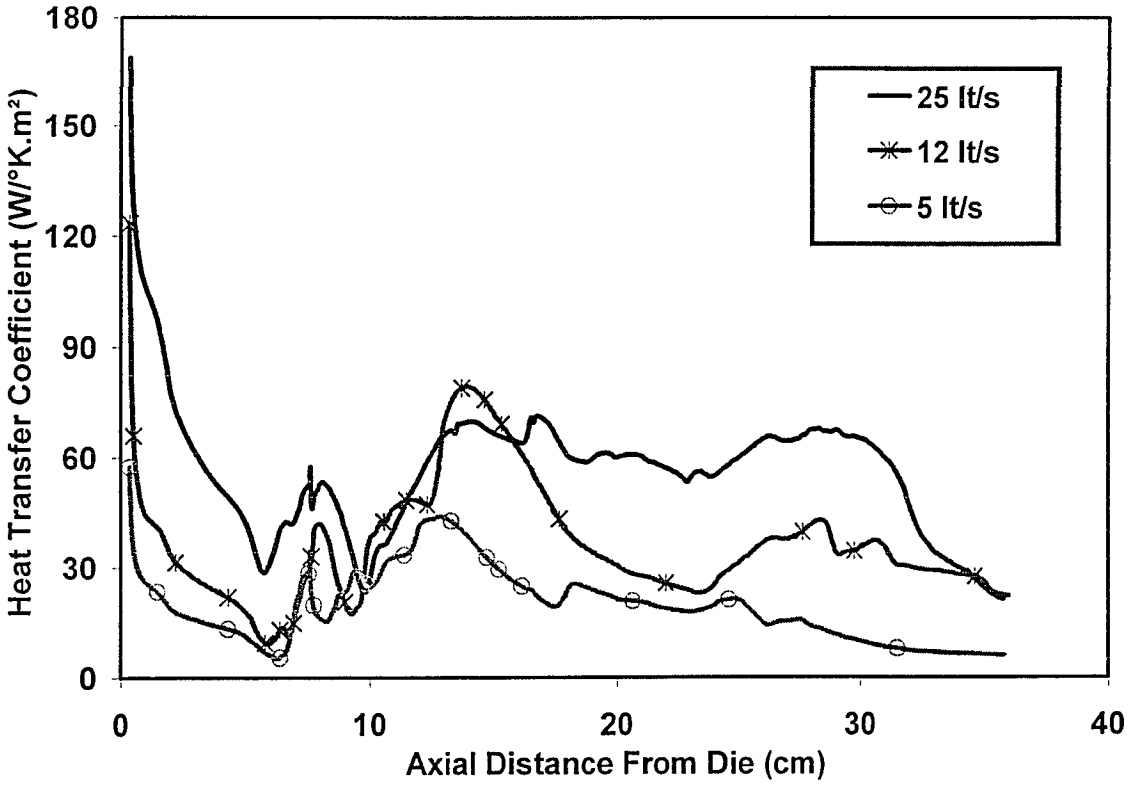

Figure 28: Heat transfer coefficient profile on the film surface at different cooling-air flow-rates (HDPE bubble shape)

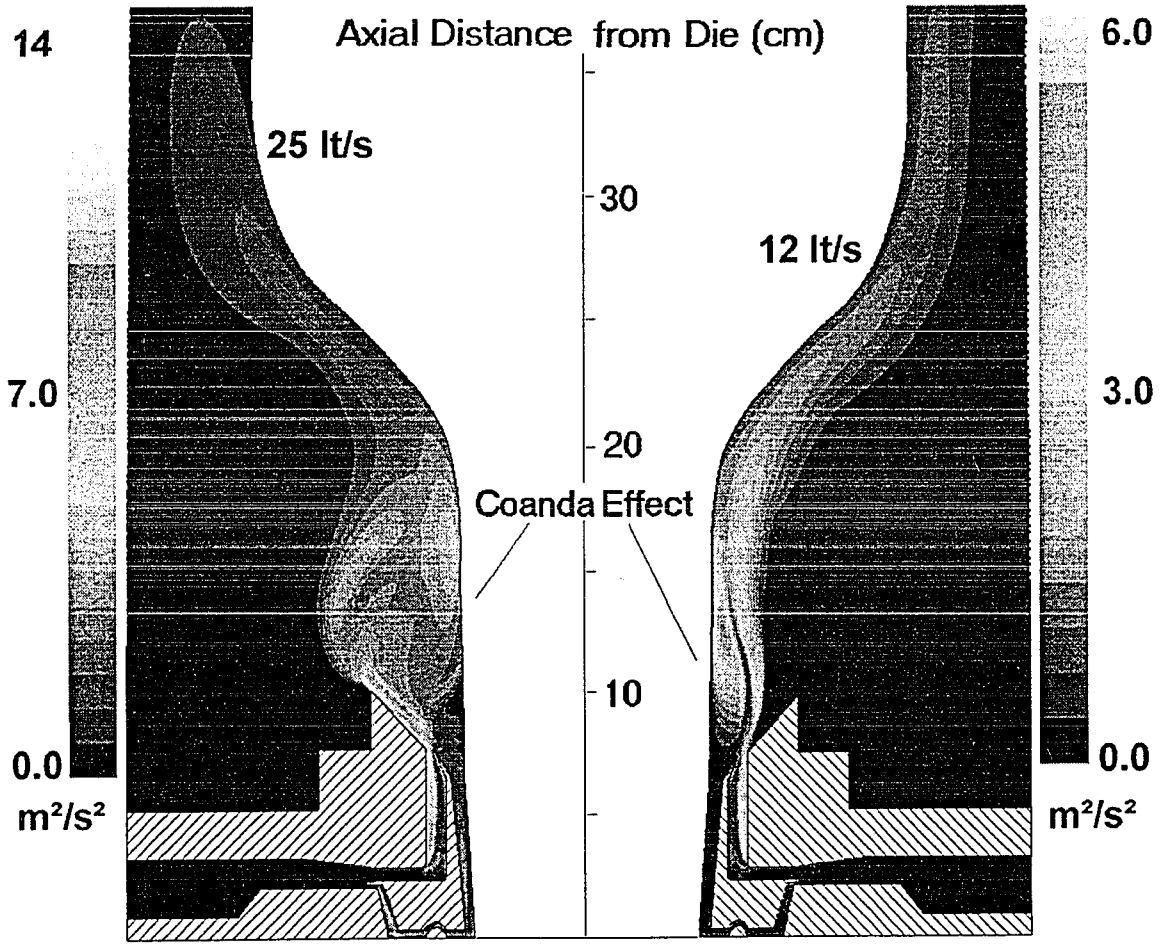

Figure 29: Kinetic energy of turbulence profiles for the high (left) and medium (right) air flow-rates (HDPE bubble shape)

2.7. Dual Orifice Air-Ring Design Considerations

The vast majority of commercially available air-rings have been designed and developed using a strenuous procedure of trial and error. This explains why it is not uncommon for a manufacturer to cut corners in the air-ring design process, since it is the least expensive part of the blown film line but requires significant resources to be allocated for a proper design. However, as blown film line throughputs continue to rise (driven by the ever-increasing demand in plastic film) elaborate and efficient air-ring designs have been reassessed from a luxury to an actual necessity.

In order to address some of the design considerations as well as make existing designs applicable to a variety of blown film lines, most manufacturers design air-rings with a high degree of adjustability. Modern designs incorporate a number of parts that can be geometrically adjusted as well as accessories that can be added to (or removed from) the air-ring. The vast majority of these adjustments can be applied in real-time by the line operators. The extra degrees of freedom in the operational setup may be very helpful, but they add another degree of complexity to the air-ring operation.

Simulations were performed to evaluate the response of a given air-ring design to minor design modifications as well as variations of the operational setup.

2.7.1. Simulation methodology

The commercially available, adjustable dual-orifice air-ring that was used in the simulations of section 2.6 was employed for another set of simulations. The simulated air ring is designed for small bubbles with initial diameter of 2 inches. In the two grid topologies that were examined, simulations were performed for minor design modifications to evaluate their effect on the fluid flow.

The operating air flow-rate was selected to be 12 lt/s (relatively moderate for small air rings). The rest of the parameters were kept unchanged, but small modifications were made to the original design, resulting in small modifications of the computational grid. The LLDPE type simulation was modified in order to correspond to different setups for the adjustable part of the air ring. In the modified simulation the part that separates the high from the low orifice flow was adjusted at a higher position (2mm higher). The difference in the position of the adjusted part corresponds to approximately a full turn of the adjustable air-ring screw (a routine air-ring adjustment during film blowing). Figure 30 shows the differences between the low setup (results already presented in section 2.6) and the high setup.

A similar set of simulations was performed on the high-stalk (HDPE) grid topology. This time the modification had to do with the initial design. The tip at the lips of the high orifice was eliminated (resulting to a simplified "straight" design) and the simulation was repeated (at 12 lt/s).

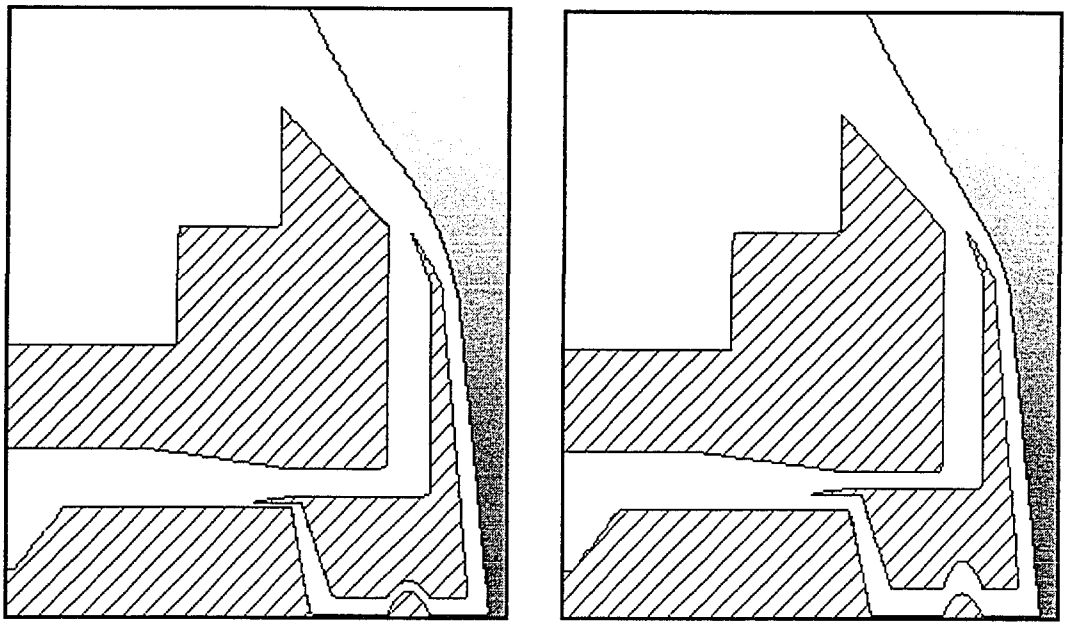

Figure 30: Operational setup of the adjustable air-ring (LLDPE simulation): low setup (left) and high setup (right)

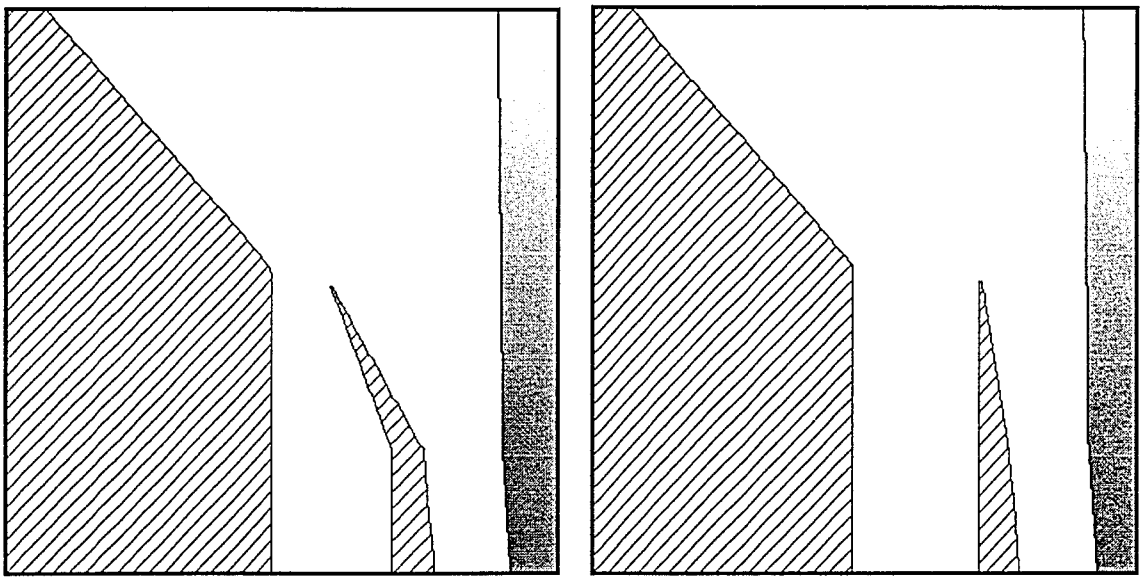

Figure 31: Air ring design modification for long neck (HDPE) simulation: original "tipped" design (left) and simplified "straight" design (right)

2.7.2. Results and Discussion

Figure 32 shows the calculated streamlines for the LLDPE bubble shape. The left side shows the results for the low position operational setup while the right side refers to the high position setup. In both cases the airflow exhibits an overall apparent similarity. There are, however, significant differences in the area close to the tip of the air-ring (where the upper-orifice jet emerges).

The simulation for the low position setup shows that most of the air-flow is directed through the higher orifice, as expected since the low orifice entrance is significantly smaller than the high orifice entrance. At the exit of the upper-lip the strong Coanda effect is creating a recirculating region. The high position simulation shows that an increased proportion of the total airflow is directed through the lower orifice. It is noteworthy, however, that the majority of the air is still injected through the higher orifice, as this is the path of least resistance. Even so, the balance between the two flows has been altered in comparison to the low setup simulation and the Coanda effect is absent from the area of the stabilization cone.

Figure 33 presents the calculated heat transfer coefficient profiles for the two studied air-ring setups. In both cases the familiar initial cooling peak is observed at the base of the air ring, where the cold air traveling through the lower orifice is impinging on the very hot polymer

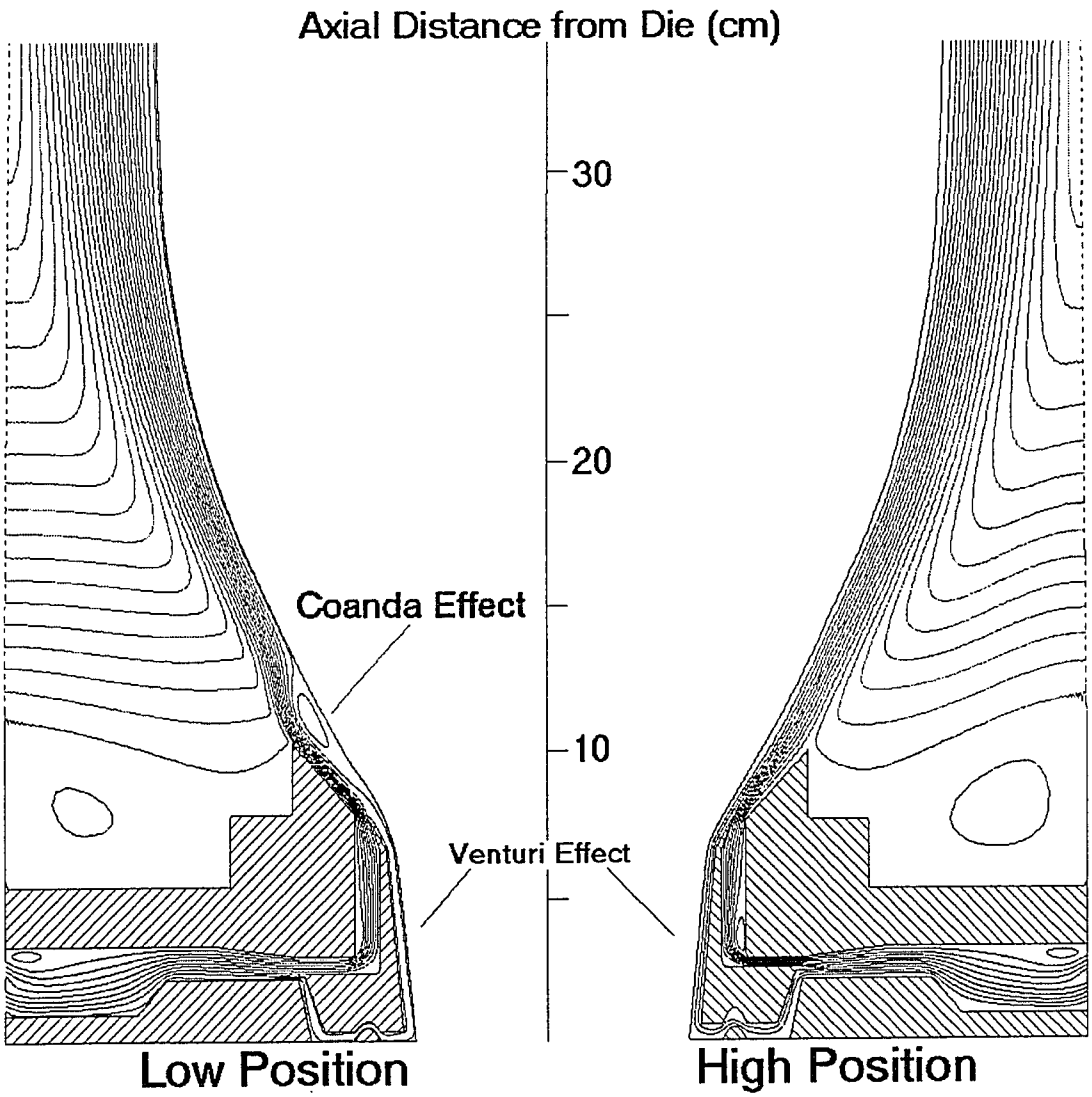

Figure 32: Cooling air streamlines (airflow 12 liters-of-air/s) around an LLDPE bubble for different operating setups of the adjustable ring. left side: low position setup, right side: high position setup

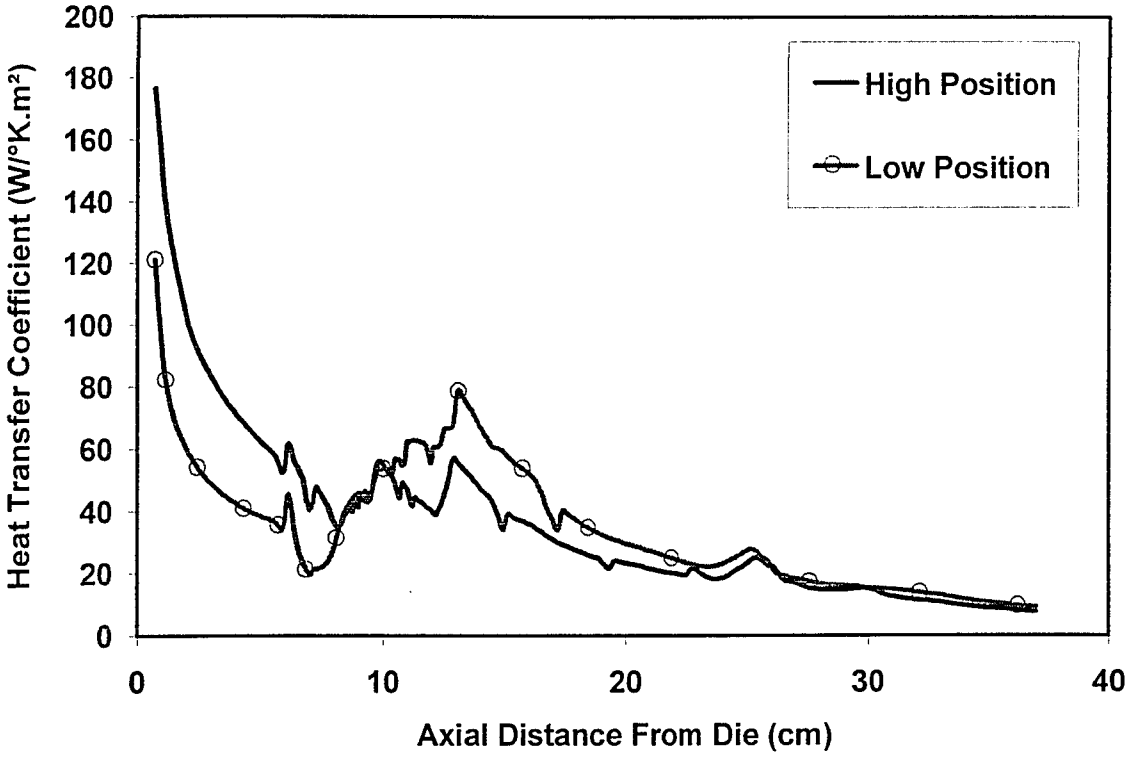

Figure 33: Heat transfer coefficient on the film surface at different adjustable air-ring positions (LLDPE bubble shape)

film. The lower-orifice airflow is quickly aligned with the bubble surface, forcing the heat transfer coefficient to rapidly drop as the flow moves higher. The initial peak is larger in the high position simulation since more air is flowing through the lower orifice. A second peak occurs after the rest of the air is injected through the upper orifice. However, in the high setup simulation the second peak is very small, even though the largest part of the air is still emerging through the higher orifice. On the whole, the heat transfer coefficient profile of the dual-orifice air ring at the high setup position is more similar in shape with profiles obtained for single orifice air rings (see section 2.5.2). The absence of the Coanda induced vortex at the tip of the stabilization cone contributes to the differences between the two calculated profiles.

The calculated profile for the kinetic energy of turbulence is presented in figure 34. It is apparent that the introduced small setup variation caused noticeable transformations in the development of turbulence inside the air-ring and in the vicinity of the film bubble. In the high setup simulation, more turbulence is predicted in the lower orifice, which explains the more pronounced early cooling peak (see figure 33). In contrast, the turbulence associated with the higher orifice flow develops inside the orifice. By the time the jet is injected towards the bubble, most of the turbulence has already dissipated and cannot provide any cooling enhancement. Also, no generation of turbulence is observed at the higher lip because the air velocities inside the two orifices are more balanced.

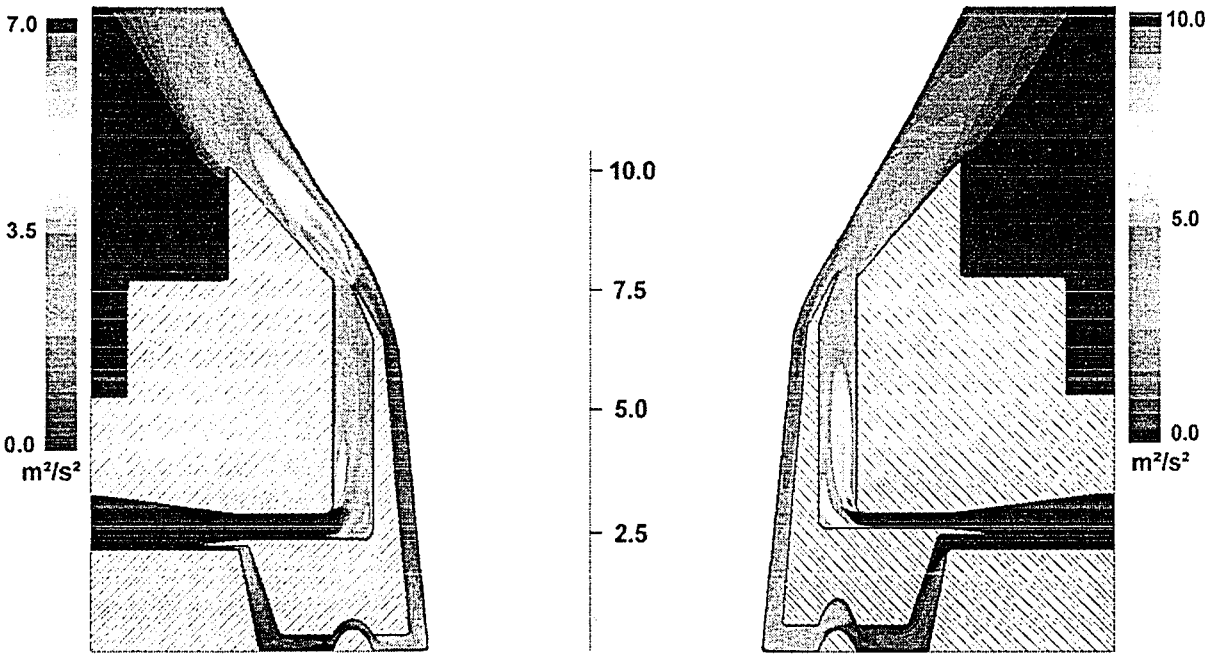

Figure 34: Kinetic energy of turbulence profiles for the low (left) and high (right) position setup simulations (detail)

It is noteworthy that the total heat transferred from the film to the cooling stream may not be largely different in the two cases. Since each setup is more efficient at certain areas and lacking in others, the overall additive cooling effect (from the die to the frost line) is not significantly altered (see Chapter 5 for a more detailed analysis). Even so, the differences between warm and cold stretching of the film (which the two different operational setups seem to instigate) are likely to influence the final film properties.

Figure 35 presents the gauge pressure profile on the external surface of the bubble for the two simulated setups. In the high setup simulation there is a significant pressure peak at the location of the low orifice, caused by the direct impingement of the air on the bubble. A similar peak also exists in the low setup simulation but it is less profound, mainly due to the reduced low-orifice airflow. In both simulations, after the lower orifice flow aligns with the bubble, it is forced to flow through the narrow gap (between the air-ring neck and the bubble) and local under-pressures (due to the Venturi effect) are generated. In both cases, the relative pressure stays negative until the air emerges from the air-ring. The relative magnitude of the Venturi effect under-pressure is very similar in the two simulations and does not seem affected by the operational setup position.

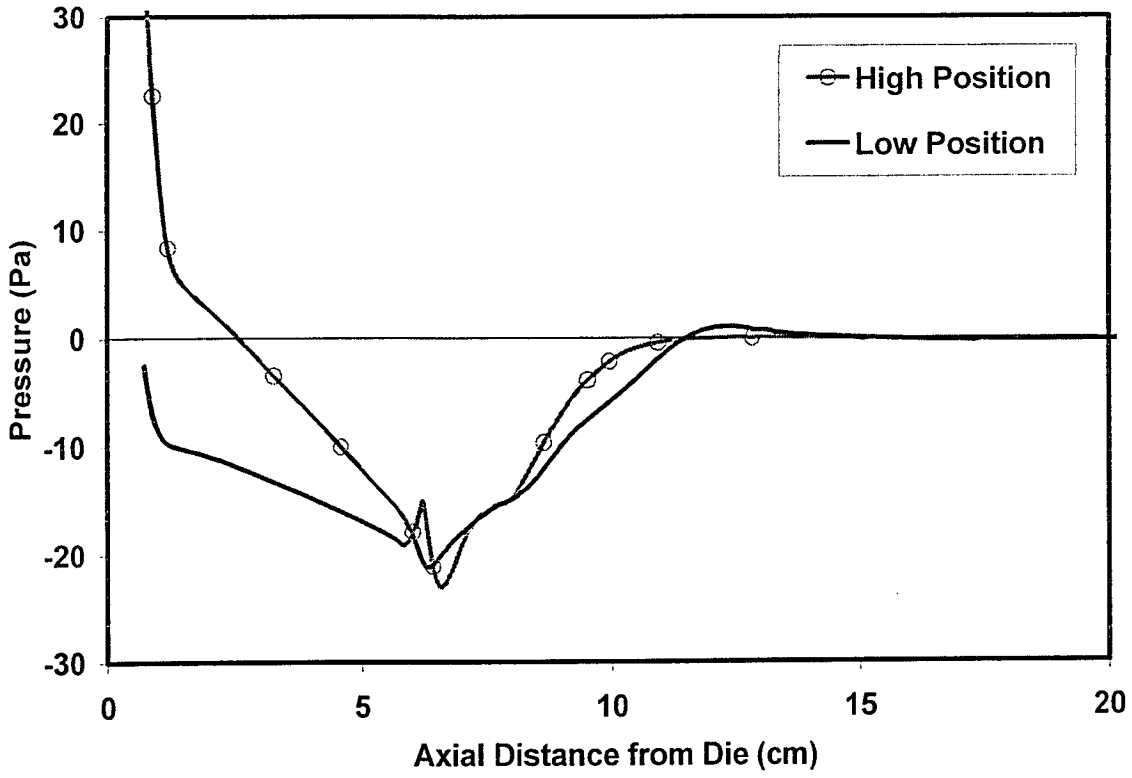

Figure 35: Gauge pressure profile on the film surface at different adjustable air-ring positions (LLDPE bubble shape)

It is worth mentioning that the initial pressure peaks are not a major cause of concern in most of the cases. The vast majority of commercial air-rings are equipped with a small metal *flow-deflector* at the lower orifice, which aid the lower orifice air-jet to redirect and flow parallel to the bubble. Direct impingement and redirection on the bubble surface is generally avoided because the film is very hot (and thus weak) close to the lower orifice lips. There is some variability in the design of the *deflector,* as various manufactures offer different implementations (some of them even offer adjustable deflectors). The *deflectors* were not incorporated in the current simulations, mainly to evaluate their necessity by calculating the pressure applied on the film in their absence.

The selective generation of Coanda effects and the local variation of the cooling peaks according to the operational air-ring setup (even with only minute setup modifications), may explain what operators of blown film lines often encounter in production lines: frequently they may manipulate the frost line and stabilize (or maybe de-stabilize) the bubble by slightly varying the adjustable air-ring setup.

In another set of simulations instead of varying the setup of the air ring, the original air-ring design was slightly modified. The higher lip was simulated in its original *tipped* design, as well as in a simplified *straight* design. The modification resulted in a small geometrical difference (in the order of 1mm) and was applied in the high-stalk (HDPE type) grid topology. The simulation was performed to verify the air-ring

manufacturer's claim that the *tipped* design was preferable in order to attain higher cooling rates.

Figure 36 compares the calculated streamlines using the moderate flow-rate (12 lt/s) for both designs. The tipped design results (already presented in section 2.6.2) show that the air-jet is originally directed away from the bubble, but a strong Coanda effect drives it to bend and subsequently impinge on the bubble surface. By comparison, the simplified straight design produces an air-jet with less bending. A Coanda effect is also present in this case (though much less profound) since the jet bends to some extent (after leaving the higher lip) in order attach in the off-set nearby film surface. Away from the air ring the air jet remains attached to the film surface and closely follows its curvature. This is a direct result of the Coanda effect (cooling air streamlines always remain closely bound to the curved wall and follow its curvature). It is noteworthy that the tipped design keeps the air-flow more closely bound to the film surface even at locations further away from the air ring.

Figure 37 shows the calculated profiles of the heat transfer coefficient on the bubble surface. Both designs generate the familiar cooling peak at the point where the low-orifice air-flow hits the bubble surface. There were no significant differences in the value and shape of the first peak between the two designs, which was expected since (at that point) the flow has not been directly affected by the design modification.

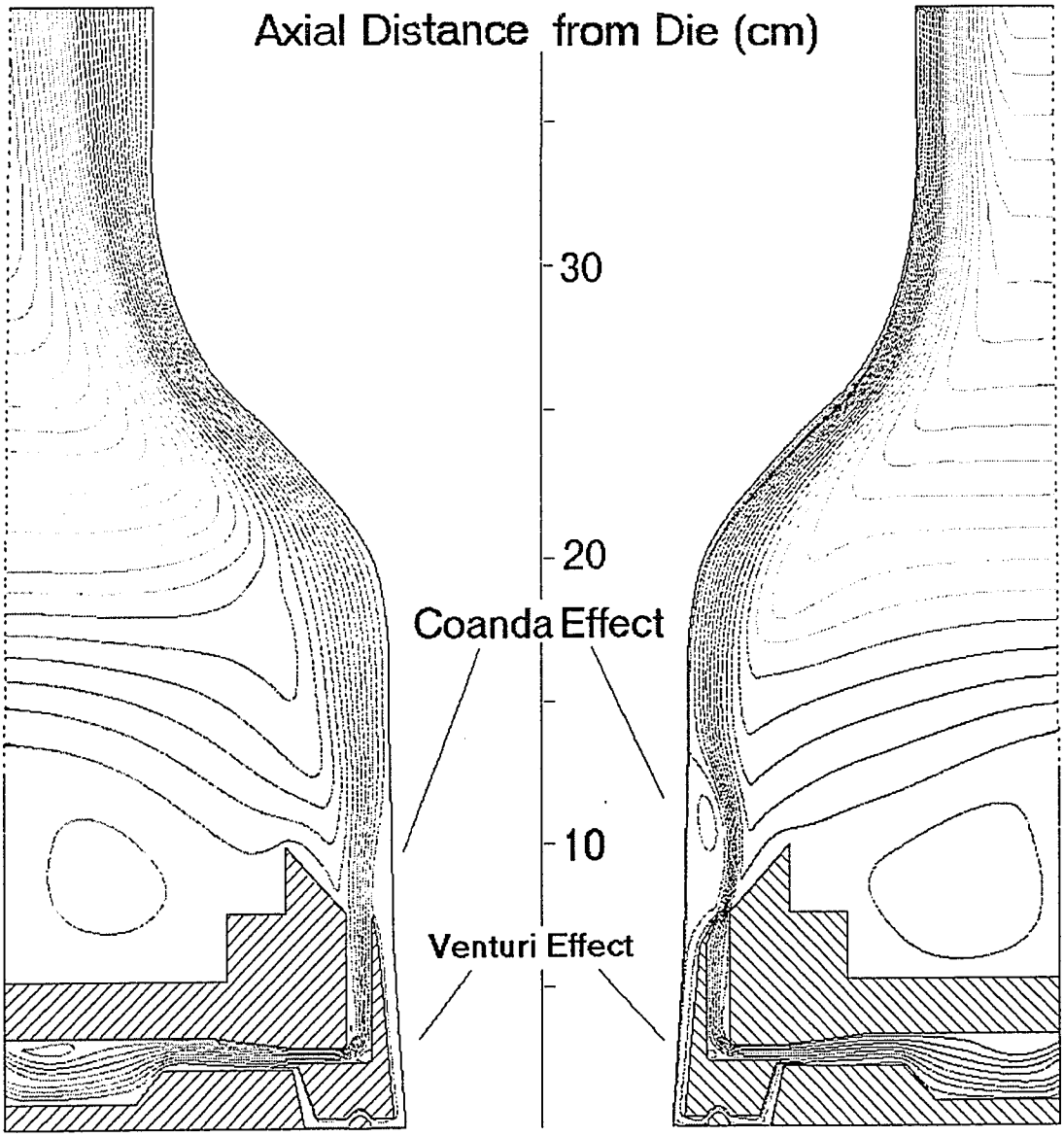

Figure 36: Cooling air streamlines (airflow 12 liter-of-air/s) around a long neck (HDPE) bubble for different upper-lip designs.
left side: straight upper lip, right side: tipped upper lip.

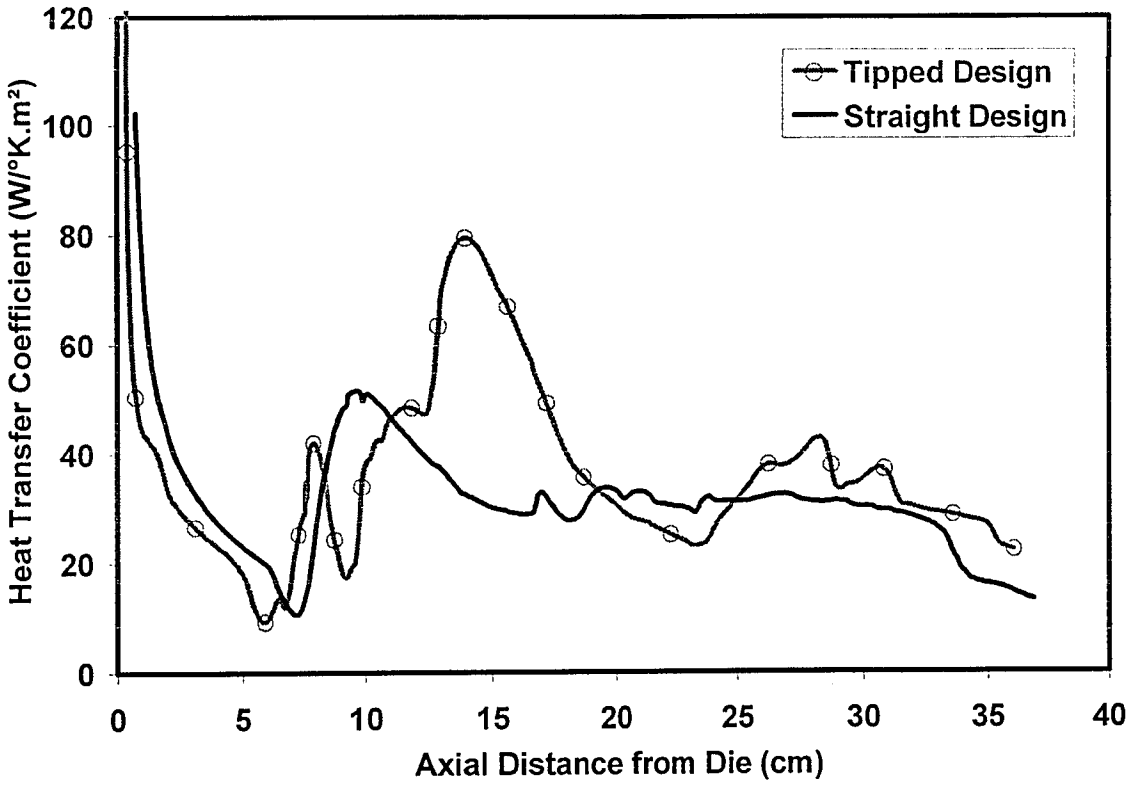

Figure 37: Heat transfer coefficient profile on the bubble surface for the original (tipped) and the modified (straight) upper-lip design (HDPE bubble shape)

A second peak occurs at the point where the high-orifice air-flow emerges. While the first peak is identical in both simulations, at the high lip (~10cm) and above the calculated cooling profiles show significant differences. The original tipped design has a higher heat removal capacity than its simplified counterpart. As the air moves away from the air ring the differences in the values of the heat transfer coefficient gradually become less profound. The simulation results verify the air-ring manufacturer's anecdotal claim that the *tipped* design provides increased cooling rates, which leads to increased production rates.

The Venturi effect is also affected by the design variation. Figure 38 presents the calculated pressure profiles on the external surface of the bubble. It is apparent that the modified design induces only small pressure variations. On the other hand, the original tipped design is generating larger and sudden variations of external pressure. The variations are caused by the flow transition from areas where the Venturi effect is predominant (causing under-pressure) to areas where the Coanda effect is directing the jet to impinge on the bubble (causing over-pressure). The calculated pressure variations (for the moderate flow-rate simulation) are not likely to cause any problem for the simulated bubble, as usually high-stalk shapes are formed in HMW-HDPE bubbles (which are very stiff and strong). However, sudden pressure variations may be responsible for serious bubble instabilities whenever combinations of low melt strength polymers (i.e. LLDPE) and high cooling-air rates are used.

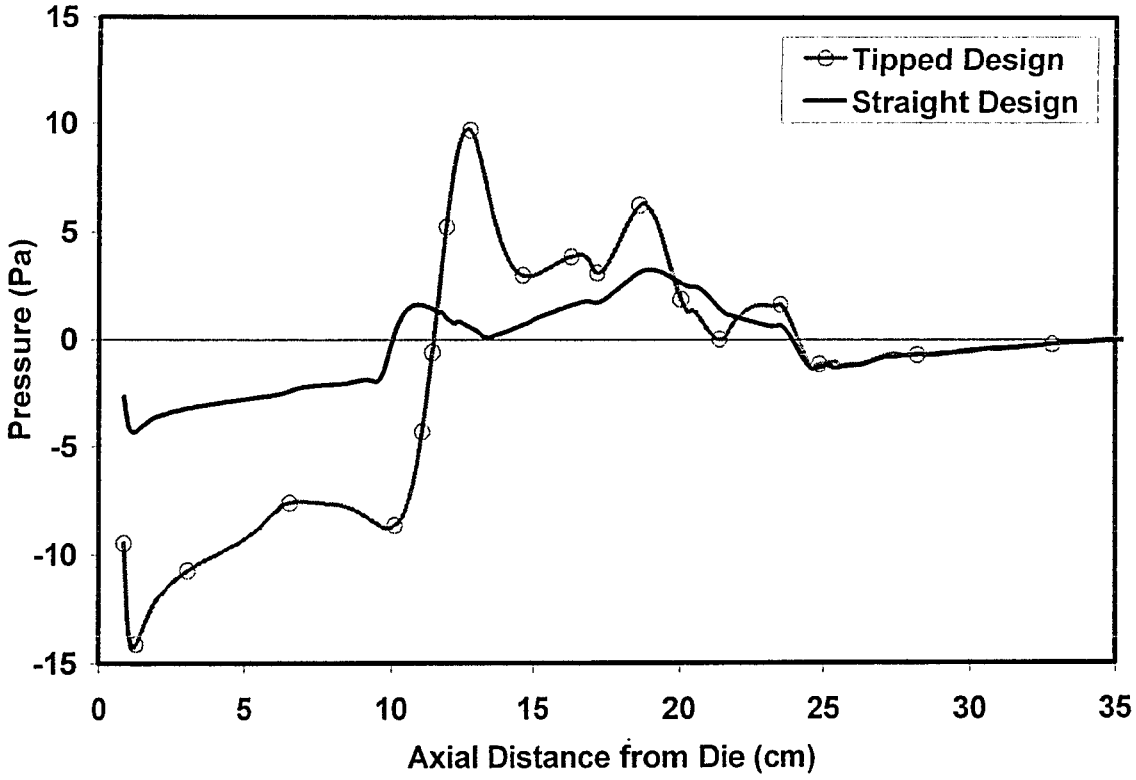

Figure 38: Gauge pressure profile on the film surface at different air flow rates (HDPE bubble shape)

Overall, the results illustrate how minor changes in the air ring design may cause substantial changes in the local cooling and pressure profiles. It is suggested that the presence and intensity of the Coanda effect is affected by minor design modifications. Therefore, the heat transfer capability of the cooling air stream may be influenced by (often neglected) minor variations in the air-ring design.

2.8. Assessment of the Calculated Heat Transfer Coefficient Profiles

The measurement of the actual heat transfer coefficients on the surface of a blown film bubble under typical operating conditions is an extremely difficult task. The presence of the measuring devices disturbs the axial symmetry of the airflow field. However small, the disturbance is enough to deform the delicate blown film bubble and significantly affect the measured values. The fact partially explains the absence of experimental data on the film surface heat transfer coefficients in film blowing.

To evaluate the calculated heat transfer coefficient profiles a test calculation was set-up, simulating an axisymmetric jet normally impinging on a solid flat plate. The simulated experiment [Mohanty & Tawfek, 1993] involved an orifice with diameter of 7mm, located 63mm away from the flat plate. The plate was equipped with heat flux sensors, which were located as far as 85mm from the stagnation point.

The simulation was set at orifice Reynolds number of 34500, corresponding to air velocity of 77 m/s at the exit of the orifice. By the time the air-jet is impinging on the plate the air velocity has dropped to ~40 m/s. After the jet hits the plate, it turns and flows parallel to the plate surface in the radial direction. The maximum radial velocity in the vicinity of the plate is 35m/s, dropping fast as the air flows in the radial direction.

The simulation results were compared with the measured values for the heat transfer coefficient. Figure 39 shows the measured values and the simulation results using the current model (RNG k-ε) as well as the more sophisticated Reynolds Stress Model (RSM). The RNG k-ε model succeeds in predicting the maximum heat transfer coefficient (at the stagnation point). Between dimensionless radial distances of 2 to 6, the calculated values are lower than the measured. At higher radial distances the differences become very small. In contrast, the RSM simulation captures more closely the radial profile of the heat transfer coefficient, but largely over-predicts the value at the stagnation point.

The selected evaluation set-up (using data from directly impinging axisymmetric jet experiments) is rather challenging for any turbulent model. Even so, the current model (RNG k-ε) performed with relative success. The actual blown film cooling simulation is less demanding in terms of turbulent modeling, because the air typically flows parallel to the film surface.

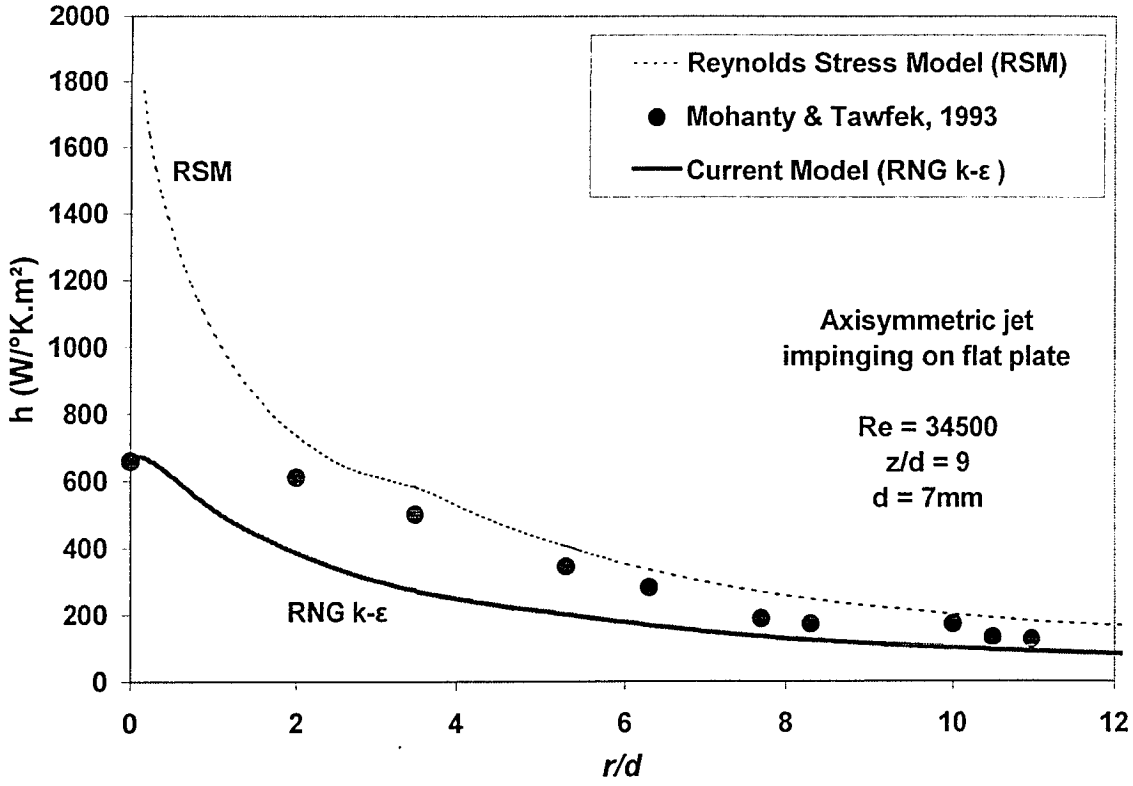

Figure 39: Comparison between measured and calculated heat transfer coefficient radial profiles on a flat plate resulting from a normally impinging round (axisymmetric) jet

For the air-ring simulations that were previously presented, the calculated bubble surface cooling profiles were not found to be significantly sensitive to different turbulence modeling options. As an example, for the LLDPE bubble with high airflow rate (already shown in figure 23), figure 40 compares the heat transfer coefficient profiles as various turbulent models calculated them. Despite the small differences, it is apparent that all the models give similar predictions for the location and the intensity of air-cooling.

For the *standard k-ε* and *RSM* models, the calculations were carried-out using the standard (most widely used) values for the turbulent parameters[1]: C_{μ}=0.09, $C_{1\varepsilon}$=1.44, $C_{2\varepsilon}$=1.92, Pr_k=1, Pr_{ε}=1.3, Pr_h=0.85. For more information see [22]. Varying the values of the constants did not produce significant differences in the calculated heat transfer coefficient profiles. The calculated heat transfer profiles has been proven to be most sensitive to the value of Pr_h (turbulent Prandtl number for the energy conservation equation). Even so, by varying Pr_h from 1 to 0.7 (a large variation for turbulent gas flows) the calculated profiles showed differences in the order of ±5%. The fact indicates that the simulation results are not heavily dependent on the selected model or the model parameters.

---

[1] In the RNG k-ε model, the constants are derived using RNG theory or locally calculated as parts of the solution (see chapter 2.4) and cannot be modified by the user

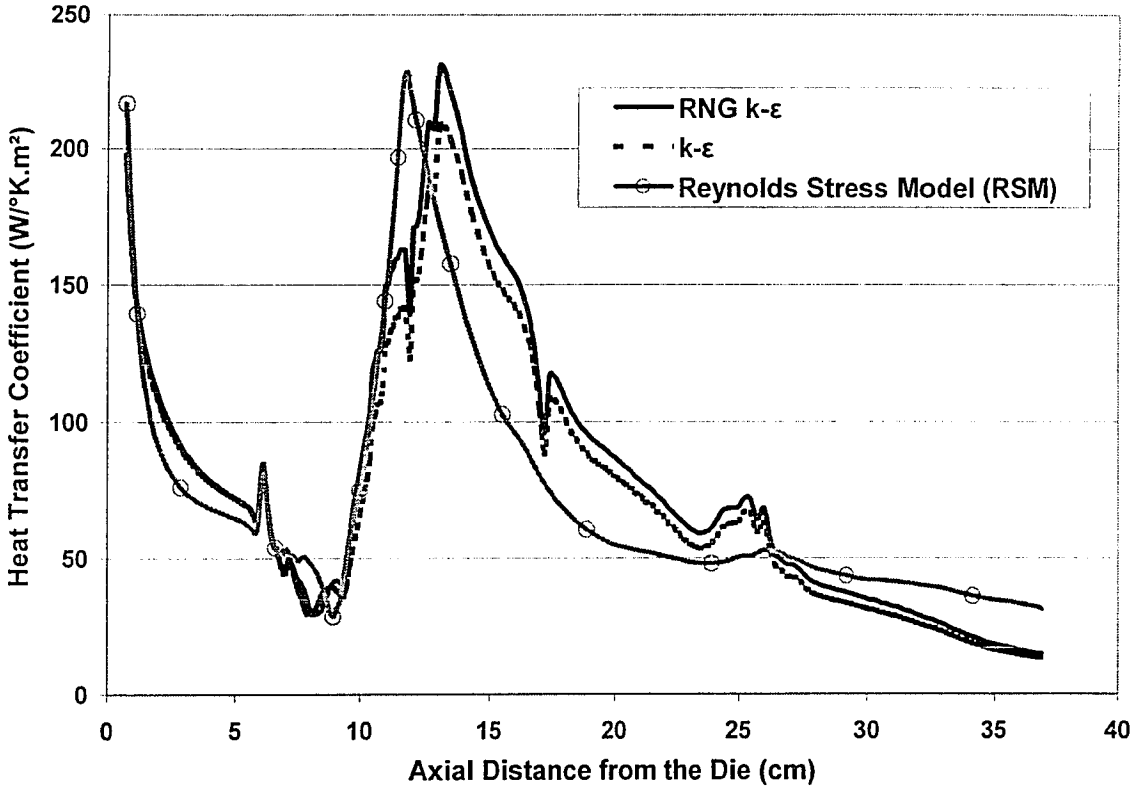

Figure 40: Heat transfer coefficient profiles (LLDPE bubble shape, airflow rate 25 liters-of-air/s) as calculated by different turbulent models (standard k-ε, RNG k-ε and Reynolds Stress Model)

The shape of the predicted cooling peaks (generated by Coanda induced jet impingements) are rather typical for impinging jets. Figure 41 shows experimentally obtained local heat transfer coefficient profiles [Gardon & Akfirat, 1966] for a two-dimensional air-jet impinging normally on a flat plate at various Reynolds numbers. The experiments that are presented in figure 41 are similar to the present bubble cooling simulations[1], though the Coanda effect usually creates jet impingements under an angle. Still, at high Reynolds numbers one may notice the secondary (smaller) peaks on each side of the main peak, which are also predicted by many of the current simulations.

---

[1] In the bubble cooling simulations presented in this work, the Reynolds numbers at the upper orifice are approximately 400, 1000 and 2000 for the low, medium and high airflow rates

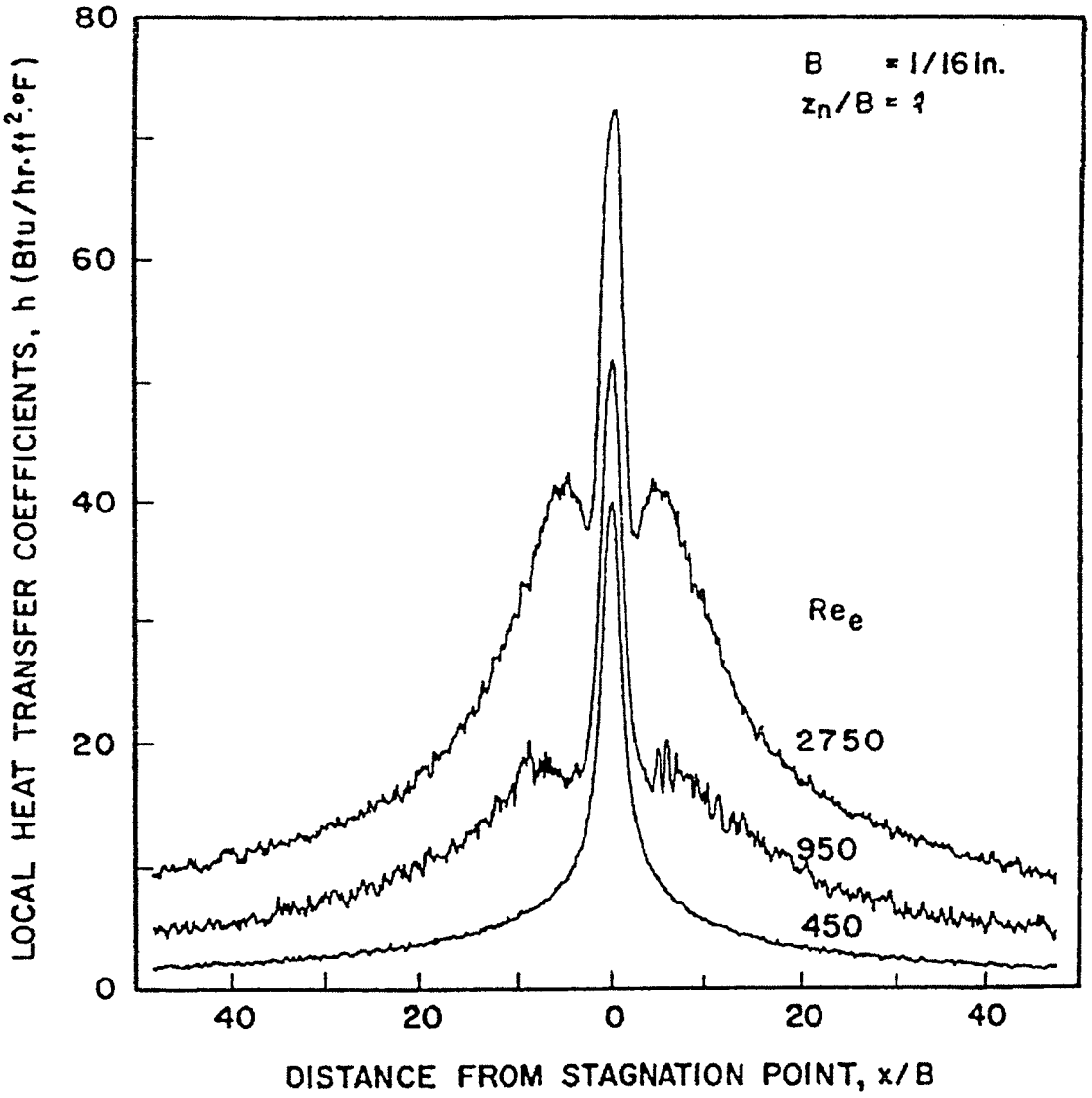

Figure 41: Effect of the orifice Reynolds number on the lateral variation of local heat transfer coefficients for a two-dimensional air-jet impinging on a flat plate (experimental data obtained by Gardon & Akfirat, 1966)

2.9. NOMENCLATURE FOR CHAPTER 2

A_μ,A_ℓ: constants

$C_{1\varepsilon}$,$C_{2\varepsilon}$: ε equation constants

C_p: heat capacity

C_μ: k-ε model constant

c_ℓ: constant

g: gravitational acceleration

k: kinetic energy of turbulence

p: pressure

Re_y: wall distance based turbulent Reynolds number

S: modulus of S_{ij} ($S = \sqrt{2S_{ij}S_{ij}}$)

S_{ij}: mean rate-of-strain tensor

T: temperature

t: time

U: average velocity

u: instantaneous velocity

u´: fluctuating velocity

y: cell wall distance

α: inverse Prandtl number (1/Pr)

ε: turbulent energy dissipation rate

μ: molecular viscosity

μ_{eff}: effective (total) viscosity ($\mu+\mu_{tur}$)

μ_{tur}: turbulent viscosity

ρ: density

ℓ_μ, ℓ_ε: length scales for the near-wall region

CHAPTER 3.

INTERNAL BUBBLE COOLING

3.1. INTRODUCTION

In the blown film process, the film bubble is typically cooled from the outside with one or more air-jets emerging from the external air-ring. Once the bubble is inflated to size, the air that is trapped inside the bubble may stay there indefinitely. The air-pressure that is required to sustain the inflation is very small, typically ranging from 25 to 500 Pa. The internal air circulates inside the bubble but since no air exchange exists, it does not increase the overall bubble cooling in any way. Naturally, a mechanism to exchange the internal air would help increase the cooling of the film which would ultimately lead to increased production rates. This process is widely known as *internal bubble cooling* (also known as IBC).

Internal bubble cooling involves specifically designed equipment, engaged in exchanging the warm internal air with colder external air and also constantly circulating and mixing the internal air. In some cases the external air is chilled before injected inside the bubble, in order to maximize the cooling benefit. Figure 42 depicts an outline of a typical IBC blown film line (not to scale).

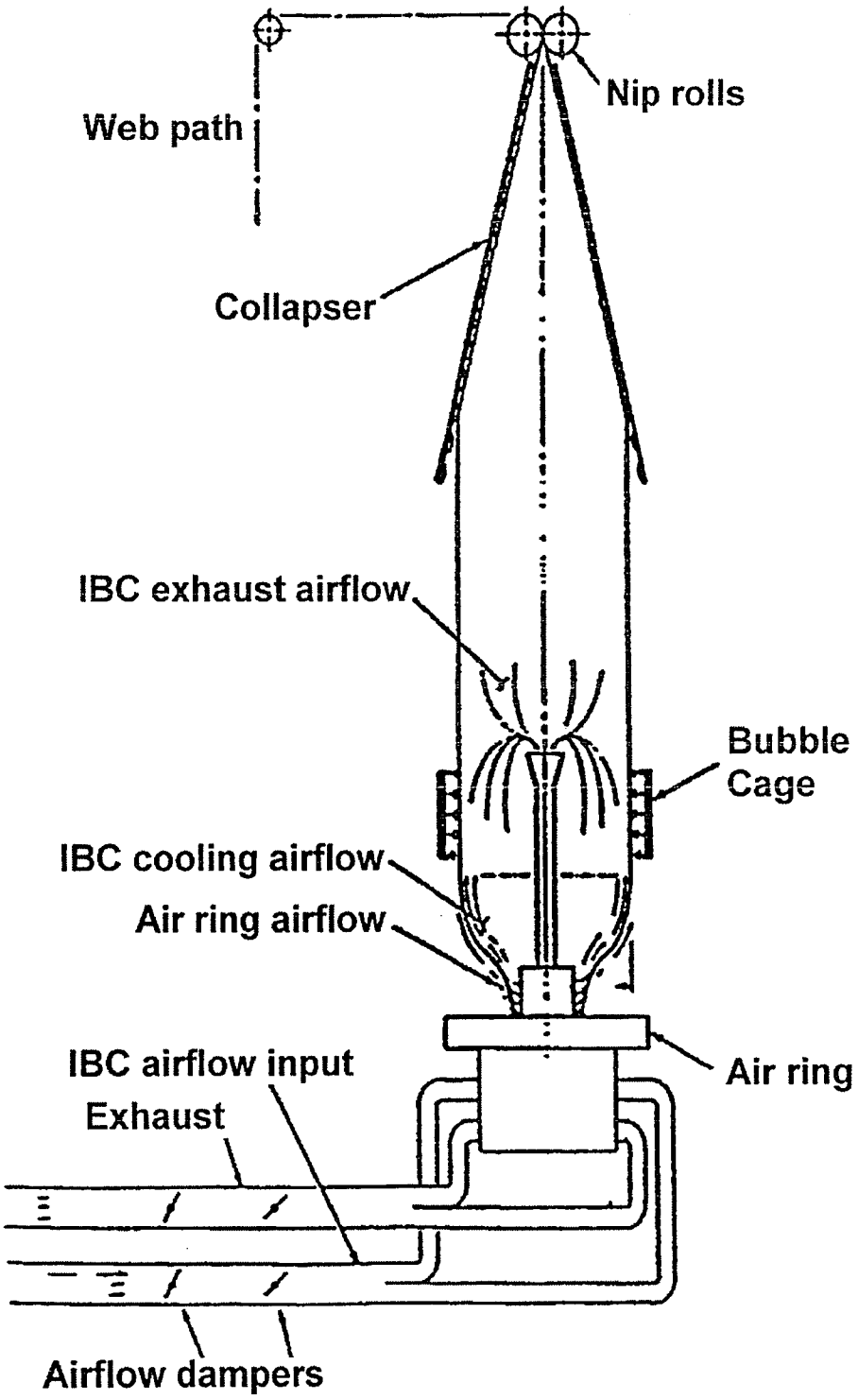

Figure 42: *Internal bubble cooling* (IBC) system

[Knittel & DeJonghe, 1992]

When using IBC, the expected production rate improvement becomes increasingly important as die size and film width increase. Production rate increases range from 20% for small bubbles (up to 8'' in die diameter) to as much as 80% for very large bubbles [Knittel, 1996].

In a typical IBC equipped blown film line, the fresh air is directed inside the bubble by means of a pressure blower. The air is forced to pass through a stack of distributor disks where it is re-directed and forced to impinge normal to the internal bubble surface. After the impingement, the heated air moves upwards inside the bubble and finally is redirected in the exhaust pipe. At the end of the exhaust pipe there may be a suction blower, which helps to reduce the high inflation pressure that occurs when operating at higher flow rates. Figure 43 depicts a typical *stacked disk* IBC configuration (not to scale).

Apart from the obvious increase in cooling efficiency (by doubling the effective area of transfer), IBC can also be used as a means to increase the cooling airflow on the outside, because of the stabilizing effect of the higher internal pressure. Calibrating equipment that may be present (designed to counteract the increased inflation pressure) further increases bubble stability. A useful side effect caused by the internal air exchange is the reduction of volatiles inside the bubble, which would otherwise be trapped and released during product processing.

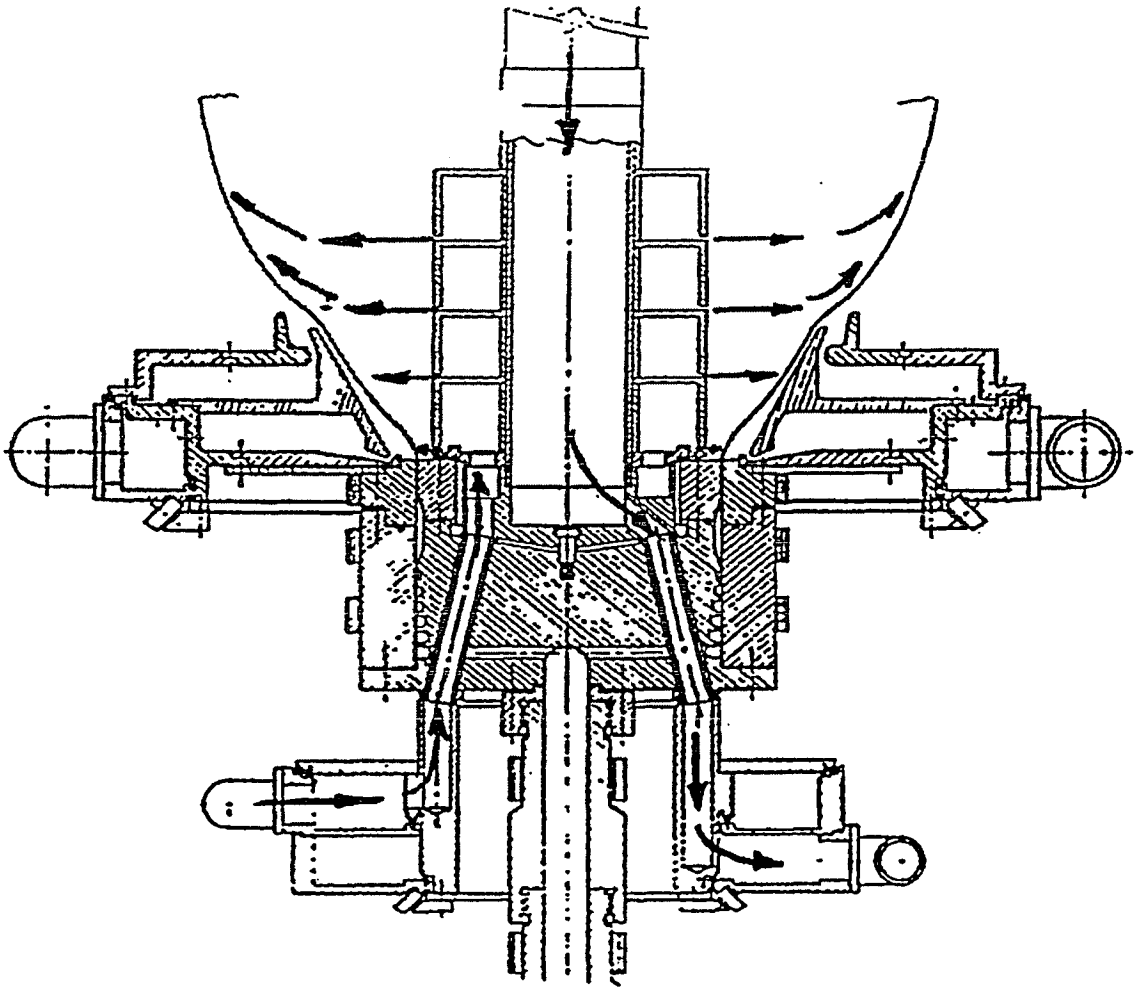

Figure 43: IBC system using stacked disks [Knittel & DeJonghe, 1992]

Although IBC systems decisively increase the production rate of numerous blown film bubbles, the expectations and the excitement [Wright, 1981] that was generated with the inception of the technology has only been partially met. The reason appears to be the increased complexity of the technology and the introduction of many additional variables, which must be controlled.

The complexity IBC systems are introducing requires close control of the operational airflow rates and the internal pressure. In fact, it is the affordability of electronic controllers in the early 80's that generated new interest for the technology [Wright, 1981]. Nonetheless, even with on-line controllers the operation of IBC systems should always be closely monitored. Also, since the IBC slits are inside the bubble, on-the-fly adjustments (which are widely used with external air-rings) are either impossible or require very expensive automated equipment.

3.2. Simulation of IBC Systems

Despite the increasing importance of internal bubble cooling in the film blowing process, a simulation of a typical IBC system has never been reported in the open literature. In much the same way, there has not been any known experimental work that deals with the IBC induced heat transfer in the internal surface of the film. In the current work, the complimentary inclusion of IBC in the LLDPE bubble studies provided a means to assess its relative importance.

3.2.1. Simulation Methodology

The die diameter and bubble shape that were used for the LLDPE shape external cooling simulations was also employed for the present simulation of IBC cooling. This way the direct comparison between the two different cooling-air streams could be attempted. All the modeling techniques, parameters and approximations that were presented in the previous chapter are also applicable in the IBC study.

The IBC slit stack that was employed in the simulation has a height equal to the height of the neck in the external air-ring (~8 cm). There are 4 slits in the IBC stack. The air is radially emerging from the 4 slits and impinges normally on the internal bubble surface. The slits have varying gaps to aid the homogenous distribution of the airflow. Figure 44 shows a schematic of the simulated IBC equipment.

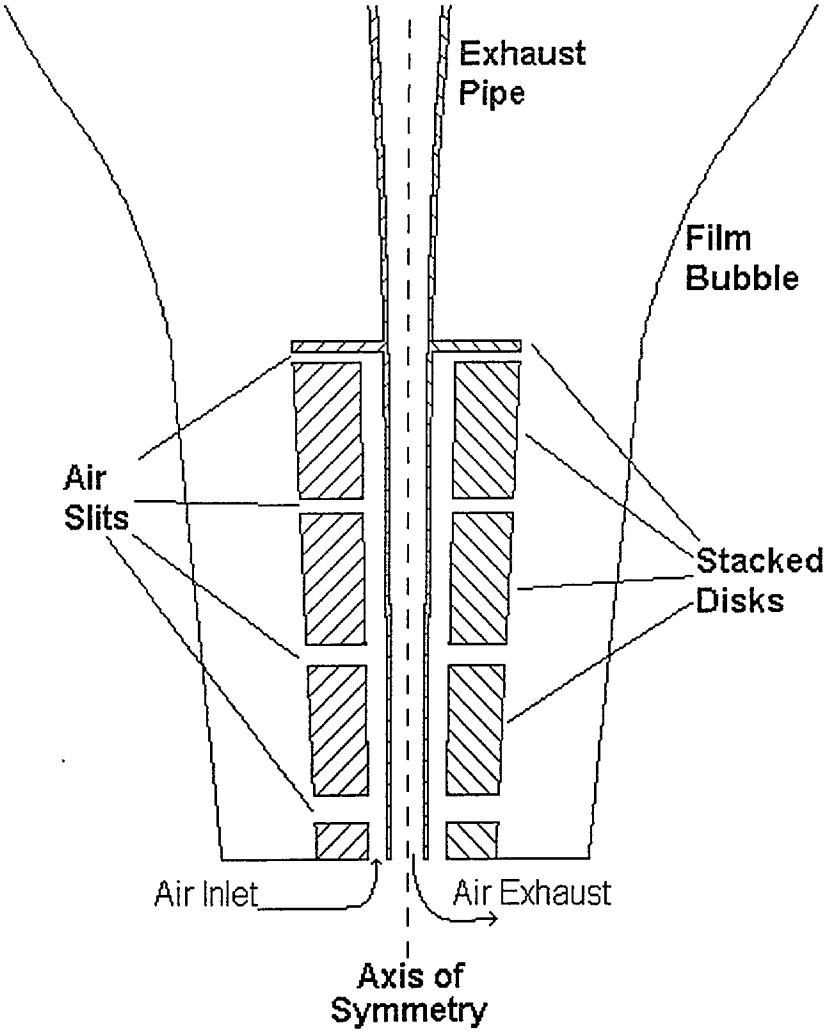

Figure 44: Schematic of the simulated stacked-disk IBC system

Since the impingement area is inside the external air-ring neck, the IBC impinging flow does not modify the bubble shape (the neck forces the film to have a specified shape that is not easily modified). As a result, it was assumed that the bubble shape is fixed for the studied airflow rates.

In the simulation, the cooling air enters the computational domain with predetermined velocity (design parameter) and temperature (35°C) to account for heating in the blower. The initial turbulent intensity is set to 10%. The film wall is considered solid and its temperature is gradually dropping in the axial direction. The implemented temperature profile is rather typical, based on available experimental data (see Appendix A).

The three different volumetric airflow rates that were used in the simulations (corresponding to low, medium and high internal cooling intensities) were selected to be 0.2, 0.5 and 1.3 liters-of-air/s. Higher airflow rates generated local velocities in the computational domain (more specifically inside the exhaust pipe) that could induce compressibility effects. For example, the high airflow rate produced exhaust air velocities in the order of 0.3 Mach (which is generally thought as the maximum to avoid compressibility effects). Compressibility can induce pressure variations harmful to bubble stability, thus limiting the maximum airflow rate that is applicable. The adverse effects of high IBC flow rates have been described in the literature as "pulsing" or "pumping" [Ryan, 1999]. So far, this behavior has been broadly attributed to "irregular or insufficient air exchange" without further explanation.

3.2.2. Results and Discussion

In accordance with the external air-ring studies, several airflow rates were implemented in order to validate the performance of the IBC stack. One may notice that, the operating IBC airflow rates are much smaller than their external equivalents. Consequently, the produced air velocities in the internal surface of the bubble are much smaller than external air velocities.

Figure 45 shows the IBC stream-lines for the low and medium airflow rates at different zoom levels (progressively focusing in the slit-stack area at the bottom of the bubble), while figure 46 shows a comparison between high and medium airflow rates. In all flow-rates, the air is initially directed to impinge normally on the film surface. Above the impingement area, the air turns and flows upwards. Just above the IBC stack a vortex is formed. The vortex dimensions increase as the airflow rate increases. In the high flow-rate simulation, one may notice that the large vortex pushes the air-jet to stay close to the film surface. In contrast, the smaller vortices that are predicted in the low and medium flow-rates fail to do so and the air flows further from the wall.

Further up inside the bubble (in the level of the exhaust pipe opening), the air turns, gets collected and flows towards the exit. The are no significant airflow or circulation patterns in the area above the exhaust pipe.

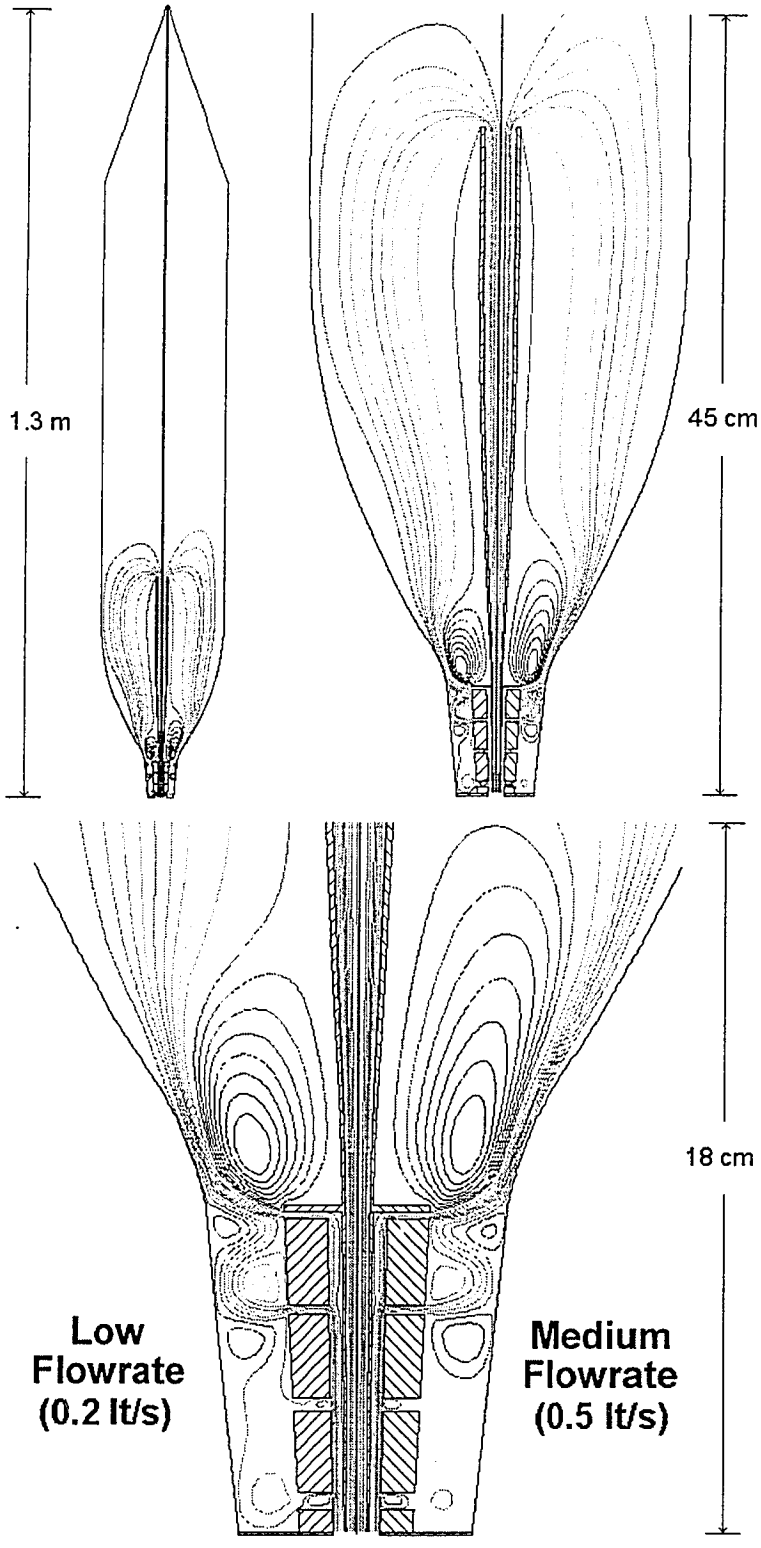

Figure 45: IBC-air stream-lines for low and medium airflow rates

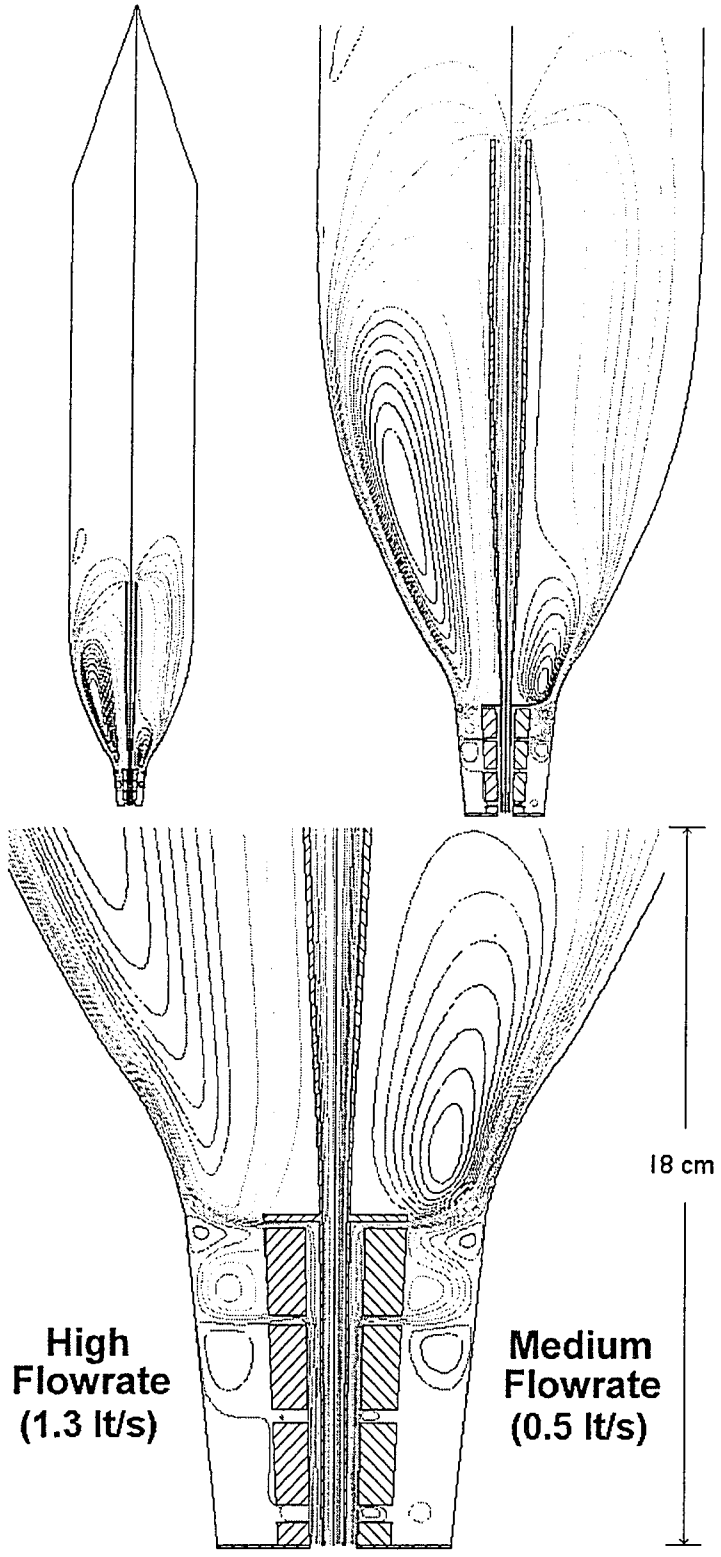

Figure 46: IBC-air stream-lines for high and medium airflow rates

Closer examination of the simulation results in the IBC stack area (at the bottom of the bubble) reveals that most of the air is injected towards the bubble from the slits on the top. The observation is true for all flow-rates despite the fact that the top-slits have been adjusted to have smaller openings. The results suggest that the phenomenon gets more pronounced as flow-rates increase.

Figure 47 shows the heat transfer coefficients on the internal surface of the bubble[1]. It is apparent that only two peaks occur regardless of flow-rate. The cooling is concentrated in the area where the air from the two top slits impinges on the bubble. The simulation results suggest that in a similar IBC design only two of the four disk openings contribute to the removal of heat from the bubble. The calculated cooling peaks are rather narrow and concentrated in the area of impingement, however they show a tendency to get wider as airflow rate increases.

Figure 48 shows the calculated relative static pressure on the internal bubble surface. The simulation predicts that the internal pressure does not vary much. Even at the high airflow rate, the pressure increase is limited to only a few Pa and is not significant. The results imply that bubble "pumping" is unlikely to be caused by the minor forces applied in the impingement zone. It is more likely that compressibility effects in the exhaust pipe cause the large internal pressure fluctuations.

---

[1] In all the simulations, the heat transfer coefficients were calculated using the average internal air temperature as reference temperature (the value varied from 60 to 65 °C)

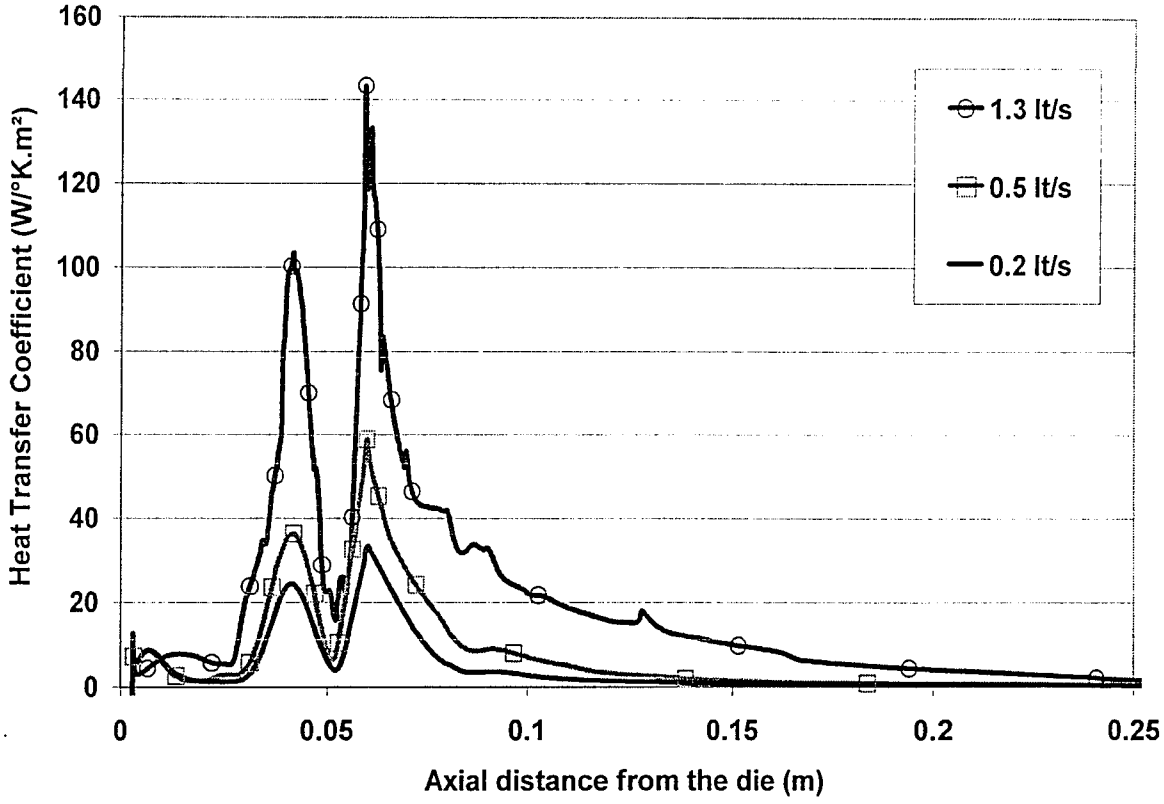

Figure 47: Heat transfer coefficient profiles applied on the internal bubble surface for different IBC airflow rates

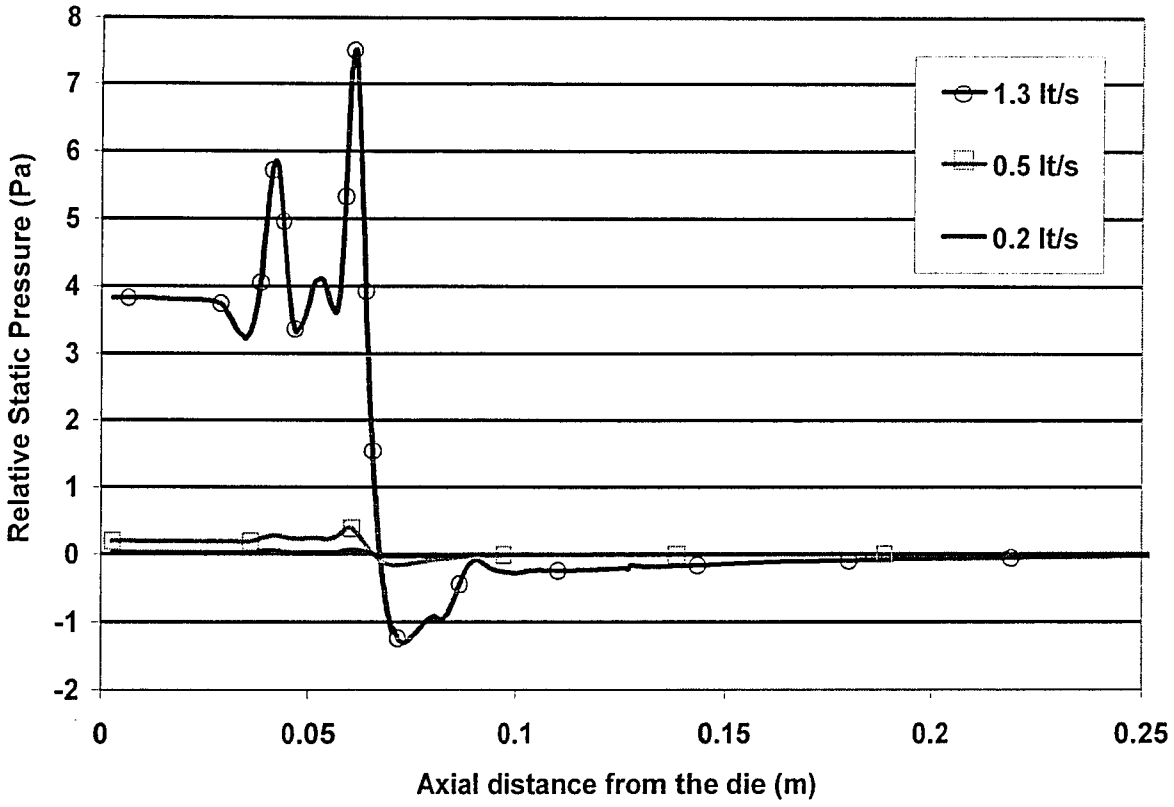

Figure 48: Relative static pressure applied on the internal bubble surface for different IBC airflow rates

3.2.3. IBC Design Sensitivity

Design modifications were applied on the already presented IBC implementation in order to estimate the performance sensitivity of the current design and IBC systems in general. It should be noted that there is a high degree of secrecy for working IBC stacks and a detailed operating design could not be obtained. Therefore, the studied design was only one of many possible arrangements. Since the current implementation showed an inability to employ all four slits in directing the air towards the bubble, the modifications were focused on the improvement of that design aspect, by forcing an improved flow balance.

In a first attempt, small air deflectors were added in the inlet pipe to force some of the airflow to turn and travel through the lower slits, instead of flowing upwards and then exiting from the top slits. Figure 49 shows both the original and modified inlet pipe designs. The deflectors were sized to reduce the gap of the inlet-flow annulus by 20% and were positioned just above the slit opening[1]. Although the implemented design modification was rather small, previous simulations (see section 2.7) have shown similar minor design modification to have a disproportionally large effect on the cooling performance of the air stream.

---

[1] Other locations to position the flow deflector (more specifically below the slit opening, in the middle of the opening and in between consecutive slits) were also tried. The presented position (above the opening) has proven to be the most effective.

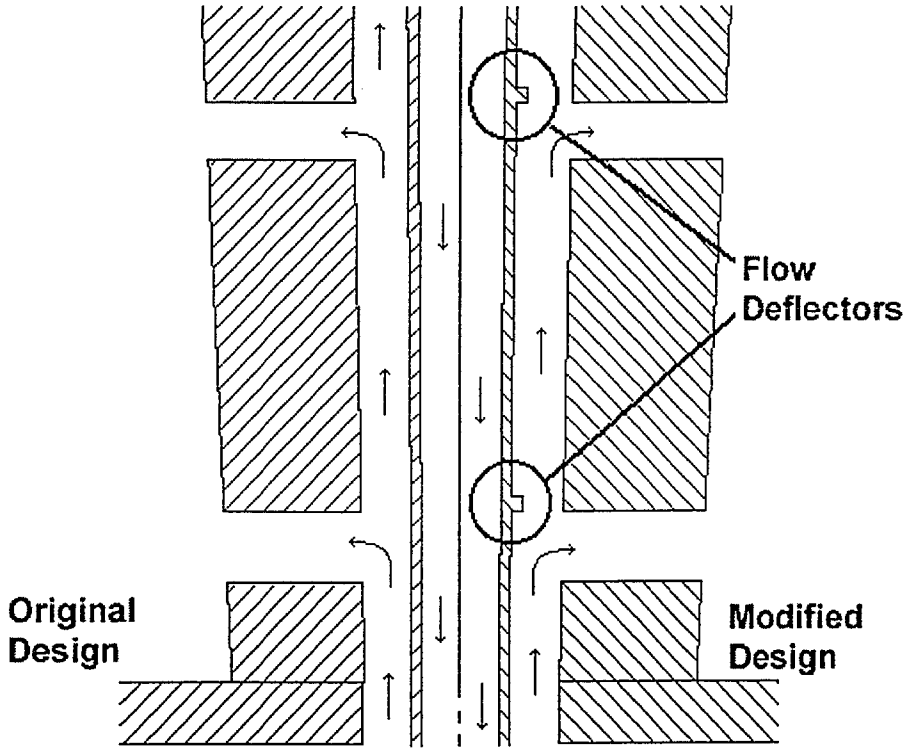

Figure 49: IBC design modification[1] with the addition of flow deflectors

[1] For full geometrical details see Appendix B

Figure 50 presents a comparison of the calculated streamlines for the original and the modified (with the addition of flow deflectors) design (medium airflow rate). Figure 50 depicts the flow-field using 30 streamlines (a larger number than the usually shown 20 streamlines – see similar figures 45 and 46) in order to better illustrate the very small variations between the two calculated flow-fields.

The simulation results suggest that a small flow-balancing improvement can be achieved, as more air is injected through the lower slits, but the cooling enhancement is not very large. Figure 51 depicts the calculated heat transfer coefficients on the bubble surface. It is apparent that the minor improvement in balancing the flow is not effectively extending the internal cooling at lower bubble positions. The simulations at the other two airflow rates showed (more or less) the same picture regarding the design modification: some increase in the airflow through the bottom slits is predicted but not enough to constitute a cooling improvement.

The simulation results suggest that the minor modification in the studied IBC design was not able to modify the cooling performance of the system. However, practical experience from manufacturers of blown-film cooling equipment suggests that IBC systems are sensitive to small design modifications. A second modification was implemented on the original design, in order to better validate the design sensitivity issue.

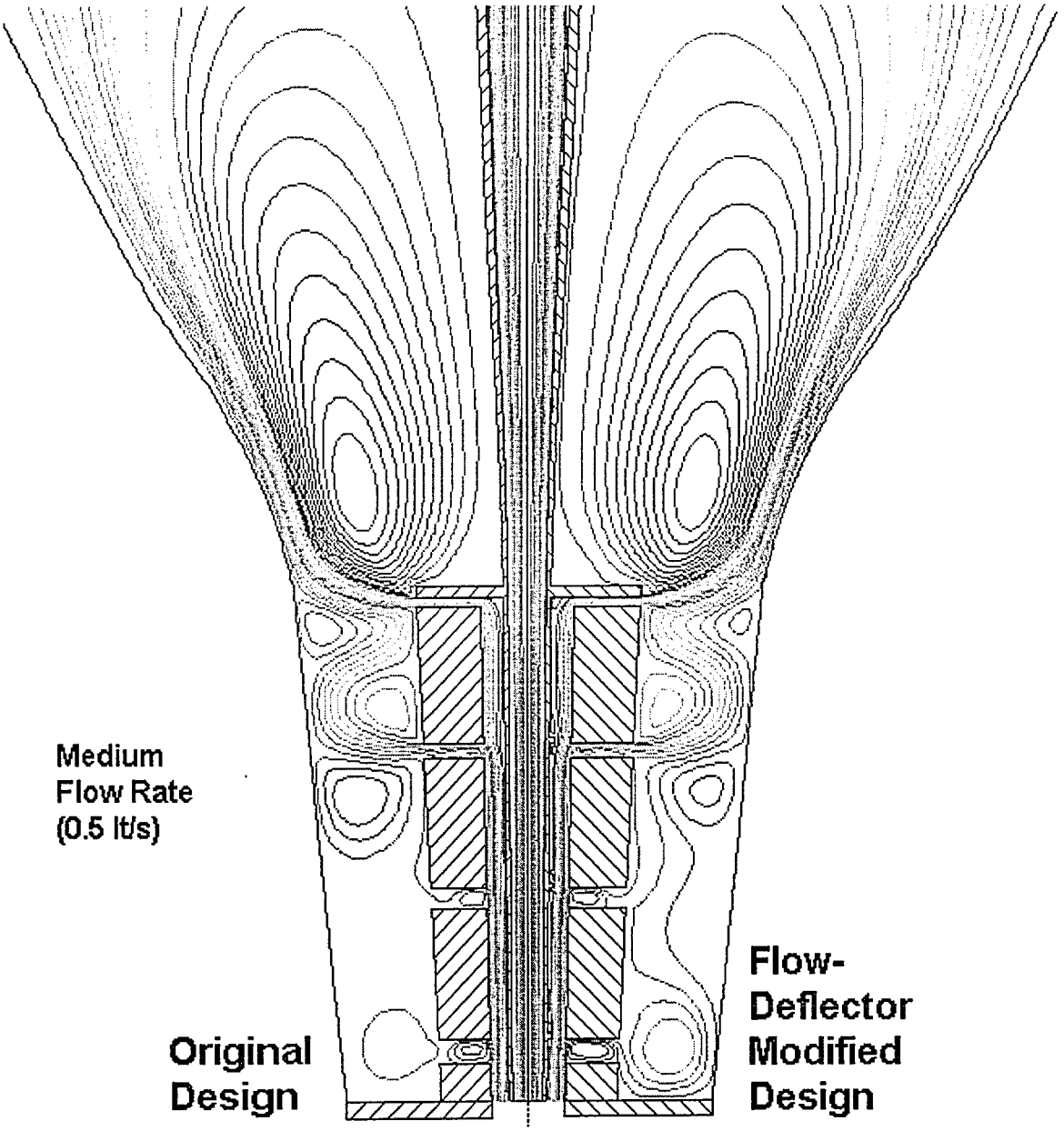

Figure 50: Medium flow-rate (0.5 liters-of-air/s) stream-line comparison between original and flow-deflector modified IBC system (30 streamlines shown)

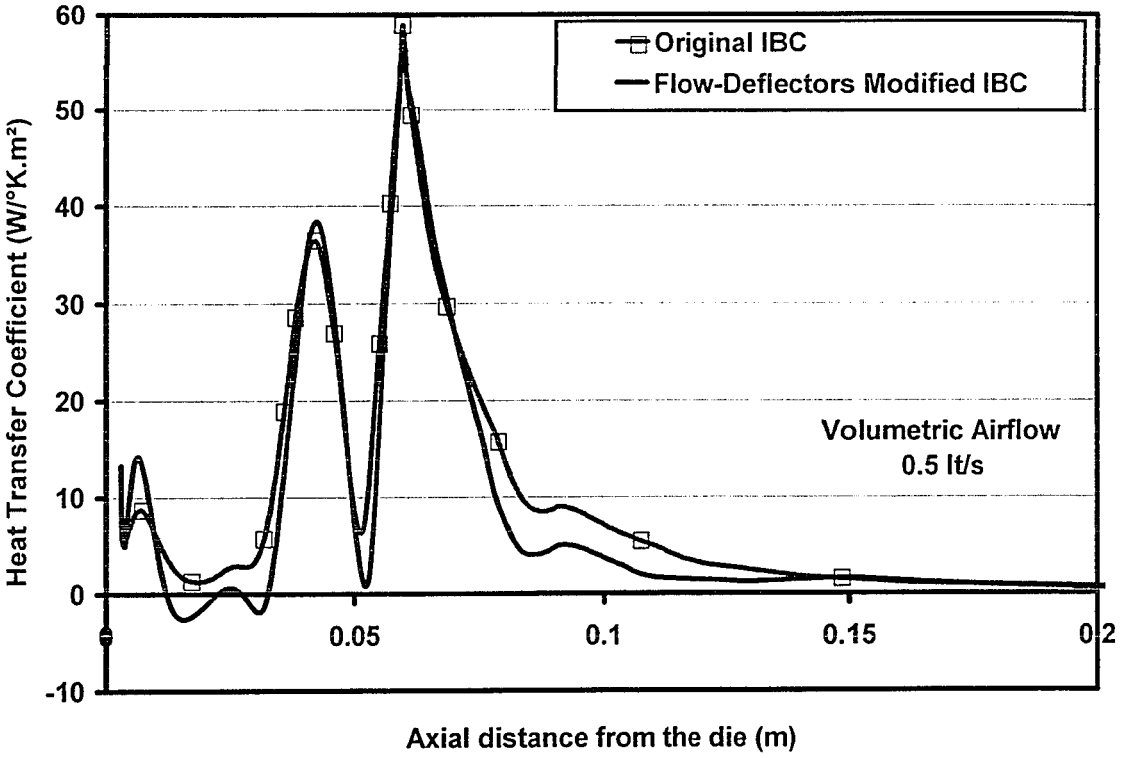

Figure 51: Calculated heat transfer coefficients (original and flow-deflector modified design) applied on the internal bubble surface for medium airflow rate (0.5 lt/s)

The new modified design uses an inlet annulus that is gradually reducing in gap as the air flows upwards. The annular gap is equal to the gap in the original design only for the forth (top) slit. Each contraction is rather small since the annular gap is reduced only by 10% (smaller than the previously used flow deflectors that restricted the gap by 20%). Figure 52 presents a comparison between the original and the new design. The part of the annular pipe that leads to the fourth slit is unchanged, but the annular gap between the third and second slit is 10% wider, the gap between the second and the first slit is 21% wider and the gap preceding the first slit is 33% wider (making for successive 10% reductions). The figure is correctly scaled, making apparent that the design modification was rather subtle.

In the simulation, the volumetric flow-rate was kept constant at the medium level (0.5 lt/s). This resulted in smaller initial velocities in the modified design, since the initial annular gap is 33% larger. Figure 53 compares the calculated streamline patterns for the original design as well as the gradually contracting inlet-gap design. The simulation results predict a flow pattern that is more balanced in the modified IBC design. Even though the top slits are still slightly favored, substantial air-jets seem to emerge from all four slits. The cooling air impinges on the bubble surface at more points, creating more contact and recirculating patterns. However, since the flow is divided in four parts (instead of two in the original design), the air-jets are less intense in the modified design.

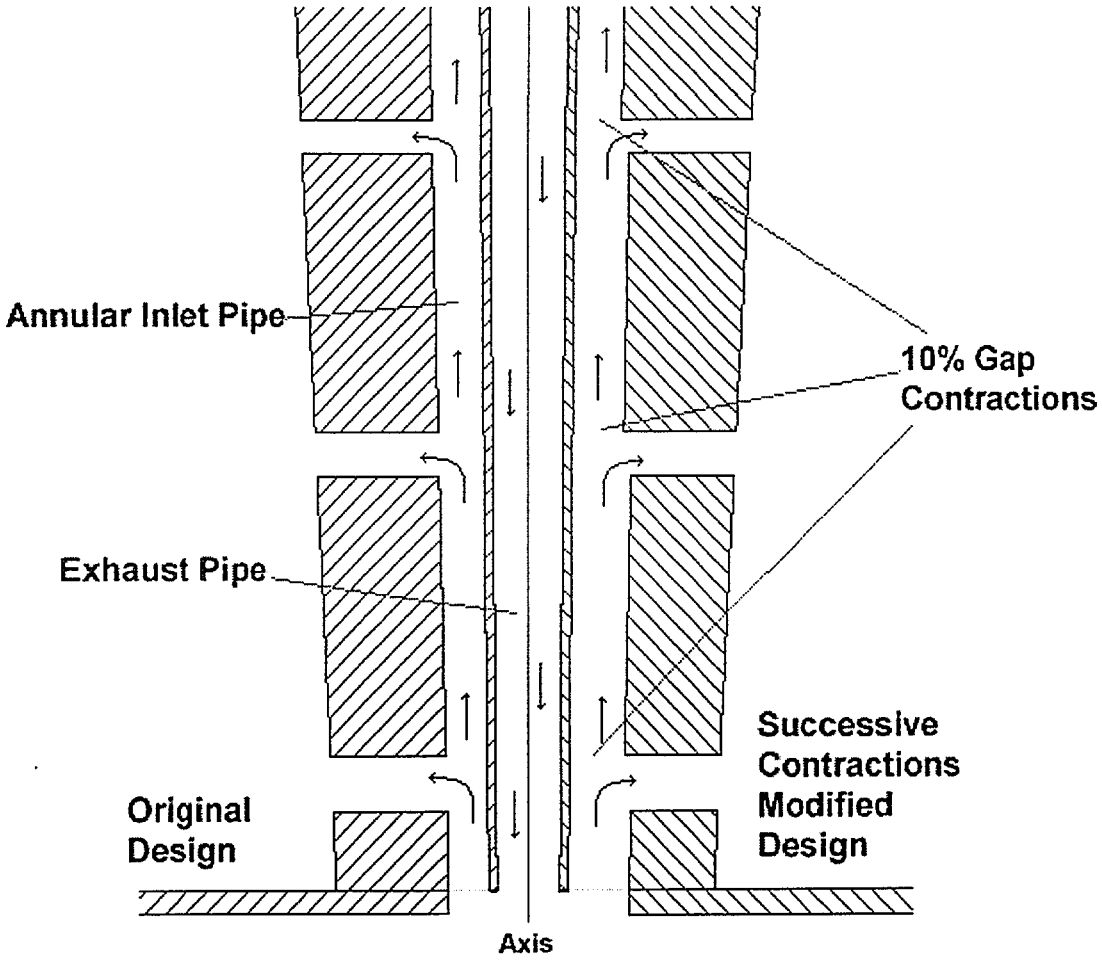

Figure 52: IBC design modification[1] with the addition of successive gap contractions (10%) of the annular inlet-pipe

[1] For full geometrical details see Appendix B

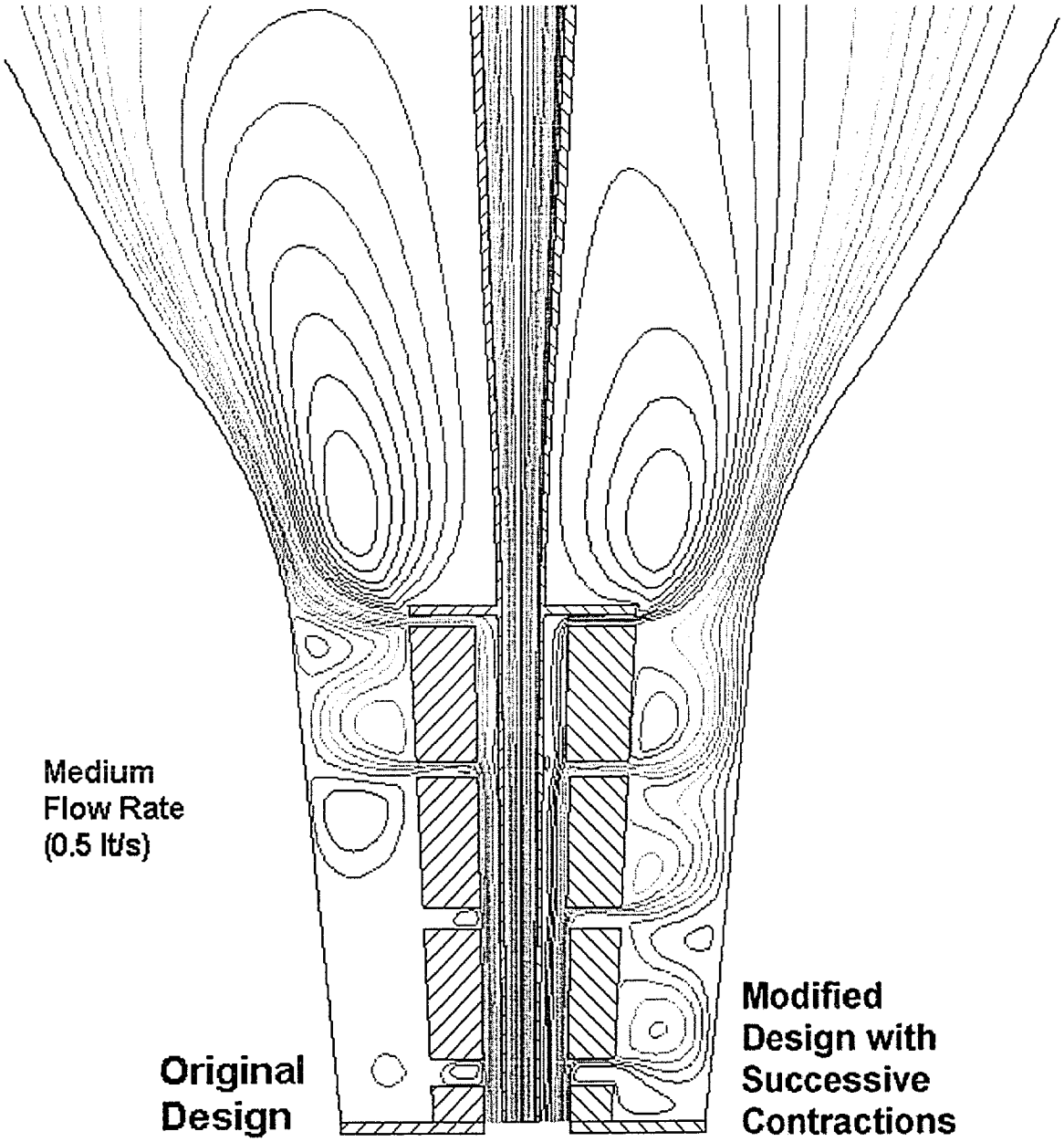

Figure 53: Medium flow-rate (0.5 liters-of-air/s) stream-line comparison between original and the modified IBC system which balances the flow by use of *successive gap contractions* at the inlet-annulus
(20 streamlines shown)

Figure 54 compares the calculated heat transfer coefficient profiles at the internal bubble surface, concentrating at the impingement area where the differences are significant. The simulation of the modified design predicts more cooling peaks than the original design, something expected since the form of the flow pattern (figure 53) suggests more impingement points. Additionally, the cooling peaks have a smaller magnitude (when compared to the original design) because the flow is evenly divided between the slits. In the area above the direct impingement zone, the heat transfer coefficient profiles for both original and modified design become indistinguishable.

It is noteworthy that in the modified design simulation, cooling peaks are gradually decreasing in magnitude, even though figure 53 suggests that still more air is emerging from the top slits. Closer examination of figure 53 reveals that the air-jets from the higher slits do not impinge directly on the bubble surface, but they impinge on the lower-slit air that flows along the bubble surface. That may explain the gradual reduction in magnitude of the cooling peaks.

Figure 54 indicates the differences in cooling performance between the two designs, but it is not immediately apparent which design is more cooling-efficient. For that, the calculated local heat transfer profiles were integrated over the bubble surface area between the die lips and the frost-line.

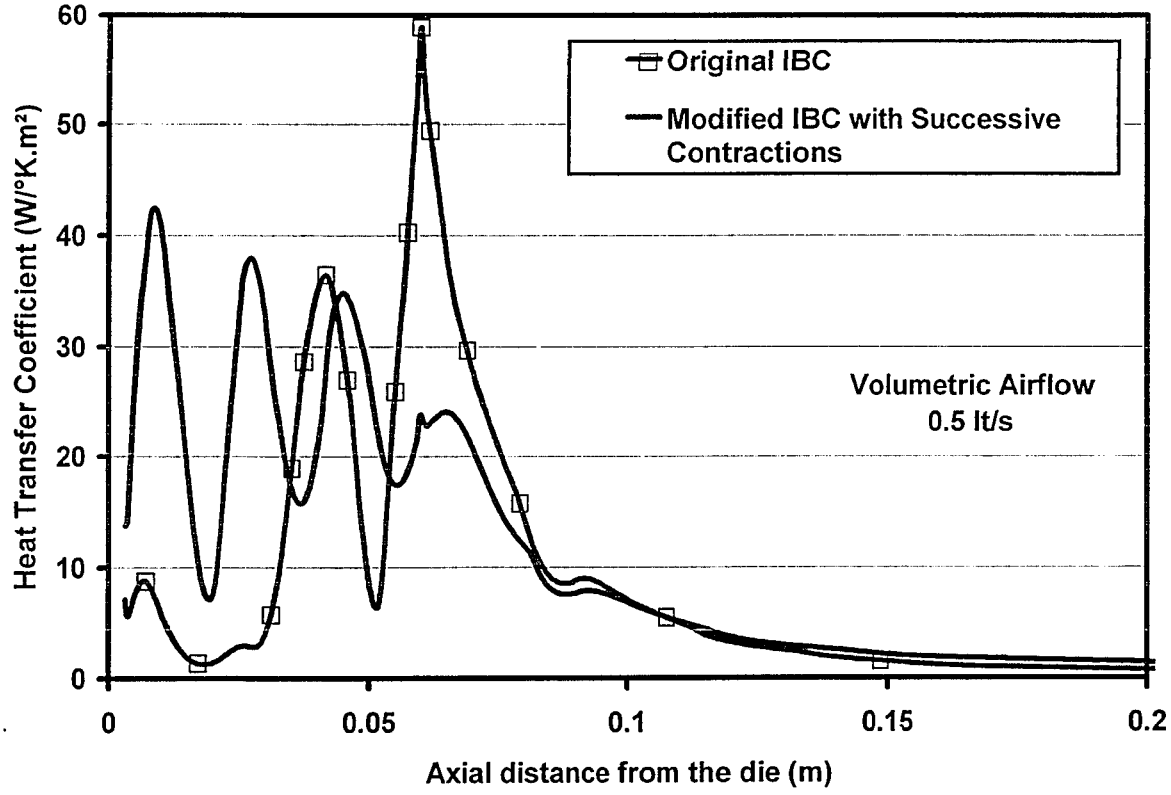

Figure 54: Calculated heat transfer coefficients (original and *successive-gap-contractions* modified design) applied on the internal bubble surface for medium airflow rate (0.5 lt/s)

The simulation results do not predict the existence of any attachments generated by the Coanda effect (which was predominantly present in the external bubble cooling simulations). It is noteworthy that the impingement region of the internal bubble surface is generally subjected to milder conditions when compared to the external surface. Both pressure variations and cooling intensity are small and concentrated in a very small area.

Figure 55 depicts the calculated air-velocity profiles for the original and modified inlet pipe design. Both simulations predict that the airflow comes through the inlet annulus having a high velocity. The velocity drops as the airflow is divided between the slits. In addition, once directed in the radial direction, the air-velocity drops rapidly as the flow moves away from the axis of symmetry[1]. By the time the air hits the internal bubble surface, its velocity has reduced to only a small fraction of the velocity it used to have in the inlet pipe. On the other hand the airflow rate in the inlet pipe (and consequently the exhaust pipe) cannot be increased indiscriminately because compressibility effects in the pipes may cause bubble instability. The problem should be more pronounced in small diameter bubbles at high flow-rates.

---

[1] This is expected as the same amount of air is flowing in the radial direction through an increasing area and conservation of mass dictates that the air-velocity will decrease

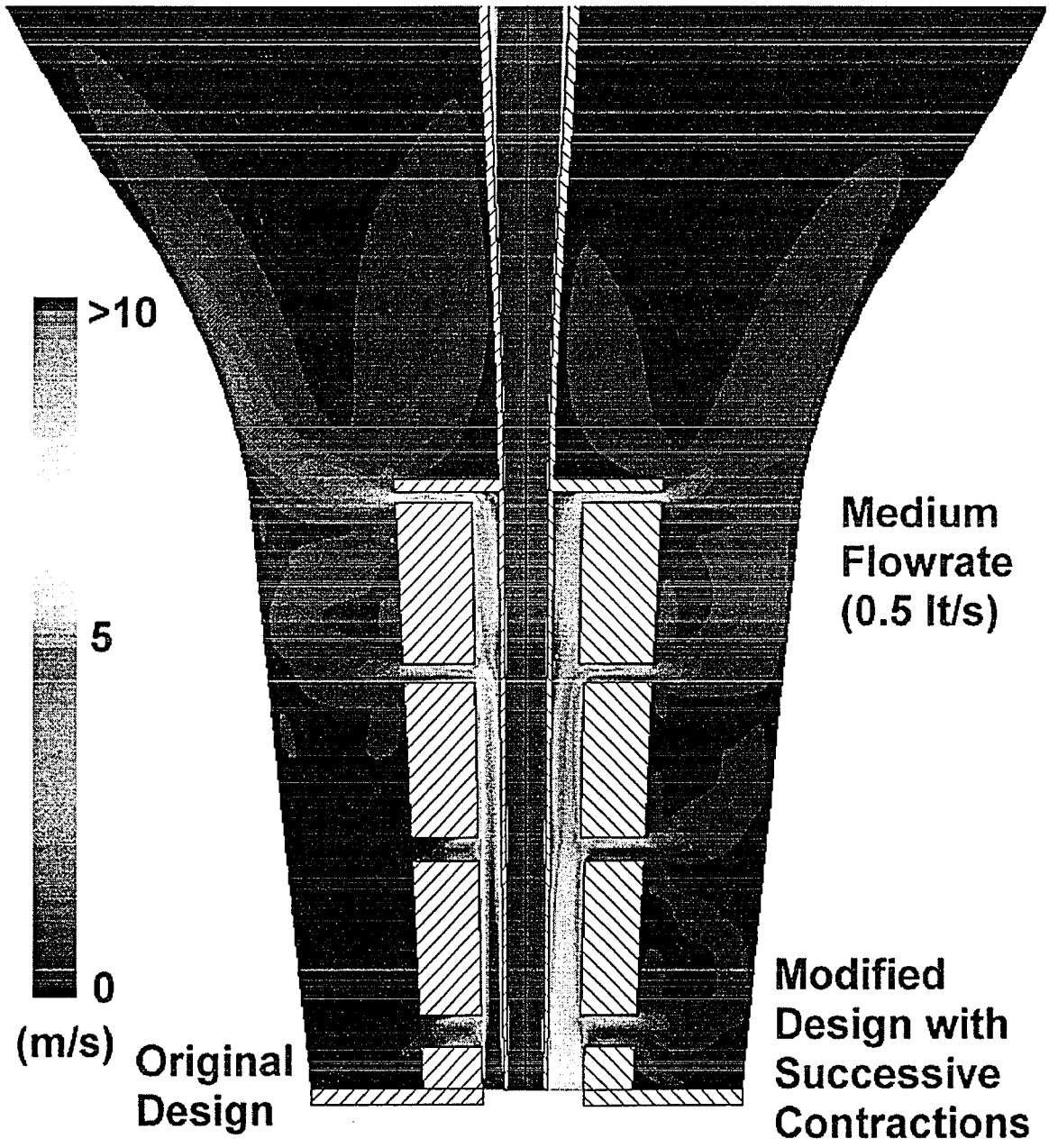

Figure 55: Calculated velocity magnitude for the original and modified IBC designs at the medium airflow rate (0.5 liters-of-air/s)

As expected, the calculated turbulent intensity of the IBC stream has a behavior related to air velocity. As the air stream flows in the radial direction and decelerates, the turbulence that was produced in the inlet pipe drastically reduces in intensity. Figure 56 shows the profiles of turbulent kinetic energy for both the original and modified design at medium airflow rate. In both cases, there is some turbulence inside the slits that is probably caused by the narrow gap between the disks. However, as the flow travels in the radial direction and decelerates the turbulent intensity is gradually reduced. By the time the internal air-jet hits the bubble surface, most of the turbulence has dissipated. As a result, the bubble surface experiences very mild conditions in regard to both turbulence as well as local air velocities.

The simulation results partially explain the empirical observation that in small bubbles IBC systems can only increase the cooling capacity by a limited amount (up to 20%), while larger bubbles enjoy more substantial cooling improvements (up to 80%) [Knittel, 1996]. Airflow limitations in the inlet or/and exhaust pipe are more pronounced in smaller bubbles simply because the physical dimensions of the pipes are more limited and the cooling airflow is forced to travel through narrower paths. On the other hand, larger bubbles can accommodate larger IBC stacks, which may be carefully designed with larger pipes to avoid air-flow overloads at the inlet and/or outlet (exhaust) pipes.

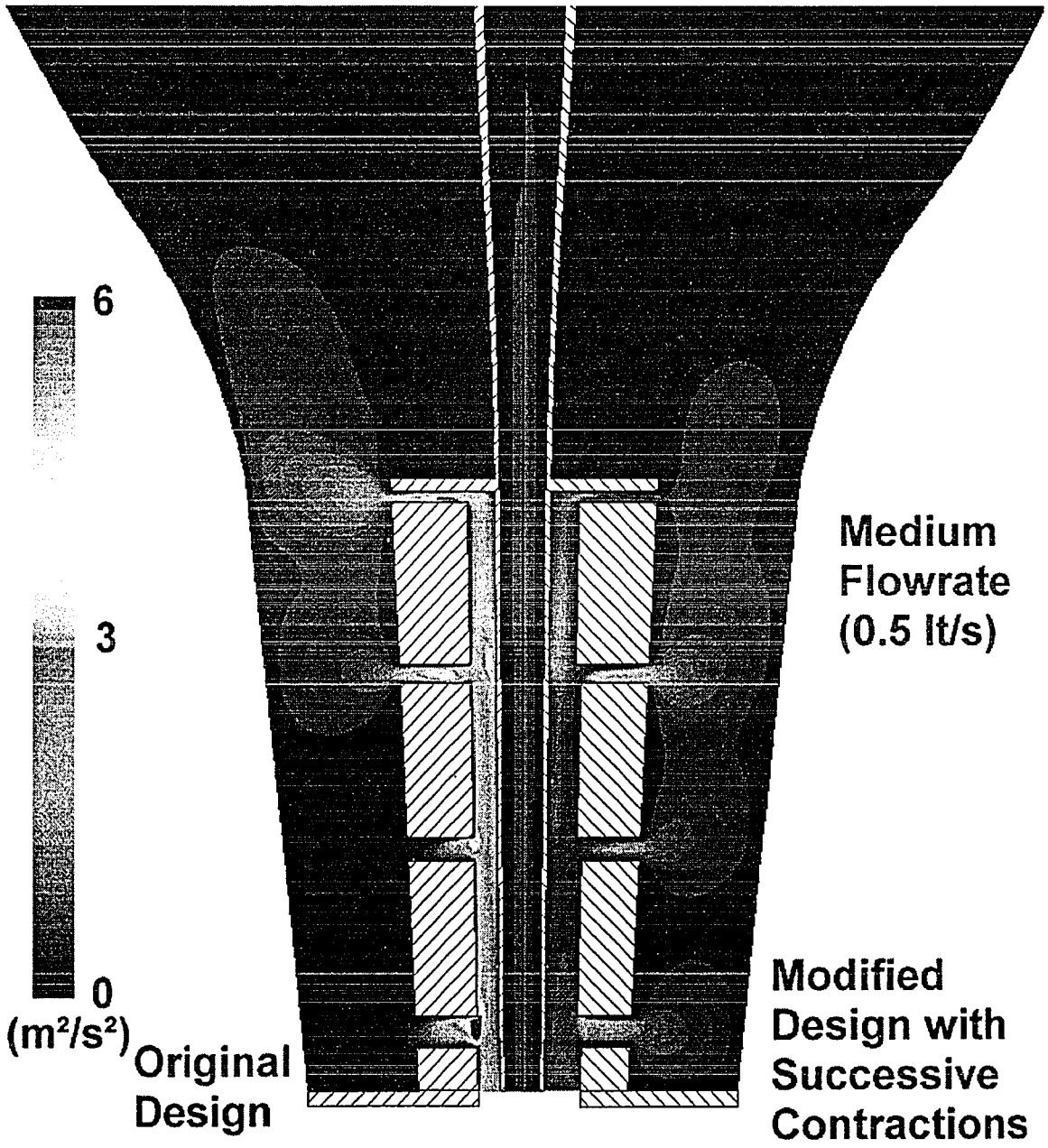

Figure 56: Contours of the turbulent kinetic energy for the original and modified IBC designs at the medium airflow rate (0.5 liters-of-air/s)

Figure 57 shows the calculated temperature profiles for the two designs. One may notice the large zone of hot air at the bottom of the bubble in the original design simulation. The hot-air area is characterized by low air circulation (see figures 45, 46 and 55) and are a direct result of the inability of the specific design to deliver cooling air through the lower slits. In contrast the successful *successive-gap-contractions* modification is predicted to perform much better in the lower bubble part.

Numerical integration at the medium flow-rate indicates that the total internal heat flow induced by the original design is 38W, while the *successive-gap-contractions* modified design generated a heat flow of 47W. This represents a 25% increase in the total cooling capacity of the specified IBC die. The cooling improvement is quite significant, especially if the subtlety of the second design modification is taken into account.

However, the fact that the *flow-deflector* design modification failed to produce any significant difference either in balancing the flow or in cooling performance indicates that IBC systems performance may be as design sensitive as the performance of external cooing air-rings. The results indicate that numerical simulation can be a useful tool in IBC equipment manufacturing and the fine-tuning of new or existing installations. The simulation may be used to avoid long and tedious trial-and-error equipment development routines.

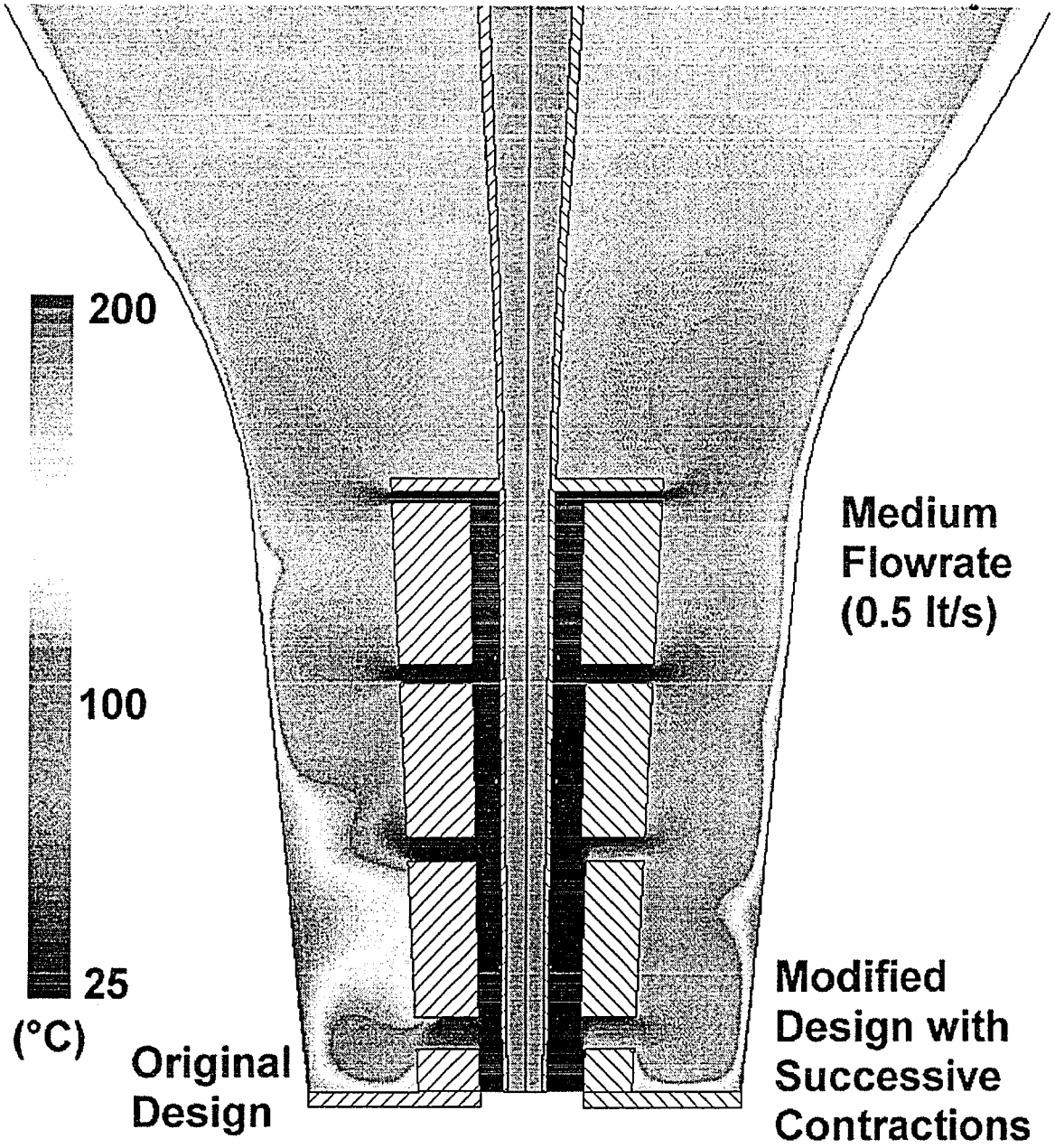

Figure 57: Calculated internal bubble temperature profiles for the original and *successive-gap-contractions m*odified IBC designs at medium airflow rate (0.5 liters-of-air/s)

3.3. Assessment of IBC Simulation Results

As with the external cooling results, the shape of the predicted cooling peaks was qualitatively compared with experimental data (available in the literature). Figure 58 shows experimentally obtained local heat transfer coefficient profiles [Gardon & Akfirat, 1966] for arrays of 2-D normally-impinging air-jets. In the present numerical study, the z/B ratio (ratio of orifice-plate distance to orifice gap) ranges from 3 to 9 and the orifice Reynolds numbers are always less than 2000. Judging from figure 58, one expects the shape of the cooling peaks to match the sharp peaks for the z/B=4 experimental data. Additionally, due to the lower Reynolds numbers, the cooling peaks are expected to be narrower (see figure 41 for the effect of Reynolds number on the shape of the peak).

The experimental profiles [Gardon & Akfirat, 1966] (shown in figures 41 and 58) make possible to claim that the calculated heat transfer coefficient profiles of the simulated IBC systems (figures 47, 51 and 54) are quite reasonable, at least qualitatively. The quantitative analysis that is presented in section 2.8 is also valid for the internal bubble cooling simulations.

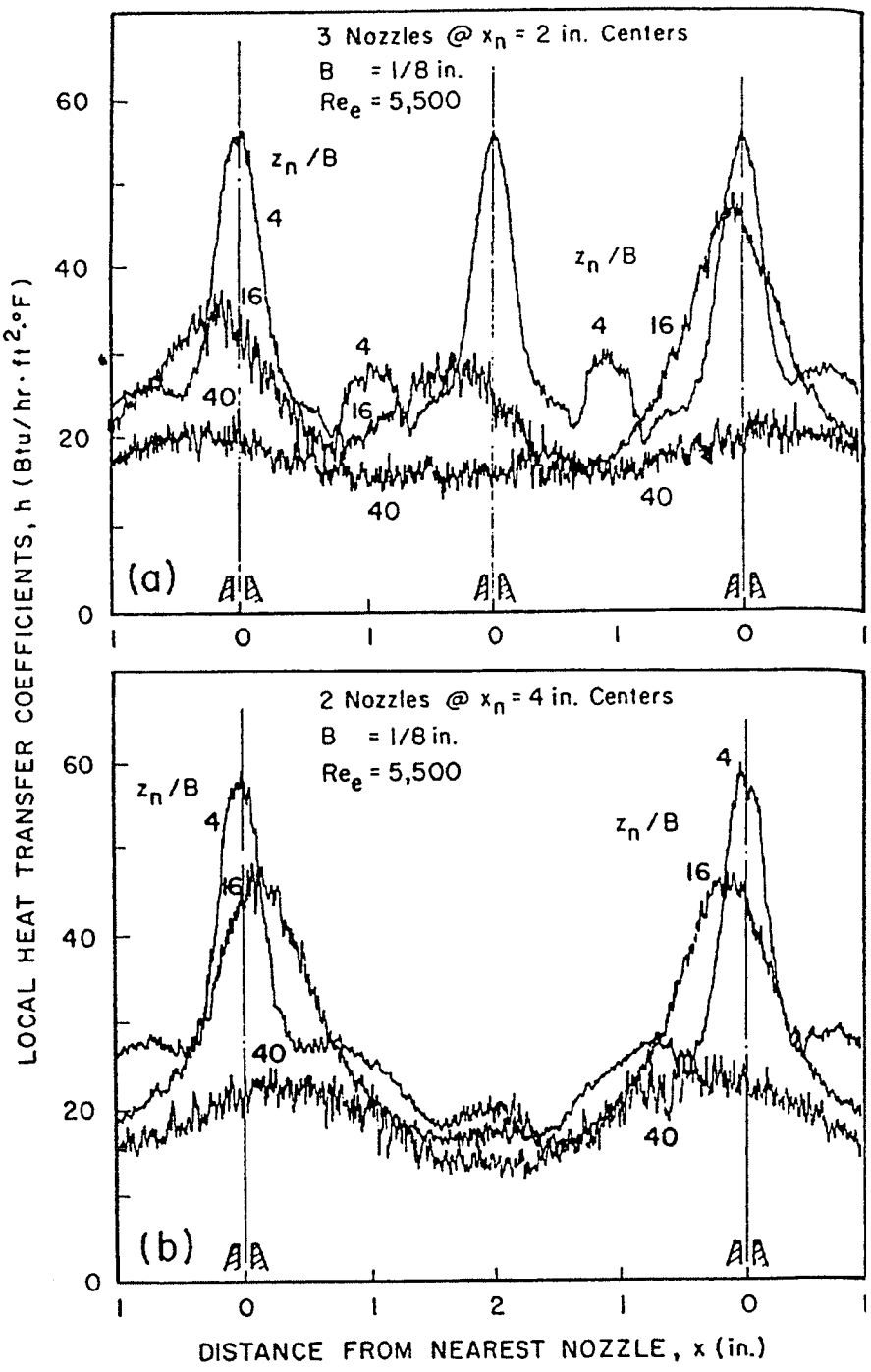

Figure 58: Lateral variation of local heat transfer coefficients between a flat plate and arrays of impinging two-dimensional air-jets (experimental data obtained by Gardon & Akfirat, 1966)

The combined results from the external cooling and IBC simulations verify the well known fact that even in IBC equipped lines the bulk of the heat transfer is still carried by the external cooling system. For example, in the external cooling simulations (already presented in Chapter 2) the medium airflow rate[1] is found to produce an integrated value (from die lips to frost line) of heat flow from the external surface of the LLDPE bubble of 480W. On the other hand, the original IBC design produced internal heat flows up to 120 Watts (at the high internal airflow rate of 1.3 lt/s).

In the configuration described above, even the original IBC design would provide a cooling improvement of 25% (which could further be increased to 29% by applying the successful *successive-gap-contractions* design modification). These values represent the best possible cooling improvement, as the high flow-rate may not be always attainable due to bubble instabilities. The medium IBC airflow increased the total cooling intensity by 11% (at best), indicating only subtle improvements.

The values presented above (derived from the numerical simulation results) are remarkably close to the cooling improvements that blown-film experts anticipate for small bubbles after the introduction of IBC equipment. The limited cooling improvement provided by small

---

[1] Corresponding to an average velocity of approximately 10 m/s at the tip of the higher orifice, a value quite typical for film blowing lines

dimension IBC stacks is well documented [Knittel, 1996]. On the contrary, at larger bubble diameters the IBC equipment can be made larger and many of the design limitations are easier to overcome. Therefore, the expected cooling improvements (and the resulting line-throughput increases) that IBC offers are relative to the bubble diameter.

CHAPTER 4.

TEMPERATURE PROFILES IN THE MELT PHASE

4.1. INTRODUCTION

The thin membrane approximation (proposed by Pearson & Petrie, 1970a, 1970b and 1970c) has been used almost exclusively in film blowing simulation. After the introduction of non-isothermal conditions in the numerical simulation [Han & Park, 1975a] the lumped capacitance method was exclusively used. A brief examination of the Biot number value shows that the assumption is quite valid for the final film product (which has been thinned down significantly) but not as valid in the region close to the die lips (where most of the heat transfer takes place).

Although cooling is a very important aspect of film blowing (and often the limiting stage in achieving higher production rates), not much work has been done to study the effect of cooling in the melt phase. Cao et al [1989] tried to measure and compare the bulk (average) temperature and the skin (surface) temperature of the film during the blowing process. Close to the die lips, they reported temperature differences as high as 10°C. Further from the die lips, the film-phase temperature gradients decrease as the film is significantly down-gaged and the cooling rate is reduced. They suggested that distributed temperature simulations might

be needed in order to make adequate predictions for the heat transfer. Using modeling, Nagarajan [1996] concluded that significant temperature gradients can develop in the film thickness.

Numerical simulation for the temperature distributions in the melt phase has been performed. The calculated profiles of heat transfer coefficients from the previous chapters have been used to calculate the convective heat transfer from the film surface(s). Consequently, the temperature profiles in the *normal* and *machine* directions were calculated.

4.2. THEORY

The heat diffusion equation in Cartesian coordinates is

$$\rho C_p \frac{\partial T}{\partial t} = k\nabla^2 T + \dot{q}_{source} \qquad (4\text{-}1)$$

The film was assumed to be axially symmetric. Since the thickness is much smaller than the other film dimensions (thin membrane approximation) all the conduction has been assumed to take place in the *normal* direction and the film may assumed to be flat. The viscous dissipation from the stretching is negligible. Then equation 4-1 can be simplified to

$$\frac{1}{\alpha}\frac{dT}{dt} = \frac{\partial^2 T}{\partial n^2} \qquad (4\text{-}2)$$

where α is the heat diffusivity.

At the film surfaces the total heat flux can be written

$$\dot{q} = \dot{q}_{conv} + \dot{q}_{rad} = h_c(T_s - T_\infty) + \varepsilon\sigma\left(T_s^4 T_{sur}^4\right) \tag{4-3}$$

where the surface temperature varies considerably with time, $T_s=f(t)$. For the internal surface, the radiation term can be dropped due to the axial symmetry.

We can write the radiation heat flux in a linearized form [Incropera & DeWitt, 1990]

$$\dot{q}_{rad} = h_r(T_s - T_\infty) \tag{4-4}$$

where

$$h_r \equiv \varepsilon\sigma(T_s + T_\infty)\left(T_s^2 + T_\infty^2\right) \tag{4-5}$$

Here we have modeled the radiation equation in a manner similar to convection. The radiation equation was linearized in order to be easily combined with the convection equation. One should note, however, that h_r is a strong function of the surface temperature. By further assuming that the temperature of the surroundings is the same as the temperature of the free air stream, a simplified form of equation 4-3 can be written

$$\dot{q} = (h_c + h_r)(T_s - T_\infty) \tag{4-6}$$

Then equation 4-2 has the following boundary conditions at the surfaces

$$-k\left.\frac{\partial T}{\partial n}\right|_{surface} = (h_c + h_r)(T_s - T_\infty) \tag{4-7}$$

where $h_r=0$ for the internal film surface.

4.2.1. Implicit Discretization Of The Heat Balance Equation

A finite difference numerical method has been employed to calculate the temperature profiles in the *machine* and *normal* (film thickness) direction. Equation 4-2 was implemented using a Lagrangian approach, where the temperature rate of change is observed by moving with a *closed* finite film element. Therefore the time derivative of equation in equation 4-2 is a *following the motion* derivative (also known as *material derivative*). The implementation is depicted in figure 59 where a *closed* control volume of film is traveling downstream in finite time intervals, while been subjected to deformation as well as convective-radiative surface heat flux.

To obtain the finite-difference form of the governing equation (4-2), central-difference approximations were used for the spatial derivative,

$$\left.\frac{\partial^2 T}{\partial n^2}\right|_i \approx \frac{T_{i+1} + T_{i-1} - 2T_i}{(\Delta n)^2} \qquad (4\text{-}8)$$

Figure 60 shows the division of the film's thickness using discrete nodal points as well as the relative locations for the internal and the surface nodes. The time derivative was also discretized. At a given nodal point (i), the time derivative is expressed in terms of the temperature difference between the new (p+1) and the previous (p) times.

$$\left.\frac{dT}{dt}\right|_i \approx \frac{T_i^{p+1} - T_i^{p}}{\Delta t} \qquad (4\text{-}9)$$

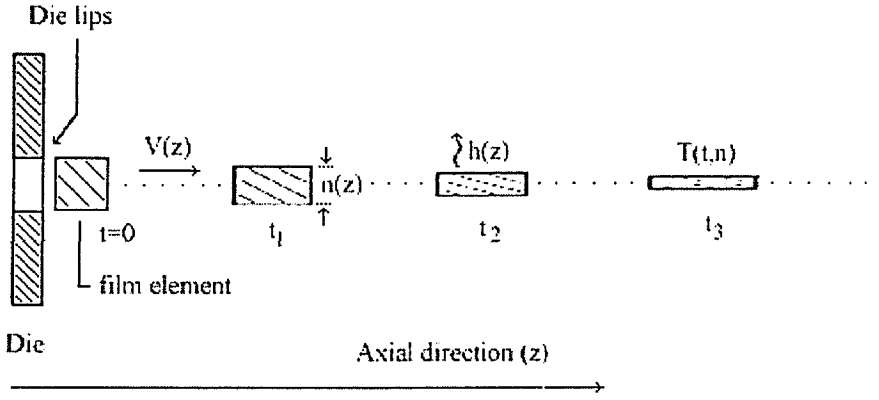

Figure 59: Blown film finite volume (*closed system*) for *material derivative* approach

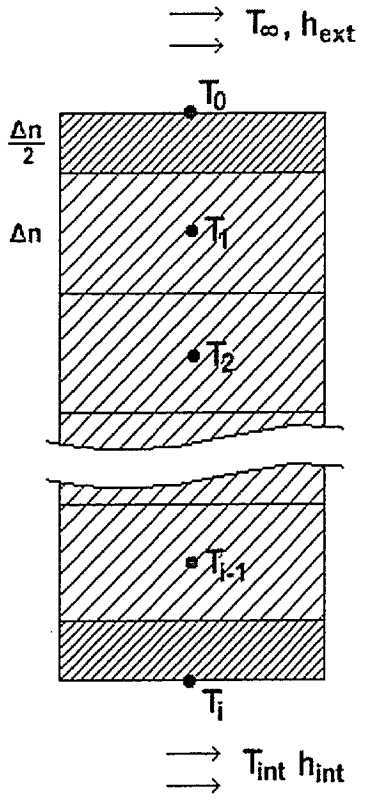

Figure 60: Film thickness discretization and nodal locations

Equations 4-8 and 4-9 can be substituted in equation 4-2 to obtain the final discretized equation. In order for the formulation to be unconditionally stable, the spatial derivative is implemented at the new (p+1) time, which makes equation 4-9 a backward-difference approximation (implicit method). The discretized form of equation 4-2 is

$$\frac{1}{\alpha}\frac{T_i^{p+1}-T_i^{p}}{\Delta t}=\frac{T_{i+1}^{p+1}+T_{i-1}^{p+1}-2T_i^{p+1}}{(\Delta n)^2} \tag{4-10}$$

Rearranging 4-10 we get

$$(1+2Fo)T_i^{p+1}-Fo\left(T_{i+1}^{p+1}+T_{i-1}^{p+1}\right)=T_i^{p} \tag{4-11}$$

where Fo is a finite-difference form of the Fourier number

$$Fo=\frac{k}{\rho C_p}\frac{\Delta t}{(\Delta n)^2} \tag{4-12}$$

Equation 4-11 is valid for the internal nodes. The application of conservation of energy for the surface node (i=0) gives,

$$-(h_c+h_r)\left(T_0^{p+1}-T_\infty\right)+\frac{k}{\Delta n}\left(T_1^{p+1}-T_0^{p+1}\right)=\rho C_p\frac{\Delta n}{2}\frac{T_0^{p+1}-T_0^{p}}{\Delta t} \tag{4-13}$$

and finally

$$-2BiFo\left(T_0^{p+1}-T_\infty\right)+2Fo\left(T_1^{p+1}-T_0^{p+1}\right)=T_0^{p+1}-T_0^{p} \tag{4-14}$$

where Bi is the finite-difference form of the Biot number

$$Bi=\frac{(h_c+h_r)\Delta n}{k} \tag{4-15}$$

An equation identical to 4-14 is implemented for the nodes located at the internal surface, but Bi_{int} excludes the radiative heat transfer part

$$Bi_{int} = \frac{h_c \Delta n}{k} \tag{4-16}$$

The resulting system of algebraic equations is solved using a Gauss-Seidel iterative method with *successive over-relaxation* -- also known as SOR [Ferziger & Peric, 1996]. Although the Gauss-Seidel method is considered computationally expensive, SOR provides a dramatic decrease in computational time. The SOR coefficient was set to 150%, a value that yielded fast convergence without jeopardizing the stability of the numerical solution.

Since time values are easily associated with positions along the bubble surface (through the calculated bubble kinematics) the simulation results can be easily translated as temperature profiles in both the *normal* and *machine* directions (fully distributed temperature field).

4.2.2. Simulation Methodology

In the current implementation, the bubble kinematics of a LLDPE bubble (having the same shape as the LLDPE bubble used in the cooling air simulations) are calculated using a non-isothermal purely viscous approach. The method involves the use of a modified viscosity-temperature function, which help to achieve very good agreement between experimental data and the calculated bubble kinematics

[Sidiropoulos, 1995, 1996a, 1996b]. The initial and final film thickness was set to 2mm and 50μm respectively (40:1 ratio). The material properties of a typical LLDPE resin (DOW 2078) were used for the purely viscous bubble kinematics approximation.

A typical polyolefin value was used for the heat capacity (2300 J/kg°K) of the molten polymer. The calculated heat transfer coefficient profiles (already presented in chapters 2 & 3) were imposed on the discretized film kinematics. The thermal conductivity and density of the molten polymer were calculated using linear-functions to describe their temperature dependence (available in literature, Incropera & DeWitt, 1990). The polymer density varied from 750 to 910 kg/m^3 (from die lips to the frost line respectively), while the heat conductivity varied from 0.3 to 0.2 W/°K·m (over the same range).

The Gauss-Seidel computation is considered converged as long as local temperature updates do not exceed 10^{-5} °C. Special attention was given to the number of discrete computational steps which will provide maximum accuracy without excessive computational load. Figures 61 and 62 show the calculated final film temperature for a single orifice air-ring, using different number of divisions for the film thickness (i) as well as the time steps (p). Using the information from figures 61 and 62, it was decided that for all subsequent calculations, the film thickness should be discretized using 20 divisions (21 nodal points) while the total process time (typically 3 to 10s) should be approximated using 200 steps.

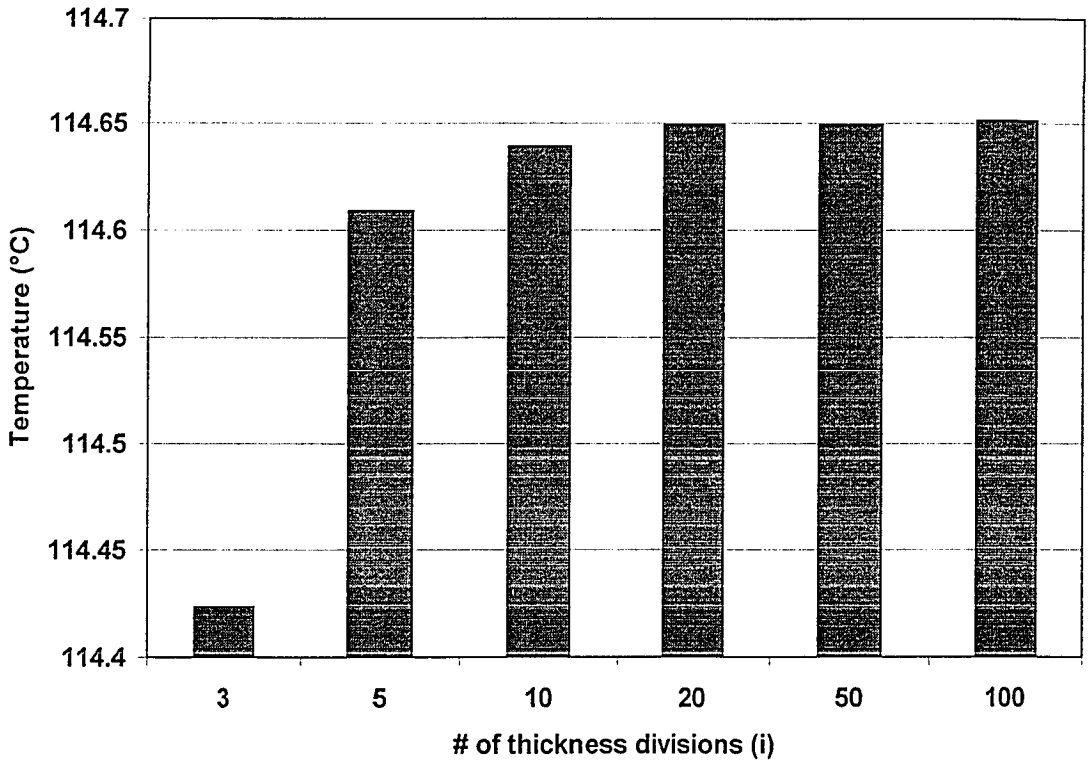

Figure 61: Sensitivity of the calculated final temperature on the number of thickness subdivisions

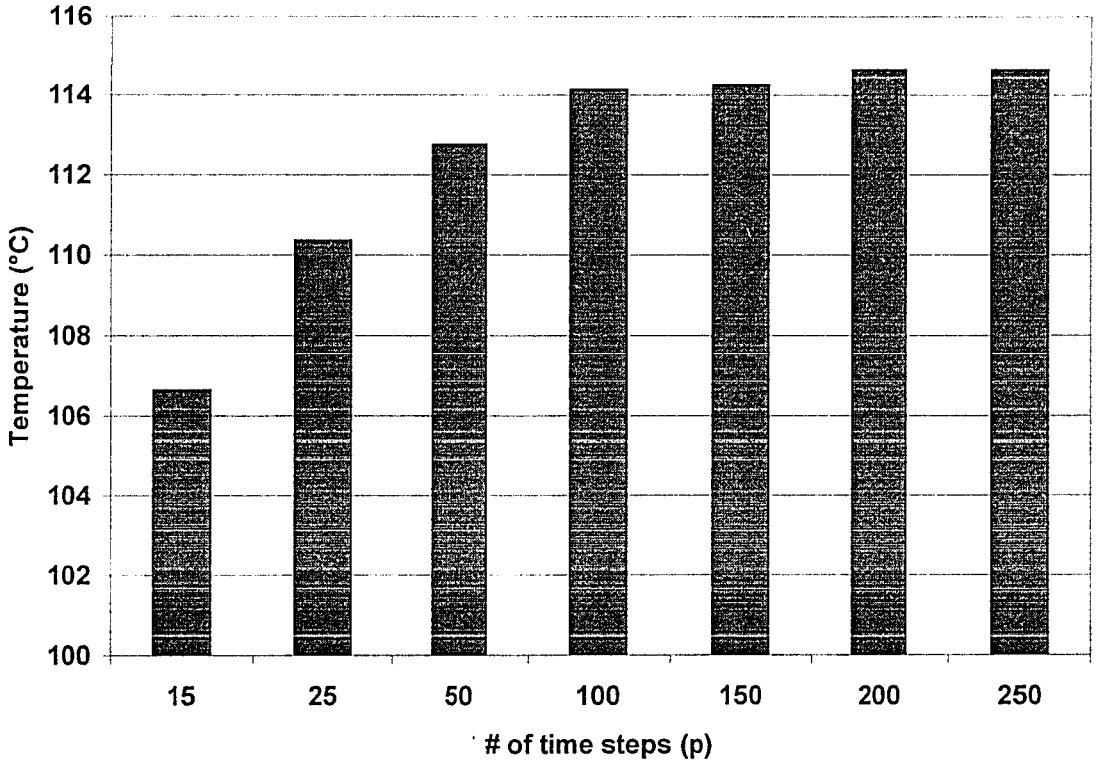

Figure 62: Sensitivity of the calculated final temperature on the number of time-steps

4.3. Temperature Profiles for External Bubble Cooling

The bubble shape that was employed in the film-phase temperature calculations was the LLDPE type bubble shape (initial diameter 2" and BUR of 3) that was used in the cooling air simulations (chapters 2 & 3). The purely viscous method (that was employed for the calculation of the bubble kinematics) has been shown [Sidiropoulos, 1995] to adequately predict the bubble kinematics of an assortment of experimental data, corresponding to many different materials and bubble dimensions.

The calculated heat transfer coefficient profiles on the bubble surface (chapter 2) were applied in the preset bubble kinematics. The kinematics were estimated for various polymer throughput rates. In all cases the frost line was kept constant[1], which in effect caused the resulting geometric characteristics of the bubble (bubble shapes and film thickness profiles) to be fairly unchanged. The differences in bubble kinematics (between different throughput rates) were concentrated in line speeds and the inflation processing time. Using an invariable frost line

---

1. In blown film production practice, the frost-line height (FLH) is kept unchanged at all times (and many times at all cost), as film properties are strongly influenced by FLH variations. Potential cooling rate improvements are mainly used to increase line throughput rates, rather than manipulate the bubble's frost-line height.

height, the differences in the bubble kinematics (for varying line flow rates) are not coupled with the local heat transfer coefficient profiles.

4.3.1. Evaluation of the Lumped Capacitance Approximation

To date, the lumped capacitance approximation (where equation 1-11 is applied) has been used almost exclusively in film blowing simulations. To compare the proposed distributed temperature approach with the standard lumped capacitance approximation, the temperature profiles in the LLDPE film were calculated for a mass-flow rate of 20 kg/hr. The heat transfer coefficient profile for the high airflow rate (see the profile for airflow 25 lt/s on figure 23) was applied on the external bubble surface. The film temperature was calculated using both methods.

Figure 63 shows the calculated temperature drop as the film travels from the die lips to the frost line. The calculated profiles for the internal as well as the external (skin) layer are also included. The figure shows a disagreement between the temperature profile that was calculated by using the lumped capacitance approximation and the thickness-average of the temperature profiles (as calculated by the distributed temperature method). To validate the applicability of the approximation, the Biot number of the film was checked along the bubble. It was found that only close to the frost line (where the film

thickness has been substantially reduced) the value of Biot number[1] was less than 0.1. Therefore, it can be argued that the lumped capacitance method can only provide rough temperature estimates.

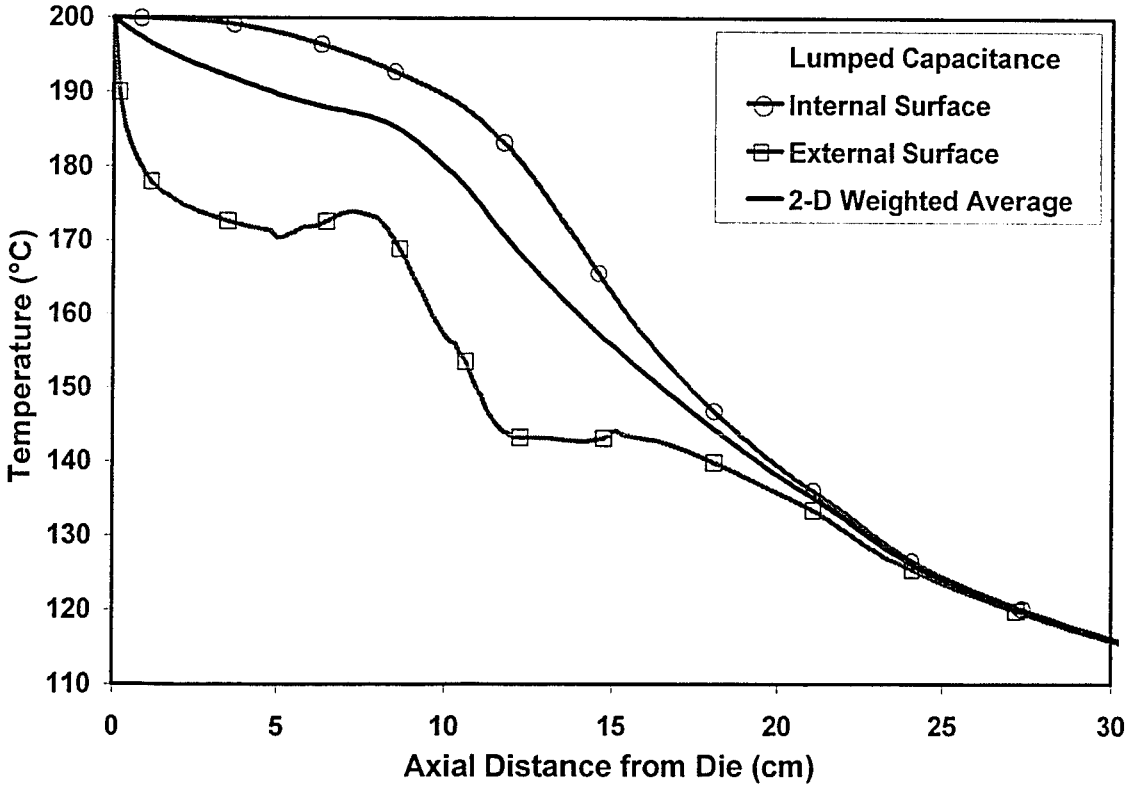

Figure 63: Machine direction temperature drop for the internal and external surface and comparison between the thickness-average and the lumped capacitance predicted temperatures

[1] The lumped capacitance method is accurate for Bi < 0.1 [Incropera & DeWitt, 1990]

Figure 63 also shows the temperature differences between the skin (external surface) and the inner (internal surface) layers, which are calculated to be large at the positions of the air-cooling peaks (locally reaching a 40°C differential). Near the frost line, the temperature differences gradually become less profound until they finally disappear.

Figure 64 shows the temperature profiles in the film *normal* (thickness) direction at different heights. To better illustrate the profiles, the *normal* position is presented as a percentage of the total local thickness. The temperature gradients when external heat transfer is high, indicating that there is significant resistance in the heat flux inside the film. The maximum cooling is applied on the external surface at axial distances between 10 and 20cm (see figure 23) and calculated *normal* temperature gradients at that area are very large. This is not surprising, as the thermal conductivity of polyolefins (as most polymeric materials) is quite small and further from the frost line the film is still thick. Approaching the frost line, the gradual reduction of the film thickness reduces the temperature gradients in the *normal* direction.

The results suggest that during the film blowing, significant temperature gradients occur in the film thickness (*normal*) direction. Thus far, film blowing computational models ignored the fact and used the lumped capacitance approximation (which assumes that *normal* temperature profiles are flat), but more accurate predictions can be obtained by using the proposed distributed temperature approach.

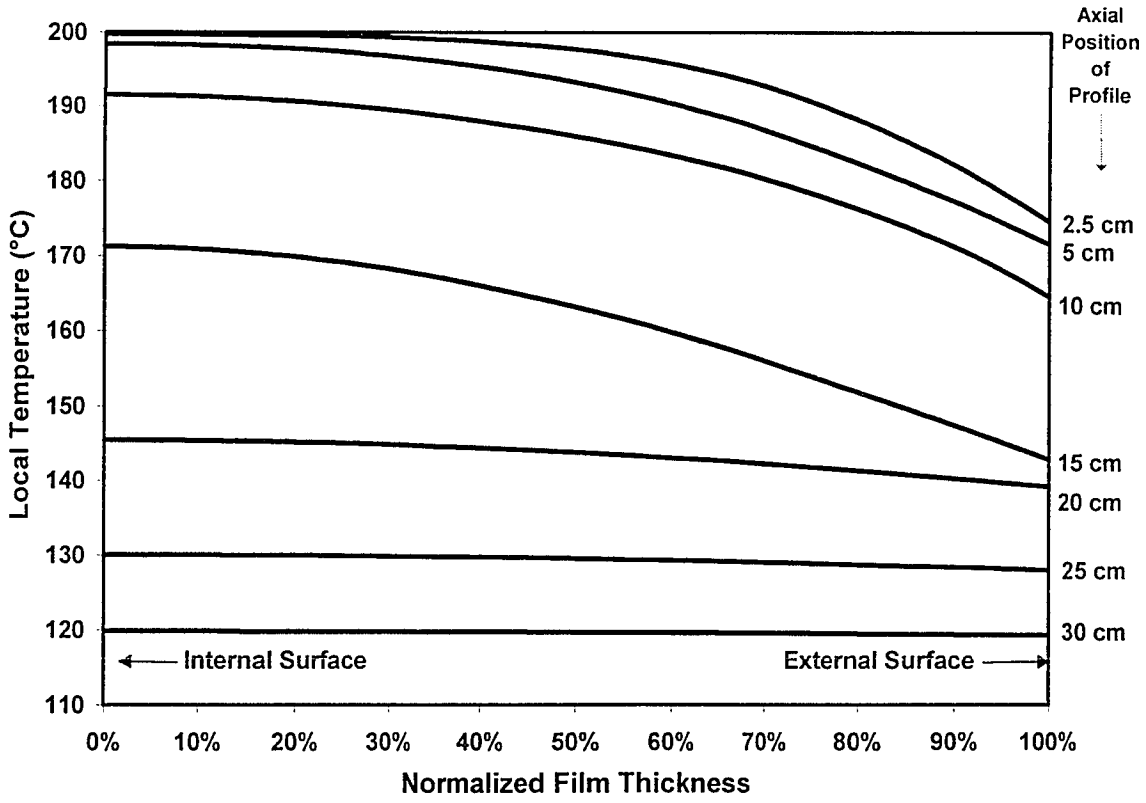

Figure 64: Calculated blown-film temperature profiles in the *normal* (thickness) direction, at various axial distances

4.3.2. Film Temperature Profiles for Dual-Orifice Air-Rings

It has been shown in section 2.7 how minor modifications in the operational setup of the studied dual-orifice air-ring created considerable variations in the local values of the heat transfer coefficient (shown on figure 33). The distributed temperature approach was used to evaluate the effect of the setup modification on the temperature profiles of the film (polymer) phase, using the profiles of figure 33 as boundary conditions.

Figure 65 shows the simulation results for the low-position air-ring setup. Close to the die lips the newly-emerged hot melt may have temperature differences between the external and the internal layer as large as 20°C. In direct contact with the cooling air, the external layer temperature initially drops fast, levels off in the area before the higher orifice (10cm above the die lips) and starts falling again when the higher orifice airflow hits the film surface. At the same time, heat flow resistance in the melt phase forces the internal surface temperature to drop in a less rapid way. Midway to the frost line, the temperature variations in the *normal* direction vanish because the film thickness has already been drastically reduced.

Figure 66 shows the calculated normal-direction temperature profiles at various axial positions. It is apparent that the local profiles are smooth and continuous (with the minimum value located at the external surface) and the profile gradients diminishing at distances further from the die lips.

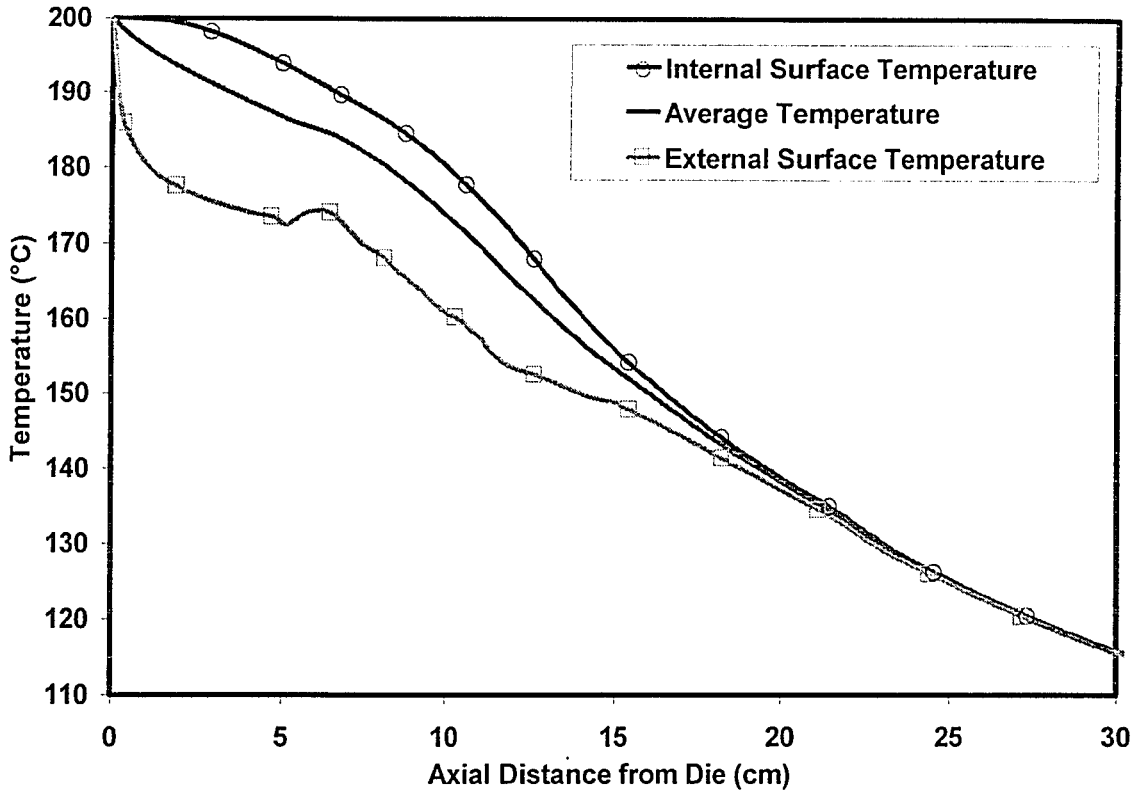

Figure 65: Machine direction temperature drop for the low position, dual-orifice setup (surface heat transfer coefficients shown in figure 33)

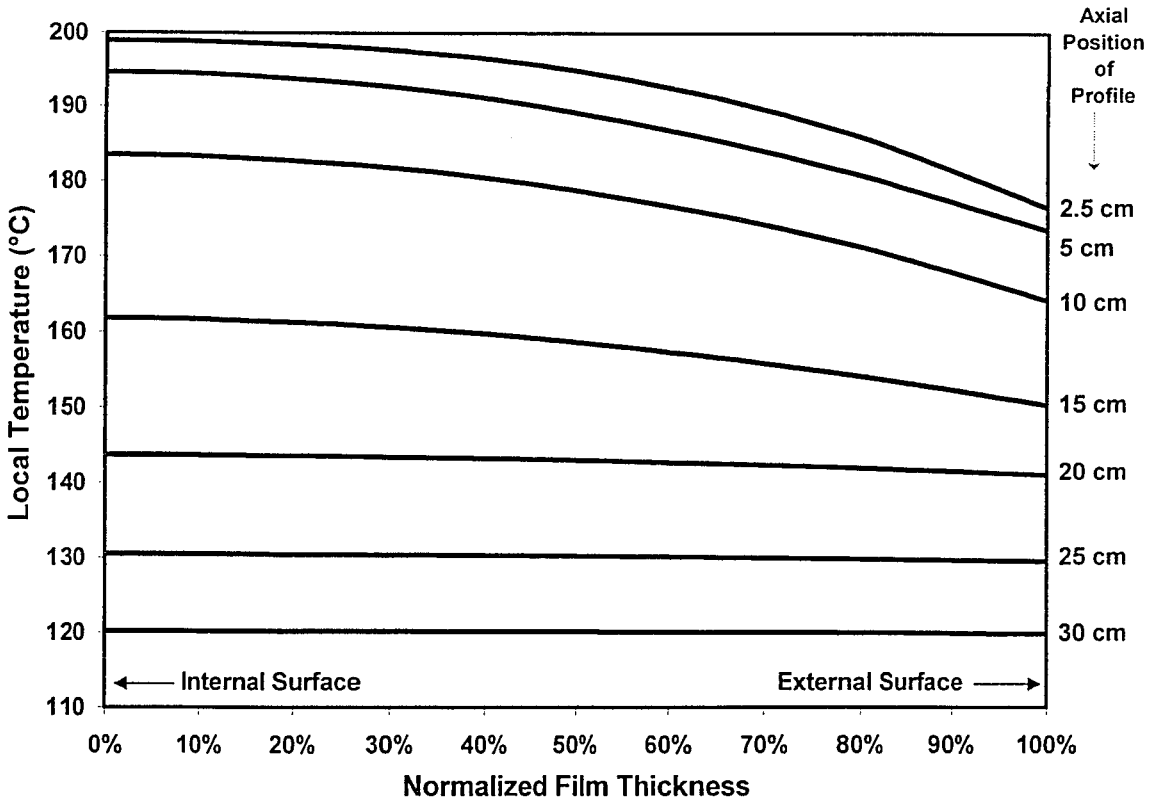

Figure 66: Calculated film temperature profiles in the *normal* (thickness) direction for the low position dual-orifice setup

Similar results obtained for the high-position setup of the simulated air-ring are depicted in figure 67. The calculated temperature gradients in the *normal* direction are larger in this case and may locally reach 30°C. As the previously presented cooling-air simulation implies (see figure 33), the high position setup focuses the cooling intensity of the air-stream in the low orifice area (close to the die lips). Since the film is thicker at lower axial locations, larger temperature gradients are developing. As in the previous case (low position setup), all temperature differences across the film thickness disappear once the film has been noticeably thinned down (approximately midway to the frost line).

Figure 68 presents a comparison of the thickness-averaged temperature drops (MD) for the two studied air-ring setups. In the low position setup the MD temperature drop is smaller in the beginning, but the drop rate is accelerated after the higher orifice airflow hits the bubble surface. In contrast, the high position setup exhibits a more uniform drop of the thickness-averaged temperature (despite the larger gradients shown in figure 67). At higher axial positions the film becomes thinner and the differences between the two profiles vanish. The frost line height is not likely to be affected by the slight air-ring setup modification, because the overall surface heat flow is calculated to be almost identical in the two simulations. However, the resulting difference in the temperature histories (and consequently in the stress histories) is likely to produce films with differences in the physical properties.

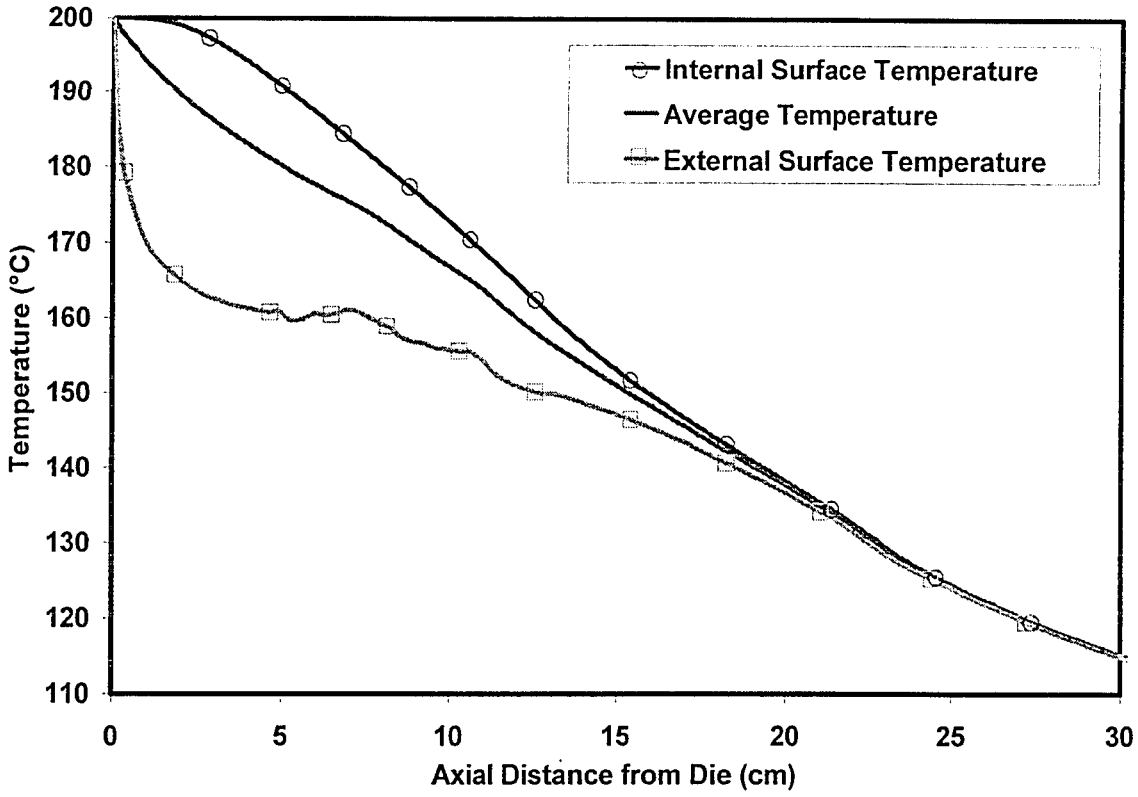

Figure 67: Machine direction temperature drop for the high position, dual-orifice setup (profile of heat transfer coefficients shown in figure 33)

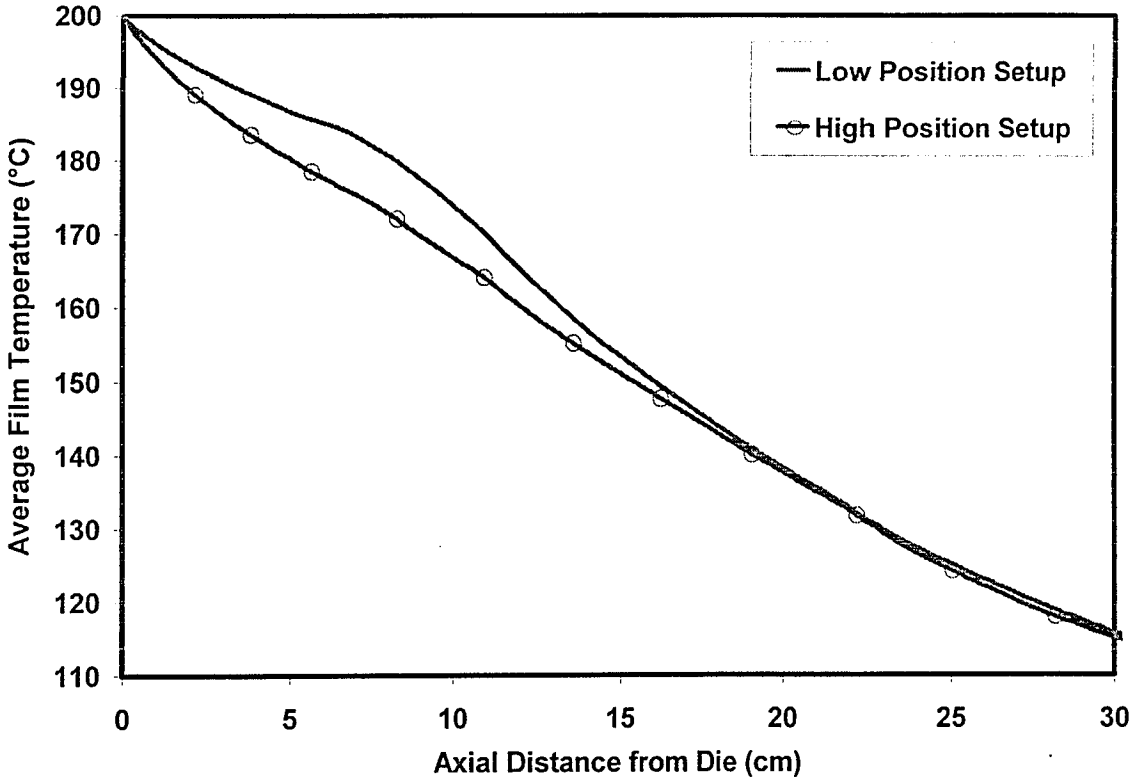

Figure 68: Average temperature drop in the machine direction for high and low position air-ring setup

4.3.3. Temperature Drop Dependence On Production Rates

In section 2.7, the cooling performance of the dual orifice air-ring (by Future Design Inc.) has been studied for varying airflow rates (all of them having a typical low position setup). Figure 23 shows the simulated heat transfer coefficient profiles on the external surface of the bubble for the three airflow rates. The temperature gradients in the melt phase (calculated for a combination of the medium airflow rate on a 10 kg/hr melt production rate) have been shown on figures 65 and 66. It is not uncommon in industrial practice to attempt to increase the external cooling rate. The action is rarely intended to modify the height of the frost line, but rather increase the production rate of the film.

The high cooling airflow is double the medium airflow (25 lt/s as opposed to 12 lt/s). The dependence of the MD temperature drop on production rate was evaluated by doubling the production rate (to 20 kg/hr) and apply the high airflow cooling profile on the external bubble surface (as opposed to 10 kg/hr and medium airflow rate). The calculated MD drop of the average temperature are shown on figure 69. Close to the frost line the two profiles look remarkably similar, which is not surprising since specific melt flow-rates were used in order for the frost line to remain at the same height. The calculated profiles have differences only in the area where the second-orifice flow impinges on the external bubble surface. However, examination of the *normal* temperature gradients shows the differences between the two simulations.

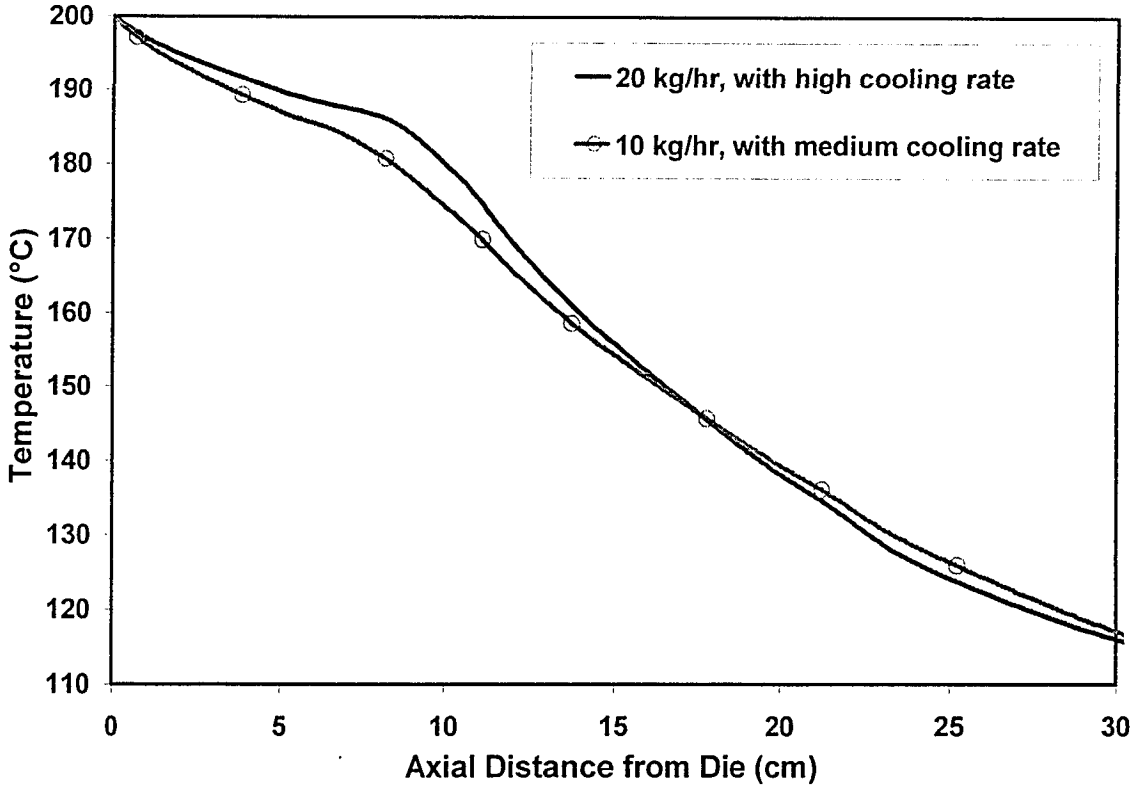

Figure 69: Calculated MD profiles of the thickness-averaged bubble temperature for a 20 kg/hr melt throughput with high intensity cooling and a 10 kg/hr melt throughput with medium intensity cooling

The simulation results for the internal and external film temperatures are shown on figure 70. Close to the frost line (where the *normal* direction temperature profiles are almost flat), the predictions are very close. However, at shorter axial distances from the die the predicted normal direction gradients are much larger in the case where both the melt flow-rate and the cooling intensity were doubled. Also, the *normal* direction gradients remain easily distinguishable even to the frost line when the production rate is doubled.

Figure 70 indicates that increases in production-rate by enhancing the external air-cooling are very likely to augment the thickness-direction temperature gradients. It should be taken into account that most film blowing lines in industrial production are expected to sustain the maximum melt flow-rate that can be possibly achieved. Thus, one may safely assume that the most commercial blown film is being produced having significant temperature gradients in the thickness direction during blowing. In that respect, during the stretching some layers of the film are hot, but other layers sustain the same deformation while having a lower temperature. The situation is similar to multi-layer film stretching where some of the polymer-layers are stiff in extension, while other layers are easy to stretch. Attempts to estimate the final film properties (by means of numerical simulation) without taking into account the viscosity differences between layers (in this case caused by temperature differences) may be lacking in accuracy.

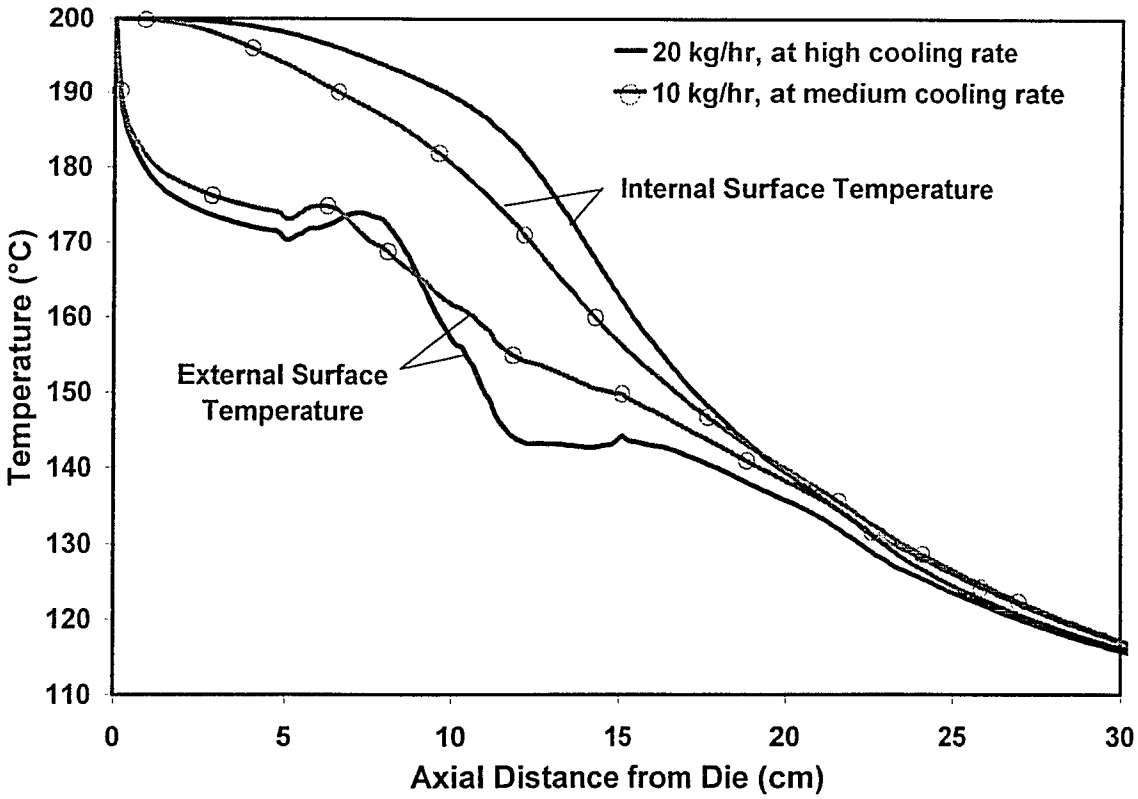

Figure 70: Calculated MD temperature drops for the external and internal surface and for 20 kg/hr melt throughput with high intensity cooling
and a 10 kg/hr melt throughput with medium intensity cooling

4.4. Temperature Profiles for IBC Assisted Bubble Cooling

In recent years, internal bubble cooling (IBC) systems have enjoyed widespread popularity, as the need for higher production rates in film blowing is intensified. The existence of IBC devices assists the external cooling system (which performs most of the heat transfer) and makes the increase in production rates possible[1]. On the other hand, the removal of heat from both surfaces of the molten bubble can significantly alter the temperature profiles in the melt phase.

Many possible combinations of external and internal cooling intensities (as presented in chapters 2 & 3) were used in the simulations. Here, the results for the combination of medium internal and external cooling intensities are presented and compared to the previously shown results for external-only cooling. Since increases in production is often the main goal, a higher melt flow rate was used for the combined internal-external cooling simulation and the frost line was kept unchanged. Previous calculations showed that the addition of medium intensity IBC to a medium intensity external cooling would produce an approximate 12.5% increase in heat flow. Therefore, the operating flow rate was increased from 10 to 11 kg/hr for the combined external-IBC

---

[1] In the majority of film blowing lines the production rate is limited by the maximum cooling rate that can be achieved without compromising bubble stability

cooling simulation. The heat transfer coefficient profiles that were used can be seen in figures 33 (airflow rate 12 lt/s, low position dual-orifice setup) and 54 (modified IBC system with successive gap contractions).

Despite the increased melt flow-rate (which imposes a higher cooling load), the simulation predicts that the temperature gradients in the *normal* direction are reduced. Figure 71 shows the calculated MD temperature drops for the two film surfaces as well as the thickness-averaged temperature. The internal air circulation forces the internal surface to cool faster. At the axial location of the IBC slits (where the internal cooling peaks are located--see figure 54) the internal temperature is dropping fast, but at axial positions where the cooling is not as high (namely in between the cooling peaks) heat from the interior of the melt flows towards the surface. This results in a wavy temperature profile, with the temperature locally dropping or raising. One may notice that the average film temperature is not much different from the internal surface temperature. That would indicate that there is more temperature homogeny in the presence of IBC supported cooling.

Figure 72 shows the temperature profiles in the *normal* direction. Noticeable gradients still exist near the die, but since the heat flows from both surfaces, the temperature variations between layers are much smaller (when compared to the cooling simulations without IBC). Also, the temperature gradients vanish faster when IBC is present.

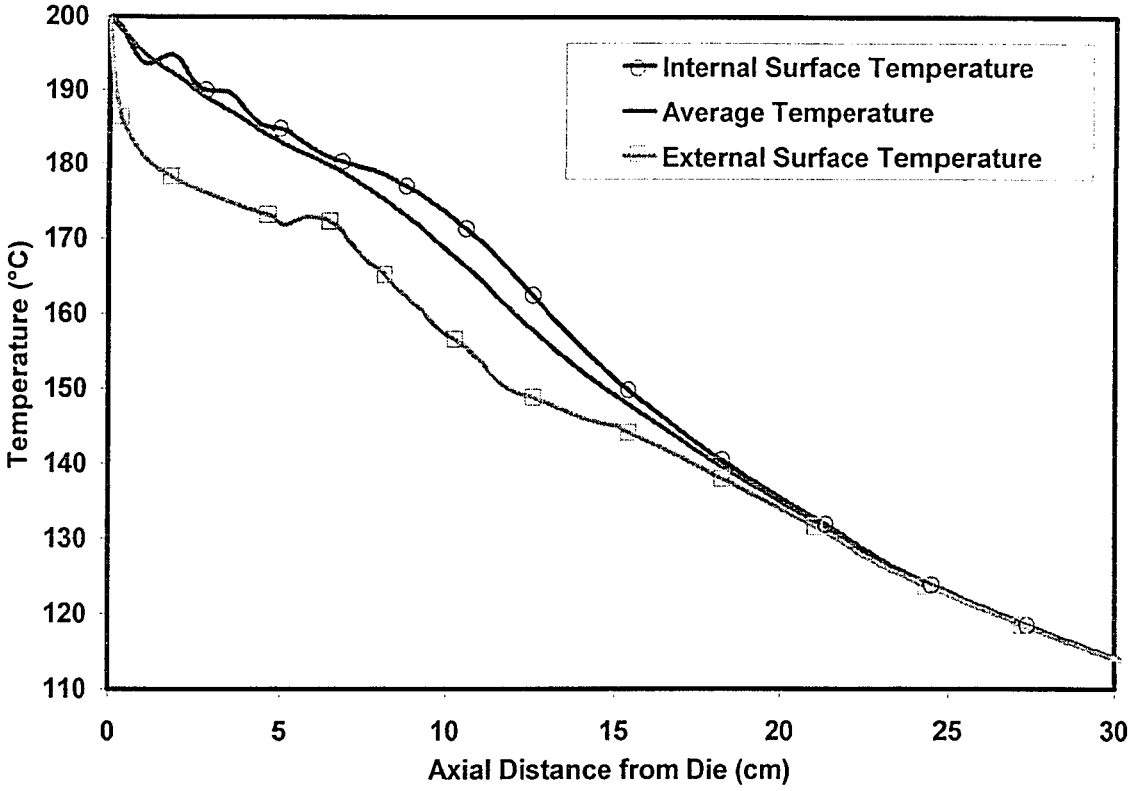

Figure 71: Machine direction (MD) temperature drop for the low position dual-orifice setup with IBC, at medium internal and external cooling intensities (surface heat transfer coefficients shown in figures 33 and 54)

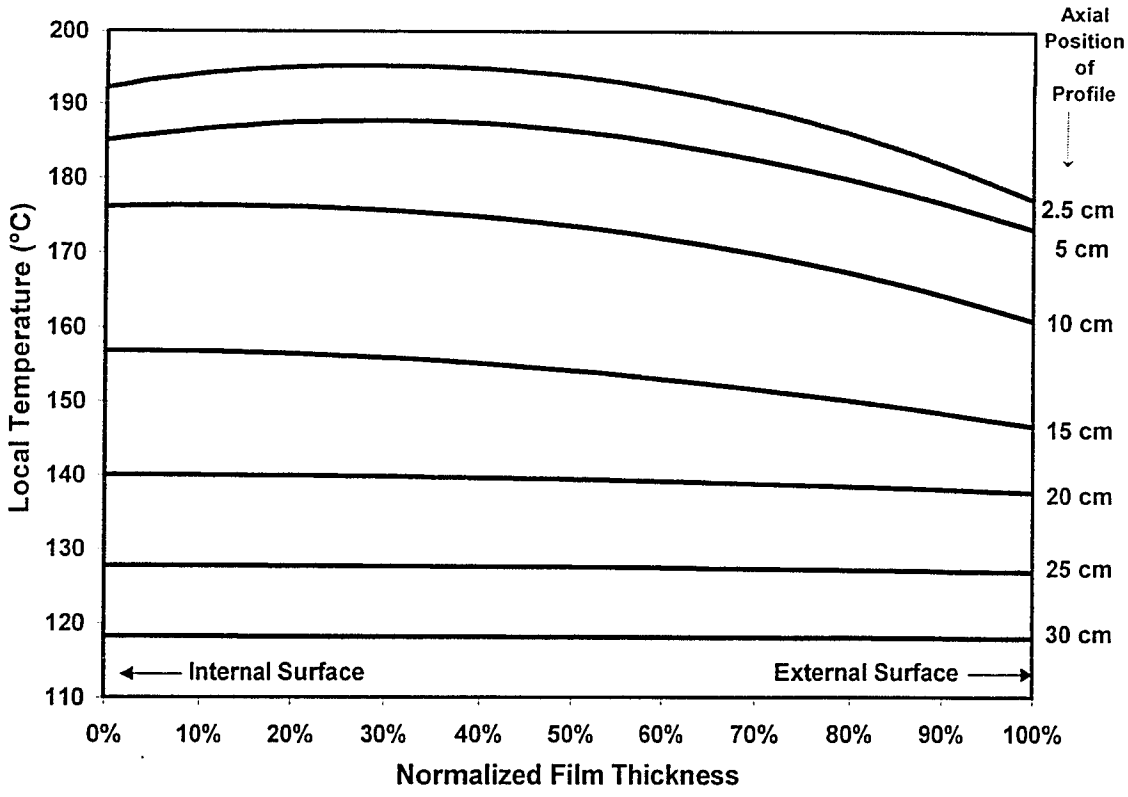

Figure 72: Calculated film temperature profiles in the *normal* (thickness) direction with the addition of IBC at medium cooling intensities

The differences in temperature gradients that occur when a blown film line is equipped with IBC are better illustrated in figure 73. The results of the external cooling simulation (at 10 kg/hr) are compared with the results of the combined external-IBC cooling setup (at the increased flow rate of 11 kg/hr). The assistance of the IBC system not only accommodates the increased melt flow-rate but also reduces the considerable local temperature gradients. It should be noted that close to the frost line there are no predicted differences, indicating that the position of the frost line is not going to be affected by the modifications. The average temperature profile for the two simulations is very similar, having only small deviations in the area around the 10 cm distance.

The addition of IBC (with the parallel increase in production rate) may give the impression that nothing is drastically modified. After all, the frost line height is not affected and the measurement of the MD film temperature profiles will reveal only minor differences. However, the results shown in figure 73 indicate the possibility of the following situation: the film used to be stretched while having significant temperature differences in the normal direction (resulting in visco-elasticity variations across the film thickness), but with the introduction of IBC these thickness-direction variations are reduced and the film properties may have been altered. The results partially explain what blown film operators know: despite the best efforts to avoid so, IBC introduction may modify the final film properties (sometimes for better).

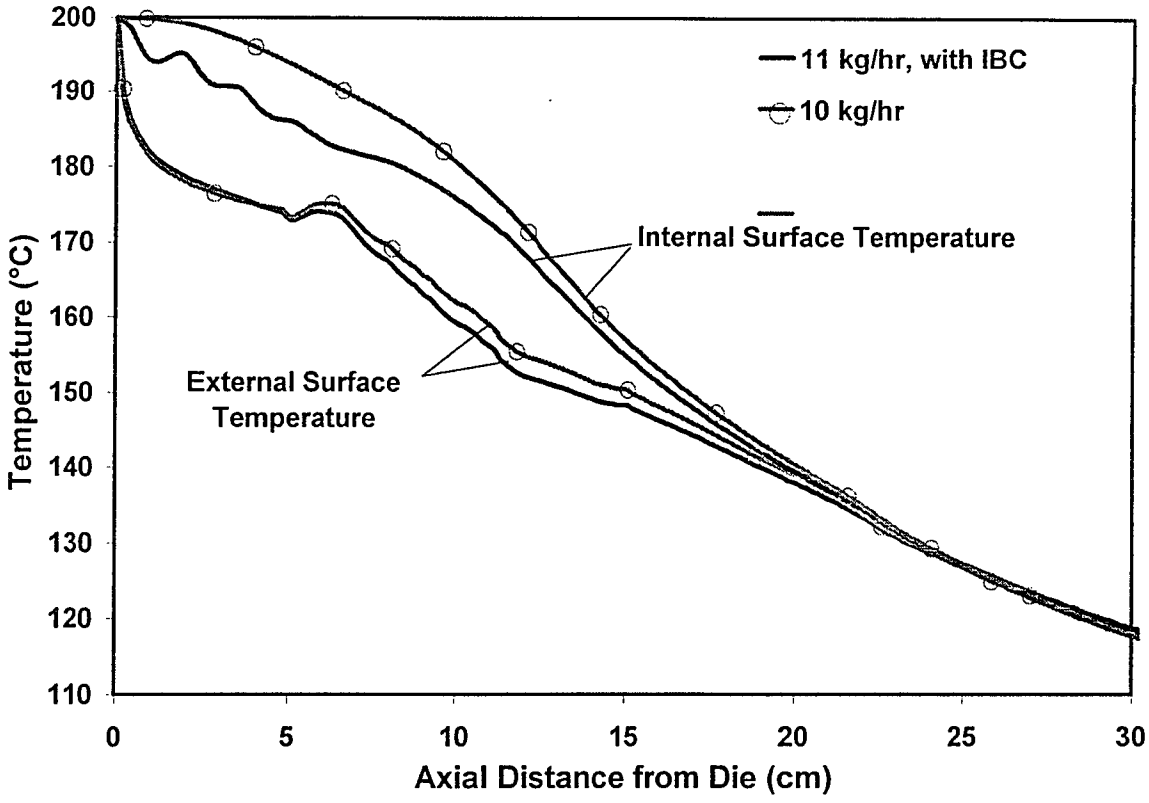

Figure 73: Calculated temperature drops in the machine direction for the external and internal surface -- 10 kg/hr melt throughput with external cooling and 11 kg/hr melt throughput with external-IBC cooling (both simulations performed at medium intensity cooling)

4.5. NOMENCLATURE FOR CHAPTER 4

α : thermal diffusivity

ρ : density

ε : emissivity

C_p : heat capacity

k : thermal conductivity

n : film thickness

h_c : convective heat transfer coefficient

h_r : radiative heat transfer coefficient

T : temperature

T_∞ : ambient air temperature

T_{sur} : temperature of the surroundings

z : axial distance

CHAPTER 5.

DETERMINATION OF STRESS PROFILES

The importance of bubble cooling as one of the most critical aspects of the film blowing process is well recognized between blown film manufacturers and experts. Apart from the obvious relation between the bubble cooling and the operating production rates[1], there is also a more subtle relationship between the cooling process and the final film properties. Unfortunately, there is only limited understanding of the mechanism of this interaction.

In the previous chapters the dynamics of bubble cooling and the resulting temperature profiles in the melt phase were studied. To achieve the simulation objective the film thickness was divided into many layers, each of which had a slightly different temperature. However, it is well known that both the viscous and elastic properties of polymeric materials are in various degrees dependent to temperature. Taking into account that in film blowing the range of operating temperatures easily exceeds 100°C (from die to frost line), the variability of the rheological properties in the melt phase can be easily understood.

---

[1] Cooling is the limiting stage in most modern film blowing lines

5.1. Viscoelastic Considerations in Modeling

In modeling the film blowing process, the elastic behavior of the polymeric material has been a major consideration for most researchers. The modeling aspect of the film blowing process was initially addressed by using a purely viscous, isothermal model [Pearson & Petrie, 1970a, 1970b and 1970c]. Based on their approach, many researchers attempted to solve to problem using more complicated constitutive equations and models.

Petrie [1975] was able to solve the isothermal problem for an elastic fluid. He concluded that the most important aspects in a modeling attempt should be the heat transfer prediction and the selection of an adequate viscoelastic model. Ast [1976] first managed to solve the energy equation and predicted the temperature profile of the film in the machine direction. Consequently, he was able to predict the bubble frost line heights for given heat transfer coefficients.

In his Ph.D. thesis Wagner [1976] presented a study on non-isothermal modeling, comparing a Newtonian, a purely elastic, and a Maxwell fluid. He was able to use a specially constructed very accurate device in order to measure the draw force. He concluded that the single mode Maxwell model was successful in predicting the draw-force (with the appropriate selection of the viscosity and relaxation time). However, the appropriately selected model parameters were very much dependent on the experiment.

Gupta [1980] also proposed a temperature dependent, modified Maxwell model. The relaxation time of the material was fitted to the calculated *machine direction* (MD) stresses (giving excellent predictions of the MD stresses). However, using the same relaxation times the prediction of the *transverse direction* (TD) stresses was not as accurate.

Later, Luo & Tanner [1985] decided to use upper convected Maxwell and Leonov models. The Leonov model was not proven to be consistent with the experimental data of Gupta [1980]. On the other hand the upper convected Maxwell approach gave reasonable predictions, but only after the relaxation time was fixed to be different than the one Gupta proposed. It was also found that the temperature dependency of the rheological properties was very important for an adequate prediction.

Cain & Denn [1988] compared the solutions for a certain problem using Newtonian, upper convected Maxwell, and Marrucci fluid. Their solutions were more stable numerically, however they were not unique: for the same take-up force and inflation pressure, more than one solutions could be obtained.

Cao & Campbell [1990] tried to address the viscoelasticity problem in a different way. They pointed out that all the viscoelastic models that had been used in the past, predicted thinning of the film (and therefore velocity increase) even after the freeze line. Therefore they introduced a new model, the visco-plastic-elastic model. They also suggested that the demarcation between the liquid and solid behavior should be altered from

the conventional frost line (dr/dz=0) to a rheologically based constraint, the plastic-elastic transition. Although their model had good agreement with Gupta's experiments, they too had to use altered material parameters. Using the same model, Ashok & Campbell [1992] simulated the tubular film blowing by dividing the bubble into three parts: liquid, liquid-solid, solid. It seems that their model is in good agreement with experimental data.

Alaie & Papanastasiou [1993] used an integral constitutive equation to simulate Gupta's experimental data. By using complex temperature shifting factors they managed to obtain good agreement with the experiments. Tas [1994] in his Ph.D. thesis compared the Wagner, Leonov, Giesekus and PTT (Phan-Thien-Tanner) models. He concluded that a non-linear viscoelastic model is essential but only the PTT model is in good agreement between calculated and experimentally determined stresses. Also, André et al [1998] studied the multiple solutions that occur when the upper convected Maxwell fluid is used.

In the current chapter, the previously presented temperature profiles will be used to provide a better prediction of the film stresses at the frost line. The PTT model will be used but only as a stress calculator. As in chapter 4, the bubble kinematics used here are calculated using a purely viscous, non-isothermal approach [Sidiropoulos, 1995]. Having fixed the bubble kinematics, the local deformation rates are pre-determined and the stress calculation is both fast and stable.

5.2. THEORY

The Phan-Thien-Tanner (PTT) model [Xue et al, 1995] has been reported to be an excellent choice for the modeling of film blowing [Tas,1994]. The model is considered to be one of the most promising differential models and has been used with relative success for a variety of polymer flow simulations. However, the complexity of the model and convergence problems (which may require special computational methods) have prevented more extensive use of the PTT model.

In the PTT model, the upper convected derivative (see eq. 1-12) is modified with the addition of a slip factor (ξ), which mainly determines the non-linear behavior in shear flow. For ξ=0 the *upper-convected* derivative is obtained. The stress term is also modified by a stress tensor trace function Y(**τ**), which captures the rheological behavior under extensional flows. The PTT proposed constitutive equation is,

$$\tau_{ij}Y(\tau)+\lambda\left(\overset{\nabla}{\tau}_{ij}+\xi\left(\gamma_{ik}\tau_{kj}+\tau_{ik}\gamma_{kj}\right)\right)=2\eta_o\gamma_{ij} \qquad (5\text{-}1)$$

where γ_{ij} is the rate of strain tensor.

In the current work, the exponential form of function Y is used,

$$Y(\tau)=exp\left(\frac{\varepsilon\lambda}{\eta_o}\tau_{kk}\right) \qquad (5\text{-}2)$$

The model parameter ξ can be fitted using data from shear or elongational experiments, but parameter ε requires elongational data.

The stresses at the die lips are also included at the simulation and the normal stresses at the die are considered the start-up stresses before the biaxial stretching begins. At the die lips there is a simple shear flow field, for which equation 5-1 can be solved for the normal stress components, giving [Baird & Collias, 1995],

$$\tau_m = \frac{\lambda\dot{\gamma}^2(2-\xi)\eta_o}{1+\xi(2-\xi)(\lambda\dot{\gamma})^2} \tag{5-3}$$

$$\tau_t = 0 \tag{5-4}$$

$$\tau_n = \frac{-\lambda\dot{\gamma}^2\xi\eta_o}{1+\xi(2-\xi)(\lambda\dot{\gamma})^2} \tag{5-5}$$

There is no need to establish the model at earlier positions (inside the die) because the PTT model does not include any memory effects. The velocity profile inside the die gap is assumed to be that of a power-law material. The shear rate at the die lips is varying in the *normal* (thickness) direction and can be approximated by the function,

$$\dot{\gamma} = -\frac{2n+1}{n} V_{ave} \frac{2}{h_o}\left(\frac{2y-h_o}{h_o}\right)^{\frac{1}{n}} \tag{5-6}$$

with y ranging from 0 to h_o (h_o is the gap at the die lips).

Equation 5-6 is derived from the *pressure-driven flow between flat plates for power-law materials* analysis [Vlachopoulos, 1997] under the assumption that the die gap (h_o) is much smaller then the die radius (R).

After the melt flows past the die lips, the biaxial extension starts and the deformation immediately becomes a shear-free, biaxial extension. Outside the die, the *rate of strain* tensor becomes,

$$\gamma_{ij} = \begin{bmatrix} \dot{\varepsilon}_m & 0 & 0 \\ 0 & -(\dot{\varepsilon}_m + \dot{\varepsilon}_t) & 0 \\ 0 & 0 & \dot{\varepsilon}_t \end{bmatrix} = \begin{bmatrix} \frac{dV_m}{dz} & 0 & 0 \\ 0 & \frac{V_m}{h}\frac{dh}{dz} & 0 \\ 0 & 0 & \frac{V_m}{R}\frac{dR}{dz} \end{bmatrix} \qquad (5\text{-}7)$$

For the deformation field shown in eq. 5-6, the diagonal components of the tensorial equation 5-1 can be expressed [Tas, 1994],

$$\lambda V_m \frac{d\tau_m}{dz} = 2\eta_o \frac{dV_m}{dz} - exp\left[\frac{\varepsilon\lambda}{\eta_o}(\tau_m + \tau_t + \tau_n)\right]\tau_m + 2\lambda(1-\xi)\frac{dV_m}{dz}\tau_m \qquad (5\text{-}8)$$

$$\lambda V_m \frac{d\tau_n}{dz} = 2\eta_o \frac{V_m}{h}\frac{dh}{dz} - exp\left[\frac{\varepsilon\lambda}{\eta_o}(\tau_m + \tau_t + \tau_n)\right]\tau_n + 2\lambda(1-\xi)\frac{V_m}{h}\frac{dh}{dz}\tau_n \qquad (5\text{-}9)$$

$$\lambda V_m \frac{d\tau_t}{dz} = 2\eta_o \frac{V_m}{R}\frac{dR}{dz} - exp\left[\frac{\varepsilon\lambda}{\eta_o}(\tau_m + \tau_t + \tau_n)\right]\tau_t + 2\lambda(1-\xi)\frac{V_m}{R}\frac{dR}{dz}\tau_t \qquad (5\text{-}10)$$

Equations 5-8 to 5-10 can be solved as a system, but use the pre-defined bubble kinematics. Since the calculated bubble kinematics have been shown to have an acceptable degree of accuracy [Sidiropoulos 1995], the extra *normal* stresses (τ_m, τ_t and τ_n) are easily calculated. Using the thin membrane aproximation, it can be easily derived [Agassant et al, 1991] that $\sigma_m = \tau_m - \tau_n$ and $\sigma_t = \tau_t - \tau_n$.

The temperature dependence of both the viscosity and relaxation time can be estimated by using the WLF equation [Ferry, 1980],

$$\lambda = \lambda_{ref}\, exp\left(\frac{-C_1(T - T_{ref})}{C_2 + (T - T_{ref})}\right) \tag{5-11}$$

and

$$\eta = \eta_{ref}\, exp\left(\frac{-C_1(T - T_{ref})}{C_2 + (T - T_{ref})}\right) \tag{5-12}$$

where T_{ref} may be the glass transition temperature or another reference temperature (in the current work the solidification temperature is used) and C_1, C_2 are constants determined by curve-fitting [Baumgärtel et al., 1994].

5.2.1. Multi-Layer Thin Membrane Analysis

The dynamics of tubular film forming for a single-layer film were initially studied by Pearson & Petrie [1970a, 1970b, and 1970c]. Their approach is based on the thin membrane approximation (where the bubble is regarded as a thin shell in tension). The tension (produced by the axial traction and the pressure difference) is the driving force for the deformation of the film membrane. Their approach is almost universally followed in blown film modeling and has already been summarized in equations 1-1 to 1-6 (section 1.3). It should be noted that the *machine* and *tangential* direction stress equations are derived from the force equilibrium, irrespective of any constitutive equation.

In the current work, the film thickness is divided into 20 sub-layers of equal thickness, each of which may have slightly different rheological properties due to the temperature variations across the film thickness. This computational situation is similar to multi-layer film blowing[1].

For any multi-layer film the total force exerted in any direction is the sum of the forces that each individual layer applies. Before continuing with the multi-layer stress relations, the concept of *equivalent stress* has to be defined:

> For any given multi-layer tubular film bubble, we locally define the *equivalent stress* as the local stress a single-layer film should have, in order to have the shape and dimensions (radius, thickness, curvatures etc.) of the multi-layer film

Just as the thin membrane analysis, the *equivalent stresses* of a multi-layer film are locally derived from the force equilibrium and are not dependent on the constitutive equation. It should also be noted that the different layers do not necessarily have to be layers of different materials (as in multi-layer film). In the current work, for example, they are layers of different temperature (and consequently different rheological properties) for a single material.

---

[1] Assuming that there is no-slippage at the interfaces and the layers "stick" to one another, which is the case in commercial film blowing with very few exceptions

The concept of the *equivalent* stress is conveniently defined so that the dynamics of film forming can be easily generalized to include multi-layer films. The generalization is obtained by replacing the stresses in equations 1-3 and 1-6 with the *equivalent* stresses[1]. The equations become

$$\frac{\Delta P}{h} = \frac{\sigma_{m,eq}}{\rho_m} + \frac{\sigma_{t,eq}}{\rho_t} \tag{5-13}$$

$$-\pi R^2 \Delta P + 2\pi R h \sigma_{m,eq} \cos\theta = F_{Total} = \text{constant} \tag{5-14}$$

Thus, the classical analysis (as presented in section 1.3) is still valid. However, it is required to express the *equivalent* stresses in terms of the stresses in the individual layers. Using the definitions presented above, it can be proven[2] that

$$\sigma_{m,eq} = \frac{1}{h}\sum_i \left(h_i \sigma_{m,i}\right) \tag{5-15}$$

and

$$\sigma_{t,eq} = \frac{1}{h}\sum_i \left(h_i \sigma_{t,i}\right) \tag{5-16}$$

Equations 5-15 and 5-16 are also derived from the force balance on the film and can be used irrespective of any constitutive equation.

---

[1] It is evident that for a single layer film the local stresses and the *equivalent* local stresses should be identical

[2] A more detailed derivation of the equations 5-15 and 5-16 is provided in Appendix C

5.3. MATERIAL CHARACTERIZATION

Two polymeric materials that are commonly used in blown film production were tested and their rheological behavior was fully characterized. The polymer resins were DOW's Dowlex 2078 (LLDPE) and 494 (LDPE). The two polymers were specifically selected because they differ rheologically. The LLDPE material exhibits low shear thinning and limited elasticity, while the LDPE is very elastic and is characterized by long memory effects and relatively high shear thinning.

For each polymer dynamic measurements (covering several decades of frequency) were performed for an extensive range of temperatures. The values of the storage and loss moduli (G' and G'' respectively) were taken over a range of angular velocities (ω) for temperatures ranging from 120 to 190°C. Using the measured values, the dynamic viscosity is calculated by

$$\eta'(\omega) = \frac{G''(\omega)}{\omega} \tag{5-17}$$

The Cox-Merz rule can be applied (Macosko, 1994) stating that the dynamic viscosity $\eta'(\omega)$ is virtually identical to the shear viscosity $\eta(\gamma)$ with the angular velocity ω corresponding to γ. The data is also used to calculate the discrete relaxation spectra of the polymers under consideration.

The relaxation time distribution was calculated by fitting simultaneously both storage and loss moduli data to a series of Maxwell-type relaxation modes (Ferry, 1980), to yield a discrete relaxation time spectrum in the form of a discrete relaxation strength, g_i and discrete relaxation time, λ_i.

The modal functions that have been used for the discrete spectrum are

$$G'(\omega) = \sum_{i=1}^{N} g_i \frac{(\omega\lambda_i)^2}{1+(\omega\lambda_i)^2} \tag{5-18}$$

and

$$G''(\omega) = \sum_{i=1}^{N} g_i \frac{(\omega\lambda_i)}{1+(\omega\lambda_i)^2} \tag{5-19}$$

For the Dowlex 2078 LLDPE a 5-mode spectrum was implemented for all the temperatures (N=5), while the 494 LDPE was adequately approximated using only 4 modes. Both spectra gave a good fit to the dynamic measurements without introducing too many modes. The optimum spectrum calculation was accomplished using non-linear regression analysis. The relative deviation between experimental data and values predicted by the model was minimized

$$\sum_n \left(\frac{\Delta G'}{G'}\right)_n^2 + \left(\frac{\Delta G''}{G''}\right)_n^2 = \text{MIN} \tag{5-20}$$

where n is the number of experimental points.

The discrete relaxation spectra for the polymeric materials (obtained by the method described above) was used for each temperature in order to obtain the zero-shear viscosity and *characteristic relaxation time* using the functions

$$\eta_o = \sum_{i=1}^{N} (g_i \lambda_i) \tag{5-21}$$

and

$$\lambda_{Char} = \frac{\sum_i (g_i \lambda_i^2)}{\sum_i (g_i \lambda_i)} \tag{5-22}$$

The discrete relaxation spectrum is a very efficient way to approximate the continuous relaxation spectrum (Baumgärtel & Winter, 1992).

The values of the zero-shear viscosity, the characteristic relaxation time and the corresponding temperature were used to determine the constants of the WLF model (equations 5-11 and 5-12). Different constants were used for each of the two equations, as the viscosity and relaxation time have significantly different temperature dependence.

5.3.1. Characterization of Dowlex 2078 LLDPE

Dynamic measurements were performed on a Rheometrics (ARES) rheometer at several melt temperatures. The rotational rheometer is equipped with a parallel plate measuring system. The plate gap was set to ~1mm and the total strain was kept at approximately 5%, to make sure that the measurement was always conducted at the linear viscoelasticity region. The measurements covered frequencies from 0.1 to 100 s^{-1}.

The measured values were fitted with a 5-mode discrete relaxation spectrum using equations 5-18 to 5-20. Figures 74 and 75 show both the measured values and the discrete spectrum function approximation for a high (190°C) and a low (125°C) temperature. The full range of measured data and the best-fit approximate functions for all the temperatures, as well as tables with all the optimum values of the discrete spectrum (g_i, λ_i) can be found in Appendix D

Using equations 5-21 and 5-22 the calculated discrete spectra can provide the characteristic relaxation time and zero shear viscosity for each temperature. The values are presented on figures 76 and 77, accompanied by a WLF model regression (using equations 5-11 and 5-12 accordingly) to describe their temperature dependence. The WLF model shows very good aggreement with the values obtained from the discrete spectra. However, the optimum values of the constants C_1 and C_2 are not the same in the two simulations.

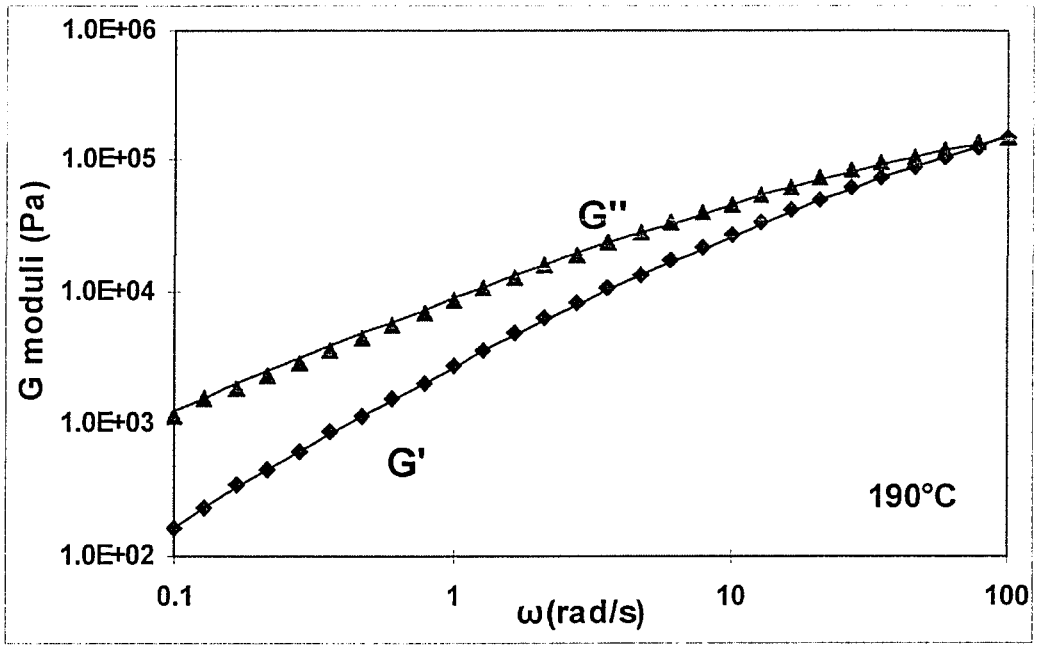

Figure 74: Storage and loss moduli measurements for Dowlex 2078 (LLDPE) at 190°C and best-fit by a 5-mode relaxation spectrum

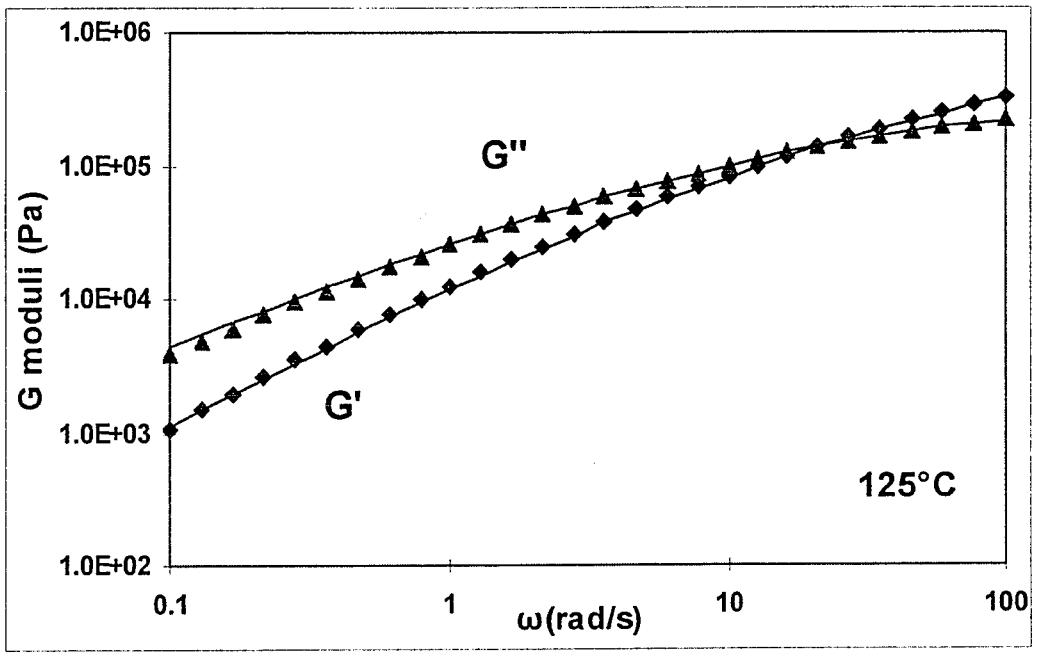

Figure 75: Storage and loss moduli measurements a for Dowlex 2078 (LLDPE) at 125°C and best-fit by a 5-mode relaxation spectrum

It is common practice in the literature [Baumgärtel et al, 1995] for temperature shifts to be handled using identical constants for the viscosity and relaxation time. Although the ensuing error is not large, the identical constants approach represents a convenient compromise. It was, therefore, decided that different constants should be used for each equation, in order to obtain the best possible agreement with the experimental data.

The values for the WLF constants that gave the best fit of the viscosity vs. temperature data were C_1=9.63 and C_2=4.66, while the values for the relaxation time vs. temperature data were C_1=2.64 and C_2=16.8. In both cases, the optimum WLF reference temperature was determined to be 106.7°C by best fitting the experimental data, a value remarkably close to the solidification temperature of the semi-crystalline polymeric material (108°C, provided by the manufacturer).

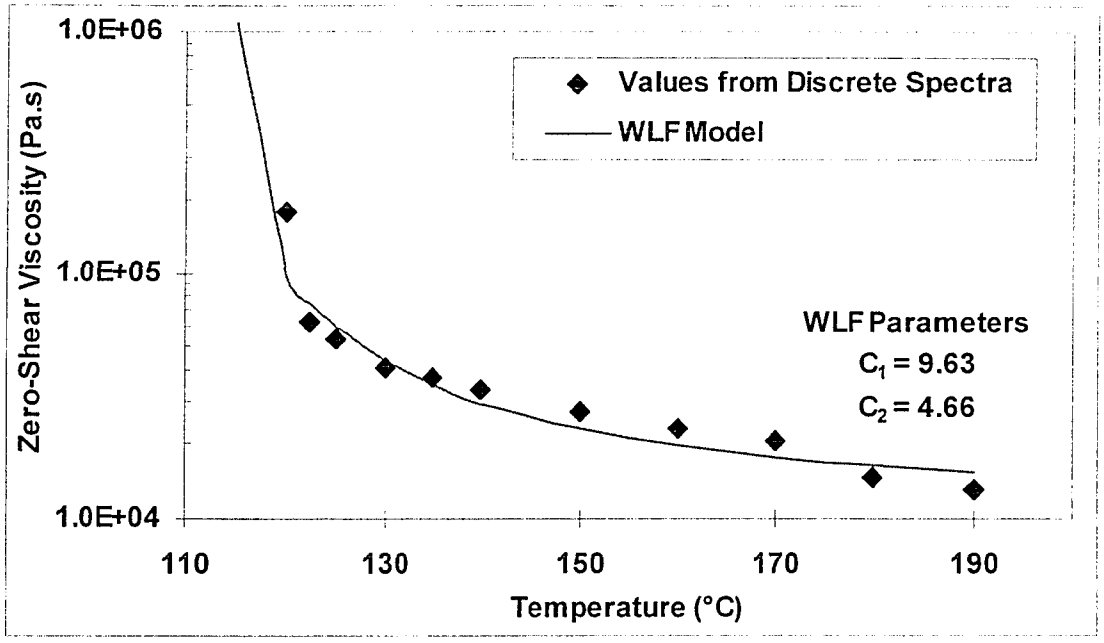

Figure 76: Zero-shear viscosity (from the relaxation spectra) vs. temperature and WLF model fitting for the 2078 LLDPE

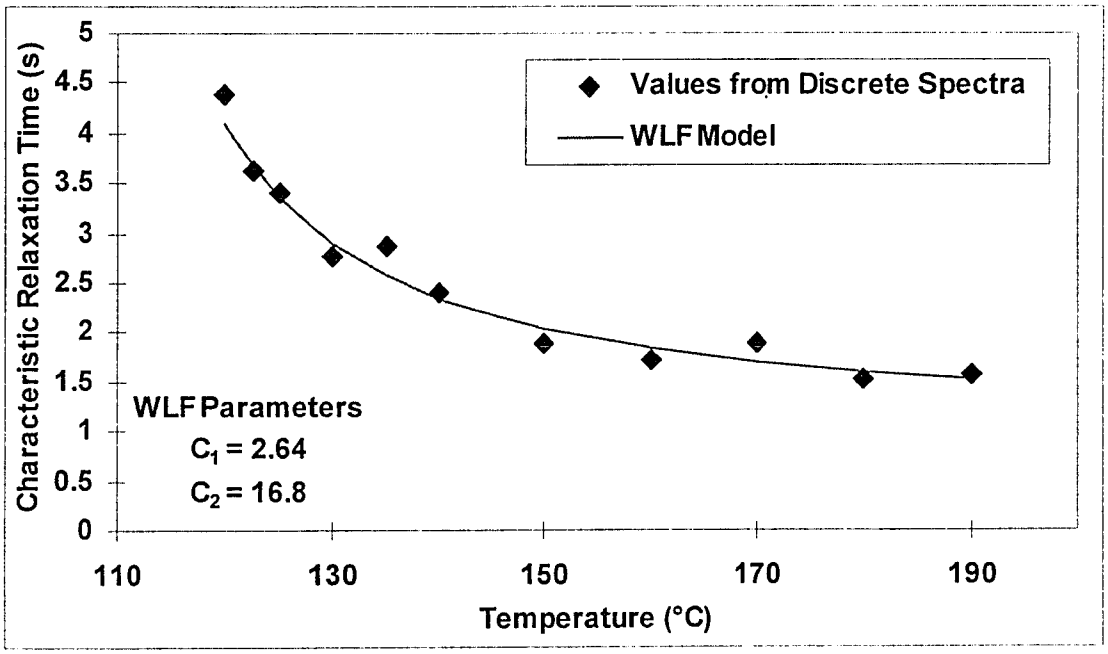

Figure 77: Characteristic relaxation time (from the relaxation spectra) vs. temperature and WLF model fitting for the 2078 LLDPE

5.3.2. Characterization of Dow 494 LDPE

Dynamic measurements were also performed for the 494 LDPE, another typical blown film material. The storage and loss moduli were measured on a Rheometrics rheometer at several melt temperatures. The measured values were fitted with a 4-mode[1] discrete relaxation spectrum using equations 5-18 to 5-20.

Figures 78 and 79 show two typical measurement sets with the moduli values and the discrete spectrum function approximation for a high (190°C) and a low (125°C) temperature. The full range of measured data and the best-fit approximate functions for all the temperatures can be found in Appendix D, accompanied by tables with the optimum-fit values of the discrete spectrum (g_i, λ_i).

The discrete relaxation spectra provided the characteristic relaxation time and zero shear viscosity for each temperature (using equations 5-21 and 5-22). The calculated values and the WLF model regression are presented on figures 80 and 81. As with the LLDPE material, the WLF model shows very good aggreement with the discrete-spectra values.

---

[1] For the 494 LDPE material, the difference in data-fit accuracy between a 5-mode and a 4-mode spectrum is insignificant. It was decided that the 4-mode spectrum is adequate.

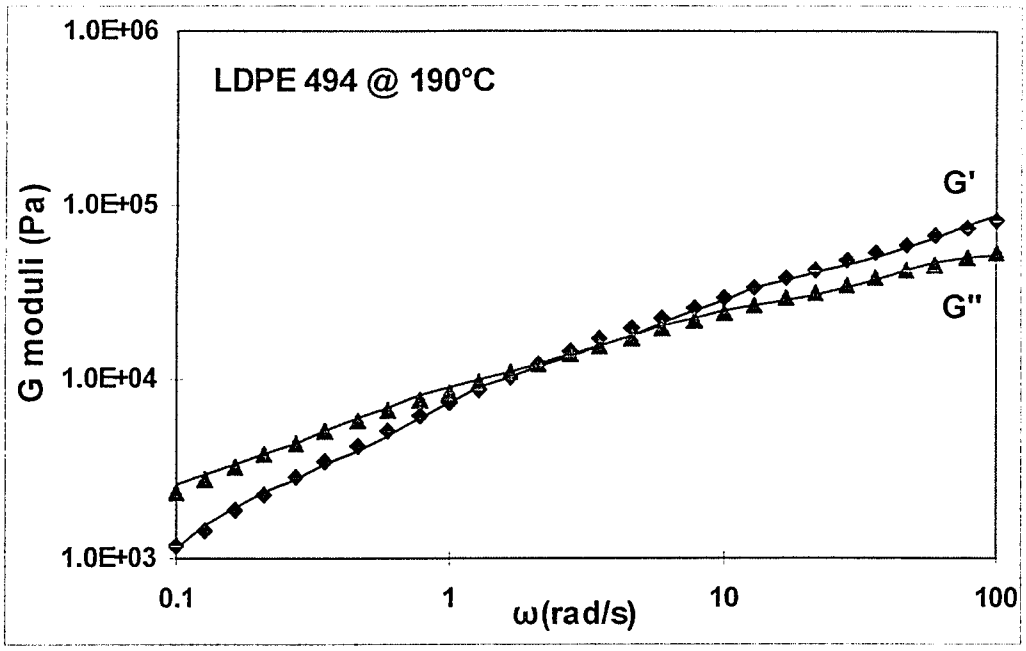

Figure 78: Storage and loss moduli measurements for Dow 494 LDPE at 190°C and best-fit by a 4-mode relaxation spectrum

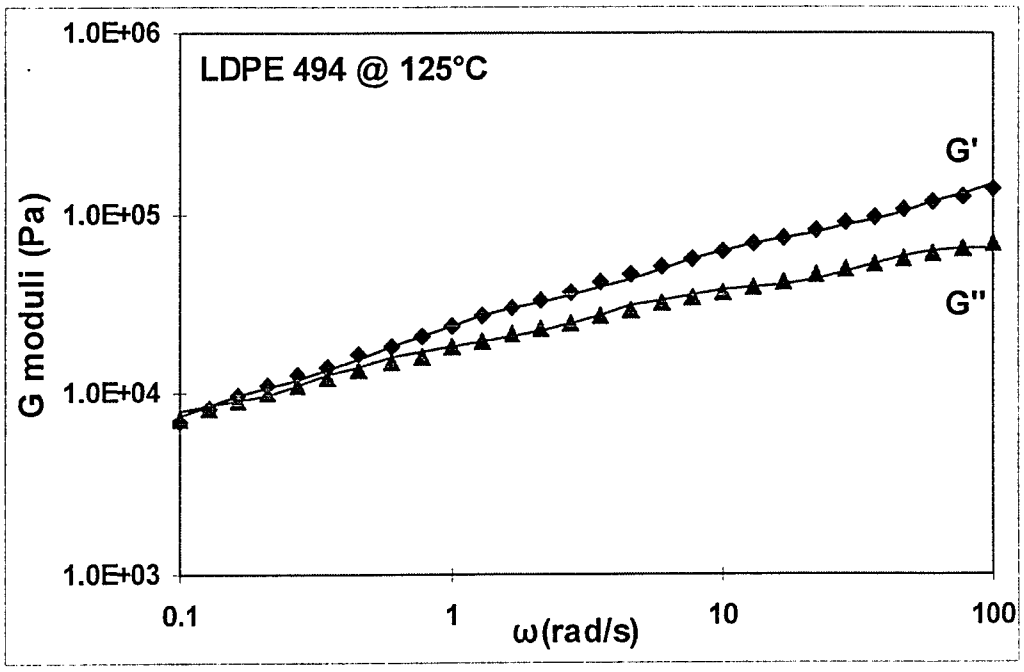

Figure 79: Storage and loss moduli measurements for Dow 494 LDPE at 125°C and best-fit by a 4-mode relaxation spectrum

The optimum values of the constants C_1 and C_2 are different for the viscosity and relaxation fitting. The fitting of the zero-shear viscosity gave the values C_1=6.22 and C_2=37.4, while the characteristic relaxation time data were optimally fitted by C_1=3.27 and C_2=86.9. The reference temperature for both fittings was 99°C, a value almost identical to the solidification temperature of the material.

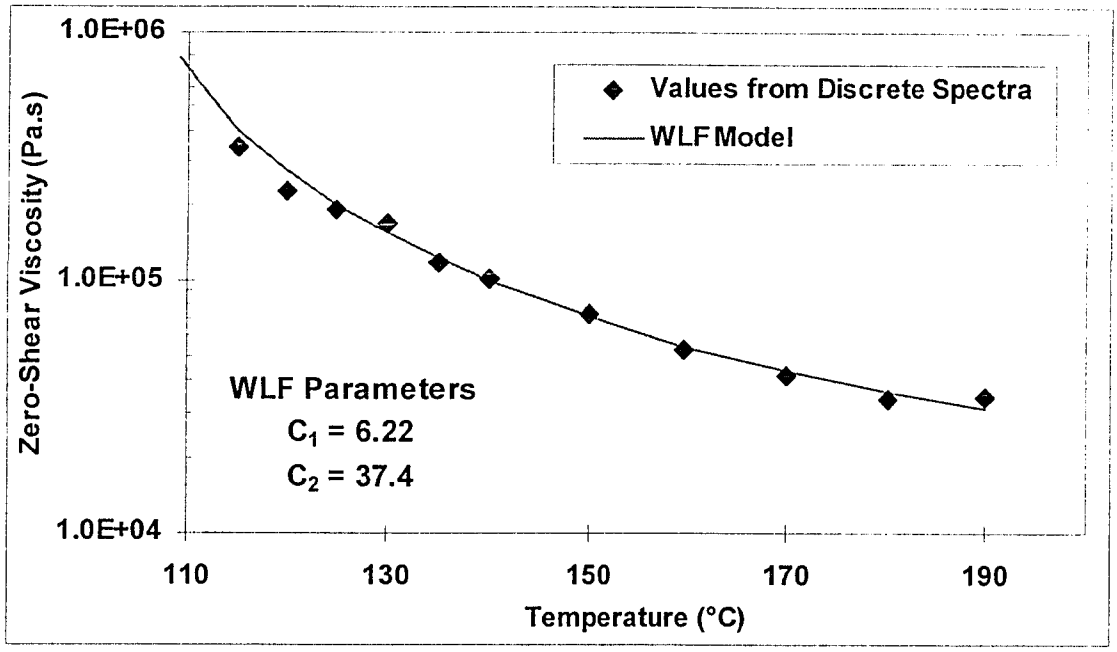

Figure 80: Zero-shear viscosity (from the relaxation spectra) vs. temperature and WLF model fitting for the 494 LDPE

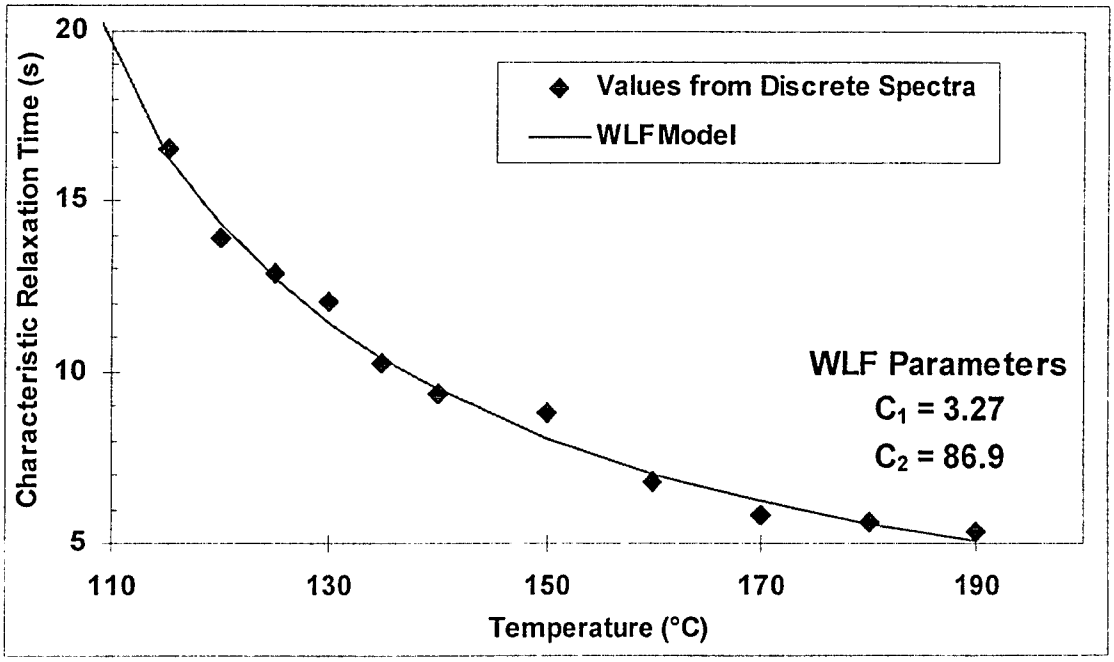

Figure 81: Characteristic relaxation time (from the relaxation spectra) vs. temperature and WLF model fitting for the 494 LDPE

5.3.3. Strain Hardening Experiments

The non-linear parameters ξ and ε of the PTT viscoelastic model are more closely related with the elongational behavior of the material and cannot be determined by steady-state shearing experiments. The strain hardening behavior of the Dowlex 2078 LLDPE was studied in order to obtain the optimum ξ and e values.

Experiments were conducted at the Rheology & Materials Processing Centre of the Royal Melbourne Institute of Technology (RMIT, Melbourne, Australia) to measure the strain hardening behavior of the material at various constant elongation rates. The measuring equipment and experimental procedures of similar experiments are described in the related Ph.D. thesis of Micic [1997]. The experimental results at 150°C and elongation rates of 1.0, 0.3 and 0.1 s^{-1} (which represent typical extension rates for the film blowing process) are shown on figure 82. The optimum values of the ξ and ε PTT constants were found to be 0.52 and 0.12 respectively. It should be noted that application of the PTT model on simple-shear flows gives a ratio of second to first normal stress difference equal to $-\xi/2$. Using the value obtained by fitting the data (ξ=0.52) we get a ratio of approximately 1:4, a value not far from experimental data.

Identical values were also used for the 494 LDPE, since there were no extensional experiments available for that material. Previous studies [Tas, 1994] have shown the non-linear parameters ξ and ε to have only slight variations between polyolefin materials.

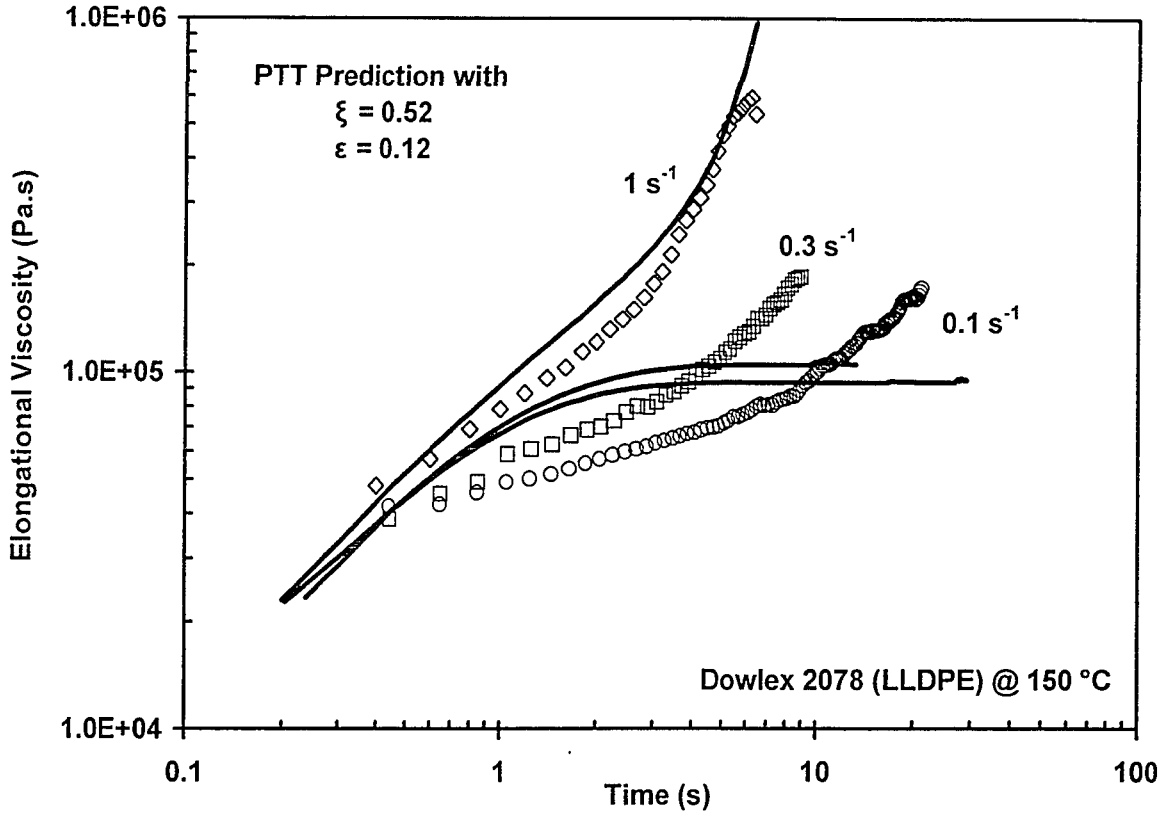

Figure 82: Strain hardening of Dowlex 2078 LLDPE under various steady elongation rates and fit by PTT model

5.4. Simulation Methodology

The blown film bubble example that was used in Chapter 4 with the corresponding film kinematics as well as the calculated temperature profiles, is also employed here. Having the bubble kinematics (for more see the simulation methodology presented on section 4.2.2) and the calculated temperature as given parameters, the stress profiles can be calculated in the melt phase. Although the strain rates are assumed to be constant throughout the film thickness at any given film position, the temperature differences cause variations in the rheological properties of the molten material.

At each axial and thickness position, the WLF approximations are used to calculate the local viscosity and relaxation time. The values are by the PTT model equations (5-3 to 5-5 and 5-8 to 5-10) to obtain the local stresses. It is apparent that the normal stresses at the die lips (just before the biaxial extension begins) are also included in the simulation.

The same procedure is used for both the simulated LLDPE and LDPE materials with the assumption that both would have the same bubble shape and kinematics. Since there is a crystallization point difference between the two materials (the LDPE material solidifies at 10°C lower) in order for the assumption to be correct, the melt temperature at the die lips was lowered to 190°C for the LDPE simulation. This way both material simulations retained the frost line at the same height.

This intervention shifted the temperature profiles for the LDPE simulation by 10°C, however the local temperature differences in the thickness (normal) direction were not significantly affected. Since it is the temperature differences in the thickness direction (rather than the local values of temperature) that are mostly of interest in the current work, the LLDPE and LDPE simulations can be directly compared without introducing much error, while at the same time retaining the validity of the common kinematics assumption.

For each computational node, the derivatives in equations 5-8 to 5-10 are resolved using upwind finite differences. Since the equations have to be solved as a system, the common Gauss-Seidel method is employed. The successive iterations continue until the updates became smaller than 0.001 Pa. The co-dependence between the equations is introduced by the non-linear term shown in equation 5-2. The contribution of the term in the current problem (transient, biaxial extension of plastic film using predefined kinematics) is rather small and the iterations converge after approximately 10 to 20 iterations.

5.5. Results and Discussion

The temperature profiles that were presented in figures 65 and 67 were combined with the local strain rates (taken from the pre-defined bubble kinematics) to calculate the two-dimensional normal stress profiles. Also, the normal stresses at the die lips were calculated using the PTT model and were used as starting values. The results of the stress simulations are presented for both the 2078 (LLDPE) and 494 (LDPE) materials.

5.5.1. Predicted Stress Profiles for the Dowlex 2078 LLDPE

5.5.1.1 Stress Profiles for the Single Layer Approach

Figure 83 compares the calculated machine (MD) and tangential (TD) direction total stresses (σ_m and σ_t respectively) for the PTT and Newtonian models. Using the thin membrane aproximation for the total stresses, it can be easily derived [Agassant et al, 1991] that $\sigma_m = \tau_m - \tau_n$ and $\sigma_t = \tau_t - \tau_n$. Using these equations, the Newtonian total stresses are derived using equations 1-7 and 1-8. The PTT total stresses are derived from the PTT extra stresses[1]. Both calculations were conducted using the traditional single-layer approach, where the melt rheological properties are evaluated for an average temperature throughout the film thickness.

---

[1] For the PTT model, the extra stresses (τ_m, τ_n and τ_t) are calculated by solving the system of differential equations 5-8 to 5-10 as described in section 5.4

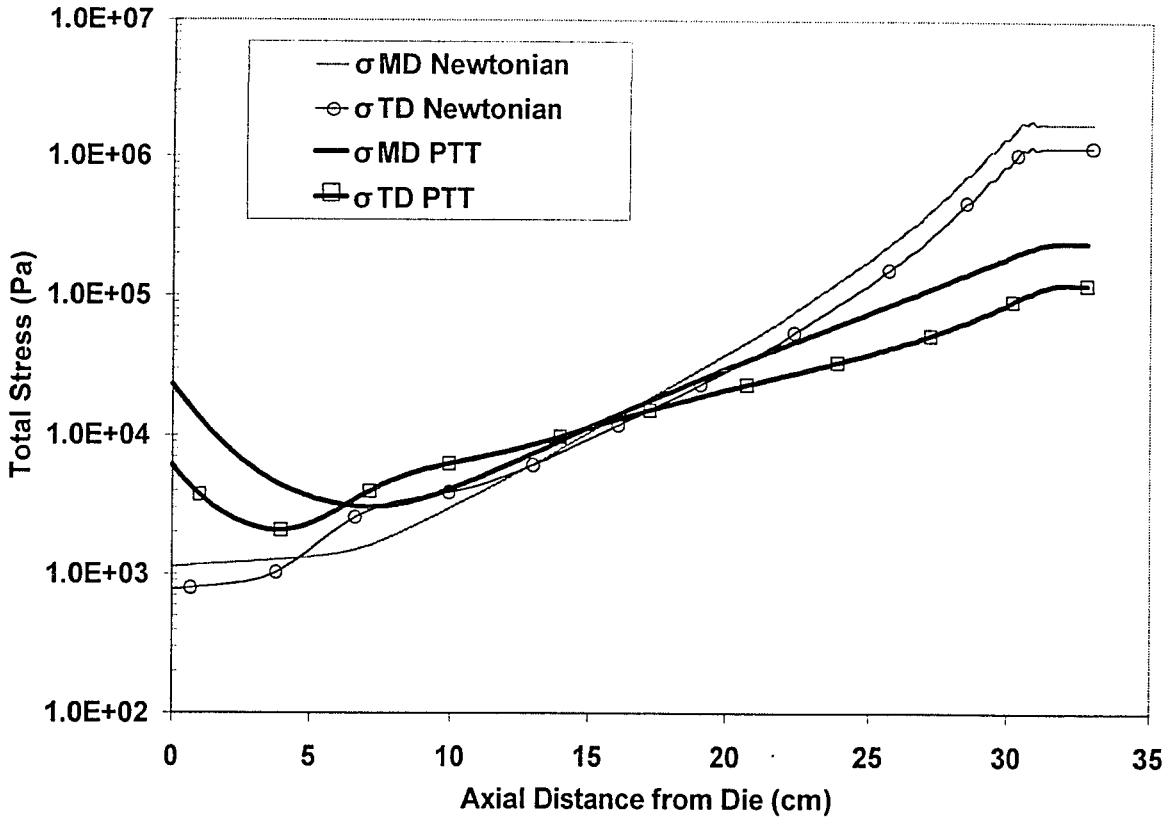

Figure 83: Comparison of Newtonian and PTT calculated stress profiles, using the single-layer method

Figure 83 shows that the PTT predicted total stresses are much smaller than the Newtonian stresses. Earlier studies [Sidiropoulos, 1995] have shown the Newtonian model to largely overpredict experimental stress values (they were calculated to be 3 to 8 times higher).

5.5.1.2 Comparison Between the Single and Multi-Layer Stress Calculation Approach

The equivalent stresses as defined by equations 5-15 & 5-16 (the equations are derived in Appendix C) can also be considered as the layer-thickness averaged stresses. Figure 84 compares the calculated machine direction (MD) stresses using the traditional single-layer approach (where the melt rheological properties are evaluated for an averaged temperature throughout the film thickness) with the *equivalent* MD stress (as obtained by the multi-layer approach). The stresses of figure 84 were obtained for the temperature profiles shown in figures 65 (corresponding to the low position setup of the dual-orifice air ring presented on section 2.7).

Figure 84 shows the two stress profiles to be almost indistinguishable in the initial stages of blowing. Both simulations predict an initial relaxation of the die normal stresses and no significant stress increase inside the air-ring cone (first 12-cm from the die). Beyond the air ring cone the stresses start to grow, with the maximum stress growth rate located close to the frost line. This kind of early stress relaxation followed by a late stress growth is consistent with similar single-layer modeling attempts [Tas, 1994].

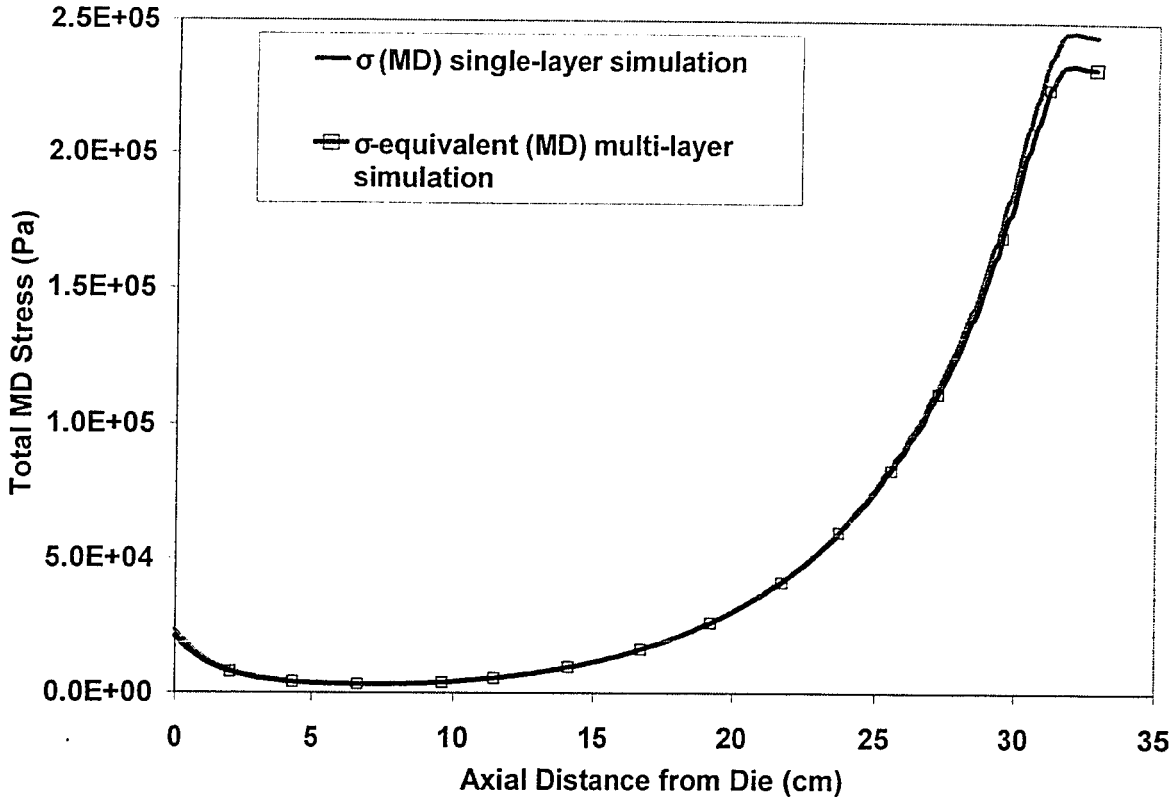

Figure 84: Calculated total stress in the machine direction (MD) vs. axial distance

However, near the location of the maximum predicted stress growth, the single and multi-layer predicted stresses start to diverge. The single-layer approach (using a thickness-averaged temperature) predicts a frost-line MD stress ~7% higher than the multi-layer approach.

Figure 85 presents a similar comparison for the predicted stresses in the tangential direction. Again, the two stress profiles are almost identical, showing an early stress relaxation followed by a late stress growth, but the calculated value at the frost line differs by almost 7%.

The simulation shows that the calculated equivalent stresses (which turned-out to be the layer-thickness averaged stresses for the multi-layer approach) differ from the single-layer calculated stresses. The results suggest that there may be some modest benefits in simulation accuracy by following the more rigorous multi-layer approach (thus avoiding the assumption of negligible temperature gradients in the *normal* direction).

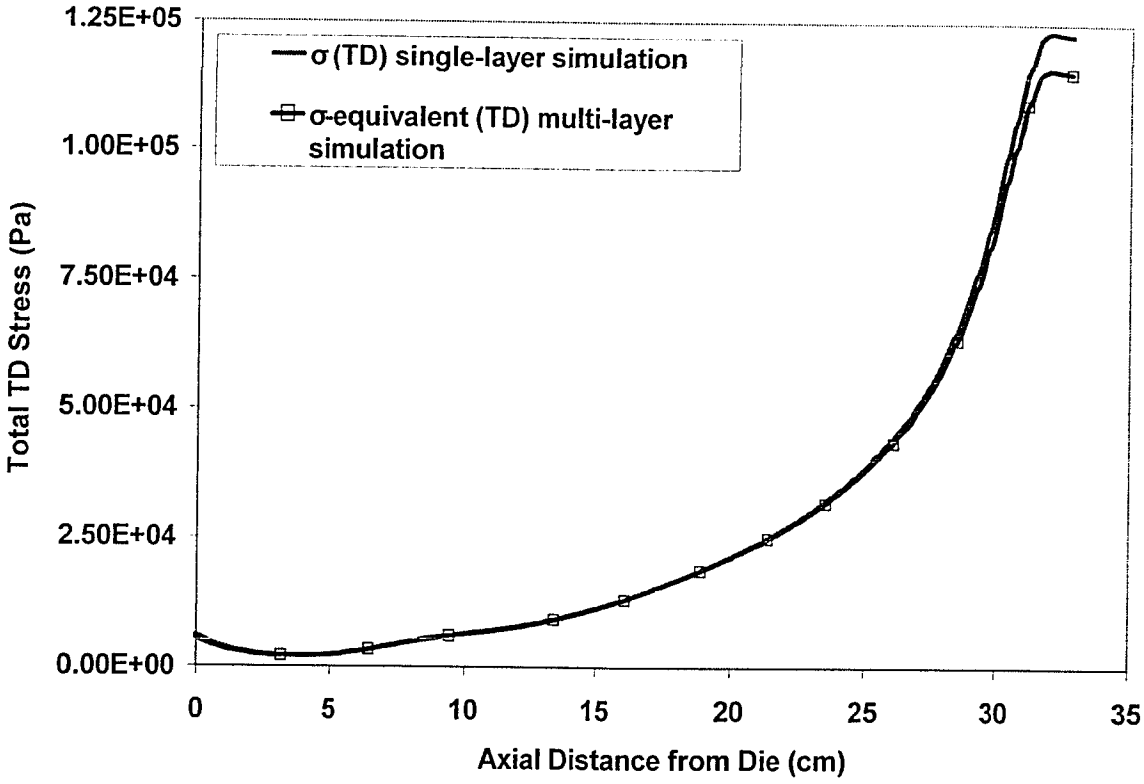

Figure 85: Calculated total stress in the tangential direction (TD) vs. axial distance

5.5.1.3 *Stress Profiles in the Film for the 2078 LLDPE*

The stress profiles on the melt (film) phase were calculated in both the machine and tangential directions, using the multi-layer approach with the preset bubble kinematics and by applying the low-position air-ring setup temperature gradients (see figure 65).

Figure 86 shows the equivalent machine direction stress profile and compares it with the stress profiles of the external surface (cold) layer of the film and the internal surface (hot) layer of the film. The simulation results suggest that all stresses follow a common[1] "initial relaxation followed by late growth" stress history and end up having an approximate 10% difference in value at the frost line.

Initial observation of figure 86 seems to indicate that the stress differences between the external and internal layers are limited to the area near the frost line. However, closer examination reveals that thickness direction stress gradients also exist at lower axial distances. Figure 87 shows the MD stress profiles in the film thickness direction, corresponding to various axial distance locations along the film bubble (from die lips to the frost line). The figure is split into a low and a high stress part, in order to retain higher resolution at the low axial distances.

---

[1] It is not surprising that the stress history is similar since the deformation rates are assumed invariable in the film thickness direction

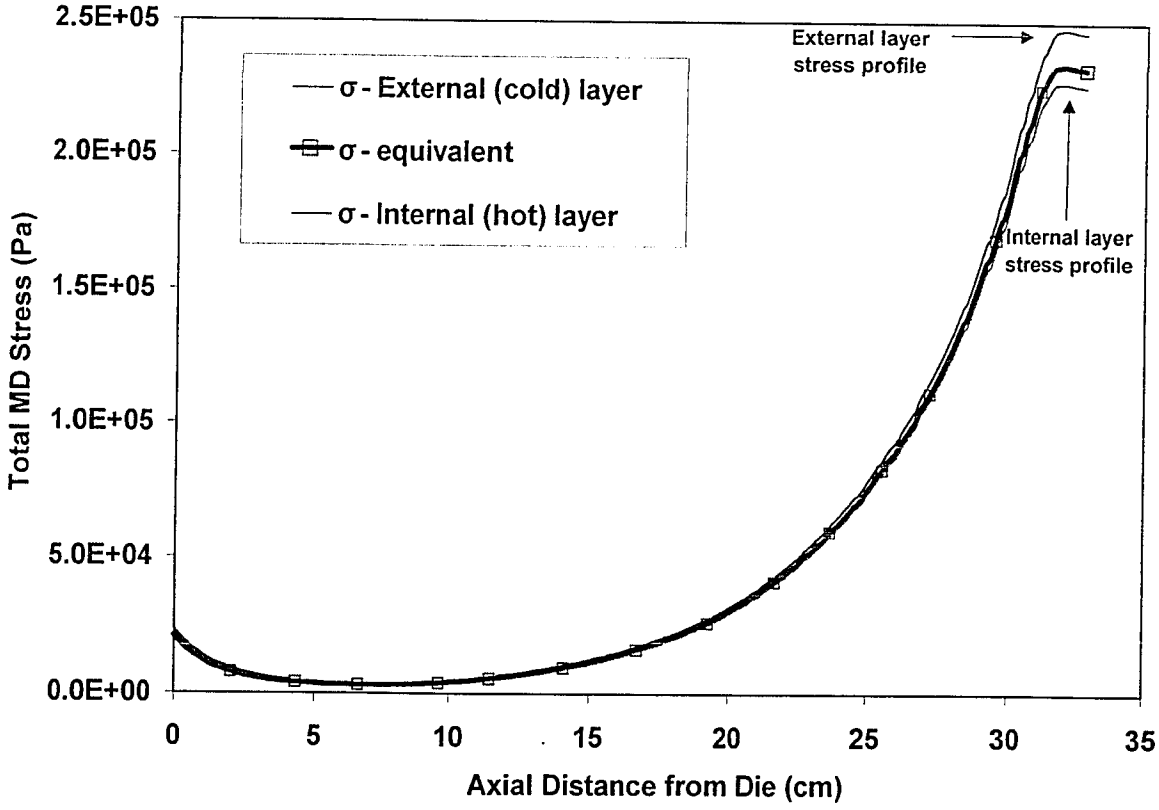

Figure 86: MD stress history at various positions along the bubble -- external (cold) surface, equivalent (averaged) and internal (hot) surface MD stress profiles are shown

Closer examination of Figure 87 reveals that the predicted stress difference between the internal and the external film layer is beginning to develop much lower than the frost line. At axial distances close to the end of the air-ring cone (~10 cm from die lips) the stress differences in the film thickness are already in the order of 10%. It should be reminded that the large temperature variations shown on Chapter 4 are mostly located in the air-ring cone area. Hence, the early variations in stresses along the film thickness should not be surprising. Moving towards the frost line the stress differences are augmented, mainly because the magnitude of the stresses rapidly increases. However, the relative difference remains approximately 10%, retaining the value it had just above the air-ring.

Figure 87 also shows the relaxation of the large, shear induced normal stresses inside the die once the polymer flow passes through the die lips. The normal stresses inside the die are predicted to have a characteristic "V" shape, with the maximum values located at the annular die walls (where the shear rate is maximum). No stress is predicted at the middle of the die gap, where the rate of shear is zero.

The value of wall normal stress at the die lips is predicted to be similar in magnitude to the wall shear stress at the same location. This ratio of normal to shear stresses is reasonable for polymer flows in channels, especially if the material does not exhibit high elasticity.

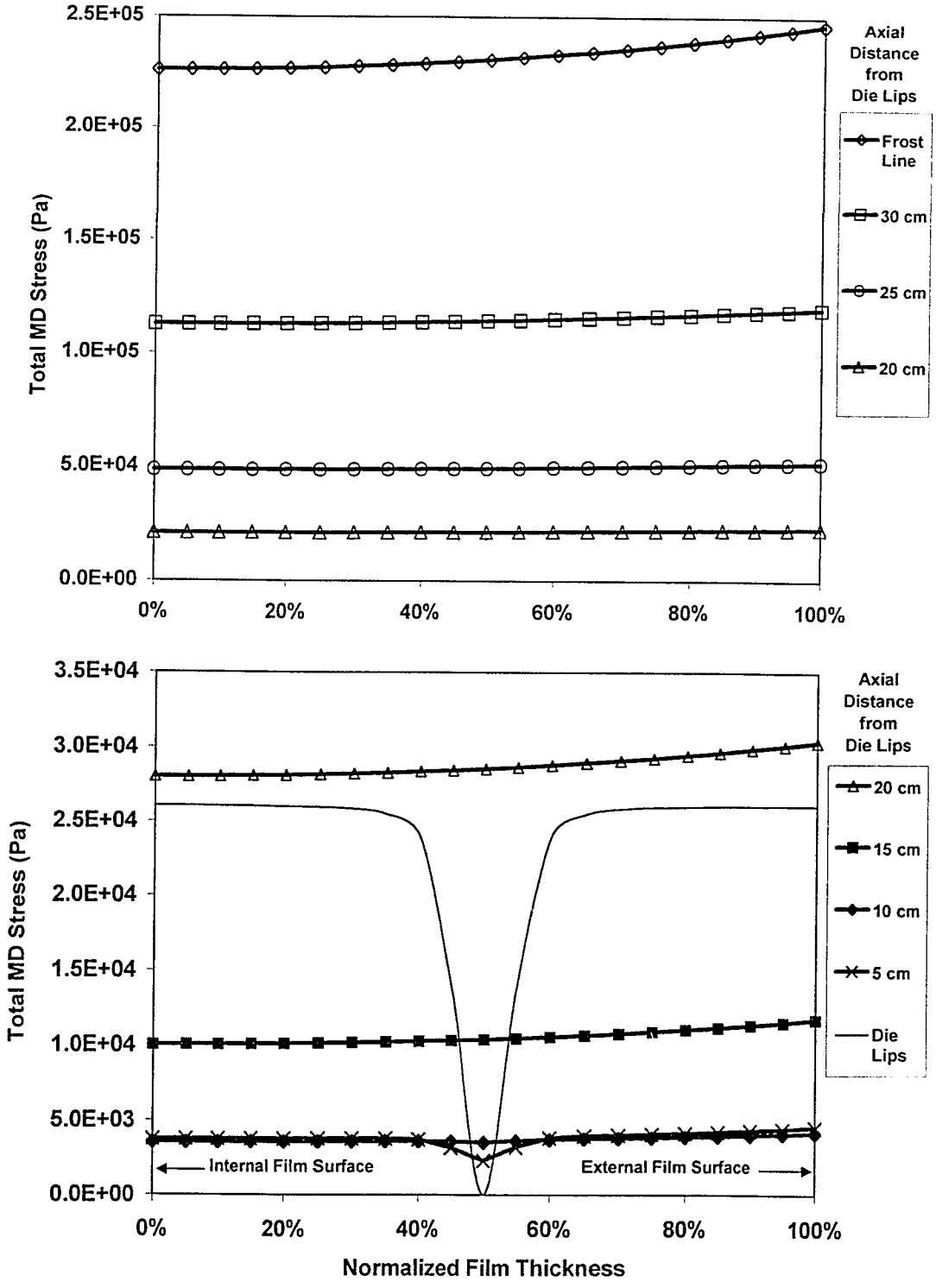

Figure 87: MD stress profiles in the film thickness direction corresponding to various axial distance locations along the film bubble (2078 LLDPE)

Once past the die lips, the normal stresses are predicted to relax and the V-shape profile quickly vanishes. At bubble positions close to the end of the air ring cone (~10 cm) all die effects on the MD stress have been relaxed.

Figure 88 shows a similar graph for the tangential direction (TD) total stress. The "V" shaped profile of normal stress is also predicted at the die lips[1], but at much lower levels. The effects of the die on the TD stresses quickly relax while the film is still inside the air-ring cone. Above the air-ring and at ~15cm axial distance from the die, TD stress differences between the internal and external film surfaces have already grown to be in the order of 20%. As the film approaches the frost line the stress differences grow in magnitude but decrease in percentage. At the frost line the calculated TD stresses show maximum differences between layers in the order of 10% (very similar to the differences of the MD stresses[2]).

Comparison between figures 87 and 88 shows that, in most positions along the bubble, the calculated MD stresses have values approximately 2 times larger than the calculated TD stresses. This value for the MD/TD total stress ratio is quite typical for LLDPE blown films.

---

[1] This is mainly due to the ability of the PTT model to calculate second normal stress differences.

[2] This is partially due to the coupling between stresses that the PTT model supports

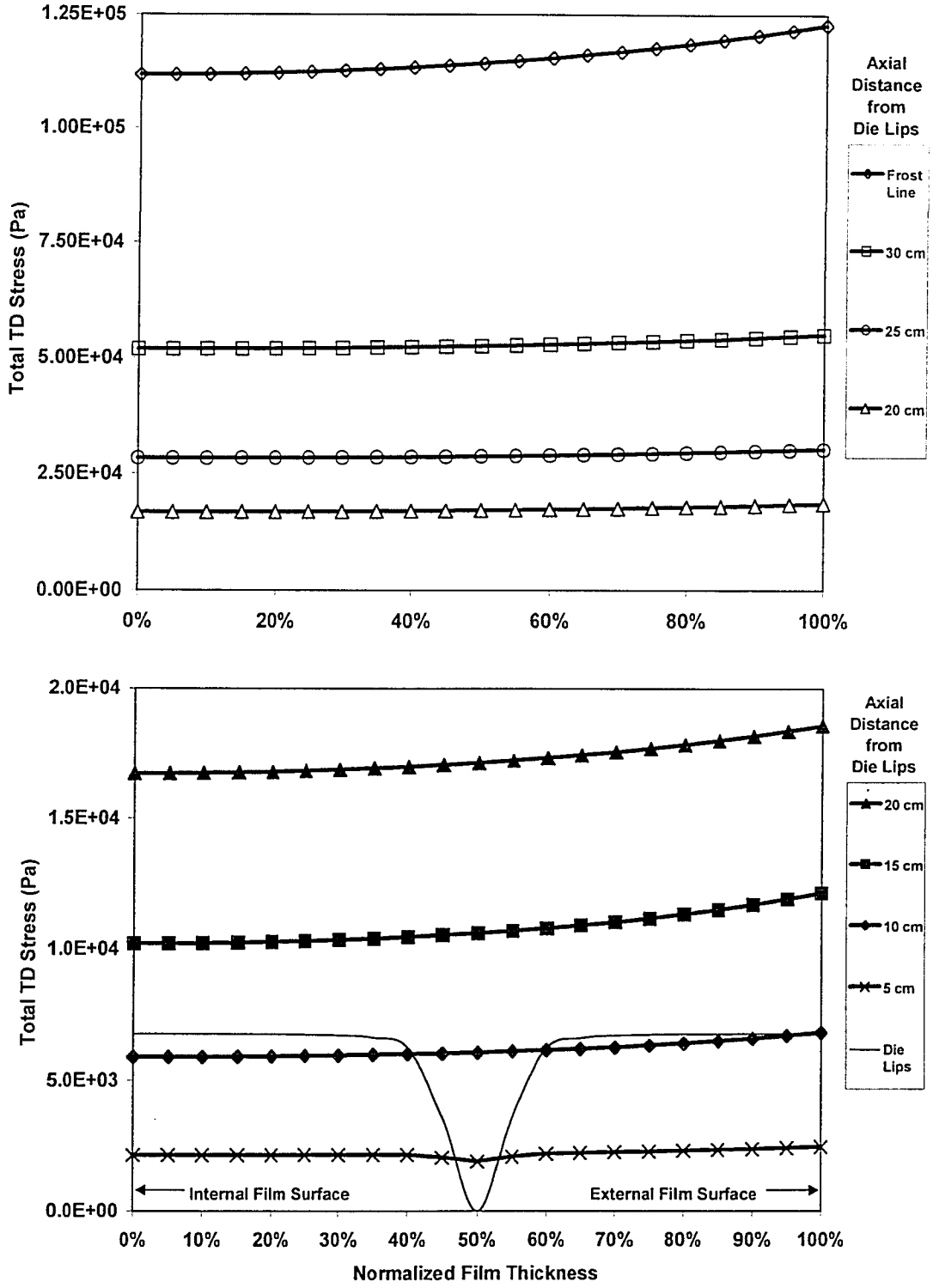

Figure 88: TD stress profiles in the film thickness direction corresponding to various axial distance locations along the film bubble (2078 LLDPE)

5.5.1.4 Stress Dependence On Production Rates (2078 LLDPE)

The dependence of the film-thickness temperature gradients on the blown film line production rates has been shown on section 4.3.3. Both the production rate and the external cooling airflow were approximately doubled and the simulation results were compared. The frost line and the machine direction temperature drop were only marginally affected (see figure 69) by the increased production rates, but closer examination revealed that the thickness direction temperature gradients were significantly increased (figure 70).

The results of the simulation of section 4.3.3 were used in order to evaluate the effect the increased production rates would have on the development of stresses profiles in the thickness direction of the film. Most of the kinematics of the film bubble (the frost line height, blow-up ratio, average temperature profile as well as the film thickness profile) were not significantly affected by the production rate increase. However, the local velocities of the film (and consequently the deformation rates) were almost doubled and the total blowing time (from die lips to frost line) was reduced (detailed bubble kinematics are listed on Appendix A).

The results of the stress simulation for the increased production rates are shown on figures 89 and 90 (for the machine and tangential direction respectively). Compared to the 10kg/hr throughput results (presented on figures 87 & 88 and corresponding to medium production and cooling rates) the machine direction stresses are quite higher.

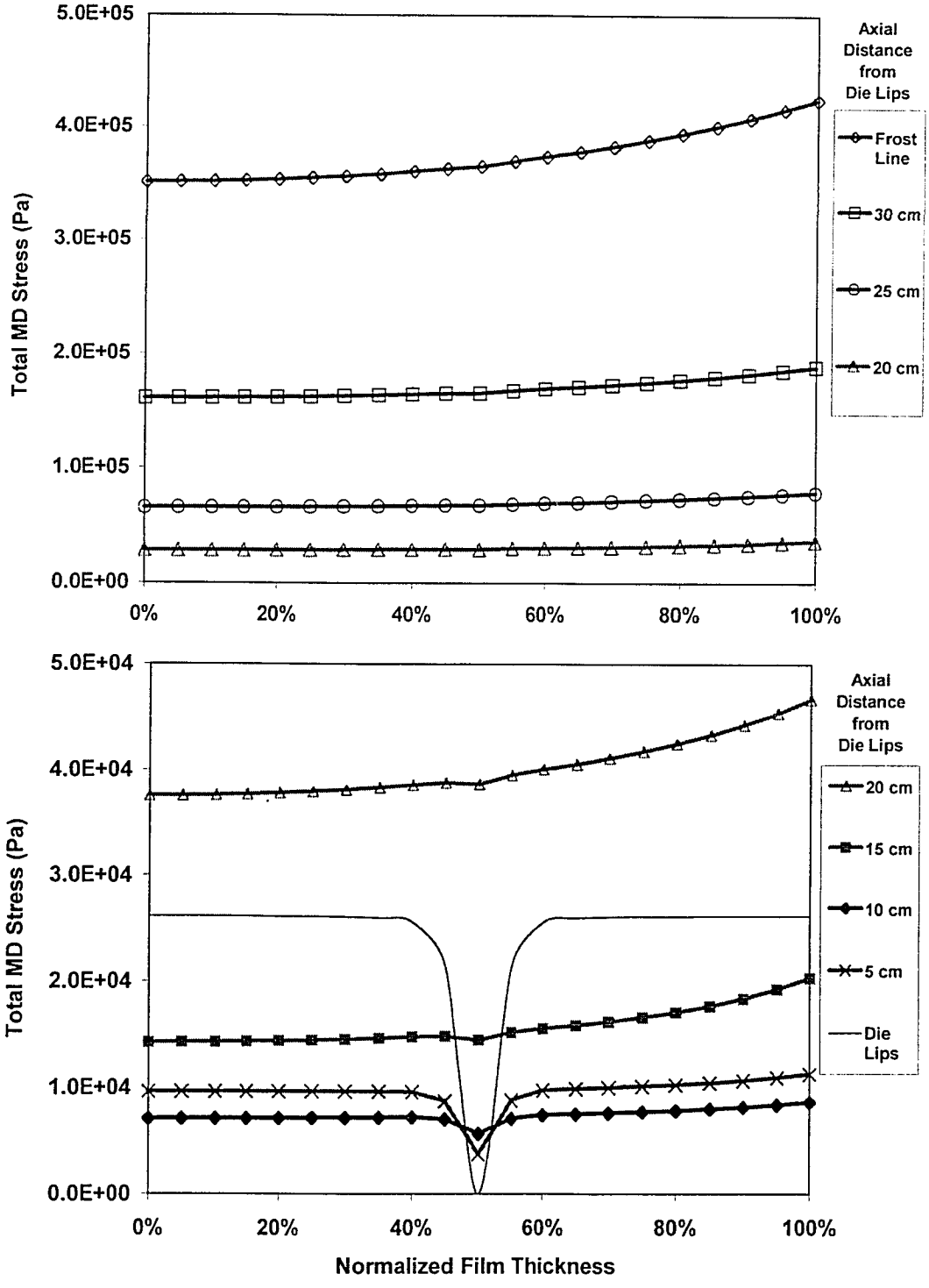

Figure 89: MD stress profiles in the film thickness direction at the increased production rate of 20kg/hr, shown at increasing axial distances (2078 LLDPE)

After flowing past the die lips, the calculated film stresses initially relax, reaching their minimum value near the end of the air-ring cone (~10cm). The stresses start to increase as the film moves away from the air-ring. As expected, the values of the stresses in the frost line are calculated to be much higher (almost double) than the stresses at the medium throughput (10kg/hr) simulation.

Close observation of the MD stress profiles in the film thickness, reveals that even midway to the frost line (~15cm) stress differences in the order of 25% are predicted in the *normal* (thickness) direction. Figure 89 suggests that, although relatively diminished, the stresses differences in the machine direction are sustained all the way up to the frost line. Figure 90 presents the calculated stress growth in the tangential direction, also showing large differences in the stresses of the external and internal film surfaces. In accordance with the MD stress calculation, the TD frost line stress differences are also in the order of 25%.

The results of the simulation suggest that increasing the production rate (and accordingly the cooling rate) of a given blown film line, tends to produce film that is unevenly stretched. It should be noted that industrial film blowing lines are usually pushed to their operating limit, in order to maximize capital returns. Thus, it is very likely that a good part of commercial blown film is being produced having significant thickness direction stress gradients during the crystallization phase of the cooling process (close to the frost-line zone).

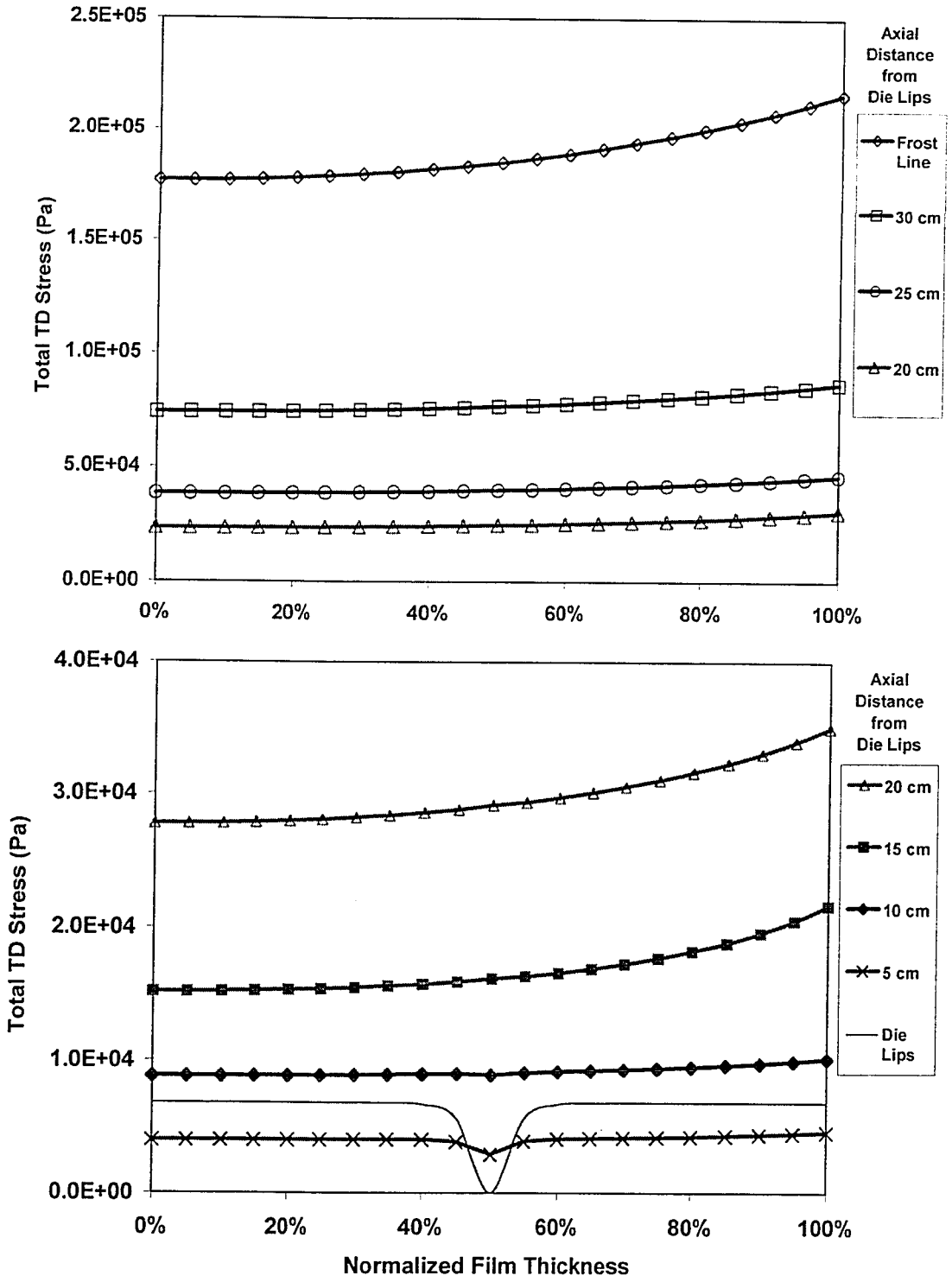

Figure 90: TD stress profiles in the film thickness direction at the increased production rate of 20kg/hr, shown at increasing axial distances (2078 LLDPE)

5.5.2. Predicted Stress Profiles for the DOW 494 LDPE

A similar set of stress calculations was conducted for the DOW 494 LDPE material. The rheological properties of the LDPE material are quite different from the previously used (2078 LLDPE), mainly characterized by increased elasticity and longer memory effects.

5.5.2.1 Stress Profiles in the Film for the 494 LDPE

The stress profiles on the melt (film) phase were calculated in both the machine and tangential directions, using the multi-layer approach with the medium throughput bubble kinematics (10kg/hr melt throughput) and by applying the low-position air-ring setup temperature gradients (see figure 65).

Figures 91 and 92 show the MD and TD stresses dependence on the axial distance from the die. In general, the simulation suggests that the LDPE material experiences a similar stress history as the LLDPE material. However, closer examination reveals differences characteristic of the two materials. The final (frost line) stresses for the LDPE material are higher, which was expected since the material is more viscous. Similarly to the LLDPE simulation, the stress differential between the colder external and the hotter internal surfaces are in the order of 10% at the frost line. However, considerable stress differences develop much earlier, just after the end of the air-ring (~15cm axial distance from the die). Figure 91 shows that MD stress growth mostly takes place close to the frost line, while the TD stresses are predicted to grow more gradually.

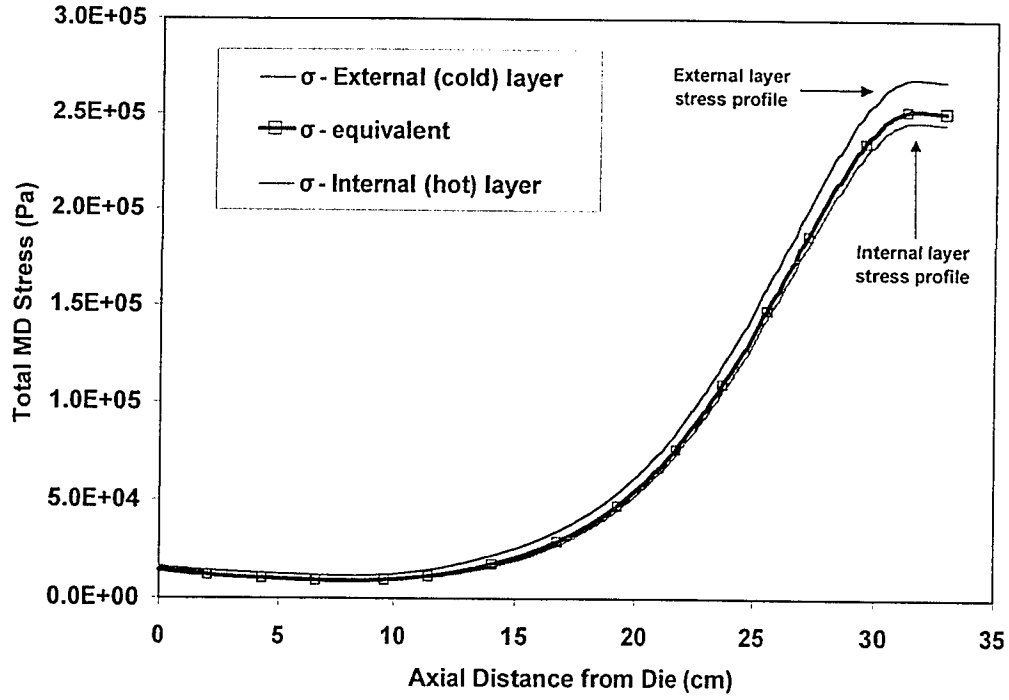

Figure 91: MD stresses at various positions along the bubble (494 LDPE)

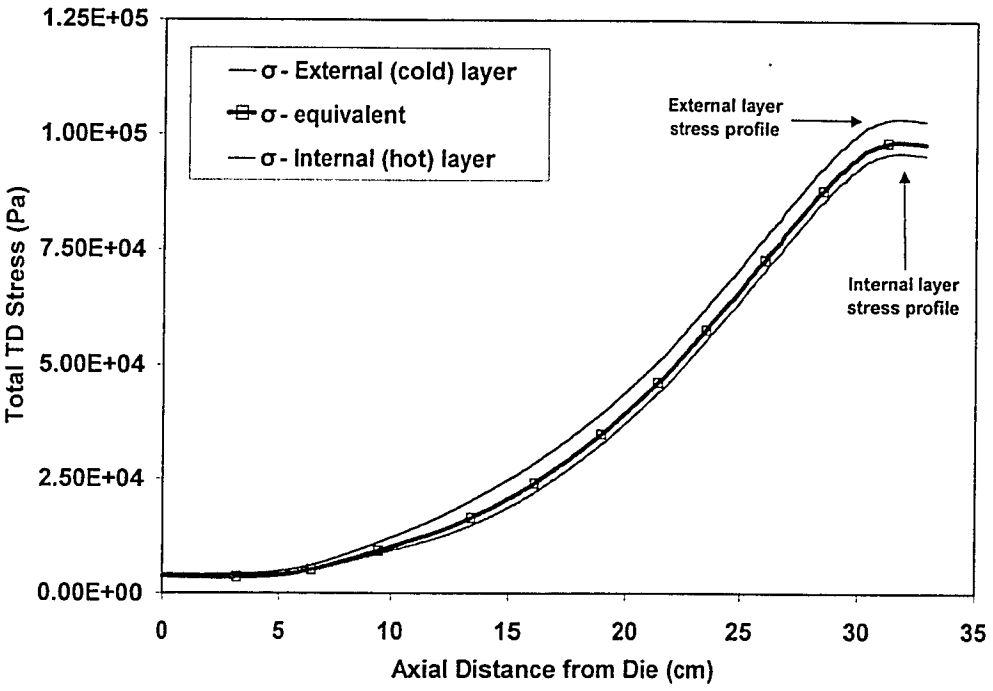

Figure 92: TD stresses at various positions along the bubble (494 LDPE)

It is characteristic that the initial stress relaxation that was observed in the LLDPE stress predictions (at the early stages of blowing) is much less pronounced in the LDPE simulation results. The most probable reason is that the 494 LDPE material has a longer relaxation time and, therefore, the stresses do not have enough time to relax as the film travels inside the air-ring cone[1]. Consequently, instead of relaxing the stresses remain relatively constant while the film travels inside the air-ring cone.

A more detailed picture of the calculated MD stresses profiles in the thickness direction can be found in figure 93. As always, the figure is split into a low and a high stress part to retain a higher resolution at the lower stresses. It is apparent that the main stress growth occurs at the later stages of blowing (at locations higher than 15cm from the die). At the 20cm height, a significant stress variation across the film thickness (in the order of 20%) has already been developed. At the frost line, the stress variations have being reduced to almost 10%. It should be noted that the characteristic "V-shape" initial stress profile (which is a result of shear-induced normal stresses inside the die gap) does not vanish.

---

[1] At the medium production rate (10kg/hr), the calculated bubble kinematics suggest that the film takes ~17 seconds to travel from die to the frost line. Approximately 8 seconds are spend inside the air-ring cone. As shown on figures **Error! Reference source not found.** and 81, the characteristic relaxation time in the vicinity of the die lips is ~2 seconds for the LLDPE and ~5 seconds for the LDPE material

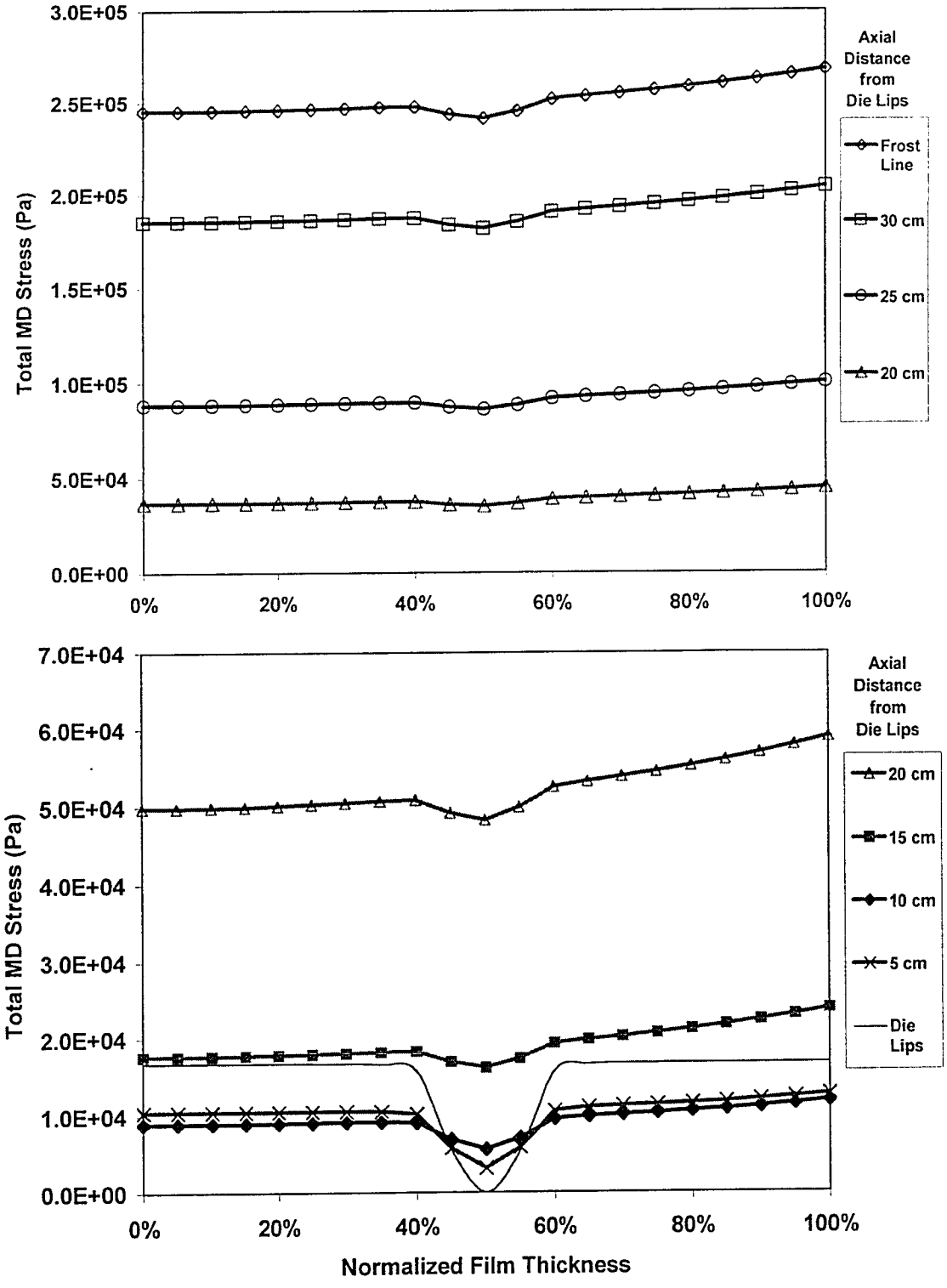

Figure 93: MD stress profiles in the film thickness direction corresponding to various axial distance locations along the film bubble (494 LDPE)

Contrary to the LLDPE material simulation (which showed the characteristic stress profile at the die to quickly vanish), the LDPE simulation predicts the "V-shape" to degrease very gradually, mainly due to the longer relaxation times. It is noteworthy that a small stress dip at the film center exists al the way up to the frost line.

Figure 94 shows similar profiles for the tangential direction (TD) film stress. Sizeable stress differences also exist across the film thickness, which are a little bit reduced before the frost line is reached. The film solidifies having an approximate 10% stress differential[1]. In this case the "V-shape" profile vanish much faster, in the area of the air-ring cone. However, instead of the characteristic dip a very small kink is developed in the film centerline (most likely caused by the MD stress dip through stress coupling, which the PTT model effectively captures).

The importance of these predictions at the film half-thickness does not lie at the extend of the small stress disturbances (which after all are not very large). More importantly, the simulation predicts that some of the die effects on the melt can be carried all the way up to the solidification region without fully relaxing. This verifies the empirically known fact that "memory" of the processing conditions inside the spiral die often (but not always) influences the final film properties.

---

[1] It should be noted that although the relative stress difference between the film surfaces is reduced as the film travels towards the frost line, the absolute value of the difference continues to grow all the way up to the frost line

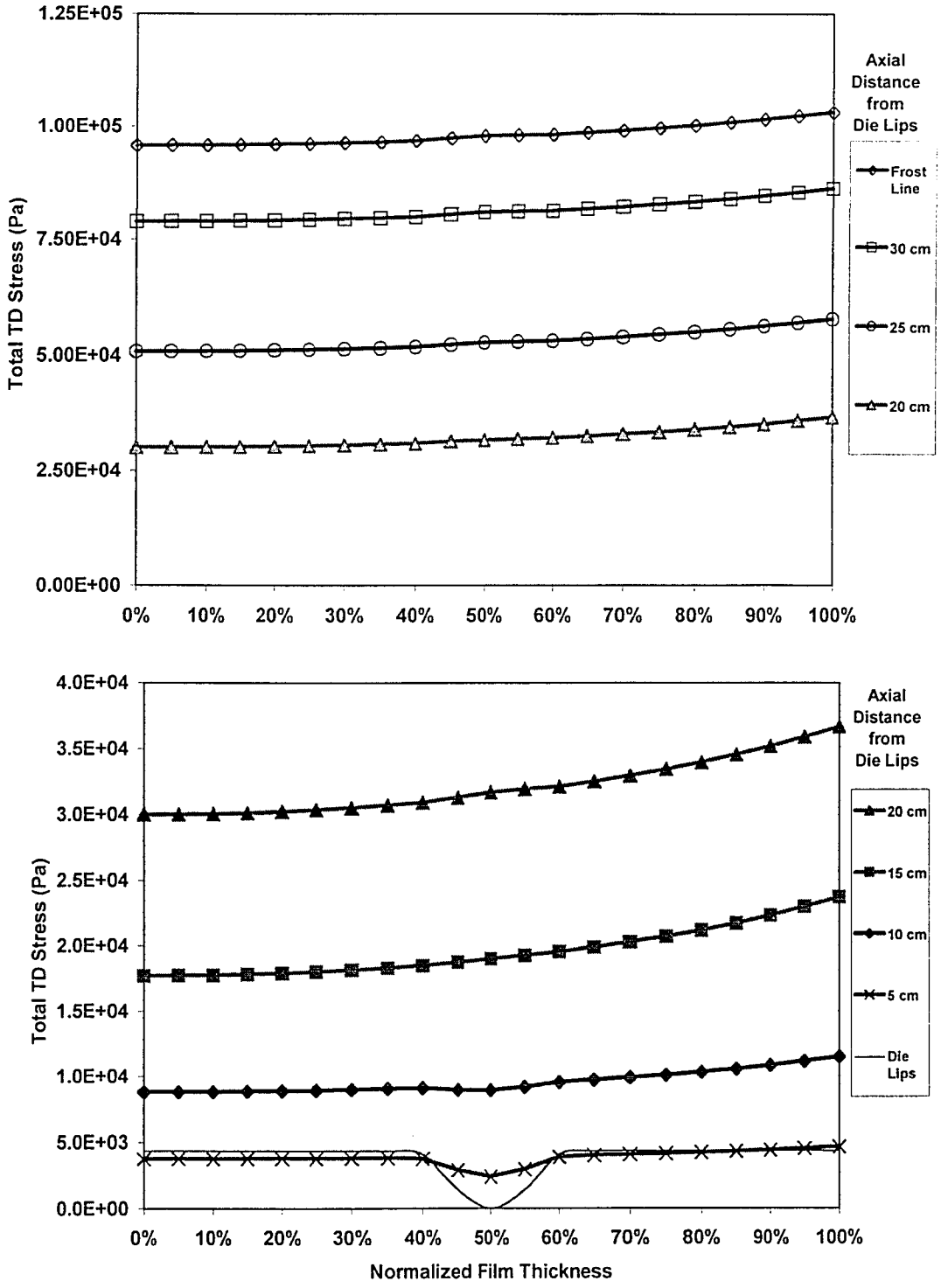

Figure 94: TD stress profiles in the film thickness direction corresponding to various axial distance locations along the film bubble (494 LDPE)

5.5.2.2 Stress Dependence On Production Rates (494 LDPE)

An increased production rate simulation (similar to the one presented in section 5.5.1.4) was also performed for the 494 LDPE material. The film production rate and the cooling rate were doubled and the temperature profiles and kinematics were used to calculate the film stresses. More details on the procedure can be found in section 5.5.1.4.

Figures 95 and 96 show the development of the machine and tangential stresses respectively. It is apparent that large stress variations in the thickness direction are predicted in both MD and TD directions. As with previously presented simulations, the largest relative stress differences are predicted to occur approximately half-way to the frost line (~35%). By the time the film reaches the frost line, the predicted stress differences across the film thickness reduce to approximately 20%.

Similarly to the calculations shown in the previous section, the die effects on the MD stresses are clearly carried all the way up to the frost line[1]. At the increased production rates, the die memory effect is more pronounced, having more than a subtle contribution in the frost line MD stress profile. On the other hand, the "V-shape" die profile of the TD stresses quickly dissipates as the film travels inside the air-ring cone.

---

[1] Which is not surprising since the film takes only 9 seconds to travel from the die to the frost line, while the characteristic relaxation time is > 5 seconds

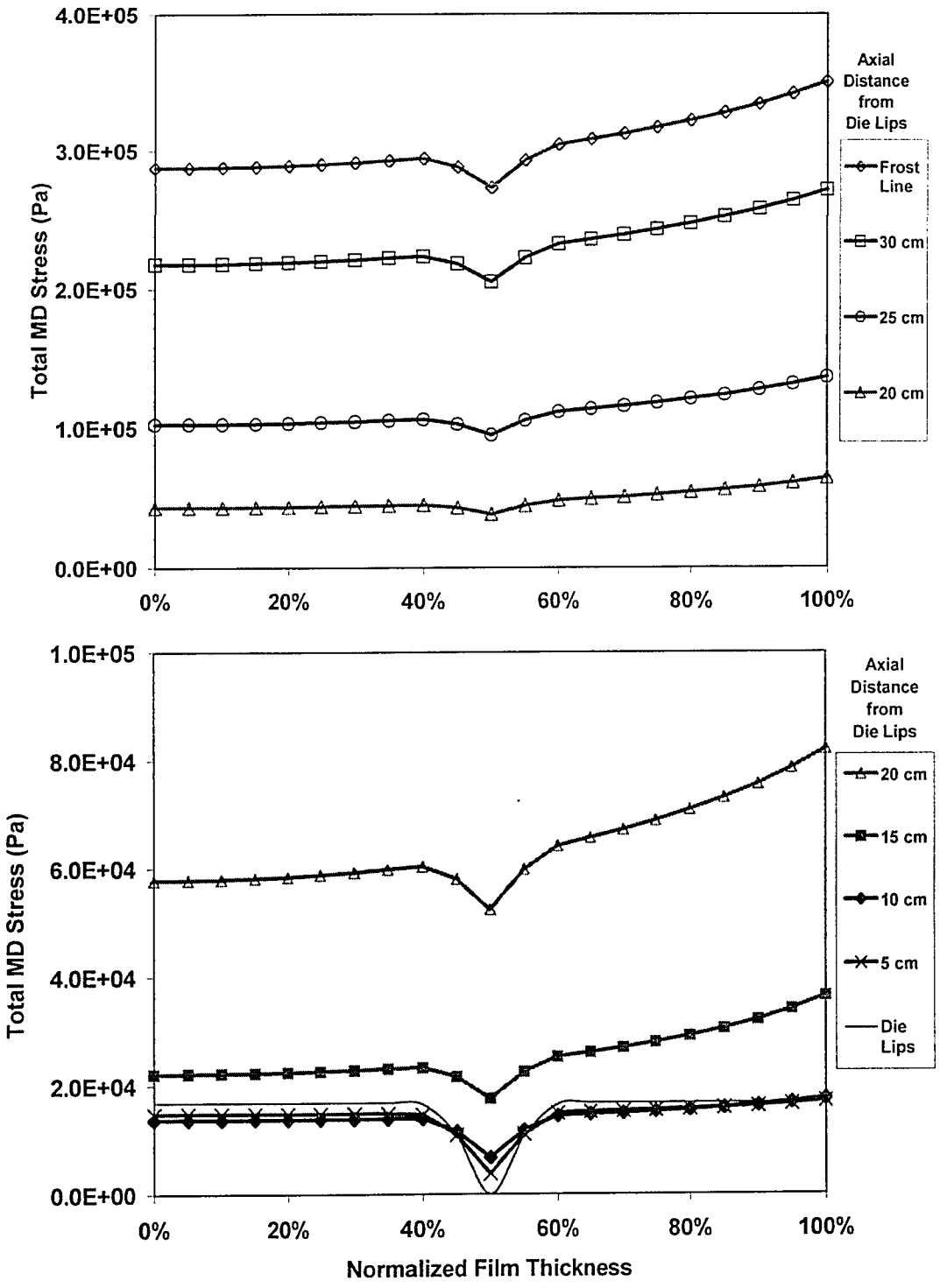

Figure 95: MD stress profiles in the film thickness direction at the increased production rate of 20kg/hr, shown at increasing axial distances (494 LDPE)

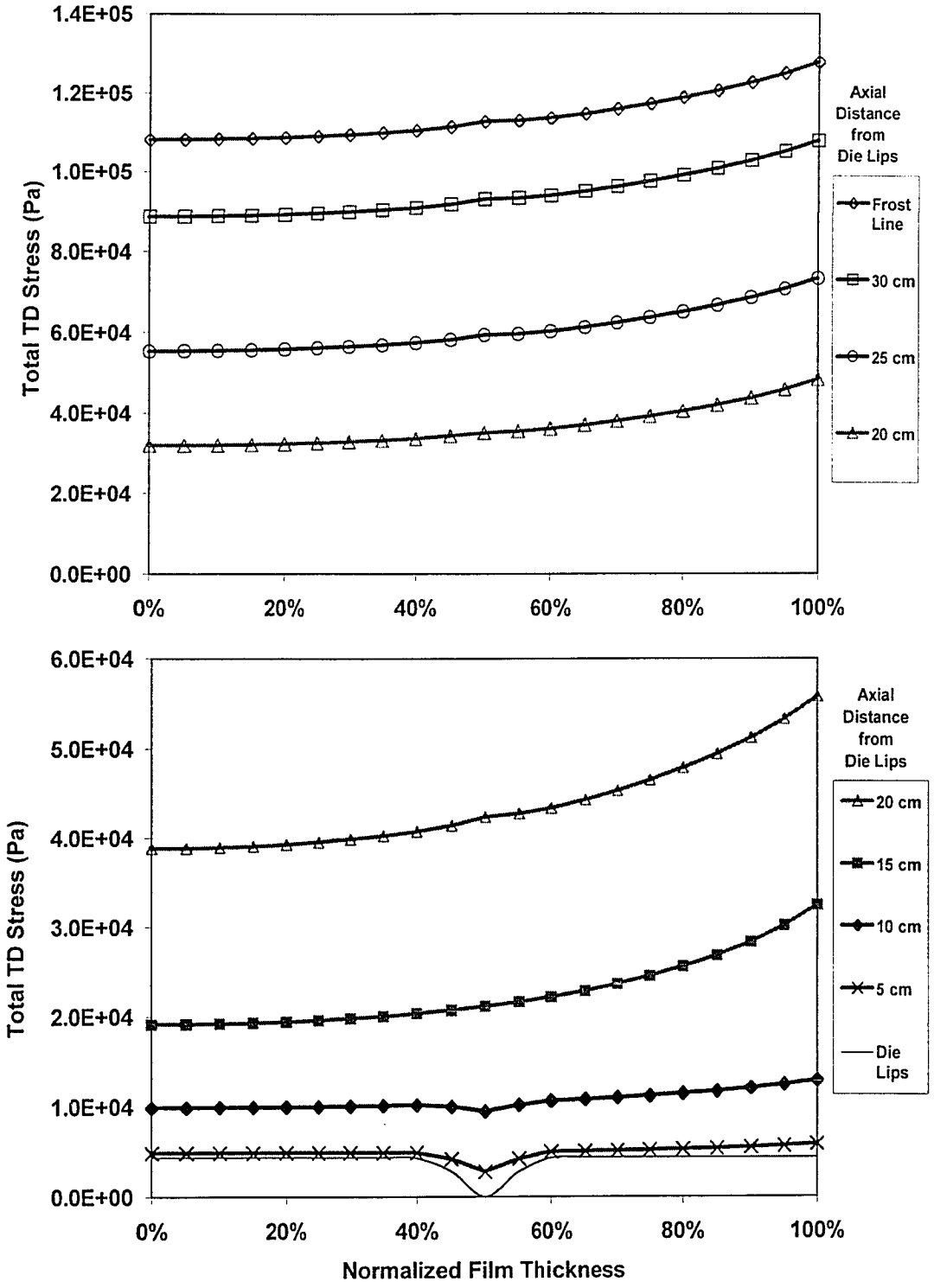

Figure 96: TD stress profiles in the film thickness direction at the increased production rate of 20kg/hr, shown at increasing axial distances (494 LDPE)

5.5.3. Stress Prediction for Bubbles Equipped With Internal Bubble Cooling (IBC)

Simulations have been performed using the temperature profiles that were calculated for the internally assisted (IBC) bubble cooling. The temperature profiles used in the simulation have already been presented in section 4.4 and are illustrated in figures 71 and 72. Temperature gradients in the thickness direction are less pronounced when IBC is present, since the heat is removed from both surfaces. When compared to the cooling simulations without IBC, the temperature variations between layers are much smaller. Also, the temperature gradients vanish faster when IBC is present.

Without going into further detail, the stress simulations showed stress gradients similar in development to the stresses presented so far, but with the stresses values increased (due to the 10% increase in production rate allowed by the IBC) and the stress differences in the thickness direction somehow reduced. Figures 97 and 98 show the MD and TD stress development in the thickness direction for the Dowlex 2078 LLDPE at production rate of 11kg/hr (the figures can be directly compared with figures 87 and 88).

The results verify the empirically known fact that the introduction of IBC in an existing line is very likely to alter the properties of the final film product.

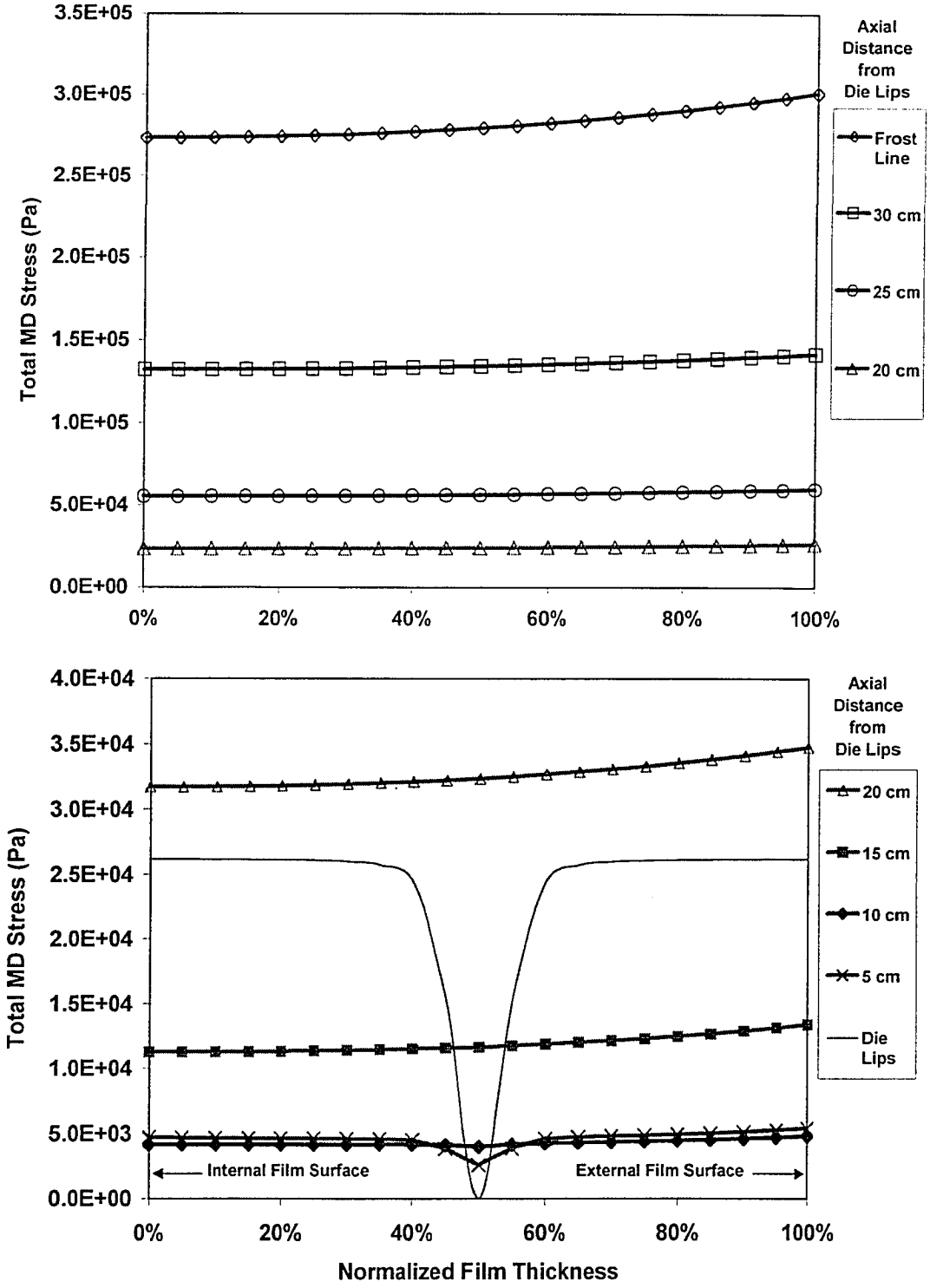

Figure 97: MD stress profiles in the film thickness direction for a bubble with IBC assisted cooling (2078 LLDPE, at 11 kg/hr)

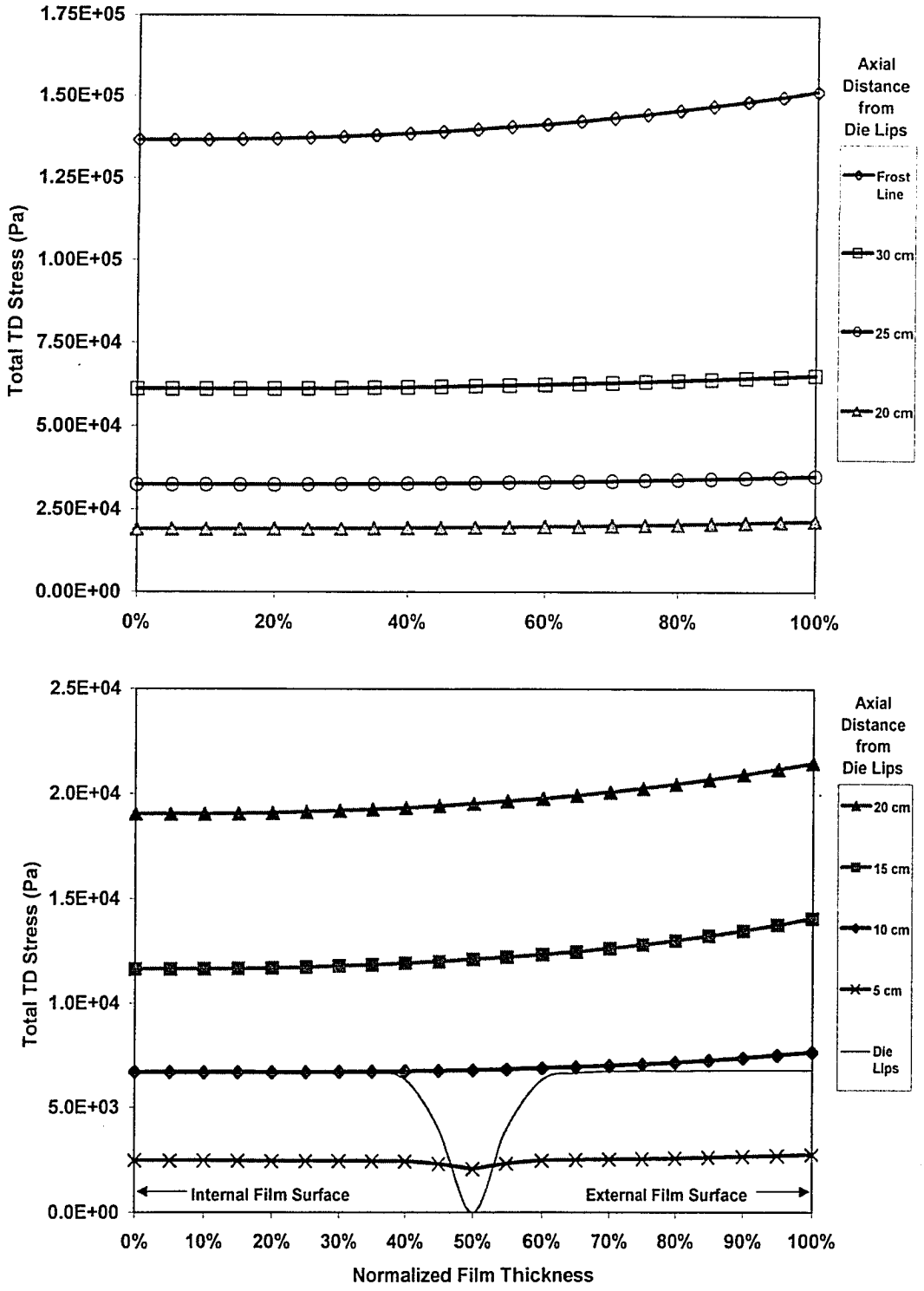

Figure 98: TD stress profiles in the film thickness direction for a bubble with IBC assisted cooling (2078 LLDPE, at 11 kg/hr)

5.6. Assessment of Stress Calculations

The stress profiles in the axial and *normal* film directions that are shown in the current chapter, have been calculated using the PTT (Phan-Thien & Tanner) viscoelastic model. A detailed evaluation of the usefulness of the PTT model for film blowing predictions has already been performed in the literature [Tas, 1994].

In his Ph.D. thesis, Tas [1994] tested the predictions of many viscoelastic models[1] against experimental film blowing data. The PTT model was found to be the most accurate of all the models (integral models included) in predicting both the final (frost line) film stresses, as well as the stress histories from the die to the frost line. Additionally, the PTT model has been consistently shown to be a good choice for predictions in processes that are dominated by extensional deformations (for example fiber spinning) and a less successful choice for shear dominated flows. Taking into consideration that film blowing is a shear-free, biaxial extension of the polymer membrane, the choice of the PTT model was judged to be the best possible alternative. As shown in section 5.3, careful steps were taken in the characterization of the materials to obtain the most accurate values of the model constants.

---

[1] Wagner, Giesekus, Phan-Thien-Tanner (PTT) and Leonov models were used to evaluate an assortment of experimental data, including film kinematics and stresses.

5.7. Film Properties and Crystallinity Considerations

The stress simulations that are presented in the current work provide indirect information on the properties of the final film products and their dependence on the processing conditions. The correlation between the molecular orientation (and therefore the frozen-in stresses[1]) and the properties of blown film products has been examined by various researchers.

Kanai [1987] suggested that the frozen-in film stresses might be related to the properties of the film and that films would have identical properties (regardless of processing conditions) provided that the have same frozen-in stresses. Similar theories on the film properties have also been proposed, but most of them have not been confirmed by experimental data.

Tas [1994] tested experimentally different polyethylene films, using an assortment of polymers and processing conditions. He concluded that LDPE and LLDPE film properties (MD tensile strength, MD elongation at break, yield stress, and the Trouser tear resistance) are dependent on the frozen-in stresses (at the frost line) and that equal stresses generally resulted in equal properties (regardless of the type of LDPE, die geometry, film thickness and processing conditions).

---

[1] For almost all blown films stresses are low enough for the stress-optical law to apply and therefore stress can be seen as a direct measure of the molecular orientation

The importance of the frozen-in stresses in the development and orientation of the film (and consequently the film properties) is widely accepted by researchers. In the current simulation results, the frozen-in (frost line) stress variations in the thickness direction have been shown to be present, ranging in the range of the 10 to 20%.

These range of stress variations could be thought small and negligible had it not been for the fact that the overwhelming majority of the commercially produced blown film is made using semi-crystalline polymeric materials. For these materials, the morphology of the crystalline structure (which is developed at the frost line region) and the ratio between the crystalline and amorphous phases are of paramount importance for the properties of the manufactured film[1]. Additionally, it has been proposed that both the development and the morphology of the crystalline phase are directly related to the stresses and orientation at the frost line.

A detailed description of the influence of film orientation on the crystallization kinetics is given by Ziabicki & Jarecki [1985]. They concluded that it should be reasonable to present the thermodynamics and kinematics of crystallization in terms of the applied film stress at the frost line.

---

[1] In fact small crystallinity variations can cause significant modifications in the properties of the film

By using LDPE experiments Kwack et al [1988] concluded that the MD stress at the frost line was affecting the crystalline axis orientation and that the film anisotropy as well as the crystalline texture were related to the stress ratio (MD stress/TD stress). A considerable number of studies that illustrate the effect of molecular orientation on the crystallization (for film blowing and fiber spinning) are reviewed by White & Cakmak [1986].

The inclusion of the crystallization kinetics in the context of the results of the present work, would allow the evaluation the importance of the thickness direction stress gradients under a new perspective. It is possible that the structure development and morphology of the crystalline phase can be significantly altered even by the presence of such (relatively small) stress variations.

This conclusion is supported by the fact that the crystallization of polyolefins has been shown to be relatively sensitive to very small orientations in the melt. For example, Lagasse & Maxwell [1976] conducted experiments using a variety of polyethylenes and reported that, at deformation rates of 10 s^{-1}, the crystallization induction time reduced by a factor of 100.

5.8. NOMENCLATURE FOR CHAPTER 5

θ : slope of bubble profile	Y : stress trace function
ε : trace function constant	z : axial distance from the die
$\dot{\varepsilon}$: rate of extension	ΔP : inflation pressure
$C_{1,2}$: WLF model constants	$\dot{\gamma}$: rate of deformation tensor
F_{Total}: total force on film bubble	η' : dynamic viscosity
g : relaxation strength	η_o : zero shear viscosity
G′ : storage modulus	λ : relaxation time
G″ : loss modulus	ξ : PTT model constant
h : film thickness	ρ_m : MD bubble curvature
h_o : spiral die gap	ρ_t : TD bubble curvature
R : bubble radius	$\boldsymbol{\sigma}$: total stress tensor
T : temperature	$\boldsymbol{\tau}$: extra stress tensor
V : film velocity	ω : angular velocity

Subscripts *m*, *t* and *n* denote the machine, tangential and normal directions respectively.

For tensors the index notation is m ≡ 11, n ≡ 22 and t ≡ 33

(for example $\sigma_m \equiv \sigma_{11}$, $\tau_n \equiv \tau_{22}$, etc.)

Subscript *eq* denotes "equivalent" stress

MD and TD denote "machine" and "tangential" directions respectively

CHAPTER 6.

CONCLUSIONS AND RECOMMENDATIONS

6.1. CONCLUDING REMARKS

Progress in blown film technology has been primarily driven by technological developments in materials and equipment, rather than advances in modeling. The situation is slowly improving in recent years, as spiral die and extruder design is increasingly aided by simulation modeling. However, the design and operation of the bubble cooling systems (air-rings, IBC systems etc.) is still an empirical process, where tweaking of the equipment is necessary for successful blown film production. Empirical methodologies are also used in the optimization and control of the cooling system. The present work proposes a methodology which can be used to achieve a better understanding and validation of bubble cooling equipment.

The simulation results illustrate the significant differences between single and dual orifice air-rings. Single orifice air-rings are concentrating their cooling action low in the bubble and, subsequently, most of the film deformation occurs at reduced film temperatures. On the other hand, the use of a dual orifice air ring spreads the convective heat transfer over a larger area on the bubble.

The results also verify the well known fact that there is a fine balance between cooling and the forming-stability of the bubble, as gains in one area reduce the effectiveness of the other. Additionally, the presented results illustrate the complexity of the bubble cooling mechanisms and partially explain why increases in cooling capacity often cannot be achieved by simply increasing the airflow rate of an existing air-ring.

The dual orifice air-ring simulations suggest that minor changes in the air ring design may cause substantial differences in the local cooling and surface pressure profiles, which is in accordance with industrial production experience. It is suggested that the presence and intensity of the Coanda effect is strongly affected by minor design modifications. Therefore, the heat transfer capability of the cooling air stream may be influenced by often neglected details in the air-ring design.

Internal bubble cooling (IBC) introduces a new set of challenges for designers and operators of film blowing equipment. The present numerical simulation results may enable us to gain a better understanding of the mechanisms of internal cooling. Limitations in the air exchange and difficulties in achieving an balanced airflow are seldom a problem for external air-rings, but are major obstacles for IBC designers. It is suggested that numerical simulation may be helpful in the identification and solution of various problems in IBC design and operation.

In the molten bubble, the thickness direction temperature profiles have, thus far, been neglected by the vast majority of blown film researchers. Although a few researchers (Cao et al [1989] and Nagarajan [1996]) have identified the temperature differences and suggested that they may be important, not much consideration has been given to the fact. In the present work, it is suggested that the large cooling rates at the film surface (combined with the typically low thermal conductivity of polymers) lead to significant temperature differences between the internal and external film surfaces. Under conditions of increased film production, the temperature differences in the film thickness direction may grow to be very large and, therefore, significant from a design and modeling perspective.

The calculation of stress profiles in the thickness direction (combined with the high sensitivity that the crystalline growth rate and film structure have on the frost line stresses) indicates that the film may not be homogenous in the thickness direction. Since minor amorphous/crystalline structure differences between similar films may produce large variations of the film properties, it is suggested that the calculated stress variations may have a disproportionally high influence on the final film product.

6.2. SUMMARY OF CONTRIBUTIONS

As part of the present work several contributions were made and are summarized below,

- Identification of the Venturi and Coanda effects as a major characteristic of the cooling air stream. It is the first time that the Coanda effect has been studied in the context of the blown film process.
- Comparison of the performance of single and dual orifice air-rings using numerical simulation. Such studies have been carried out in the past by industry practitioners, but never before using simulation of turbulent airflow using the k-ε modeling
- Illustrations of the sensitivity of air-ring performance on small design and/or setup modifications. For the first time, numerical simulations have confirmed results known from industrial practice
- Simulation of IBC equipment, quantification of its performance and redesign to balance airflow. Illustration of the advantages and challenges introduced by IBC. The aerodynamics of internal bubble cooling have never been studied before in the open literature.
- Numerical simulation of the ensuing temperature profiles in the film thickness direction and evaluation of their importance in blown film cooling. So far, the issue has been neglected by the vast majority of researchers.

- Examination of the effect the temperature profiles have on the melt rheology (and consequently the final film stresses for two polymeric materials). And calculation of stress profiles in the thickness direction throughout the bubble (from the die lips to the frost line).

Apart from their theoretical significance, the above contributions help improve the understanding in the areas of equipment design and film properties prediction by means of numerical simulation.

6.3. Recommendations and Future Directions

Numerical simulation has provided useful insight on the performance and relative importance of various film blowing cooling equipment and mechanisms. An study involving a larger number of air-ring configurations and designs may be helpful in further advancing the understanding of the cooling mechanisms film blowing. The inclusion of dynamic effects (like shedding of vortexes) in the simulation may provide further insight on the process dynamics and stability. At the same time experiments can be performed on artificial "rigid body" bubbles, to validate the applicability of the simulations.

The properties of the final film product are strongly influenced by the frost line stresses (frozen-in stresses), the molecular orientation in the solid phase and the crystalline morphology of the film. In the present work, it has been conjectured that film morphology (and consequently the film properties) is likely to be affected by the predicted stress anisotropy in the thickness direction. A more detailed study on the issue, using crystallization modeling and morphology experiments may help increase our understanding of the subject.

6.4. Publications Resulting From the Present Work

Refereed Journals

- Sidiropoulos, V., and Vlachopoulos, J., "Temperature distributions in Blown Film Bubbles", in preparation
- Sidiropoulos, V., and Vlachopoulos, J., "Numerical Study of Internal Bubble Cooling (IBC) in Film Blowing", in preparation
- Sidiropoulos, V., and Vlachopoulos, J., "MD and TD Stress Calculations in Film Blowing", in preparation
- Sidiropoulos, V., and Vlachopoulos, J., "The Effects Of Dual-Orifice Air-Ring Design On Blown Film Cooling", *Polymer Engineering & Science*, **40**, pp. 1611-1618, 2000
- Sidiropoulos, V., and Vlachopoulos, J., "An Investigation of Venturi and Coanda Effects in Blown Film Cooling", *International Polymer Processing*, **15**, pp. 40-45, 2000
- Sidiropoulos, V., Wood, P. E., and Vlachopoulos, J., "The Aerodynamics of Cooling of Blown Film Bubbles", *Journal of Reinforced Plastics and Composites*, **18**, p. 529, 1999

APPENDIX A:

BUBBLE KINEMATICS USED IN SIMULATIONS

The following tables present the preset bubble kinematics for the three melt flowrates used in various parts of the present work. The bubble radius, estimated average temperature, film thickness, elapsed time of blowing and the meridional direction velocity (V_m) are plotted at various axial distances from the die.

Bubble kinematics for mass flowrate of 10 kg/hr

Axial Distance	Radius	Temperature	Thickness	Time	Velocity
cm	cm	°C	mm	s	cm/s
0	2.7	200.0	2	0	1.023
0.1658	2.704	198.7	1.986	0.1616	1.029
0.3317	2.708	197.6	1.972	0.3224	1.035
0.4975	2.712	196.6	1.959	0.4823	1.04
0.6633	2.716	195.6	1.945	0.6413	1.046
0.8291	2.72	194.7	1.932	0.7995	1.051
0.995	2.725	193.9	1.919	0.9569	1.057
1.161	2.729	193.1	1.906	1.113	1.063
1.327	2.733	192.3	1.893	1.269	1.068
1.492	2.737	191.6	1.88	1.424	1.074
1.658	2.742	190.9	1.867	1.578	1.079
1.824	2.746	190.3	1.855	1.731	1.085
1.99	2.75	189.6	1.842	1.884	1.091
2.156	2.755	189.0	1.83	2.036	1.096
2.322	2.759	188.3	1.818	2.187	1.102
2.487	2.764	187.7	1.806	2.337	1.107
2.653	2.768	187.2	1.793	2.486	1.113
2.819	2.773	186.6	1.781	2.635	1.119
2.985	2.778	186.0	1.77	2.783	1.124
3.151	2.783	185.5	1.758	2.93	1.13
3.317	2.789	184.9	1.746	3.077	1.135

3.482	2.794	184.4	1.734	3.222	1.141
3.648	2.8	183.9	1.722	3.367	1.146
3.814	2.807	183.4	1.71	3.512	1.151
3.98	2.814	182.9	1.698	3.656	1.157
4.146	2.822	182.4	1.686	3.799	1.162
4.312	2.83	181.9	1.674	3.942	1.167
4.477	2.84	181.5	1.661	4.084	1.171
4.643	2.85	181.0	1.649	4.225	1.176
4.809	2.862	180.6	1.636	4.366	1.18
4.975	2.875	180.1	1.623	4.507	1.185
5.141	2.889	179.6	1.609	4.647	1.189
5.307	2.905	179.1	1.596	4.787	1.192
5.472	2.922	178.7	1.582	4.927	1.196
5.638	2.942	178.3	1.567	5.066	1.199
5.804	2.963	177.9	1.552	5.206	1.202
5.97	2.986	177.5	1.537	5.345	1.204
6.136	3.011	177.1	1.522	5.484	1.206
6.302	3.038	176.7	1.505	5.623	1.208
6.467	3.067	176.3	1.489	5.762	1.21
6.633	3.098	175.9	1.472	5.902	1.212
6.799	3.131	175.6	1.455	6.041	1.213
6.965	3.165	175.2	1.438	6.181	1.215
7.131	3.202	174.9	1.42	6.321	1.216
7.296	3.24	174.5	1.401	6.46	1.217
7.462	3.28	174.0	1.383	6.601	1.218
7.628	3.322	173.6	1.364	6.741	1.219
7.794	3.364	173.1	1.345	6.881	1.221
7.96	3.408	172.7	1.326	7.022	1.222
8.126	3.453	172.2	1.307	7.162	1.224
8.291	3.498	171.7	1.288	7.302	1.226
8.457	3.545	171.2	1.269	7.443	1.229
8.623	3.592	170.6	1.249	7.583	1.232
8.789	3.639	170.1	1.23	7.723	1.235
8.955	3.687	169.6	1.211	7.862	1.238
9.121	3.734	169.1	1.191	8.001	1.242
9.286	3.782	168.6	1.172	8.14	1.247
9.452	3.83	168.1	1.153	8.278	1.252
9.618	3.879	167.6	1.133	8.416	1.257
9.784	3.927	167.1	1.114	8.553	1.263
9.95	3.975	166.6	1.095	8.689	1.27
10.11	4.023	166.1	1.076	8.825	1.277
10.28	4.071	165.6	1.057	8.96	1.284
10.44	4.12	165.1	1.038	9.094	1.292
10.61	4.168	164.7	1.019	9.227	1.301
10.77	4.217	164.2	1	9.359	1.31
10.94	4.266	163.7	0.9817	9.491	1.32
11.11	4.315	163.1	0.963	9.621	1.33
11.27	4.364	162.4	0.9445	9.751	1.341

11.44	4.413	161.8	0.926	9.88	1.352
11.6	4.463	161.2	0.9076	10	1.364
11.77	4.514	160.6	0.8893	10.13	1.377
11.94	4.565	160.0	0.871	10.25	1.39
12.1	4.616	159.4	0.8529	10.38	1.404
12.27	4.668	158.8	0.8349	10.5	1.418
12.43	4.721	158.2	0.8169	10.62	1.433
12.6	4.774	157.7	0.7991	10.74	1.449
12.76	4.828	157.1	0.7814	10.86	1.465
12.93	4.882	156.6	0.7638	10.98	1.482
13.1	4.938	156.1	0.7463	11.1	1.5
13.26	4.994	155.6	0.7289	11.22	1.518
13.43	5.051	155.1	0.7117	11.33	1.537
13.59	5.109	154.6	0.6947	11.44	1.557
13.76	5.168	154.1	0.6778	11.56	1.578
13.93	5.227	153.6	0.661	11.67	1.599
14.09	5.288	153.1	0.6444	11.78	1.622
14.26	5.349	152.6	0.6281	11.89	1.645
14.42	5.411	152.1	0.6119	11.99	1.669
14.59	5.474	151.6	0.5959	12.1	1.694
14.75	5.538	151.1	0.5801	12.2	1.72
14.92	5.603	150.7	0.5645	12.3	1.747
15.09	5.668	150.2	0.5492	12.41	1.775
15.25	5.735	149.7	0.5341	12.51	1.804
15.42	5.802	149.3	0.5192	12.6	1.835
15.58	5.87	148.8	0.5046	12.7	1.866
15.75	5.938	148.3	0.4902	12.8	1.898
15.92	6.007	147.9	0.4761	12.89	1.932
16.09	6.077	147.4	0.4623	12.98	1.967
16.25	6.148	147.0	0.4487	13.07	2.003
16.42	6.219	146.5	0.4354	13.16	2.041
16.58	6.29	146.0	0.4224	13.25	2.08
16.75	6.363	145.6	0.4097	13.34	2.12
16.91	6.435	145.2	0.3973	13.42	2.161
17.08	6.508	144.7	0.3852	13.5	2.205
17.25	6.581	144.2	0.3733	13.59	2.249
17.41	6.655	143.7	0.3618	13.67	2.295
17.58	6.729	143.3	0.3505	13.74	2.343
17.74	6.803	142.9	0.3396	13.82	2.392
17.91	6.878	142.4	0.3289	13.9	2.443
18.08	6.952	141.9	0.3186	13.97	2.495
18.24	7.027	141.5	0.3085	14.04	2.549
18.41	7.102	141.0	0.2987	14.11	2.605
18.57	7.177	140.6	0.2892	14.18	2.662
18.74	7.251	140.1	0.28	14.25	2.722
18.9	7.326	139.7	0.2711	14.31	2.783
19.07	7.401	139.2	0.2624	14.38	2.845
19.24	7.475	138.8	0.254	14.44	2.91

19.4	7.549	138.4	0.2459	14.5	2.977
19.57	7.624	137.9	0.2381	14.56	3.045
19.73	7.697	137.5	0.2305	14.62	3.115
19.9	7.771	137.0	0.2231	14.68	3.187
20.07	7.844	136.6	0.216	14.74	3.262
20.23	7.917	136.1	0.2091	14.79	3.338
20.4	7.989	135.6	0.2025	14.85	3.416
20.56	8.061	135.2	0.1961	14.9	3.496
20.73	8.132	134.8	0.1899	14.95	3.577
20.89	8.203	134.3	0.184	15	3.661
21.06	8.274	133.9	0.1782	15.05	3.747
21.23	8.343	133.5	0.1727	15.09	3.835
21.39	8.413	133.1	0.1674	15.14	3.925
21.56	8.481	132.6	0.1622	15.19	4.017
21.72	8.549	132.2	0.1573	15.23	4.111
21.89	8.616	131.7	0.1525	15.27	4.206
22.06	8.683	131.2	0.1479	15.32	4.304
22.22	8.748	130.7	0.1434	15.36	4.404
22.39	8.813	130.2	0.1392	15.4	4.505
22.55	8.878	129.6	0.1351	15.44	4.609
22.72	8.941	129.2	0.1311	15.47	4.714
22.88	9.003	128.6	0.1273	15.51	4.821
23.05	9.065	128.0	0.1237	15.55	4.93
23.22	9.126	127.5	0.1201	15.58	5.041
23.38	9.186	126.9	0.1167	15.62	5.153
23.55	9.245	126.5	0.1135	15.65	5.267
23.71	9.303	126.1	0.1103	15.68	5.383
23.88	9.36	125.6	0.1073	15.72	5.5
24.05	9.416	125.2	0.1044	15.75	5.619
24.21	9.472	124.8	0.1017	15.78	5.74
24.38	9.526	124.4	0.09898	15.81	5.861
24.54	9.579	124.0	0.0964	15.84	5.984
24.71	9.631	123.6	0.09393	15.87	6.108
24.87	9.682	123.4	0.09156	15.89	6.234
25.04	9.732	123.0	0.08928	15.92	6.36
25.21	9.781	122.6	0.08709	15.95	6.487
25.37	9.829	122.2	0.08498	15.98	6.616
25.54	9.876	121.8	0.08296	16.01	6.744
25.7	9.922	121.5	0.08103	16.03	6.874
25.87	9.967	121.1	0.07917	16.06	7.004
26.04	10.01	120.8	0.07738	16.08	7.134
26.2	10.05	120.5	0.07567	16.1	7.264
26.37	10.09	120.0	0.07403	16.13	7.394
26.53	10.13	119.7	0.07246	16.15	7.525
26.7	10.17	119.4	0.07096	16.17	7.655
26.86	10.21	119.1	0.06952	16.19	7.784
27.03	10.24	118.6	0.06814	16.22	7.913
27.2	10.28	118.3	0.06683	16.24	8.041

27.36	10.31	118.0	0.06557	16.26	8.167
27.53	10.35	117.7	0.06437	16.28	8.293
27.69	10.38	117.4	0.06323	16.3	8.417
27.86	10.41	117.1	0.06214	16.32	8.539
28.03	10.44	116.8	0.0611	16.34	8.659
28.19	10.47	116.5	0.06012	16.36	8.776
28.36	10.5	116.2	0.05919	16.38	8.892
28.52	10.52	115.9	0.0583	16.4	9.004
28.69	10.55	115.7	0.05747	16.41	9.113
28.85	10.57	115.4	0.05668	16.43	9.219
29.02	10.59	115.1	0.05594	16.45	9.321
29.19	10.62	114.8	0.05525	16.47	9.418
29.35	10.64	114.5	0.0546	16.49	9.512
29.52	10.65	114.4	0.054	16.5	9.601
29.68	10.67	114.0	0.05345	16.52	9.684
29.85	10.69	113.7	0.05294	16.54	9.763
30.02	10.7	113.6	0.05247	16.55	9.835
30.18	10.72	113.3	0.05205	16.57	9.902
30.35	10.73	113.0	0.05167	16.59	9.963
30.51	10.74	112.7	0.05134	16.61	10.01
30.68	10.75	112.5	0.05104	16.62	10.06
30.84	10.76	112.3	0.05079	16.64	10.1
31.01	10.77	112.1	0.05059	16.65	10.13
31.18	10.78	111.8	0.05042	16.67	10.16
31.34	10.78	111.6	0.05028	16.69	10.18
31.51	10.79	111.4	0.05019	16.7	10.2
31.67	10.79	111.1	0.05012	16.72	10.21
31.84	10.79	110.9	0.05008	16.74	10.22
32	10.79	110.7	0.05006	16.75	10.22
32.17	10.8	110.5	0.05005	16.77	10.22
32.34	10.8	110.3	0.05004	16.78	10.22
32.5	10.8	110.1	0.05004	16.8	10.22
32.67	10.8	109.8	0.05004	16.82	10.22
32.83	10.8	109.7	0.05004	16.83	10.22
33	10.8	109.4	0.05004	16.85	10.22

Bubble kinematics for mass flowrate of 20 kg/hr

Axial Distance	Radius	Temperature	Thickness	Time	Velocity
cm	cm	°C	mm	s	cm/s
0	2.7	200.0	2	0	2.047
0.1658	2.704	198.7	1.986	0.0808	2.059
0.3317	2.708	197.6	1.971	0.1611	2.071
0.4975	2.712	196.6	1.957	0.241	2.082
0.6633	2.716	195.6	1.943	0.3205	2.094
0.8291	2.72	194.7	1.929	0.3995	2.106
0.995	2.725	193.9	1.916	0.478	2.117
1.161	2.729	193.1	1.902	0.5562	2.129
1.327	2.733	192.3	1.889	0.6338	2.141
1.492	2.737	191.6	1.876	0.7111	2.153
1.658	2.741	190.9	1.863	0.788	2.164
1.824	2.746	190.3	1.85	0.8644	2.176
1.99	2.75	189.6	1.837	0.9404	2.188
2.156	2.755	189.0	1.824	1.016	2.2
2.322	2.759	188.3	1.812	1.091	2.211
2.487	2.764	187.7	1.799	1.166	2.223
2.653	2.768	187.2	1.787	1.241	2.235
2.819	2.773	186.6	1.774	1.315	2.246
2.985	2.778	186.0	1.762	1.388	2.258
3.151	2.783	185.5	1.75	1.461	2.27
3.317	2.788	184.9	1.738	1.534	2.281
3.482	2.794	184.4	1.726	1.607	2.292
3.648	2.8	183.9	1.714	1.679	2.304
3.814	2.806	183.4	1.701	1.751	2.315
3.98	2.813	182.9	1.689	1.823	2.326
4.146	2.821	182.4	1.677	1.894	2.336
4.312	2.83	181.9	1.664	1.965	2.347
4.477	2.839	181.5	1.652	2.035	2.357
4.643	2.85	181.0	1.639	2.106	2.366
4.809	2.861	180.6	1.626	2.176	2.375
4.975	2.875	180.1	1.613	2.246	2.384
5.141	2.889	179.6	1.599	2.315	2.392
5.307	2.905	179.1	1.585	2.385	2.4
5.472	2.923	178.7	1.571	2.454	2.407
5.638	2.942	178.3	1.556	2.524	2.414
5.804	2.963	177.9	1.541	2.593	2.42
5.97	2.986	177.5	1.526	2.662	2.425
6.136	3.011	177.1	1.51	2.731	2.43
6.302	3.038	176.7	1.494	2.8	2.435
6.467	3.067	176.3	1.478	2.869	2.438
6.633	3.098	175.9	1.461	2.938	2.442
6.799	3.131	175.6	1.444	3.008	2.445
6.965	3.166	175.2	1.426	3.077	2.448

7.131	3.203	174.9	1.408	3.146	2.451
7.296	3.241	174.5	1.39	3.216	2.454
7.462	3.281	174.0	1.371	3.285	2.456
7.628	3.322	173.6	1.353	3.355	2.459
7.794	3.365	173.1	1.334	3.424	2.463
7.96	3.409	172.7	1.315	3.494	2.466
8.126	3.454	172.2	1.296	3.563	2.47
8.291	3.499	171.7	1.276	3.633	2.475
8.457	3.545	171.2	1.257	3.702	2.48
8.623	3.592	170.6	1.238	3.772	2.486
8.789	3.639	170.1	1.218	3.841	2.492
8.955	3.687	169.6	1.199	3.91	2.5
9.121	3.735	169.1	1.18	3.979	2.508
9.286	3.783	168.6	1.161	4.048	2.518
9.452	3.831	168.1	1.141	4.116	2.528
9.618	3.879	167.6	1.122	4.184	2.539
9.784	3.927	167.1	1.103	4.252	2.552
9.95	3.975	166.6	1.084	4.32	2.565
10.11	4.023	166.1	1.065	4.387	2.579
10.28	4.072	165.6	1.046	4.454	2.595
10.44	4.12	165.1	1.027	4.52	2.611
10.61	4.169	164.7	1.008	4.586	2.629
10.77	4.217	164.2	0.9898	4.651	2.648
10.94	4.266	163.7	0.9712	4.716	2.668
11.11	4.315	163.1	0.9526	4.781	2.688
11.27	4.365	162.4	0.9342	4.845	2.711
11.44	4.415	161.8	0.9158	4.909	2.734
11.6	4.465	161.2	0.8975	4.972	2.758
11.77	4.515	160.6	0.8793	5.034	2.784
11.94	4.566	160.0	0.8612	5.096	2.81
12.1	4.618	159.4	0.8432	5.158	2.838
12.27	4.67	158.8	0.8253	5.219	2.868
12.43	4.723	158.2	0.8074	5.279	2.898
12.6	4.777	157.7	0.7897	5.339	2.93
12.76	4.831	157.1	0.7721	5.398	2.963
12.93	4.886	156.6	0.7546	5.457	2.998
13.1	4.942	156.1	0.7373	5.515	3.034
13.26	4.998	155.6	0.7201	5.572	3.071
13.43	5.056	155.1	0.703	5.629	3.11
13.59	5.114	154.6	0.6861	5.685	3.15
13.76	5.173	154.1	0.6693	5.741	3.192
13.93	5.233	153.6	0.6527	5.796	3.236
14.09	5.294	153.1	0.6362	5.85	3.282
14.26	5.355	152.6	0.62	5.903	3.329
14.42	5.418	152.1	0.6039	5.956	3.378
14.59	5.481	151.6	0.5881	6.008	3.429
14.75	5.545	151.1	0.5724	6.06	3.482
14.92	5.611	150.7	0.557	6.111	3.537

15.09	5.676	150.2	0.5418	6.161	3.594
15.25	5.743	149.7	0.5268	6.21	3.653
15.42	5.811	149.3	0.5121	6.259	3.714
15.58	5.879	148.8	0.4976	6.306	3.778
15.75	5.948	148.3	0.4834	6.354	3.844
15.92	6.017	147.9	0.4695	6.4	3.912
16.09	6.087	147.4	0.4558	6.446	3.983
16.25	6.158	147.0	0.4424	6.49	4.057
16.42	6.23	146.5	0.4292	6.534	4.133
16.58	6.301	146.0	0.4164	6.578	4.212
16.75	6.374	145.6	0.4038	6.62	4.294
16.91	6.447	145.2	0.3916	6.662	4.379
17.08	6.52	144.7	0.3796	6.703	4.466
17.25	6.594	144.2	0.3679	6.743	4.557
17.41	6.668	143.7	0.3565	6.783	4.65
17.58	6.742	143.3	0.3454	6.821	4.747
17.74	6.816	142.9	0.3346	6.859	4.847
17.91	6.891	142.4	0.324	6.896	4.95
18.08	6.966	141.9	0.3138	6.933	5.056
18.24	7.04	141.5	0.3039	6.968	5.166
18.41	7.115	141.0	0.2942	7.003	5.279
18.57	7.19	140.6	0.2848	7.037	5.396
18.74	7.265	140.1	0.2758	7.071	5.517
18.9	7.34	139.7	0.267	7.103	5.641
19.07	7.415	139.2	0.2584	7.135	5.768
19.24	7.489	138.8	0.2502	7.166	5.899
19.4	7.564	138.4	0.2422	7.197	6.034
19.57	7.638	137.9	0.2344	7.227	6.173
19.73	7.712	137.5	0.2269	7.256	6.316
19.9	7.785	137.0	0.2197	7.284	6.462
20.07	7.858	136.6	0.2127	7.312	6.613
20.23	7.931	136.1	0.2059	7.339	6.767
20.4	8.003	135.6	0.1994	7.365	6.925
20.56	8.075	135.2	0.1931	7.391	7.087
20.73	8.147	134.8	0.187	7.416	7.253
20.89	8.218	134.3	0.1812	7.441	7.424
21.06	8.288	133.9	0.1755	7.465	7.598
21.23	8.358	133.5	0.1701	7.488	7.776
21.39	8.427	133.1	0.1648	7.511	7.958
21.56	8.495	132.6	0.1598	7.533	8.144
21.72	8.563	132.2	0.1549	7.555	8.334
21.89	8.63	131.7	0.1502	7.576	8.528
22.06	8.696	131.2	0.1457	7.597	8.725
22.22	8.762	130.7	0.1413	7.617	8.927
22.39	8.827	130.2	0.1371	7.637	9.133
22.55	8.891	129.6	0.1331	7.656	9.342
22.72	8.954	129.2	0.1292	7.675	9.555
22.88	9.016	128.6	0.1254	7.693	9.771

23.05	9.078	128.0	0.1219	7.711	9.991
23.22	9.139	127.5	0.1184	7.729	10.21
23.38	9.198	126.9	0.1151	7.746	10.44
23.55	9.257	126.5	0.1119	7.762	10.67
23.71	9.315	126.1	0.1088	7.779	10.9
23.88	9.372	125.6	0.1058	7.795	11.14
24.05	9.428	125.2	0.103	7.81	11.38
24.21	9.483	124.8	0.1003	7.825	11.62
24.38	9.537	124.4	0.09764	7.84	11.86
24.54	9.59	124.0	0.09512	7.855	12.11
24.71	9.642	123.6	0.09269	7.869	12.36
24.87	9.693	123.4	0.09037	7.883	12.61
25.04	9.743	123.0	0.08813	7.896	12.87
25.21	9.791	122.6	0.08599	7.91	13.12
25.37	9.839	122.2	0.08393	7.923	13.38
25.54	9.886	121.8	0.08195	7.935	13.64
25.7	9.931	121.5	0.08005	7.948	13.9
25.87	9.976	121.1	0.07823	7.96	14.16
26.04	10.01	120.8	0.07649	7.972	14.42
26.2	10.06	120.5	0.07482	7.984	14.68
26.37	10.1	120.0	0.07322	7.995	14.94
26.53	10.14	119.7	0.07168	8.007	15.2
26.7	10.18	119.4	0.07022	8.018	15.46
26.86	10.21	119.1	0.06881	8.029	15.71
27.03	10.25	118.6	0.06747	8.039	15.97
27.2	10.29	118.3	0.06619	8.05	16.23
27.36	10.32	118.0	0.06496	8.06	16.48
27.53	10.35	117.7	0.0638	8.071	16.73
27.69	10.39	117.4	0.06268	8.081	16.97
27.86	10.42	117.1	0.06162	8.09	17.21
28.03	10.45	116.8	0.06062	8.1	17.45
28.19	10.47	116.5	0.05967	8.11	17.68
28.36	10.5	116.2	0.05876	8.119	17.9
28.52	10.53	115.9	0.05791	8.128	18.12
28.69	10.55	115.7	0.0571	8.138	18.34
28.85	10.58	115.4	0.05634	8.147	18.54
29.02	10.6	115.1	0.05563	8.156	18.74
29.19	10.62	114.8	0.05496	8.165	18.93
29.35	10.64	114.5	0.05434	8.173	19.11
29.52	10.66	114.4	0.05377	8.182	19.28
29.68	10.67	114.0	0.05324	8.191	19.44
29.85	10.69	113.7	0.05275	8.199	19.59
30.02	10.71	113.6	0.05231	8.208	19.73
30.18	10.72	113.3	0.0519	8.216	19.86
30.35	10.73	113.0	0.05155	8.224	19.97
30.51	10.74	112.7	0.05123	8.233	20.07
30.68	10.75	112.5	0.05096	8.241	20.16
30.84	10.76	112.3	0.05072	8.249	20.24

31.01	10.77	112.1	0.05053	8.257	20.3
31.18	10.78	111.8	0.05037	8.266	20.35
31.34	10.78	111.6	0.05025	8.274	20.39
31.51	10.79	111.4	0.05016	8.282	20.42
31.67	10.79	111.1	0.0501	8.29	20.44
31.84	10.79	110.9	0.05006	8.298	20.45
32	10.79	110.7	0.05004	8.306	20.45
32.17	10.8	110.5	0.05003	8.314	20.46
32.34	10.8	110.3	0.05002	8.322	20.46
32.5	10.8	110.1	0.05002	8.331	20.46
32.67	10.8	109.8	0.05002	8.339	20.46
32.83	10.8	109.7	0.05002	8.347	20.46
33	10.8	109.4	0.05002	8.355	20.46

Bubble kinematics for mass flowrate of 11 kg/hr

Axial Distance	Radius	Temperature	Thickness	Time	Velocity
cm	cm	°C	mm	s	cm/s
0	2.7	200.0	2	0	1.126
0.1658	2.704	198.7	1.986	0.1469	1.132
0.3317	2.708	197.6	1.972	0.2931	1.138
0.4975	2.712	196.6	1.959	0.4384	1.144
0.6633	2.716	195.6	1.945	0.583	1.151
0.8291	2.72	194.7	1.932	0.7267	1.157
0.995	2.725	193.9	1.918	0.8698	1.163
1.161	2.729	193.1	1.905	1.012	1.169
1.327	2.733	192.3	1.892	1.154	1.175
1.492	2.737	191.6	1.879	1.294	1.182
1.658	2.742	190.9	1.867	1.434	1.188
1.824	2.746	190.3	1.854	1.574	1.194
1.99	2.75	189.6	1.841	1.712	1.2
2.156	2.755	189.0	1.829	1.85	1.206
2.322	2.759	188.3	1.817	1.987	1.213
2.487	2.764	187.7	1.804	2.124	1.219
2.653	2.768	187.2	1.792	2.259	1.225
2.819	2.773	186.6	1.78	2.394	1.231
2.985	2.778	186.0	1.768	2.529	1.238
3.151	2.783	185.5	1.756	2.663	1.244
3.317	2.788	184.9	1.744	2.796	1.25
3.482	2.794	184.4	1.732	2.928	1.256
3.648	2.8	183.9	1.721	3.06	1.262
3.814	2.807	183.4	1.709	3.191	1.268
3.98	2.814	182.9	1.697	3.322	1.273
4.146	2.821	182.4	1.684	3.452	1.279
4.312	2.83	181.9	1.672	3.581	1.285
4.477	2.839	181.5	1.66	3.71	1.29
4.643	2.85	181.0	1.647	3.839	1.295
4.809	2.862	180.6	1.634	3.967	1.3
4.975	2.875	180.1	1.621	4.095	1.305
5.141	2.889	179.6	1.608	4.222	1.309
5.307	2.905	179.1	1.594	4.349	1.313
5.472	2.922	178.7	1.58	4.476	1.317
5.638	2.942	178.3	1.565	4.603	1.32
5.804	2.963	177.9	1.55	4.729	1.323
5.97	2.986	177.5	1.535	4.856	1.326
6.136	3.011	177.1	1.52	4.982	1.329
6.302	3.038	176.7	1.504	5.108	1.331
6.467	3.067	176.3	1.487	5.235	1.333
6.633	3.098	175.9	1.47	5.361	1.335
6.799	3.13	175.6	1.453	5.488	1.336
6.965	3.165	175.2	1.436	5.614	1.338

7.131	3.202	174.9	1.418	5.741	1.339
7.296	3.24	174.5	1.4	5.868	1.341
7.462	3.28	174.0	1.381	5.996	1.342
7.628	3.321	173.6	1.362	6.123	1.343
7.794	3.364	173.1	1.344	6.25	1.345
7.96	3.408	172.7	1.325	6.378	1.347
8.126	3.453	172.2	1.305	6.505	1.349
8.291	3.498	171.7	1.286	6.633	1.351
8.457	3.544	171.2	1.267	6.76	1.354
8.623	3.591	170.6	1.247	6.887	1.357
8.789	3.638	170.1	1.228	7.014	1.36
8.955	3.686	169.6	1.209	7.141	1.364
9.121	3.734	169.1	1.189	7.267	1.369
9.286	3.782	168.6	1.17	7.393	1.374
9.452	3.83	168.1	1.151	7.518	1.379
9.618	3.878	167.6	1.132	7.643	1.385
9.784	3.926	167.1	1.112	7.767	1.392
9.95	3.974	166.6	1.093	7.891	1.399
10.11	4.022	166.1	1.074	8.014	1.407
10.28	4.071	165.6	1.055	8.137	1.415
10.44	4.119	165.1	1.036	8.258	1.424
10.61	4.168	164.7	1.018	8.379	1.433
10.77	4.216	164.2	0.9988	8.499	1.444
10.94	4.265	163.7	0.9801	8.619	1.454
11.11	4.314	163.1	0.9615	8.737	1.466
11.27	4.363	162.4	0.9429	8.855	1.478
11.44	4.413	161.8	0.9245	8.971	1.49
11.6	4.463	161.2	0.9061	9.087	1.503
11.77	4.513	160.6	0.8878	9.202	1.517
11.94	4.564	160.0	0.8696	9.316	1.532
12.1	4.615	159.4	0.8515	9.428	1.547
12.27	4.667	158.8	0.8335	9.54	1.563
12.43	4.72	158.2	0.8156	9.651	1.579
12.6	4.773	157.7	0.7978	9.761	1.596
12.76	4.827	157.1	0.7801	9.869	1.614
12.93	4.882	156.6	0.7625	9.977	1.633
13.1	4.937	156.1	0.7451	10.08	1.653
13.26	4.993	155.6	0.7277	10.18	1.673
13.43	5.051	155.1	0.7105	10.29	1.694
13.59	5.108	154.6	0.6935	10.39	1.716
13.76	5.167	154.1	0.6766	10.49	1.739
13.93	5.227	153.6	0.6599	10.59	1.762
14.09	5.287	153.1	0.6434	10.69	1.787
14.26	5.349	152.6	0.627	10.79	1.813
14.42	5.411	152.1	0.6108	10.89	1.839
14.59	5.474	151.6	0.5949	10.98	1.867
14.75	5.538	151.1	0.5791	11.08	1.895
14.92	5.603	150.7	0.5636	11.17	1.925

15.09	5.668	150.2	0.5482	11.26	1.956
15.25	5.735	149.7	0.5332	11.35	1.988
15.42	5.802	149.3	0.5183	11.44	2.022
15.58	5.87	148.8	0.5037	11.53	2.056
15.75	5.938	148.3	0.4894	11.62	2.092
15.92	6.007	147.9	0.4753	11.7	2.129
16.09	6.077	147.4	0.4615	11.79	2.167
16.25	6.148	147.0	0.448	11.87	2.207
16.42	6.219	146.5	0.4347	11.95	2.249
16.58	6.291	146.0	0.4217	12.03	2.291
16.75	6.363	145.6	0.409	12.11	2.336
16.91	6.436	145.2	0.3966	12.18	2.381
17.08	6.509	144.7	0.3845	12.26	2.429
17.25	6.582	144.2	0.3727	12.33	2.478
17.41	6.656	143.7	0.3612	12.41	2.529
17.58	6.73	143.3	0.35	12.48	2.581
17.74	6.804	142.9	0.339	12.55	2.635
17.91	6.879	142.4	0.3284	12.62	2.691
18.08	6.953	141.9	0.318	12.68	2.749
18.24	7.028	141.5	0.308	12.75	2.808
18.41	7.103	141.0	0.2982	12.81	2.87
18.57	7.178	140.6	0.2887	12.87	2.933
18.74	7.252	140.1	0.2795	12.94	2.998
18.9	7.327	139.7	0.2706	13	3.066
19.07	7.402	139.2	0.262	13.05	3.135
19.24	7.476	138.8	0.2536	13.11	3.206
19.4	7.551	138.4	0.2455	13.17	3.279
19.57	7.625	137.9	0.2377	13.22	3.354
19.73	7.699	137.5	0.2301	13.28	3.432
19.9	7.772	137.0	0.2227	13.33	3.511
20.07	7.845	136.6	0.2157	13.38	3.593
20.23	7.918	136.1	0.2088	13.43	3.677
20.4	7.99	135.6	0.2022	13.48	3.763
20.56	8.062	135.2	0.1958	13.53	3.851
20.73	8.134	134.8	0.1896	13.57	3.941
20.89	8.205	134.3	0.1837	13.62	4.033
21.06	8.275	133.9	0.178	13.66	4.128
21.23	8.345	133.5	0.1724	13.7	4.224
21.39	8.414	133.1	0.1671	13.75	4.323
21.56	8.483	132.6	0.162	13.79	4.424
21.72	8.551	132.2	0.157	13.83	4.528
21.89	8.618	131.7	0.1523	13.87	4.633
22.06	8.684	131.2	0.1477	13.9	4.741
22.22	8.75	130.7	0.1432	13.94	4.85
22.39	8.815	130.2	0.139	13.98	4.962
22.55	8.879	129.6	0.1349	14.01	5.076
22.72	8.943	129.2	0.1309	14.05	5.192
22.88	9.005	128.6	0.1271	14.08	5.31

23.05	9.067	128.0	0.1235	14.11	5.429
23.22	9.128	127.5	0.12	14.15	5.551
23.38	9.187	126.9	0.1166	14.18	5.675
23.55	9.246	126.5	0.1133	14.21	5.801
23.71	9.305	126.1	0.1102	14.24	5.928
23.88	9.362	125.6	0.1072	14.27	6.057
24.05	9.418	125.2	0.1043	14.3	6.188
24.21	9.473	124.8	0.1015	14.32	6.32
24.38	9.527	124.4	0.09887	14.35	6.454
24.54	9.58	124.0	0.0963	14.38	6.589
24.71	9.633	123.6	0.09383	14.41	6.725
24.87	9.684	123.4	0.09146	14.43	6.863
25.04	9.734	123.0	0.08919	14.46	7.002
25.21	9.783	122.6	0.087	14.48	7.142
25.37	9.831	122.2	0.08491	14.5	7.283
25.54	9.878	121.8	0.08289	14.53	7.424
25.7	9.924	121.5	0.08096	14.55	7.566
25.87	9.968	121.1	0.0791	14.57	7.709
26.04	10.01	120.8	0.07733	14.59	7.852
26.2	10.05	120.5	0.07562	14.62	7.995
26.37	10.09	120.0	0.07399	14.64	8.138
26.53	10.13	119.7	0.07242	14.66	8.281
26.7	10.17	119.4	0.07092	14.68	8.424
26.86	10.21	119.1	0.06949	14.7	8.566
27.03	10.25	118.6	0.06811	14.72	8.707
27.2	10.28	118.3	0.0668	14.74	8.847
27.36	10.32	118.0	0.06555	14.76	8.986
27.53	10.35	117.7	0.06435	14.78	9.124
27.69	10.38	117.4	0.06321	14.79	9.26
27.86	10.41	117.1	0.06213	14.81	9.393
28.03	10.44	116.8	0.0611	14.83	9.525
28.19	10.47	116.5	0.06012	14.85	9.654
28.36	10.5	116.2	0.05919	14.86	9.78
28.52	10.52	115.9	0.05831	14.88	9.903
28.69	10.55	115.7	0.05748	14.9	10.02
28.85	10.57	115.4	0.0567	14.92	10.13
29.02	10.59	115.1	0.05596	14.93	10.24
29.19	10.62	114.8	0.05527	14.95	10.35
29.35	10.64	114.5	0.05463	14.96	10.45
29.52	10.65	114.4	0.05403	14.98	10.55
29.68	10.67	114.0	0.05348	15	10.64
29.85	10.69	113.7	0.05297	15.01	10.73
30.02	10.7	113.6	0.05251	15.03	10.81
30.18	10.72	113.3	0.05209	15.04	10.88
30.35	10.73	113.0	0.05172	15.06	10.94
30.51	10.74	112.7	0.05139	15.07	11
30.68	10.75	112.5	0.0511	15.09	11.05
30.84	10.76	112.3	0.05085	15.1	11.1

31.01	10.77	112.1	0.05064	15.12	11.14
31.18	10.78	111.8	0.05047	15.13	11.17
31.34	10.78	111.6	0.05034	15.15	11.19
31.51	10.79	111.4	0.05025	15.16	11.21
31.67	10.79	111.1	0.05018	15.18	11.22
31.84	10.79	110.9	0.05014	15.19	11.22
32	10.79	110.7	0.05012	15.21	11.23
32.17	10.8	110.5	0.05011	15.22	11.23
32.34	10.8	110.3	0.05011	15.24	11.23
32.5	10.8	110.1	0.05011	15.25	11.23
32.67	10.8	109.8	0.05011	15.27	11.23
32.83	10.8	109.7	0.05011	15.28	11.23
33	10.8	109.4	0.05011	15.29	11.23

APPENDIX B:

DIMENSIONS OF THE IBC EQUIPMENT

The dimensions of the IBC equipment are given below. The original and modified (with successive contractions) designs are presented

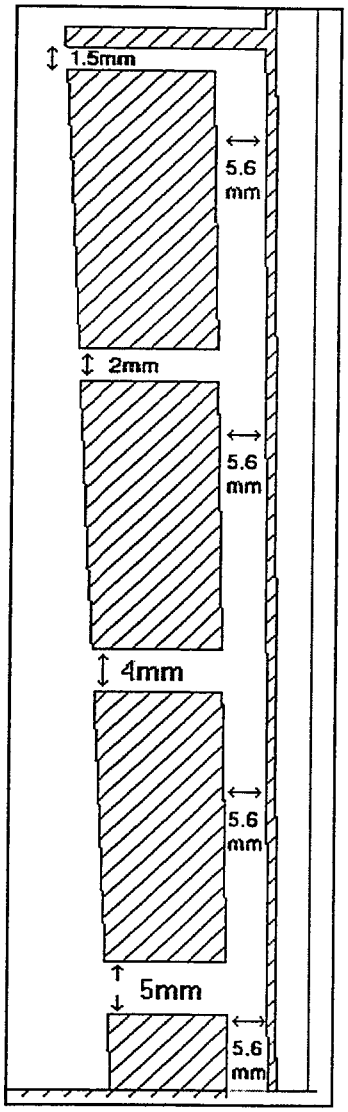

Original

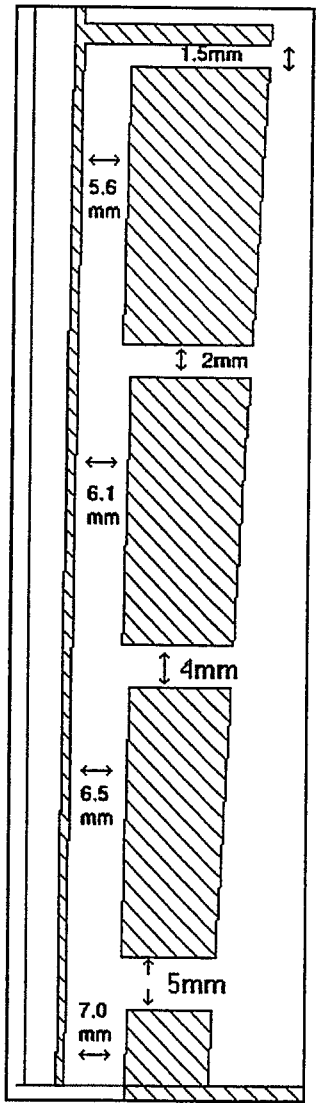

Modified

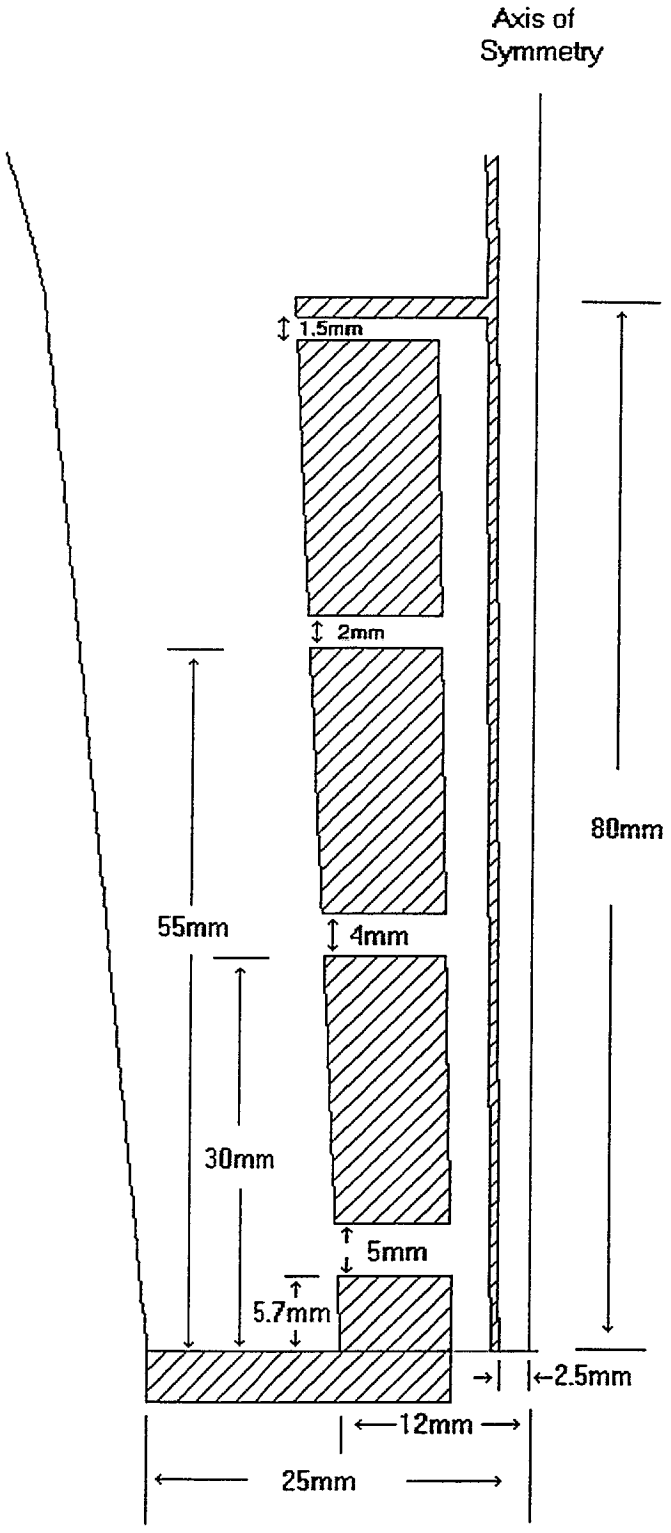

Original design

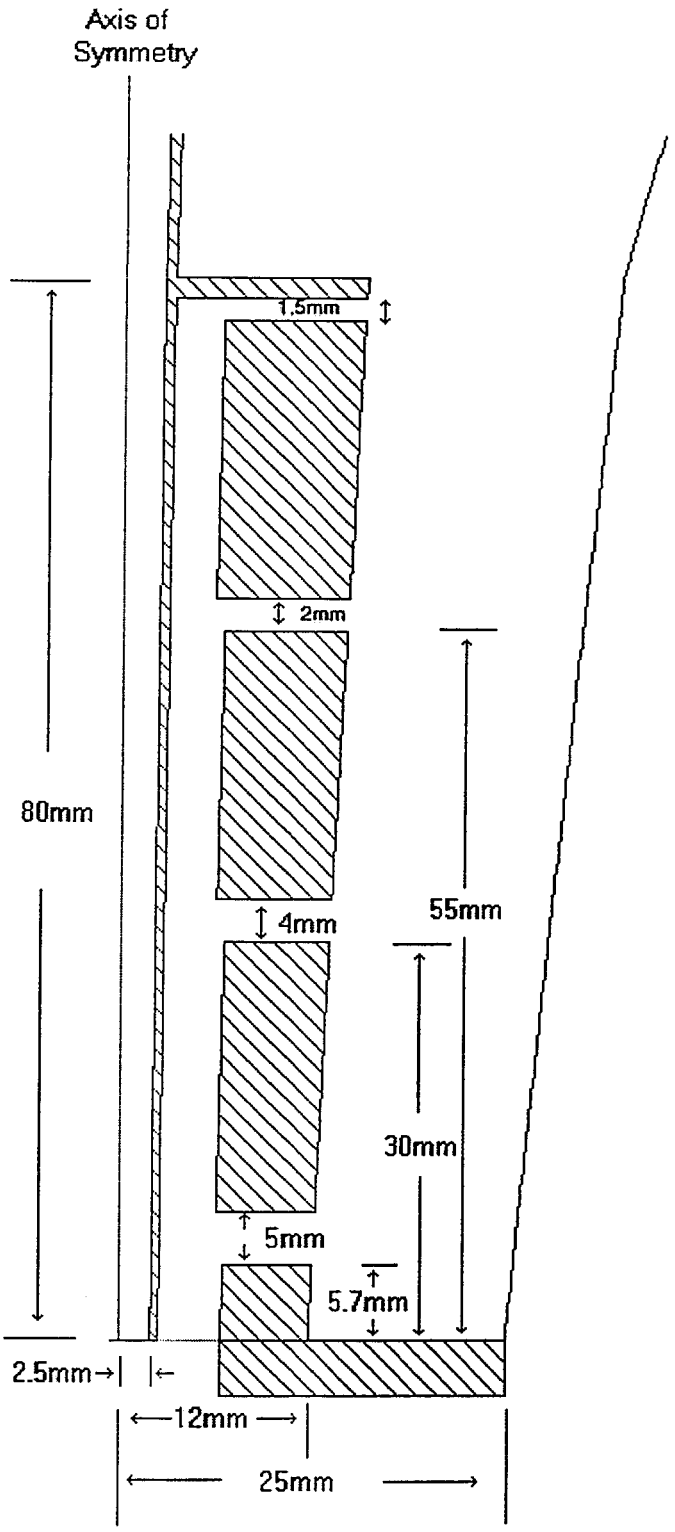

Modified design, with successive contractions of the inlet annulus

APPENDIX C:

EQUIVALENT STRESSES

FOR MULTI-LAYER THIN MEMBRANE

Definition

σ_{eq} ∴ the stress of a single layer membrane that would produce the same shape, curvatures and kinematics as the given multi-layer membrane

Assumptions

The weight of the film can be ignored

R>>h, (thin membrane approximation)

Purely extensional flow (no velocity gradients in the normal direction), local deformation rates are equal for all layers

Meridional (m) direction

The meridional stress σ_m at any position z is related to the local body force (Agassant et al, 1991)

$$F = 2\pi R h \sigma_m \cos\theta \qquad \text{(c-1)}$$

where R, h, σm and θ are varying with axial position.

According to the definition of *equivalent* stress, for a multi-layer film equation c-1 can be generalized:

$$F = 2\pi R h \sigma_{m,eq} \cos\theta \qquad \text{(c-2)}$$

Since h<<R, the force that each layer (i) exerts in the meridional direction can be expressed

$$F_i = 2\pi R h_i \sigma_{m,i} \cos\theta \qquad \text{(c-3)}$$

where h_i is the thickness and $\sigma_{m,i}$ the meridional stress of the layer.

If we sum equation c-3 for all layers we get,

$$\sum_i F_i = F = 2\pi R \cos\theta \sum_i \left(h_i \sigma_{m,i}\right) \qquad \text{(c-4)}$$

By combining equations c-2 and c-4, we get

$$\sigma_{m,eq} = \frac{1}{h}\sum_i \left(h_i \sigma_{m,i}\right) \qquad \text{(c-4)}$$

Tangential (t) direction

A similar procedure can be followed to derive the tangential direction (TD) *equivalent* stress, from the TD stresses of each layer.

The normal direction force balance on a small membrane element yields (Agassant et al, 1991)

$$F_n = A\Delta P = Ah\left(\frac{\sigma_m}{\rho_m} + \frac{\sigma_t}{\rho_t}\right) \qquad \text{(c-5)}$$

Equation c-5 can be generalized for more than one layers,

$$F_n = A\Delta P = Ah\left(\frac{\sigma_{m,eq}}{\rho_m} + \frac{\sigma_{t,eq}}{\rho_t}\right) \qquad \text{(c-6)}$$

where F_n is the force in the *normal* direction of the film element.

Assuming that the curvature of each layer is equal to the curvature of the membrane (valid since h<<R), we can write the normal force for each layer,

$$F_{n,i} = Ah_i\left(\frac{\sigma_{m,i}}{\rho_m} + \frac{\sigma_{t,i}}{\rho_t}\right) \qquad \text{(c-7)}$$

If we sum equation c-7 for all layers we get,

$$\sum_i F_{n,i} = A\sum_i\left(\frac{h_i\sigma_{m,i}}{\rho_m} + \frac{h_i\sigma_{t,i}}{\rho_t}\right) \qquad \text{(c-8)}$$

or

$$\sum_i F_{n,i} = F_n = \frac{A}{\rho_m}\sum_i\left(h_i\sigma_{m,i}\right) + \frac{A}{\rho_t}\sum_i\left(h_i\sigma_{t,i}\right) \qquad \text{(c-9)}$$

Combining equations c-6 and c-9 we get,

$$\frac{h\sigma_{m,eq}}{\rho_m} + \frac{h\sigma_{t,eq}}{\rho_t} = \frac{\sum_i\left(h_i\sigma_{m,i}\right)}{\rho_m} + \frac{\sum_i\left(h_i\sigma_{t,i}\right)}{\rho_t} \qquad \text{(c-10)}$$

Substituting c-4 into c-10 the meridional components vanish and we get

$$\sigma_{t,eq} = \frac{1}{h}\sum_i\left(h_i\sigma_{t,i}\right) \qquad \text{(c-11)}$$

APPENDIX D:

RELAXATION SPECTRA

Dowlex 2078 LLDPE

Discrete 5-mode relaxation spectra for all temperatures

190°C		180°C		170°C	
g_i (Pa)	λ_i (s)	g_i (Pa)	λ_i (s)	g_i (Pa)	λ_i (s)
306939.61	0.0059154	331211.4	0.0055225	331402.3	0.0071638
60768.707	0.0426642	73344.54	0.0365516	74584.302	0.0461377
14613.719	0.2279674	19905.974	0.1818755	21301.688	0.2116877
2551.6869	1.0948191	4026.4652	0.8675842	5117.7755	0.9236691
440.58222	6.1758915	687.23428	5.345	917.62058	6.0532236

160°C		150°C		140°C	
g_i (Pa)	λ_i (s)	g_i (Pa)	λ_i (s)	g_i (Pa)	λ_i (s)
355277.84	0.005902	352046.57	0.0059974	360132.81	0.0065794
93659.945	0.0402826	99358.972	0.0359277	110218.77	0.0418751
25215.283	0.2027969	34795.391	0.1573966	35727.029	0.2156536
6106.2066	0.8697136	9763.3057	0.7303525	7914.1926	1.1161971
1346.1056	5.01269	1736.4682	5.1095	1361.8556	7.0522468

135°C		130°C		125°C	
g_i (Pa)	λ_i (s)	g_i (Pa)	λ_i (s)	g_i (Pa)	λ_i (s)
357936.24	0.0068895	353697.96	0.0101984	391303.10	0.0075939
109077.87	0.0433194	94488.05	0.0951295	132542.15	0.0482558
38448.918	0.2077695	17789.65	0.7606821	46138.209	0.2453752
9310.97	1.1183217	2084.7012	6.9756279	11276.033	1.3234005
1439.2068	8.0242606	6.6398189	2.9510943	1975.3971	8.95263

122.5°C		120°C	
g_i (Pa)	λ_i (s)	g_i (Pa)	λ_i (s)
445964.39	0.00892057	843063.85	0.00875720
148176.64	0.06463662	319183.53	0.04553114
40552.333	0.37851298	157127.53	0.21843475
8944.7932	2.08794288	41590.804	1.34868192
1179.1520	12.3526029	6267.6169	10.5678

Measured values of the storage (G') and loss (G'') moduli and the discrete relaxation function fit (using the values shown above) are presented in the following figures for all the measured temperatures

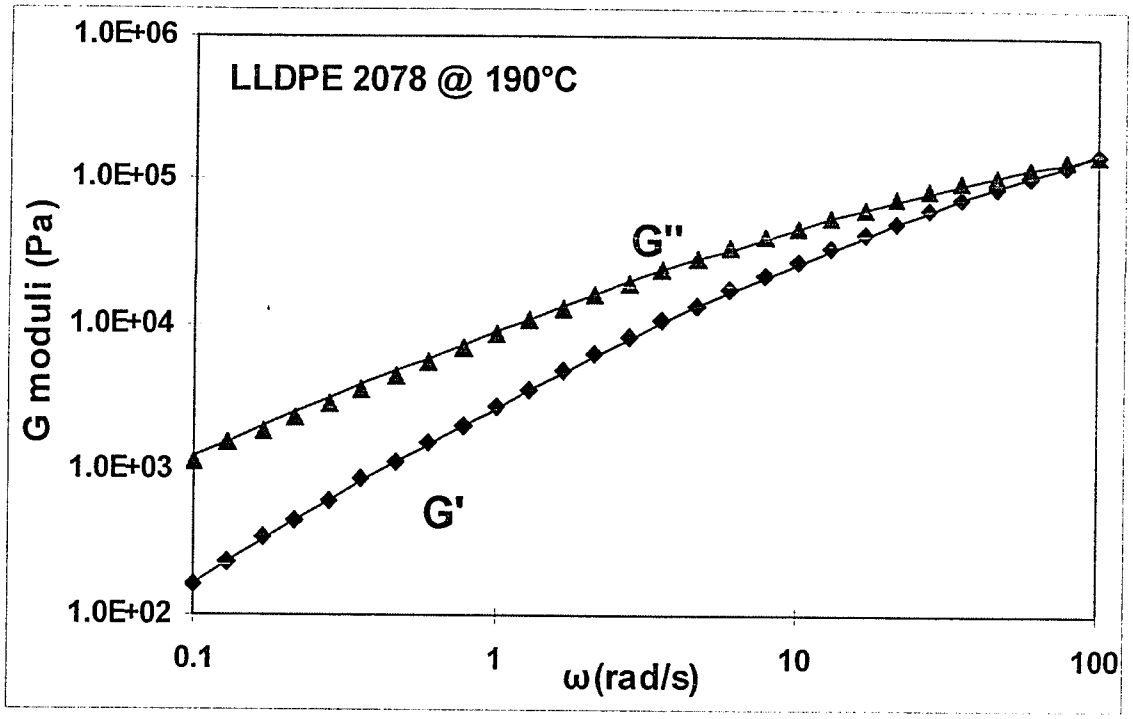
LLDPE 2078 @ 190°C
G moduli (Pa)
1.0E+06
1.0E+05
1.0E+04
1.0E+03
1.0E+02
G''
G'
0.1
1
10
100
ω(rad/s)

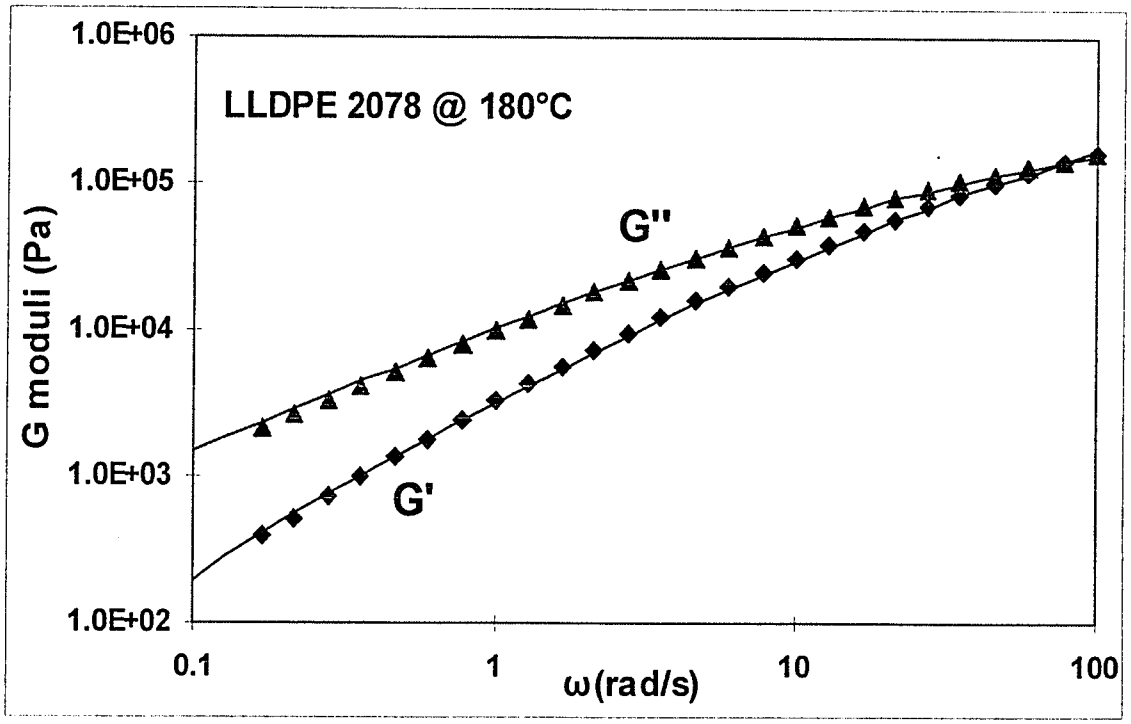
LLDPE 2078 @ 180°C
G moduli (Pa)
1.0E+06
1.0E+05
1.0E+04
1.0E+03
1.0E+02
G''
G'
0.1
1
10
100
ω(rad/s)

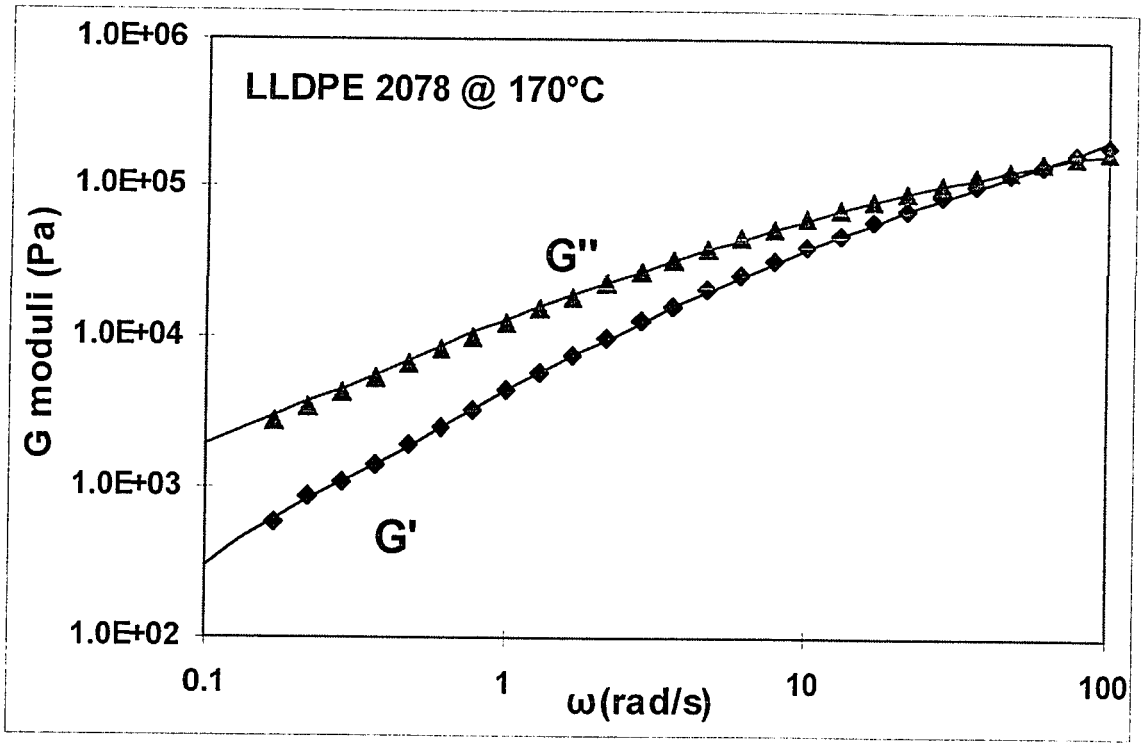
LLDPE 2078 @ 170°C
G moduli (Pa)
1.0E+06
1.0E+05
1.0E+04
1.0E+03
1.0E+02
G''
G'
0.1
1
10
100
ω(rad/s)

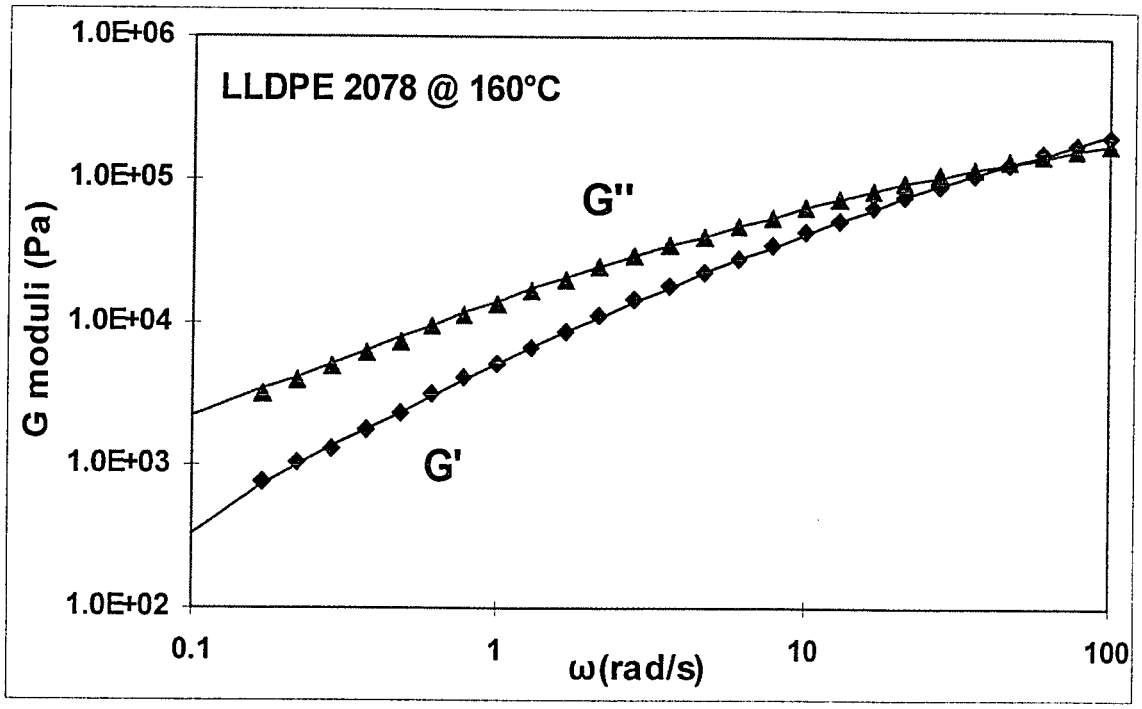
LLDPE 2078 @ 160°C
G moduli (Pa)
1.0E+06
1.0E+05
1.0E+04
1.0E+03
1.0E+02
G''
G'
0.1
1
10
100
ω(rad/s)

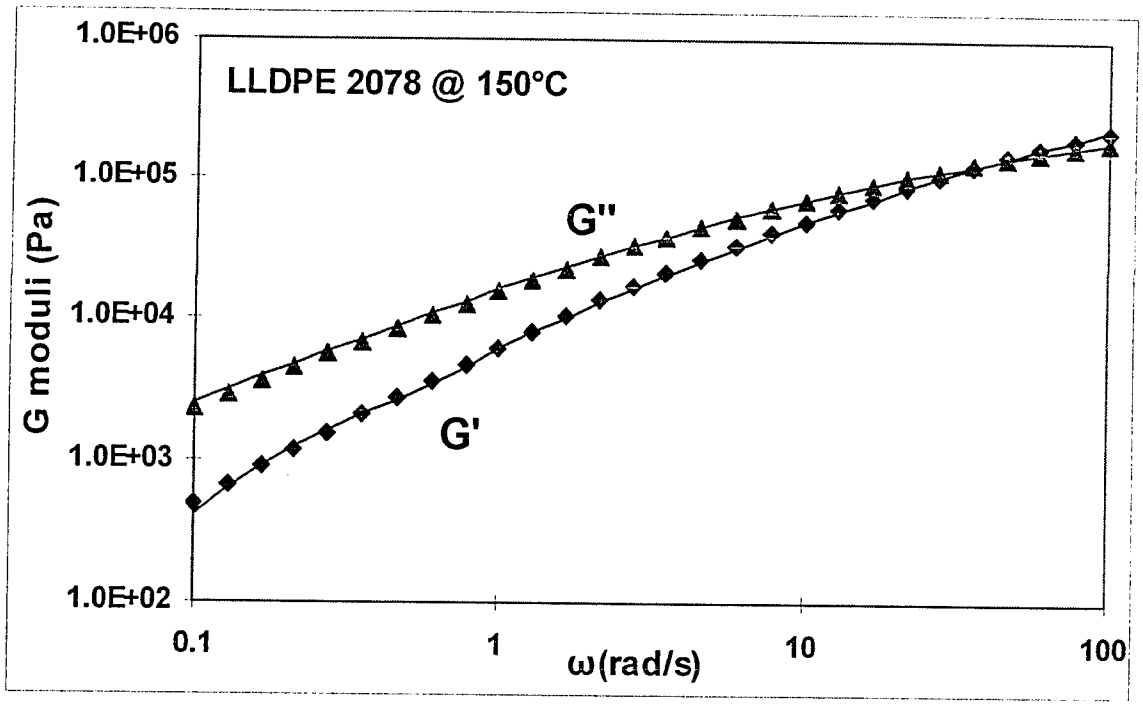
LLDPE 2078 @ 150°C
G" moduli (Pa)
1.0E+06
1.0E+05
1.0E+04
1.0E+03
1.0E+02
G"
G'
0.1
1
10
100
ω(rad/s)

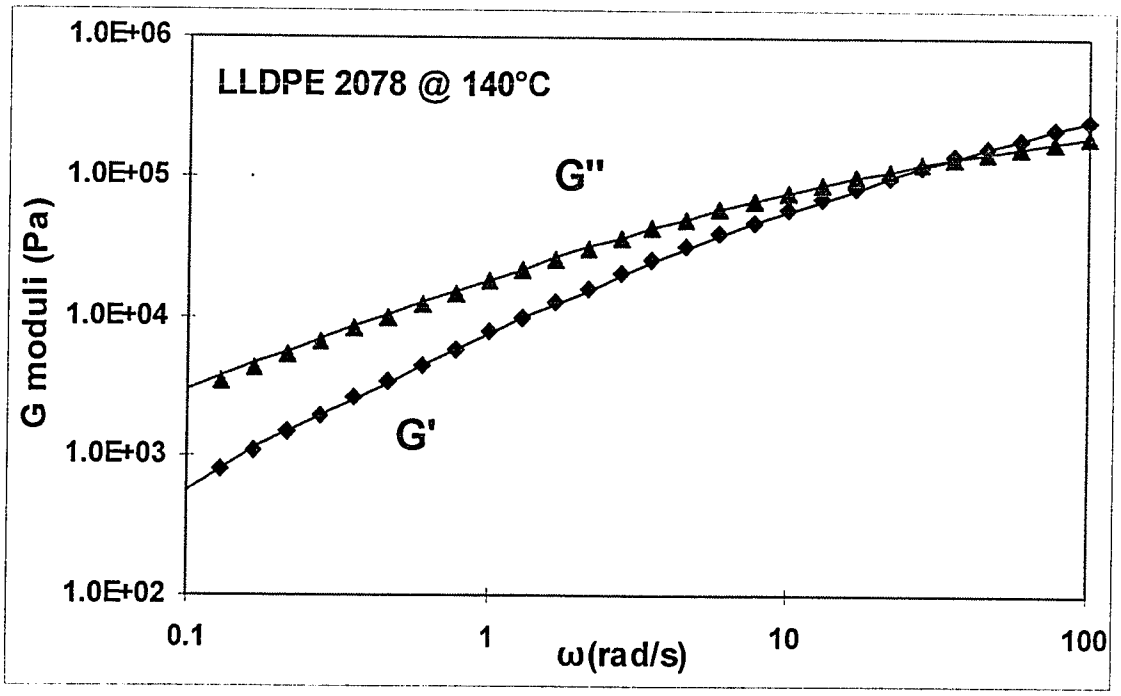
LLDPE 2078 @ 140°C
G" moduli (Pa)
1.0E+06
1.0E+05
1.0E+04
1.0E+03
1.0E+02
G"
G'
0.1
1
10
100
ω(rad/s)

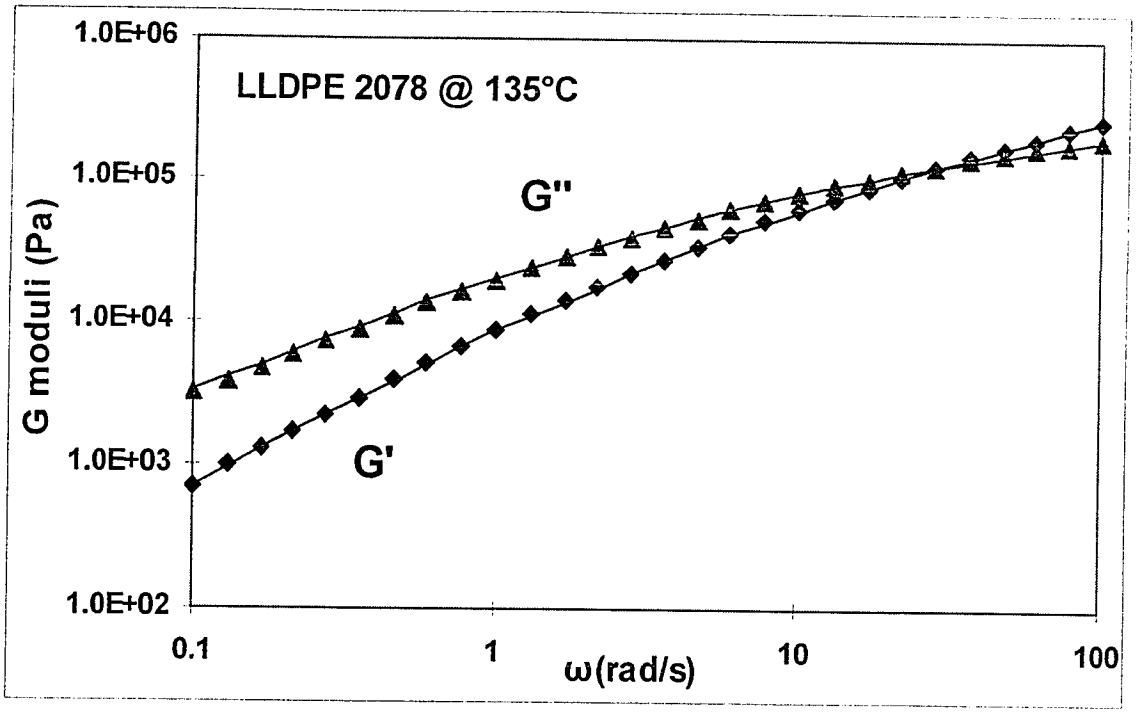
LLDPE 2078 @ 135°C
G"
G'
G moduli (Pa)
1.0E+06
1.0E+05
1.0E+04
1.0E+03
1.0E+02
0.1
1
10
100
ω(rad/s)

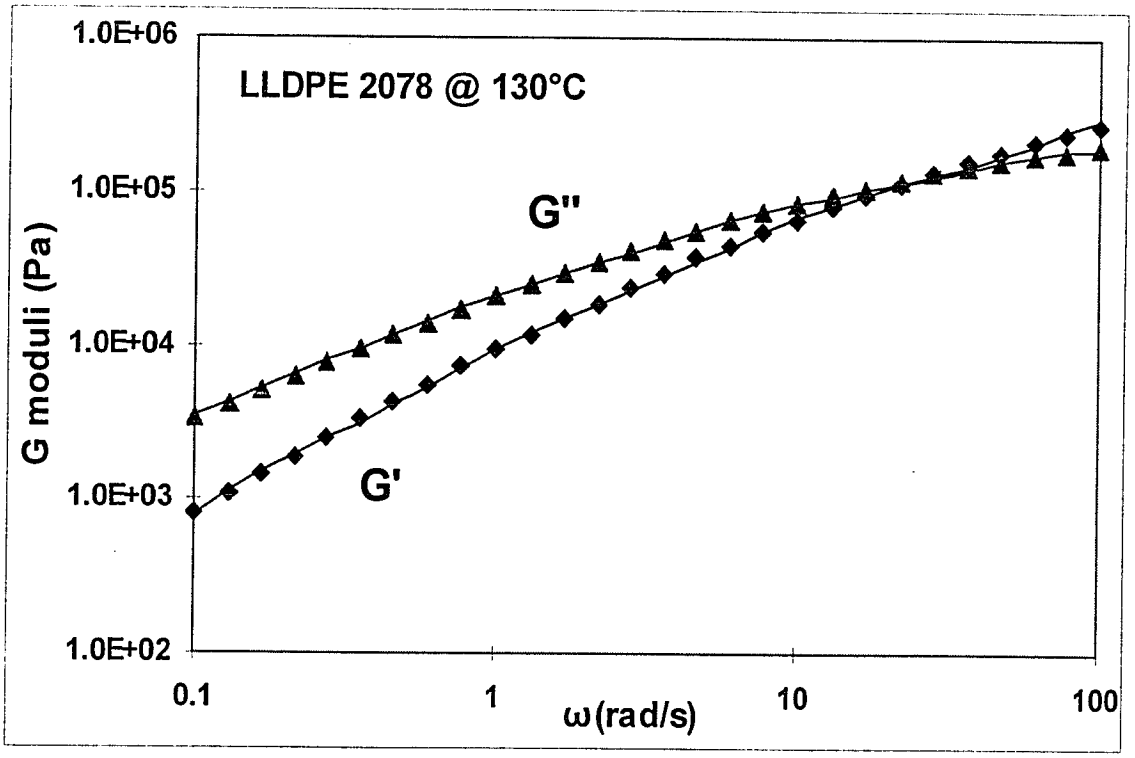
LLDPE 2078 @ 130°C
G"
G'
G moduli (Pa)
1.0E+06
1.0E+05
1.0E+04
1.0E+03
1.0E+02
0.1
1
10
100
ω(rad/s)

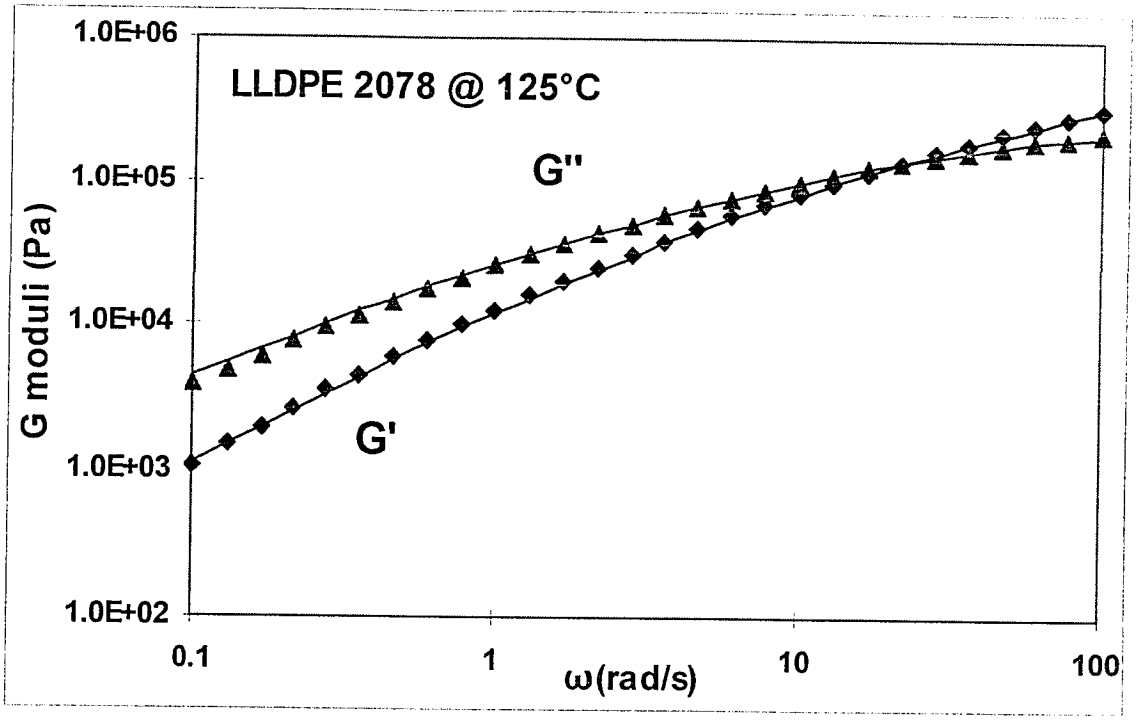
LLDPE 2078 @ 125°C
G''
G'
G moduli (Pa)
1.0E+06
1.0E+05
1.0E+04
1.0E+03
1.0E+02
0.1
1
10
100
ω(rad/s)

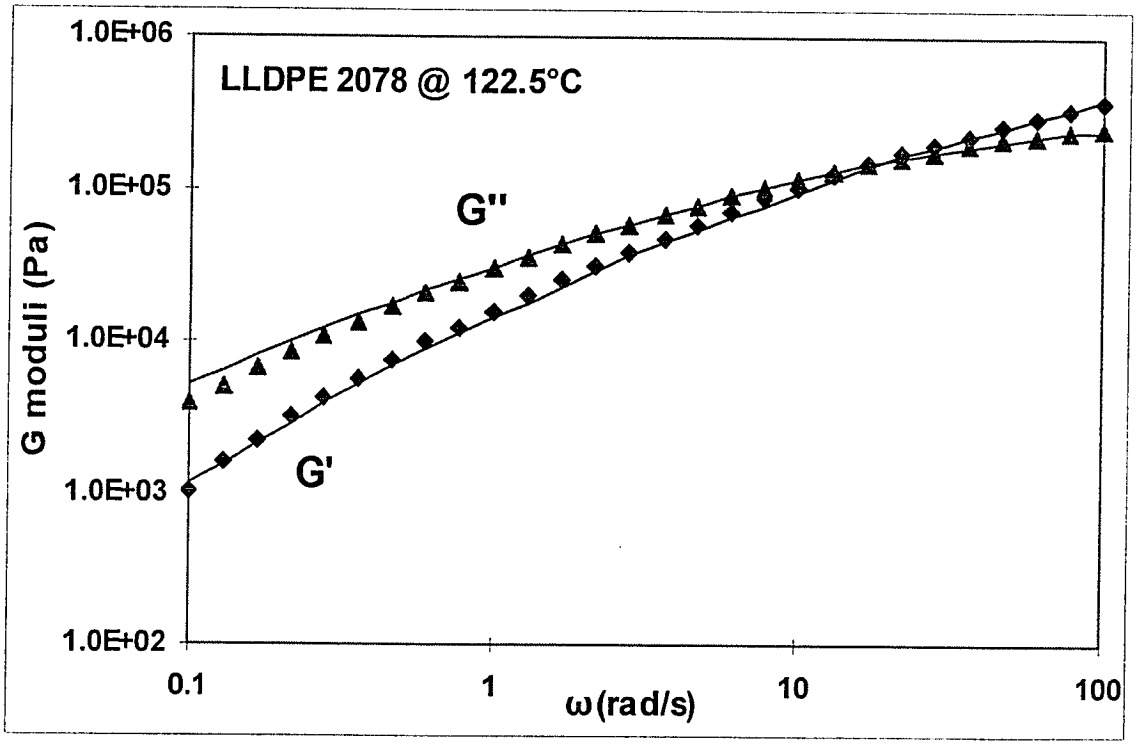
LLDPE 2078 @ 122.5°C
G''
G'
G moduli (Pa)
1.0E+06
1.0E+05
1.0E+04
1.0E+03
1.0E+02
0.1
1
10
100
ω(rad/s)

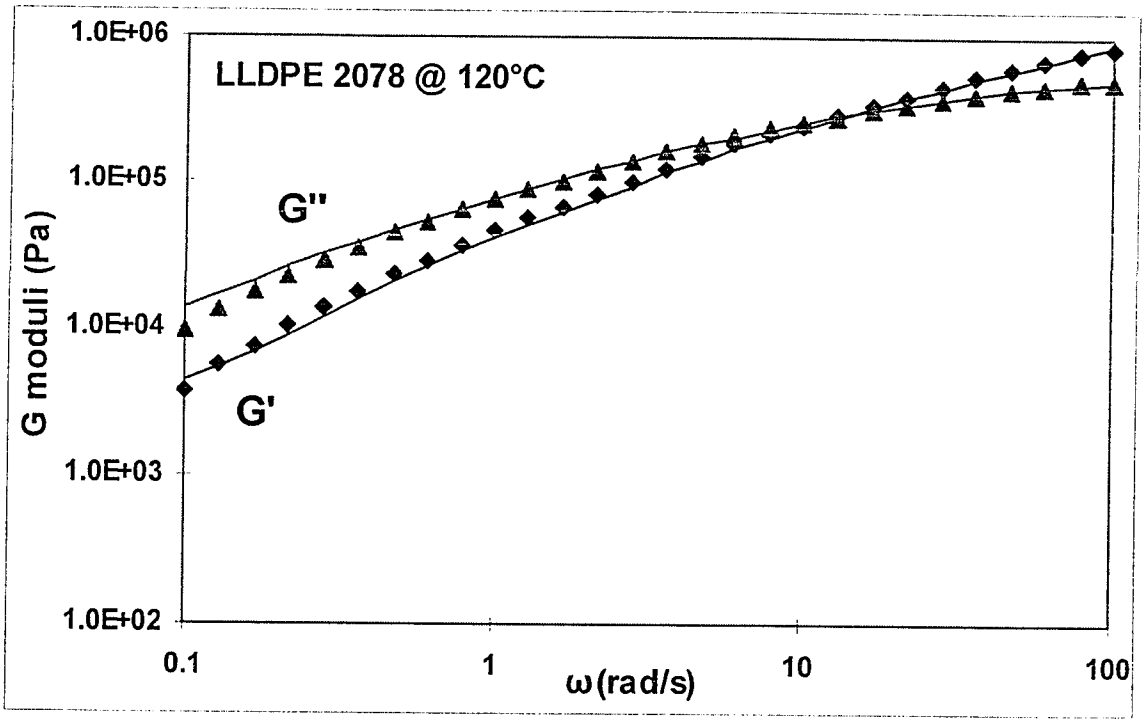

Dow 494 LDPE

Discrete 4-mode relaxation spectra for all the temperatures

190°C		**180°C**		**170°C**	
g_i (Pa)	λ_i (s)	g_i (Pa)	λ_i (s)	g_i (Pa)	λ_i (s)
96007.8	0.009496	93350.86	0.0091007	101687.4	0.009654
28826.19	0.10509	27753.60	0.1017011	30971.10	0.108384
10156.40	0.9144	9686.46	0.88726	10918.30	0.945812
2592.817	8.2095	2588.7	8.4112	3157.845	8.620681

160°C		150°C		140°C	
g_i (Pa)	λ_i (s)	g_i (Pa)	λ_i (s)	g_i (Pa)	λ_i (s)
107067.65	0.0100079	106991.16	0.0101548	121517.71	0.0105250
34144.913	0.1124752	35363.071	0.1172112	42043.250	0.1234067
12616.215	1.0097660	14000.436	1.0862748	17234.507	1.1680705
3678.5603	9.7322416	4481.9815	11.837208	6026.1414	12.360164

135°C		130°C		125°C	
g_i (Pa)	λ_i (s)	g_i (Pa)	λ_i (s)	g_i (Pa)	λ_i (s)
123628.58	0.0106554	120418.93	0.0115044	122429.12	0.0111733
43548.701	0.1252457	44328.480	0.1376032	46438.788	0.1329905
18342.428	1.2025451	19790.385	1.3077102	21326.795	1.2940285
6667.5897	13.273522	9111.4057	14.782729	10077.025	15.529456

120°C		115°C	
g_i (Pa)	λ_i (s)	g_i (Pa)	λ_i (s)
130800.0	0.0116445	182514.9	0.0121394
50002.58	0.1413410	71323.18	0.1477164
23100.00	1.3863998	33634.97	1.4997194
11076.54	16.735192	13849.53	20.02947

Measured values of the storage (G') and loss (G") moduli and the discrete relaxation function fit (using the values shown above) are presented in the following figures for all the measured temperatures

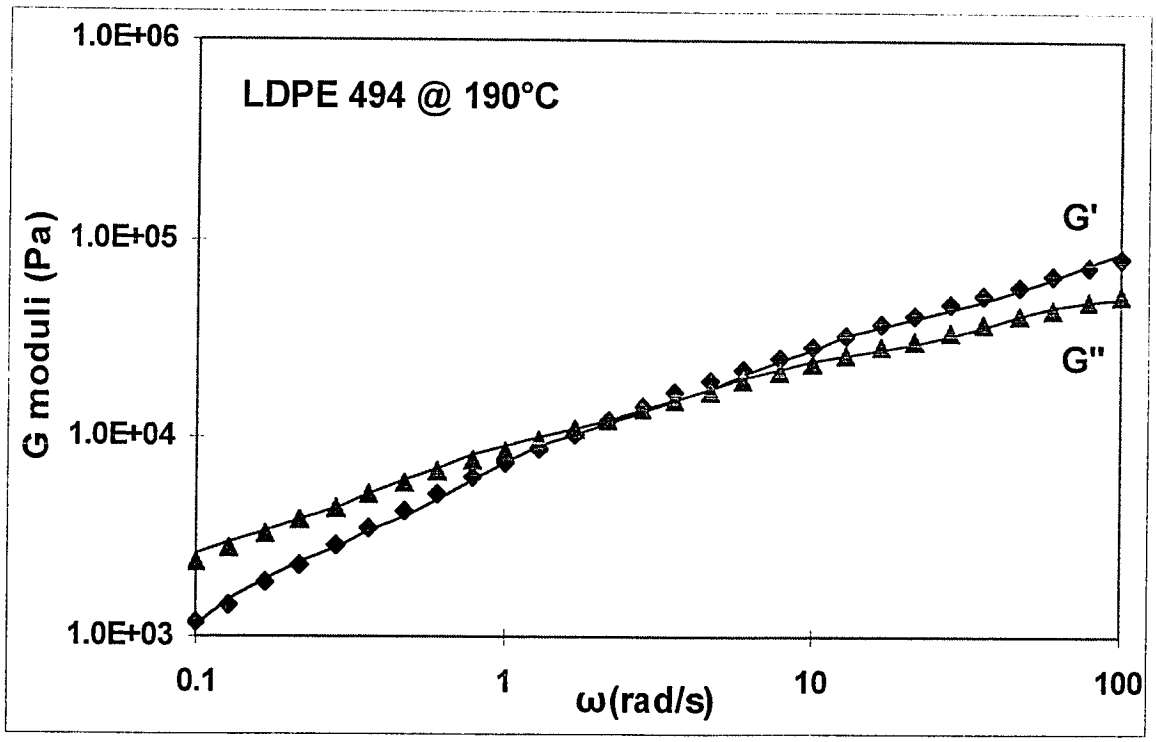

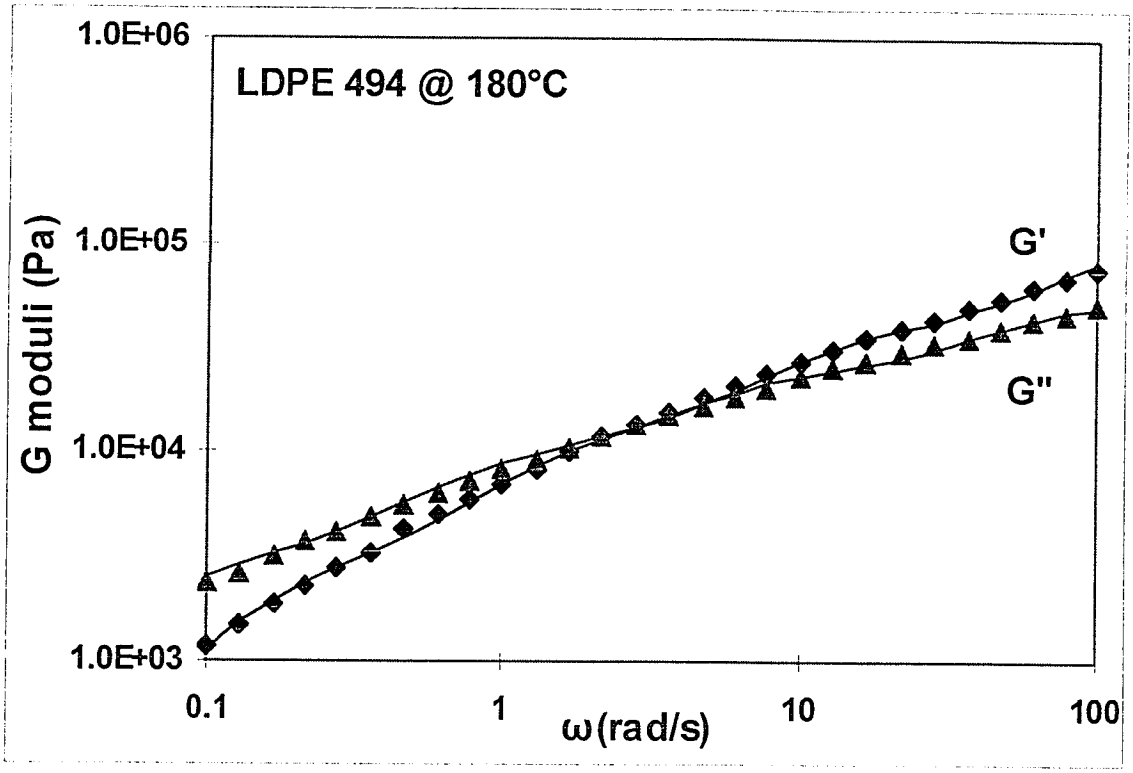
LDPE 494 @ 180°C
G moduli (Pa)
1.0E+06
1.0E+05
1.0E+04
1.0E+03
G'
G"
0.1
1
10
100
ω(rad/s)

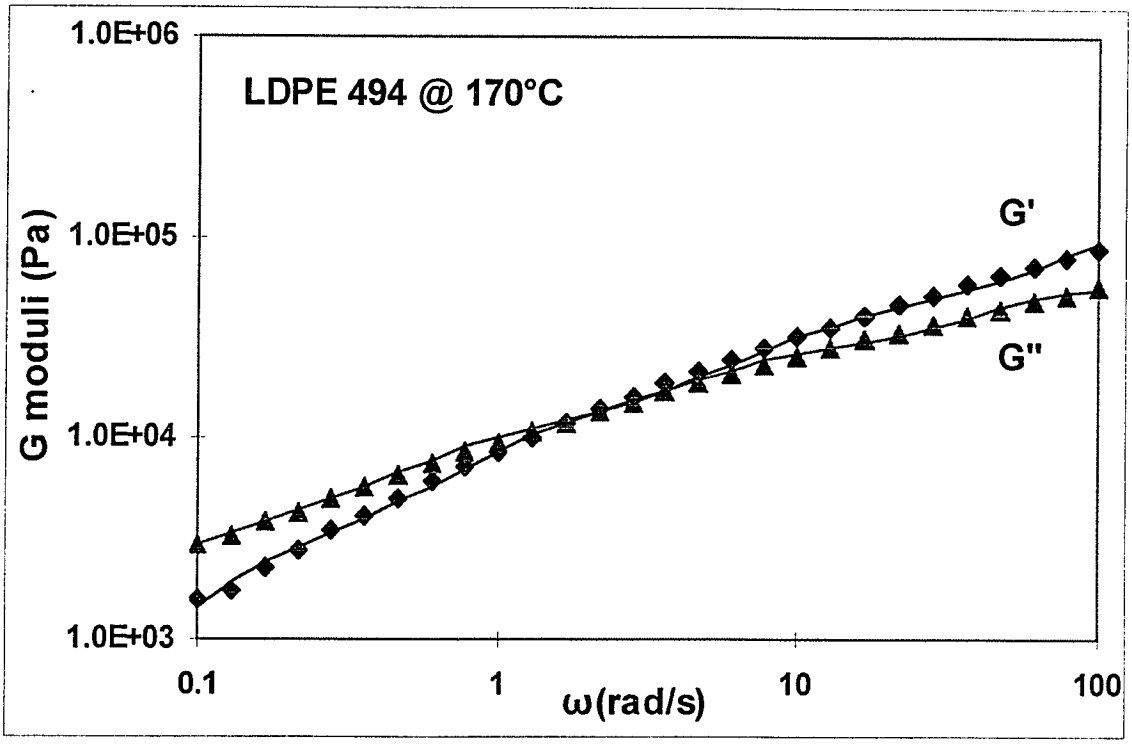
LDPE 494 @ 170°C
G moduli (Pa)
1.0E+06
1.0E+05
1.0E+04
1.0E+03
G'
G"
0.1
1
10
100
ω(rad/s)

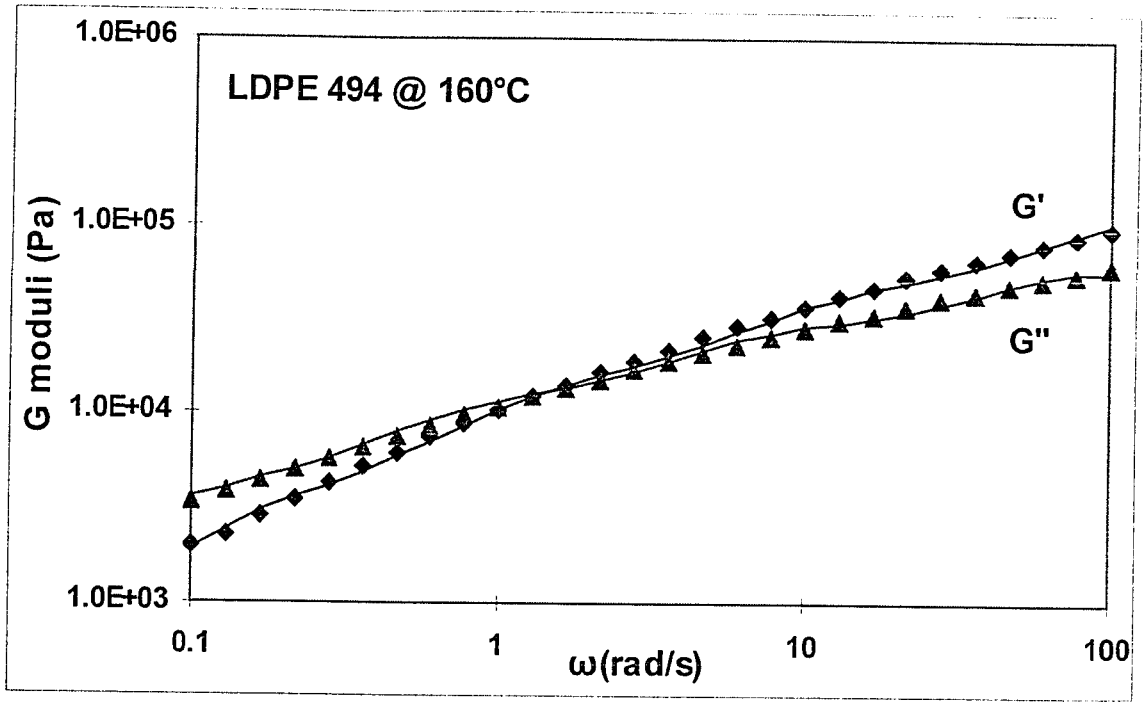
LDPE 494 @ 160°C
G moduli (Pa)
1.0E+06
1.0E+05
1.0E+04
1.0E+03
0.1
1
10
100
ω(rad/s)
G'
G"

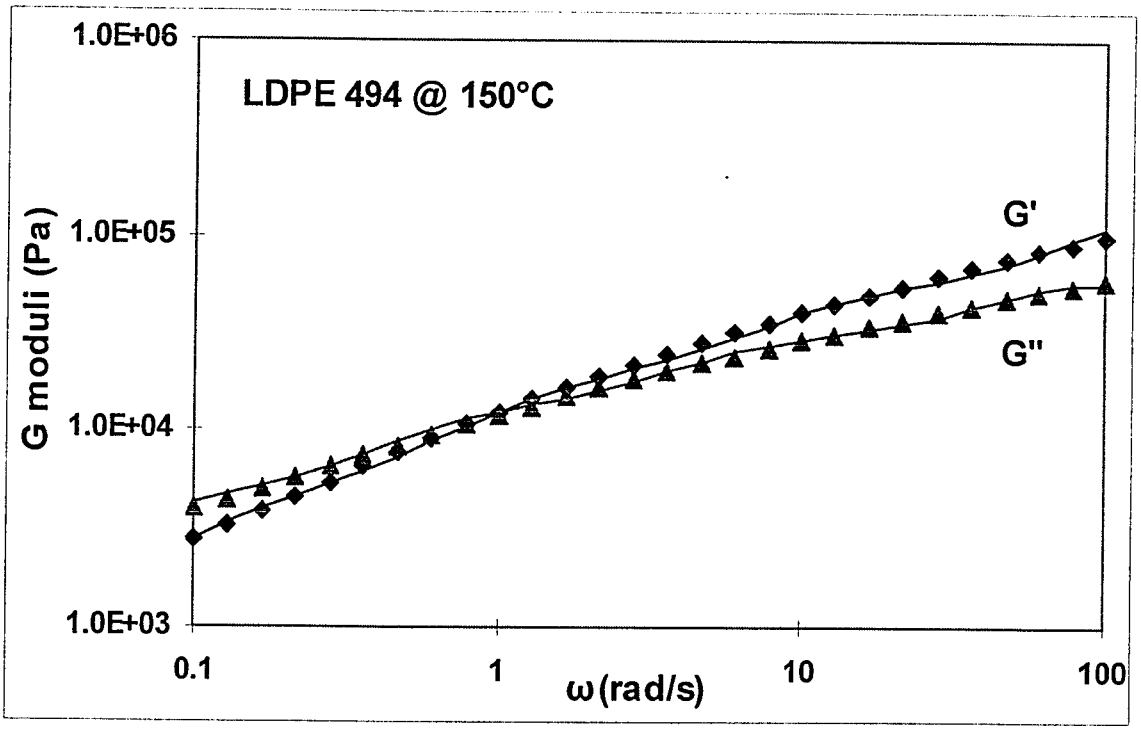
LDPE 494 @ 150°C
G moduli (Pa)
1.0E+06
1.0E+05
1.0E+04
1.0E+03
0.1
1
10
100
ω(rad/s)
G'
G"

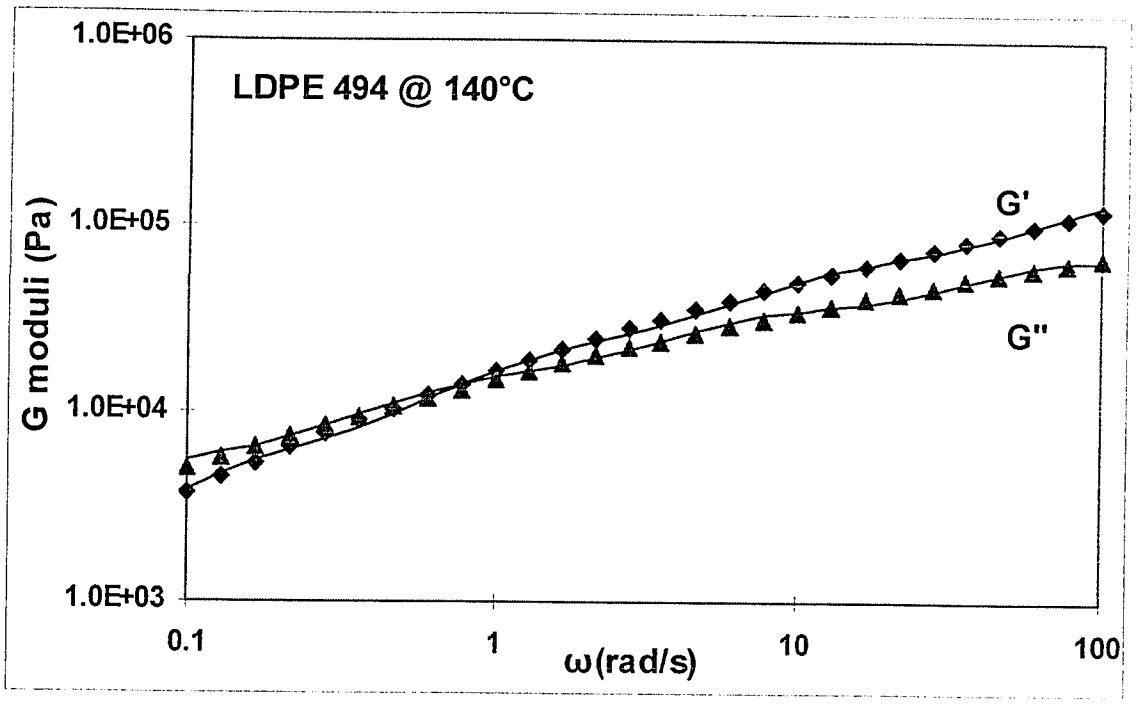
LDPE 494 @ 140°C
G moduli (Pa)
1.0E+06
1.0E+05
1.0E+04
1.0E+03
0.1
1
10
100
ω(rad/s)
G'
G"

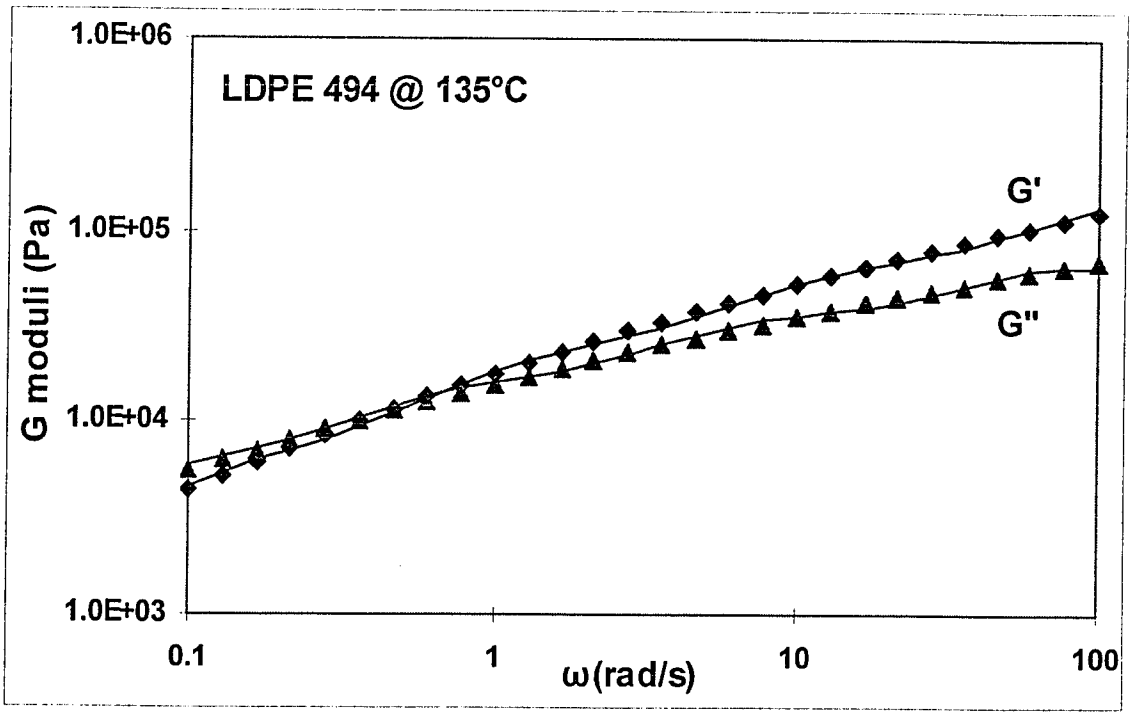
LDPE 494 @ 135°C
G moduli (Pa)
1.0E+06
1.0E+05
1.0E+04
1.0E+03
0.1
1
10
100
ω(rad/s)
G'
G"

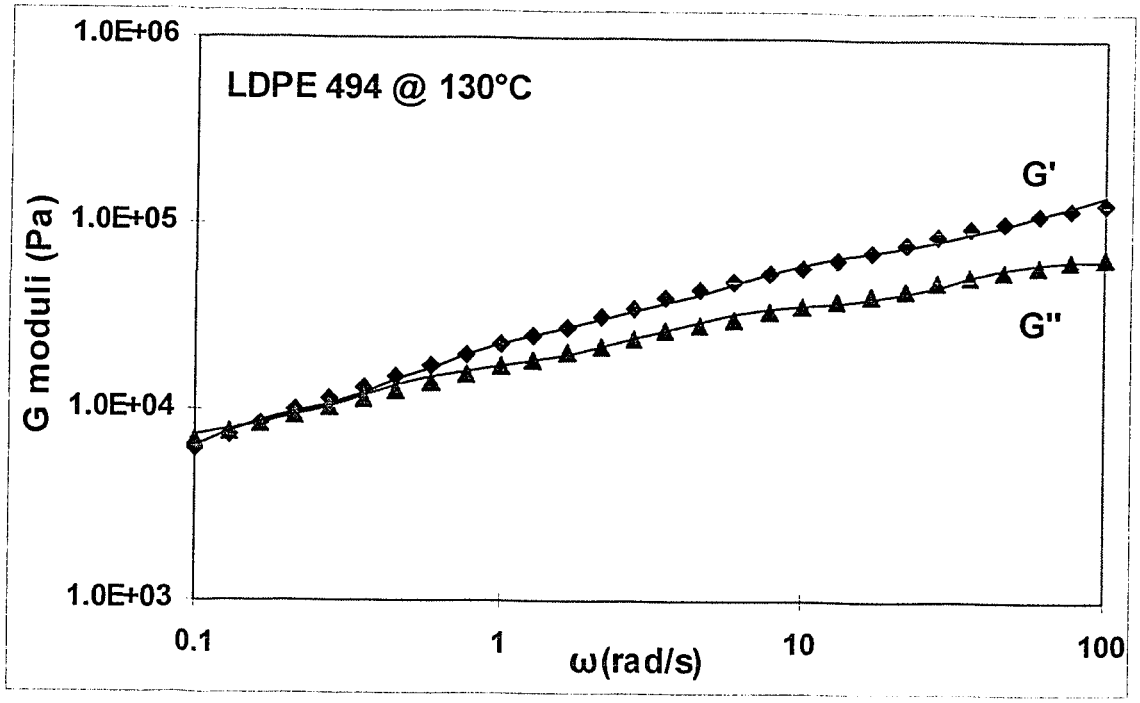
LDPE 494 @ 130°C
G moduli (Pa)
1.0E+06
1.0E+05
1.0E+04
1.0E+03
0.1
1
10
100
ω(rad/s)
G'
G"

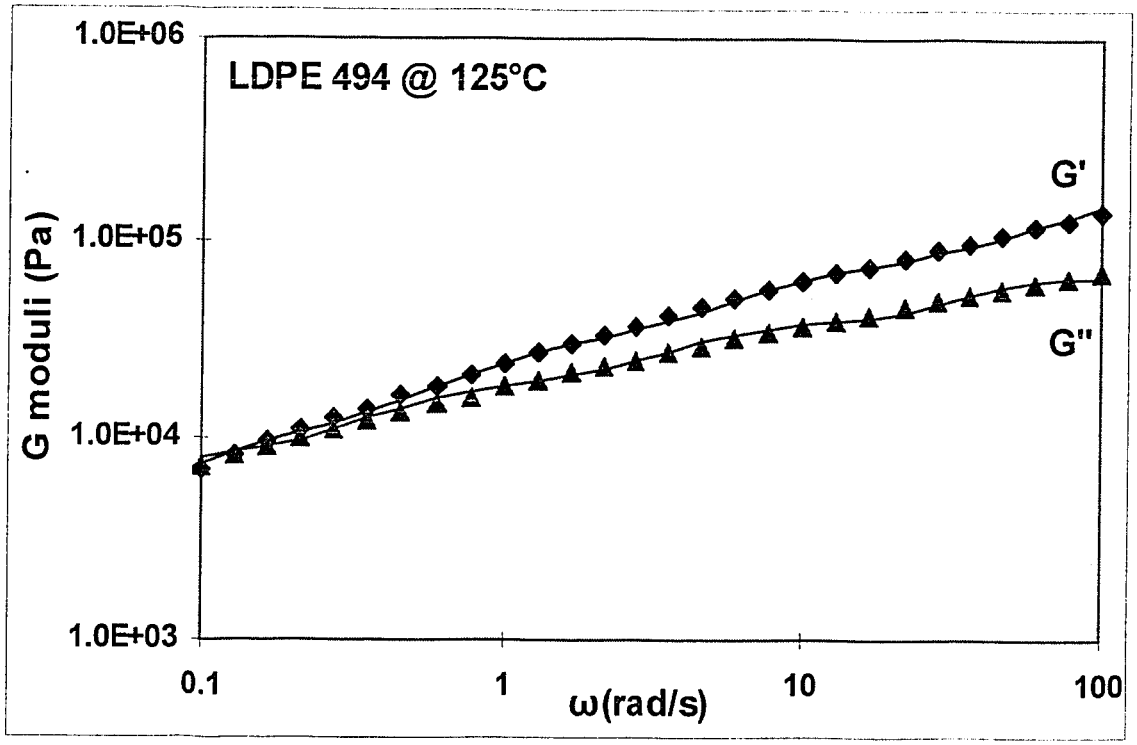
LDPE 494 @ 125°C
G moduli (Pa)
1.0E+06
1.0E+05
1.0E+04
1.0E+03
0.1
1
10
100
ω(rad/s)
G'
G"

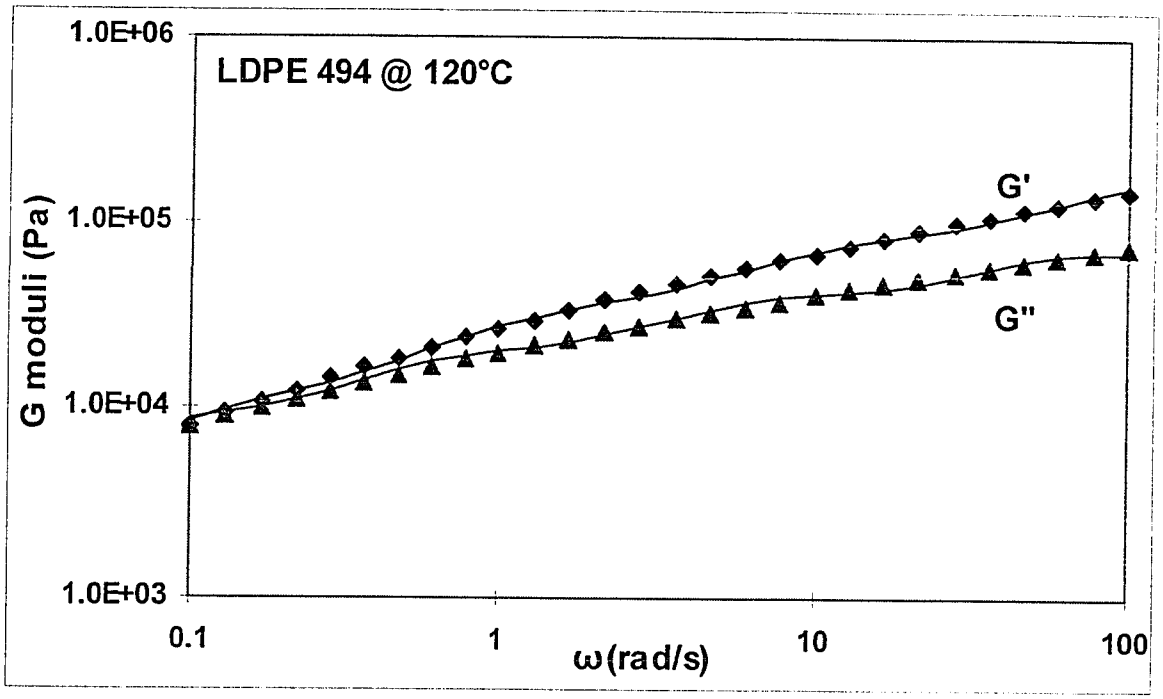
LDPE 494 @ 120°C
G moduli (Pa)
1.0E+06
1.0E+05
1.0E+04
1.0E+03
0.1
1
10
100
ω(rad/s)
G'
G"

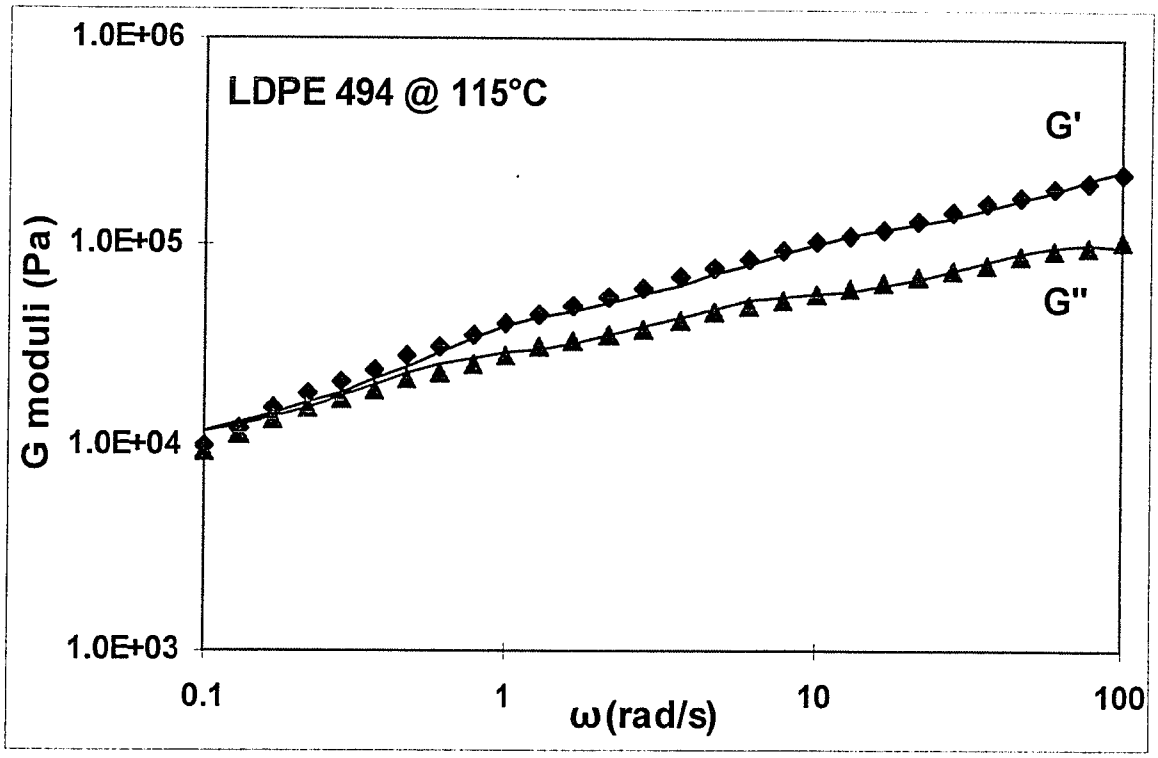
LDPE 494 @ 115°C
G moduli (Pa)
1.0E+06
1.0E+05
1.0E+04
1.0E+03
0.1
1
10
100
ω(rad/s)
G'
G"

REFERENCES

1. Agassant, J. F., Avenas, P., Sergent, J. P., Carreau, P. J., "Polymer Processing: Principles and Modeling", Hanser Publishers, New York, 1991

2. Akaike, O., Tsuji, T., and Nagano, Y., "Simulation of Blown Film Process Taking Account of Cooling-Air Effect", International Polymer Processing, **14**, pp. 168-174, 1999

3. Alaie, S. M. and Papanastasiou, T. C., "Modeling of Non-Isothermal Film Blowing with Integral Constitutive Equations", International Polymer Processing, **7**, pp. 51, 1993

4. André, J. M., Agassant, J. F., Demay, Y., Haudin, J. M. and Monasse, B., "Numerical Modeling of the Polymer Film Blowing Process", Intern. J. Form. Proc., **1**, pp. 187-210, 1998

5. Ashok, B. K., and Campbell, G. A., "Two-phase simulation of tubular film blowing of crystalline polymers", International Polymer Processing, vol. 7, No. 3, pp.240, 1992

6. Ast, W., "Extrusion Von Schlauchfolien. Theoretische Und Experimentele Under-Suchungen Des Abkühlvorganges", Ph.D. thesis, IKT Stuttgart, 1976

7. Baird, D. G. and Collias, D. I., "Polymer Processing Principles and Design", Butterworth-Heinemann, Boston, 1995

8. Baumgärtel, M., and Winter H. H., "Interrelation Between Continuous and Discrete Relaxation Time Spectra", Journal of Non-Newtonian Fluid Mechanics, **44**, pp. 15-36, 1992

9. Baumgärtel, M., Soskey, P. R., and Winter H. H., "IRIS 5: Innovative Rheological Interface Software", IRIS Development, Amherst, MA, 1995

10. Bourque, C., and Newman, B. C., "Reattachment of a Two-Dimensional Incompresible Jet to an Adjacent Flat Plate", The Aeronautical Quarterly, 11, pp. 201-232, 1960

11. Butler, T. I., and Patel, R., "Blown Film Bubble Forming And Quenching Effects On Film Properties", SPE ANTEC Proceedings, pp. 51, 1993

12. Butler, T. I., Lai, S., Spuria J. E., and Patel, R., "Blown Film Frost Line-Freeze Line Interactions", SPE ANTEC, pp. 15, 1994

13. Cain, J. J., and Denn, M. M., "Multiplicities And Instabilities In Film Blowing", Polymer Engineering and Science, **28**, pp. 1527-1541, 1988

14. Campbell, G.A., Obot, N.T., and Cao, B., " Aerodynamics in the Blown Film Process", Polymer Engineering and Science, **32**, pp. 751-759, 1992

15. Cao, B., and Campbell, G. A., "Viscoplastic-Elastic Modeling Of Tubular Blown Film Processing", AIChE Journal, **36**, pp. 420, 1990

16. Cao, B., Sweeney, P., and Campbell, G. A., "Simultaneous Surface And Bulk Temperature Measurement Of Polyethylene During Film Blowing", SPE ANTEC Proceedings, 1989

17. Chen, H. C., and Patel, V. C., AIAA Journal, **26(6)**, pp. 641, 1988

18. Farber, R., and Dealy, J., "Strain History Of The Melt In Film Blowing", Polymer Engineering and Science, vol. 14, No. 6, pp. 435, 1974

19. Feron, B., Wolf, D., and Wortberg, J., "Optimized Cooling and Gauge Tolerences in Blown Film Extrusion", Polymer Engineering and Science, **37**, pp. 876-881, 1997

20. Ferry, J. D., "Viscoelastic Properties of Polymers", 3rd ed., Wiley, 1980

21. Ferziger, J. H. and Peric, M., " Computational Methods for Fluid Dynamics", Springer, Berlin, 1996

22. Fluent Inc., "Fluent Manual", Release 4.4, Lebanon, NY, 1996

23. Gupta, R. K., "A Non-Isothermal Rheological Constitutive Equation And Its Application To Industrial Film Blowing Process", Ph.D. thesis, University of Delaware, 1980

24. Han, C. D. and J. Y. Park, "Studies On Blown Film Extrusion: 2. Analysis Of The Deformation And Heat Transfer Process", Journal of Applied Polymer Science, vol.19, 3277-3290, 1975b

25. Han, C. D. and J. Y. Park, "Studies On Blown Film Extrusion: 3. Bubble Instability", Journal of Applied Polymer Science, vol.19, 3291-3297, 1975c

26. Han, C. D. and J. Y. Park, "Studies On Blown Film Extrusion: 1. Experimental Determination Of Elongational Viscosity", Journal of Applied Polymer Science, vol.19, 3257-3276, 1975a

27. Hauck, J. and Michaeli, W., "Investigation Into the Cooling Characteristics of Blown Film Extrusion Lines", Proceedings SPE ANTEC, Atlanta, pp.123, 1998

28. Incropera, F. P. and DeWitt, D. P., "Introduction to Heat Transfer", 2nd Edition, Wiley, New York, 1990

29. Kanai, T., "Theoretical analysis of tubular film extrusion and its applications for HMW-HDPE", International Polymer Processing, **1**, pp. 137, 1987

30. Kanai, T., and White, J., "Dynamics, Heat Transfer And Structure Development In Tubular Film Extrusion Of Polymer Melts: A Mathematical Model And Predictions", Journal of Polymer Engineering, **5**, pp. 136-157, 1985

31. Kanai, T., and White, J., "Kinematics, Dynamics And Stability Of The Tubular Film Extrusion Of Various Polyethylenes", Polymer Engineering and Science, **24**, pp. 1184-1200, 1984

32. Knittel, R. R., "A Review of the Blown Film Process", SPE ANTEC Proceedings, pp.92, Indianapolis, 1996

33. Knittel, R.R., and DeJonghe, J., "Blown Film Cooling Systems", Film Extrusion Manual, Ch. 12, TAPPI Press, Atlanta, GA, 1992

34. Kwack, T. H., Han, C. D., and Vickers M. E., "Development Of Crystalline Structure During Tubular Film Blowing Of Low-Density Polyethylene", Journal of Applied Polymer Science, **35**, 363-389, 1988

35. Lagasse, R. R. and Maxwell, B., "An Experimental Study of the Kinetics of Polymer Crystallization During Shear Flow", Polymer Engineering Science, **16**, pp. 189, 1976

36. Launder, B.E. and Spalding, D.B., "The Numerical Computation of Turbulent Flows", Computer Methods in Applied Mechanics and Engineering, **3**, pp. 269-289, 1974

37. Liu, C. C., Bogue, D. C., and Spruiell, J. E., "Tubular Film Blowing. Part 1: On-line Experimental Studies", International Polymer Processing, **10**, pp. 226-229, 1995a

38. Liu, C. C., Bogue, D. C., and Spruiell, J. E., "Tubular Film Blowing. Part 2: Theoretical Modeling", International Polymer Processing, **10**, pp. 230-236, 1995b

39. Luo, X. L., and Tanner, R. I., "A Computer Study Of Film Blowing", Polymer Engineering and Science, **25**, pp. 620-629, 1985

40. Macosko, C. W., "Rheology Principles, Measurements and Applications", VCH Publishers, Weinheim, 1994

41. Micic, P., "Melt Strength Enhancement of Linear Low Polyethylene", Ph.D. Thesis, RMIT, Melburne, Australia, 1997

42. Mohanty, A. K., and Tawfek, A. A., "Heat Transfer Due To A Round Jet Impinging Normal To A Flat Surface", International Journal of Heat and Mass Transfer, **36**, No.6, pp.1639-1647, 1993

43. Moriarity, G., "Air Rings -- Make Them Work For You, Not Against You", Plastics Technology, **45**, vol. 4, pp. 60-62, 1999

44. Nagarajan, G., and Campbell, G. A., "Experimental Determination of Heat Transfer Coefficient in Blown Film Process", SPE ANTEC Proccedings, Boston, 1995

45. Nagarajan, G., Modeling of Blown Film Process: Heat Transfer Analysis and Development of Physical Properties in Crystalline Polymers", Ph.D. Thesis, Clarkson University, Potsdam, 1996

46. Pearson, J. R. A., and Petrie, C. J. S., "A Fluid Mechanical Analysis Of The Film-Blowing Process", Plastics & Polymers, April, pp. 85, 1970a

47. Pearson, J. R. A., and Petrie, C. J. S., "The Flow Of A Tubular Film. Part 1. Formal Mathematical Representation ", Journal of Fluid Mechanics, **40**, pp.1-19, 1970b

48. Pearson, J. R. A., and Petrie, C. J. S., "The flow of a tubular film. Part 2. Interpretation of the model and discussion of solutions", Journal of Fluid Mechanics, **42**, pp.609-625, 1970c

49. Perdikoulias, J., Vlcek, J., and Vlachopoulos, J., Chapter 2.2 in Campbell, G. A., and Kanai, T. (Eds), "Film Processing", Hanser, Munich, 1999

50. Petrie, C. J. S., "A comparison of theoretical predictions with published experimental measurements on the blown film process", AIChE Journal, **21**, pp. 275, 1975

51. Ryan, S. R., "15 Ways To Raise Blown Film Productivity", Plastics Technology, **45**, vol. 2, pp. 44-49, 1999

52. Sidiropoulos, V., "Comparison Of Experiments With A Model Of The Blown Film Process", Master Thesis, McMaster University, Hamilton, 1995

53. Sidiropoulos, V., and Vlachopoulos, J., "An Investigation of Venturi and Coanda Effects in Blown Film Cooling", International Polymer Processing, **15**, pp. 40-45, 2000

54. Sidiropoulos, V., and Vlachopoulos, J., "The Effects Of Dual-Orifice Air-Ring Design On Blown Film Cooling", Polymer Engineering & Science, in Print

55. Sidiropoulos, V., Tian, J. J., and Vlachopoulos, J., "Computer Simulation of Film Blowing", TAPPI Journal, **79**, pp. 113-118, 1996a

56. Sidiropoulos, V., Tian, J. J., and Vlachopoulos, J., "Computer Simulation of Film Blowing", Journal of Plastic Film & Sheeting, **12**, pp.107-129, 1996b

57. Sidiropoulos, V., Wood, P. E., and Vlachopoulos, J., "The Aerodynamics of Cooling of Blown Film Bubbles", Journal of Reinforced Plastics and Composites, **18**, pp. 529, 1999

58. Simpson, D. A., "A Study Of The Effects Of Processing Parameters On The Morphologies And Mechanical Properties Of Polyethylene Blown Films", Ph.D. thesis, Pennsylvania State University, 1993

59. Tanner, R. I., "Engineering Rheology", Clarendon Press, Oxford, 1985.

60. Tas, P. P., "Film blowing: from polymer to Product", Ph.D. thesis, Eindhoven University of Technology, 1994

61. Tennekes, H. and Lumley, J. L., "A First Course in Turbulence", 16th Edition, MIT Press, Cambridge MA, 1997

62. Tucker, C. L. (editor), "Fundamentals of computer modeling for polymer processing", Hanser Publishers, New York, 1989

63. Vlachopoulos, J., "Introduction to Plastics Processing", Lecture Notes, Dept. of Chem. Eng., McMaster University, Hamilton, 1997

64. Wagner, M. H., "Ein Rheologisch-Thermodynamisches Prozessmodell Des Folien-Blasverfahrens", Ph.D. thesis, IKT Stuttgart, 1976

65. White, J. L., and Cakmak, M., Advanced Polymer Technology, **8**, pp.27, 1988

66. Winkler, G., Chapter 4 in Hensen, F. (Ed) "Plastics Extrusion Technology", Hanser, Munich, 1997

67. Wolf, D., Feron, B., and Wortberg, J., "Numerical Analysis of Cooling Air Systems in Film Blowing", International Polymer Processing, **12**, pp. 38-44, 1997

68. Wolfstein, M., International Journal of Heat & Mass Transfer, **12**, pp. 301, 1969

69. Wright, W. D., "Blown-Film Cooling Joins The March Toward More Efficient Processing", Plastics Engineering, pp. 30-33, Sept., 1981

70. Xue, S. C., Phan-Thien, N., and Tanner, R. I., "Numerical Study Of Secondary Flows Of Viscoelastic Fluid In Straight Pipes By An Implicit Finite Volume Method", Journal of Non-Newtonian Fluid Mechanics, **59**, pp. 191-213, 1995

71. Ziabicki, A. and Jarecki, L., in "High Speed Fiber Spinning" by Ziabicki, A., and Kawai, H. (Eds), J. Wiley & Sons, New York, 1985